

## Systems biology of energy metabolism in skeletal muscle

**Citation for published version (APA):**

Schmitz, J. P. J. (2012). *Systems biology of energy metabolism in skeletal muscle*. [Phd Thesis 1 (Research TU/e / Graduation TU/e), Biomedical Engineering]. Technische Universiteit Eindhoven.  
<https://doi.org/10.6100/IR739234>

**DOI:**

[10.6100/IR739234](https://doi.org/10.6100/IR739234)

**Document status and date:**

Published: 01/01/2012

**Document Version:**

Publisher's PDF, also known as Version of Record (includes final page, issue and volume numbers)

**Please check the document version of this publication:**

- A submitted manuscript is the version of the article upon submission and before peer-review. There can be important differences between the submitted version and the official published version of record. People interested in the research are advised to contact the author for the final version of the publication, or visit the DOI to the publisher's website.
- The final author version and the galley proof are versions of the publication after peer review.
- The final published version features the final layout of the paper including the volume, issue and page numbers.

[Link to publication](#)

**General rights**

Copyright and moral rights for the publications made accessible in the public portal are retained by the authors and/or other copyright owners and it is a condition of accessing publications that users recognise and abide by the legal requirements associated with these rights.

- Users may download and print one copy of any publication from the public portal for the purpose of private study or research.
- You may not further distribute the material or use it for any profit-making activity or commercial gain
- You may freely distribute the URL identifying the publication in the public portal.

If the publication is distributed under the terms of Article 25fa of the Dutch Copyright Act, indicated by the "Taverne" license above, please follow below link for the End User Agreement:

[www.tue.nl/taverne](http://www.tue.nl/taverne)

**Take down policy**

If you believe that this document breaches copyright please contact us at:

[openaccess@tue.nl](mailto:openaccess@tue.nl)

providing details and we will investigate your claim.

# **Systems Biology of Energy Metabolism in Skeletal Muscle**

Joep Schmitz

A catalogue record is available from the Eindhoven University of Technology Library.

ISBN: 978-90-386-3279-7

Copyright © 2012 by Joep Schmitz

Cover design: Joep Schmitz and Koen Pieterse

Printed by: Ipskamp Drukkers, Enschede, the Netherlands

The research described in this thesis was performed within the framework of CTMM, the Center for Translational Molecular Medicine, project PREDICt grant 01C-104, supported by the Netherlands Heart Foundation, Dutch Diabetes Research Foundation and Dutch Kidney Foundation.

# **Systems Biology of Energy Metabolism in Skeletal Muscle**

PROEFSCHRIFT

ter verkrijging van de graad van doctor aan de  
Technische Universiteit Eindhoven, op gezag van de  
rector magnificus, prof.dr.ir. C.J. van Duijn, voor een  
commissie aangewezen door het College voor  
Promoties in het openbaar te verdedigen  
op donderdag 6 december 2012 om 16.00 uur

door

Jozef Petrus Johannes Schmitz

geboren te Roermond

Dit proefschrift is goedgekeurd door de promotor:

prof.dr. P.A.J. Hilbers

Copromotoren:

dr. J.A.L. Jeneson

en

dr.ir. N.A.W. van Riel





## CONTENTS

<b>Chapter 1</b>	General introduction	1
<b>Chapter 2</b>	Silencing of glycolysis in skeletal muscle : experimental observation and numerical analysis	21
<b>Chapter 3</b>	Combined <i>in vivo</i> and <i>in silico</i> investigations of activation of glycolysis in contracting skeletal muscle	45
<b>Chapter 4</b>	Magnitude and control of mitochondrial sensitivity to ADP	73
<b>Chapter 5</b>	Prediction of muscle energy states at low metabolic rates requires feedback control of mitochondrial respiratory chain activity by inorganic phosphate	97
<b>Chapter 6</b>	Mitochondrial function in skeletal muscle: numerical dissection of a multi - factorial process	121
<b>Chapter 7</b>	Integration of <i>in vivo</i> , <i>in vitro</i> and <i>in silico</i> methods for systems biology of mitochondrial function	141
<b>Chapter 8</b>	<i>In vivo</i> and <i>in silico</i> studies of the regulation of glycolytic versus mitochondrial flux in normoxic skeletal muscle	157
<b>Chapter 9</b>	Summarizing discussion and future perspective	179
	Summary	189
	Nederlandse samenvatting	
	Dankwoord	
	List of Publications	
	Curriculum Vitae	





# Chapter 1

## *General introduction*

In part adapted from

J.P.J. Schmitz, J. Vanlier, N.A.W. van Riel, J.A.L. Jeneson  
*Computational modeling of mitochondrial energy transduction*  
Critical Reviews in Biomedical Engineering, 2011, 39(5):363-377

## INTRODUCTION

The primary function of skeletal muscle tissue is to produce force or cause motion. To perform this task, chemical energy stored in nutrients (glucose and fatty acids) has to be converted into an energy currency that can drive muscle contraction. This process is known as 'energy metabolism' or 'bioenergetics' of skeletal muscle cells. It comprises a large number of chemical reactions, which are organized in metabolic pathways. In these pathways chemicals are transformed by a series of steps into other chemicals, often catalyzed by a sequence of enzymes. Unraveling the makeup of this complex network is interesting from a fundamental biological perspective, but also essential to understand how a disturbance of muscle bioenergetics can cause metabolic disorders. The need for this information is becoming all the more pressing because as a result of modern Western lifestyle (physical inactivity and excessive food intake) the society is faced by an epidemic growth of metabolic disorders like type 2 diabetes (1).

<sup>31</sup>P magnetic resonance spectroscopy (MRS) has emerged as one of the premier methods to study bioenergetics of skeletal muscle *in vivo*. It enables non-invasive measurements of key metabolites in skeletal muscle during rest – exercise – recovery protocols. Analyses of these dynamics play a vital role in achieving a better understanding of many basic aspects of muscle function. In addition, <sup>31</sup>P MRS provides an important tool for diagnostic procedures as well as to monitor the effects of therapeutic and lifestyle interventions for diseases that have an increasing impact in modern society, e.g., type 2 diabetes (2-4) and aging (5,6). Extracting relevant information about muscle physiology from these metabolite dynamics is however not a trivial procedure. It often requires combining measurement results with prior knowledge and specific assumptions on muscle physiology. Mathematical modeling has been proven a powerful tool to facilitate these analyses. As such, it can be considered an essential aspect in the application of <sup>31</sup>P MRS to study muscle physiology.

For a long time, application of mathematical models for analyses of <sup>31</sup>P MRS data has remained limited to rather straightforward phenomenological models. Examples of successful application of these models are: investigations of the control of mitochondrial respiration (7,8), quantification of oxidative capacity in skeletal muscle (9,10) or estimation of glycolytic flux from pH time course data (11). The phenomenological modeling approaches are particularly successful in quantification of macroscopic physiological parameters, e.g. mitochondrial function or glycolytic flux. They are however much less suited for connecting macroscopic *in vivo* observations to a detailed mechanistic understanding at the level of the metabolic networks. Metabolic diseases are however often caused by a disturbance at pathway level. It would therefore be potentially very powerful if the available methods could be supplemented by new techniques that enable mapping of observed metabolite dynamics to a more detailed mechanistic understanding at the level of the metabolic pathways.

The scientific discipline known as systems biology aims to bridge the gap between macroscopic physiological observations and mechanistic understanding by application of detailed computational modeling (12,13). This thesis describes a series of studies in which detailed mechanistic models of muscle bioenergetics were developed and applied for analyses of skeletal muscle bioenergetics.

This chapter provides an overview of the background of the thesis. First, the processes involved in skeletal muscle energy metabolism are summarized. Next, a short introduction in  $^{31}\text{P}$  nuclear magnetic resonance spectroscopy will be provided, followed by a brief section discussing phenomenological models which are considered particularly relevant for design, testing or application of the mechanistic modeling strategy proposed in this thesis. Developing models that capture the full complexity of the relevant metabolic pathway represents a daunting task. Obviously, it cannot be achieved in a single effort. It requires an iterative model building strategy tailored to overcome challenges associated with the degree of complexity involved. In this chapter, formalisms for the development of mechanistic models designed with these challenges in mind will be discussed. Next, the progress resulting from previous studies that are a basis for the studies described in this dissertation is briefly summarized. Finally, the outline of the thesis is provided.

## **SKELETAL MUSCLE ENERGY METABOLISM**

Muscle contractions require large amounts of energy; the metabolic rate of muscle cells is increased over hundred-fold during rest to vigorous exercise conditions (14,15). Adenosine-triphosphate (ATP) is used to drive most of all energy depending cellular processes, including muscle contraction (16). ATP can therefore be considered the energy currency of the cell. The two phosphor-anhydride bonds in ATP are responsible for the high energy content of the molecule; energy stored in ATP is released upon hydrolysis of the terminal anhydride bond, thereby forming adenosine-diphosphate (ADP) and inorganic phosphate (Pi).

The amount of ATP in muscle cells is only sufficient to maintain contractions for a couple of seconds. Therefore the ADP has to be rephosphorylated back to ATP. Skeletal muscle cells contain three main mechanisms for rephosphorylation of ADP (Figure 1). Human muscle cells can store large amounts of glycogen (16). Cleavage of glycogen results in formation of glucose-1-phosphate which can enter the glycolytic pathway. In this pathway the phosphorylated sugar is broken down to pyruvate yielding 2 molecules of ATP. The glycolytic pathway has the ability to produce large amounts of ATP in the absence of oxygen. However, it can extract only a relative small amount of the chemical energy from the glucose molecules.

The major part of energy stored in glucose and fatty acids is extracted from these nutrients in mitochondria. These organelles can therefore be considered the 'powerhouse' of the cell. The organelle is surrounded by two lipid bilayer membranes: the inner and outer membrane. The inner cavity of mitochondria (matrix) contains enzymes which are involved in the oxidation of carbohydrates and fatty acids. These enzymes are organized in the tricarboxylic acid (TCA) cycle and the  $\beta$ -oxidation pathway, respectively (16). Pyruvate is transported into the matrix and converted by the pyruvate dehydrogenase complex (PDH) to acetyl-CoA. Fatty acids are also broken down into acetyl-CoA in the  $\beta$ -oxidation pathway, thereby yielding high energy molecules: nicotinamide adenine dinucleotide (NADH) and flavin adenine dinucleotide ( $\text{FADH}_2$ ). Next, acetyl-CoA enters the next step in the oxidative process: the TCA cycle, which again yields NADH and  $\text{FADH}_2$ . The electron donors NADH and  $\text{FADH}_2$  transfer their electrons to oxygen in a sequence of steps called the electron transport chain (ETC). The enzymes that catalyze these reactions

simultaneously create a proton and electrochemical gradient across the inner mitochondrial membrane. This proton gradient is used by the  $F_1F_0$ -ATP synthase complex to form ATP from ADP and  $P_i$ .

Glycolysis and mitochondria use the chemical energy stored in nutrients to synthesize ATP, the third source uses the energy stored in the high energy phosphate bond in phosphocreatine (PCr). The reaction (Eq. 1) is catalyzed by creatine kinase (CK).

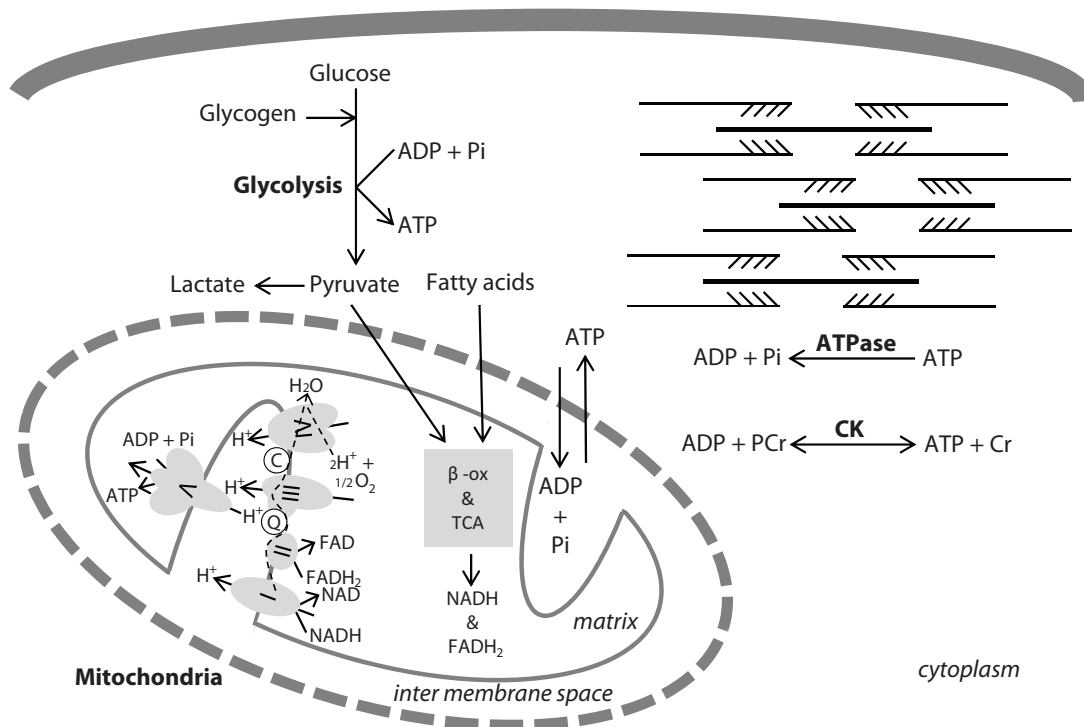
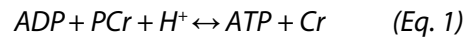


**Figure 1.** Schematic overview of ATP metabolism in skeletal muscle. ATP is hydrolyzed to drive energy dependent processes like e.g., basal metabolism, contractile proteins and ion pumps (ATPase). ATP is resynthesized by rephosphorylation of ADP by 3 processes: (i) glycolysis in cytoplasm, (ii) oxidative phosphorylation in the mitochondria, (iii) PCr hydrolysis in the cytoplasm (CK).

## <sup>31</sup>P NUCLEAR MAGNETIC RESONANCE SPECTROSCOPY

The first papers demonstrating the use of *in vivo* <sup>31</sup>P magnetic resonance spectroscopy to study the cellular bioenergetics date back to the seventies and eighties (17,18). For a review of the early progress of the field we refer to Chance et al. (19). Nuclear magnetic resonance spectroscopy exploits the property of nuclei that within the same or between different molecules they absorb and emit energy at different frequencies, directly related to its chemical environment. In case of phosphorous nuclei in skeletal muscle tissue, typically, 7 resonances can be distinguished: phosphor-monoesters (PME), inorganic phosphate (Pi), phosphor-diester (PDE), phosphocreatine

(PCr), gamma-ATP, alpha-ATP and beta-ATP. Figure 2A shows a  $^{31}\text{P}$  MRS spectrum recorded in resting human quadriceps muscle at a magnetic field strength of 1.5T. Resonances of the different metabolites are indicated in Figure 2A. The intensity of a resonance reflects the cellular concentration of the corresponding metabolite(s). They can be converted to molar concentrations by using an internal or external reference. In case of human skeletal muscle tissue often the ATP resonance is used as internal reference (for an extensive review see (20)). In addition, the chemical shift differences between Pi and PCr provides an accurate measure of cellular pH (21).

Figure 2B shows a stack plot of a series of spectra recorded during a rest – exercise – recovery protocol. At the onset of exercise, cellular ATP demand is larger than ATP synthesis flux. The imbalance between ATP demand and supply fluxes is not reflected by a decrease of the ATP resonances, instead, a drop in PCr concentration and corresponding increase in Pi is observed. During intense muscle contractions these metabolite dynamics are paralleled by a decreasing pH, which is predominantly a result of lactate and  $\text{CO}_2$  accumulation in the muscle cells (16). During the recovery period the imbalance between ATP demand and supply flux is reversed (ATP production exceeds demand). As a result, Pi is consumed and the PCr pool is replenished again. During contraction, ATP is supplied by both the mitochondrial and glycolytic pathways. During recovery period following exercise, glycolytic flux is rapidly deactivated (11,14,22). It is therefore assumed that during recovery period ATP is supplied almost purely oxidative.

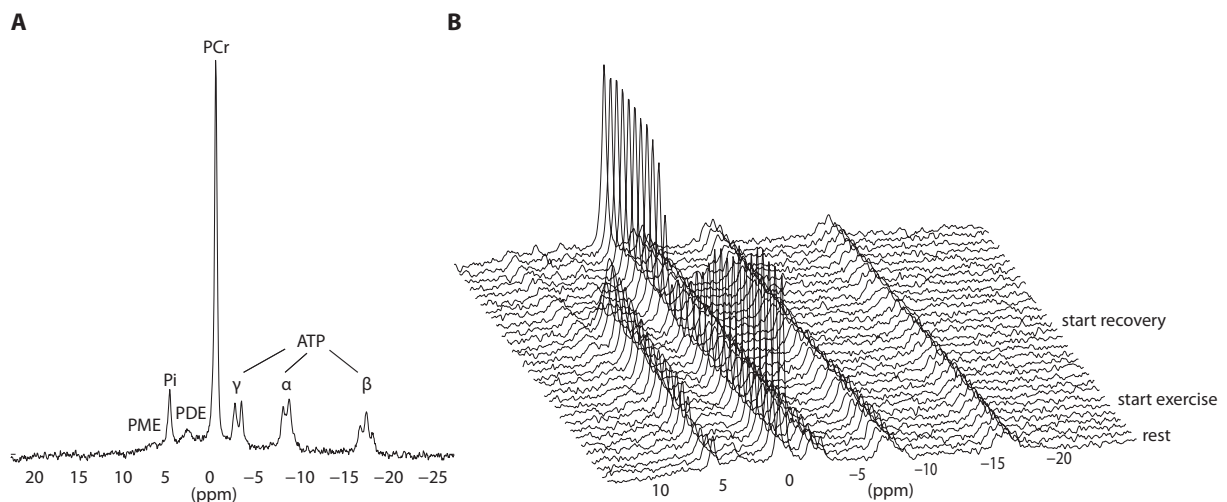


**Figure 2.** Typical example of a  $^{31}\text{P}$  MRS spectrum recorded in human quadriceps muscle at rest (A). The individual resonances are indicated in the image. Stack-plot of a series of spectra recorded during a rest – exercise – recovery protocol (B). Time resolution of the spectra is 30 seconds. The spectra are processed with 10Hz line broadening.

Creatine kinase (CK) catalyzes the reversible transfer of phosphate between PCr and ATP. Its biochemical properties play a central role in ATP metabolism of muscle cells. In fact, several key assumptions underlying interpretation of  $^{31}\text{P}$  MRS data are related to CK enzyme kinetics. Therefore, these enzyme properties will be described in more detail.

Although there is some controversy about the actual value (23), the enzyme has a very high activity *in vivo*. For the physiological range of [PCr], [Cr], [ATP], [ADP] and pH the enzyme is therefore assumed to be close to equilibrium (10). The equilibrium relation is given by Eq. 2.

$$[\text{ADP}] \cdot [\text{H}^+] \cdot [\text{PCr}] \cdot K_{app} = [\text{Cr}] \cdot [\text{ATP}] \quad (\text{Eq. 2})$$

Where,  $K_{app}$  is the apparent CK equilibrium constant which has a value of about  $1.66 \cdot 10^9$  (24).

This relation is often exploited to estimate cellular [ADP] from the observed [PCr], [ATP] and [H<sup>+</sup>] according to Eq. 3.

$$[ADP] = ([Cr] \cdot [ATP]) / ([H^+] \cdot [PCr] \cdot K_{app}) \quad (Eq. 3)$$

Estimation of [ADP] requires specific assumptions about the [Cr] at rest. In general, for human skeletal muscle tissue, it is assumed that the total creatine (TCr) content is ~ 42mM (20) and ~85% of the total creatine pool is phosphorylated at rest (20). Kemp et al. summarized data on metabolite concentrations in skeletal muscle at rest (20). Their results indicated a rather large spread in TCr content (40 – 50mM) and resting [PCr] (30 – 40mM) reported between studies. In addition, a significant correlation between [TCr] and [PCr] was reported. This correlation indicated that although [PCr] and [TCr] may vary between subjects, the estimate that ~85% of the [TCr] pool is phosphorylated at rest can be considered quite reliable.

The equilibrium relation combined with the assumption that the enzyme is always near – equilibrium provides a basic model of CK. An alternative model can be constructed by considering the enzymes detailed kinetic properties (see e.g.: (23,25,26)). These investigations indicated that during rapid changes in ATP consumption rates there is probably a small transient disequilibrium of up to a few percent. The consequences of this disequilibrium on muscle bioenergetics are however small. It seems therefore an appropriate reduction of model complexity to apply the equilibrium equation for analysis and modeling of skeletal muscle bioenergetics.

## PHENOMENOLOGICAL MODELING

### ***Mitochondrial input – output relation***

The means by which mitochondrial respiration has been thought to be controlled has undergone several revisions over the last decades (see e.g., (27)). Single lumped equation models have been developed to test several of these hypotheses. In these studies mitochondria were reduced to a single unit characterized by input – output behavior. This input – output behavior refers to a classical control scheme in which the inputs reflect the primary regulators and the output is mitochondrial respiration or ATP production. The mathematical equation captured a certain hypothesis (regarding primary regulator(s) and their mechanism of action) and, by comparing model simulations against available experimental data, it was possible to test the hypothesis. This strategy has been successfully applied to identify several models that describe the input – output behavior by some kinetic (23), hybrid kinetic/thermodynamic (7), or purely thermodynamic mechanisms (10). These results indicated that the relation between [ADP] and mitochondrial ATP synthesis flux ( $J_p$ ) or phosphate potential ( $\Delta G_p = \Delta G_p^{\circ} + RT \ln ([ADP][Pi]/[ATP])$ ) and  $J_p$  captured macroscopic regulatory properties of mitochondria skeletal muscle tissue *in vivo* well. These transduction functions therefore provide an important testable criterion that can be used in the process of developing mechanistic models.

### **Quantification of mitochondrial capacity**

The capacity of skeletal muscle cells to synthesize ATP oxidatively, often referred to as the mitochondrial function, is one of the primary clinical parameters that is frequently derived from  $^{31}\text{P}$  MRS measurements. During post – exercise metabolic recovery ATP is produced predominantly by oxidative phosphorylation in mitochondria (11,14,22). Because the CK reaction maintains a (near-) equilibrium state the PCr recovery rate mirrors mitochondrial ATP synthesis flux. There are different methods to quantify mitochondrial function from these dynamics (see e.g., (9)). However the by far most applied method is fitting of a mono-exponential function (Eq. 4) to the PCr recovery data. The calculated time constant of recovery ( $\tau_{\text{PCr}}$ ) is used as measure of mitochondrial function.

$$\text{PCr}(t) = \text{PCr}_e - \Delta\text{PCr} \times e^{(-t/\tau_{\text{PCr}})} \quad (\text{Eq. 4})$$

Where,  $\text{PCr}_e$  is the PCr level after recovery,  $\Delta\text{PCr}$  is the difference between the PCr levels after recovery and at the end of exercise, and  $\tau_{\text{PCr}}$  is the time constant for PCr resynthesis.

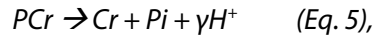
This apparent first – order behavior of PCr recovery kinetics was not only established by empirical evidence. In addition, analysis of a simple electrical analog model elegantly showed that these dynamics were consistent with the chemiosmotic control theory of oxidative phosphorylation (10).

The time-constant of the mono-exponential function provides a macroscopic measure of mitochondrial capacity. It is frequently used to diagnose differences in mitochondrial function between patient and control groups (see e.g., (3,4)). What this method however cannot do is determine the origin of a decreased mitochondrial capacity, which can be the result of e.g., a shift in muscle fiber type to fibers containing less mitochondria, decreased muscle perfusion, decreased number of mitochondria, decreased number of mitochondrial proteins or intrinsic mitochondrial dysfunction. To identify such possible changes in muscle physiology analyses of muscle biopsy samples can be performed. For the analysis of the combined datasets ( $^{31}\text{P}$  MRS + muscle biopsy samples) typically intuitive and statistical approaches are applied (see e.g., (28,29)). Important questions that cannot be answered by these methods are: (i) to which extent can the changes in muscle physiology identified by the analysis of the muscle biopsy samples explain the decreased mitochondrial capacity *in vivo*; (ii) what is the contribution of individual changes to the *in vivo* functioning of the mitochondria. Answering these questions requires a thorough understanding of the oxidative ATP metabolism. Predictive mechanistic models seek to offer such understanding captured in a mathematical language. Application of these models to relate the results of the muscle biopsy samples to *in vivo* read-outs of mitochondrial function provides therefore interesting opportunities for application of mechanistic modeling.

### **Estimation of glyco(geno)lytic ATP synthesis flux**

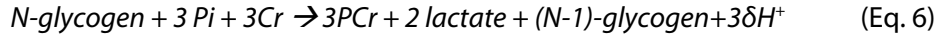
While quantification of mitochondrial function by fitting of a mono-exponential function is a straightforward procedure, estimation of glyco(geno)lytic ATP flux requires more complicated calculations. During ischemic exercise, glycogen is converted into lactate and protons. The pH dynamics provide thus an indirect measure of glycolytic flux which can be used to estimate glycolytic flux. Biochemical reactions involve substrates and products whose  $\text{pK}_a$  values differ so that net uptake or release of  $\text{H}^+$  occurs in amounts that depend on pH. For example, the CK reaction is coupled to ATP utilization and resynthesis. The sum of these reactions is known as the Lohman reaction (Eq. 5).





Where,  $\gamma = 27.239 - 13.593 \text{ pH} + 2.144 \text{ pH}^2 - 0.108875 \text{ pH}^3$  (30)

Glycolytic ATP production reverses the Lohman reaction and involves the following reaction (Eq. 6):



Where,  $\delta = -27.57 + 14.006 \text{ pH} - 2.2014 \text{ pH}^2 + 0.115 \text{ pH}^3$  (30)

To derive the glycolytic flux from pH dynamics the  $H^+$  stoichiometry of these reactions has to be taken into account. In addition, protons are buffered in muscle cells by e.g., metabolites, proteins or bicarbonate buffer, which can be modeled according to Eq7:

$$\beta_{\text{tot}} = \beta_{\text{fixed}} + \beta_{\text{Pi}} + \beta_{\text{PME}} + \beta_{\text{B}}, \quad (Eq. 7)$$

Where,  $\beta_{\text{fixed}}$  represent the static proton buffer of muscle cells (for human skeletal muscle typically set to 20 slykes (31,32));  $\beta_{\text{Pi}}$  represents the contribution of Pi ( $\beta_{\text{Pi}} = 2.303 [H^+] 1.58 \cdot 10^{-7} [Pi] / (1.58 \cdot 10^{-7} [H^+])^2$ );  $\beta_{\text{PME}}$  represents the contribution of PME ( $\beta_{\text{PME}} = 2.303 [H^+] 6.3 \cdot 10^{-7} [PME] / (6.3 \cdot 10^{-7} [H^+])^2$ );  $\beta_{\text{B}}$  represents the contribution of the bicarbonate buffer

In a closed system such as ischemic muscle the contribution of the bicarbonate buffer ( $\beta_{\text{B}}$ ) is assumed zero (11). By combining the change in protons in the tissue ( $dpH/dt \cdot \beta_{\text{tot}}$ ) and the protons consumed in the CK reaction ( $\gamma \cdot dPCr/dt$ ) the equation for the glycolytic ATP ( $J_{ATPGly}$ ) synthesis flux becomes (Eq. 8):

$$J_{ATPGly} = 3 \cdot (dpH/dt \cdot \beta_{\text{tot}} + \gamma \cdot dPCr/dt) / (3 \cdot \delta) \quad (Eq. 8)$$

This phenomenological proton handling model has been successfully validated in ischemic skeletal muscle by comparison of predicted lactate ( $[H^+]$ ) accumulation and biochemical measurements of freeze-clamped muscle tissue samples (33). So also for this pathway rates obtained from the phenomenological model are well suited for testing of mechanistic models.

## FORMALISMS FOR MECHANISTIC MODELING

### *Design of initial model*

Detailed mechanistic models seek to reconstruct biological networks based on quantitative kinetic and thermodynamic information of individual network components. However, the scope of the emerging complexity problem is in many cases daunting. For example, with respect to mitochondrial biology, recent estimates of the number of proteins that make up the organelles hardware are close to 3000 (34-36). Building computational models strictly based on mechanistic details requires quantitative information on e.g., reaction mechanisms, kinetic parameters, rate constants and molecular concentrations. For most processes this information is not available and, consequently, a more practical approach for mechanistic modeling is required. For example biochemical data and model parameters are often collected from different species, experimental

settings, and cell types (37-39). Moreover, in case mechanistic information is unclear, it is necessary to fill the gaps with preferably simple mechanisms without having any kinetic parameters available (40). Sometimes it is possible to clamp model variables at physiological concentrations, reducing the complexity of the model. By applying this sort of practical solutions (semi)mechanistic models can be developed that represent the current state of knowledge of biology.

### ***Model parameterization***

A major challenge in developing mechanistic models is model parameterization. Parameter values are usually obtained from 3 different sources: (i) experimentally determined values, (ii) values estimated based on some experimental data by application of a parameter estimation algorithm and (iii) values estimated in previous computational studies. A first problem encountered is that parameters values have typically been determined *in vitro*. However, *in vivo* interactions with other agents are not included in the *in vitro* assay environment (e.g., the cytoskeletal matrix) may affect enzyme behavior and influence corresponding kinetic parameters. An example of the possible impact of the difference between *in vitro* and *in vivo* conditions is provided by the work of Teusink and colleagues (41) who reconstructed the yeast glycolysis pathway purely based on *in vitro* kinetic data, but failed to reproduce *in vivo* observed behavior with this model. A second problem is that point values are typically not available for all model parameters, either in the literature or because of practical problems encountered when trying to obtain the value experimentally. Consequently, inferring the unknown values from (dynamical) systems behavior by applying a parameter optimization algorithm is required. The number of parameter values that can be accurately inferred from the data depends on the amount of information accessible from the data (practical identifiability) and the formulation of the model equations (structural identifiability) (42,43). When a parameter is non-identifiable, many of the applied parameter estimation algorithms are still able to assign a value to such a parameter. However, these values are often poorly constraint, non-unique and therefore provide a potentially unreliable point estimate of the parameter value (44-46).

### ***Model (hypothesis) testing***

The mechanistic models provide a basis to test the body of knowledge captured by the model against experimental observations. The outcome of such a test can either be that the model is consistent with the experimental data or, alternatively that model predictions fail to reproduce the experimental data. The first case confirms that the hypotheses captured by the model indeed explain the specific biological phenomenon. It is important to realize that this result can never rule out the possibility that alternative hypotheses can describe the data as well. This view is identical to Karl Poppers' statement that in the empirical science true validation of a hypothesis is not possible; hypotheses can only be invalidated (47). Compared to model verification, falsification can therefore be equally informative. It can indicate either a problem with the model parameterization or can point towards missing regulatory mechanism(s). For model falsification to become truly informative it is necessary to identify problems in model parameterization or sites and mechanisms of missing regulation. This can be achieved through intuitive analyses. However, as a result of the complexity of these models intuitive analyses are often impractical. A powerful alternative is provided by application of mathematical techniques, such as parameter sensitivity analysis.

### ***Model analyses; parameter sensitivity analysis***

Parameter sensitivity analysis (PSA) investigates the effect of a variation in parameter values on model predictions. The response of interest of the systems output(s) needs to be translated into a scalar value, which subsequently can be analyzed and interpreted. Examples of responses that have been used are: the area under the curve of an output; deviation from a steady state; or the sum of squared difference between model output and experimental data (39). There are different methods available to perform PSA (48,49). Local parameter sensitivity analysis (LPSA) is most frequently applied. It quantifies the difference in model output as a result of a perturbation of a single parameter. By scanning all model parameters in a stepwise approach it is possible to identify sensitive parameters (causing a large change in model output) and insensitive parameters (affecting model output only minor). The LPSA identifies a causal relation between parameter changes and model predictions assuming an accurate model. However, in many cases parameter values have only a limited accuracy. Global PSA offers a means to take into account the limited accuracy of these parameters (50). They typically explore a larger part of the parameter space by simultaneously varying all parameters. To this end, often, a Monte Carlo simulation scheme is applied: parameter values are randomly selected from distributions that reflect the parameter uncertainty. By (re)performing these simulations a large number of times it is possible to numerically sample the parameter space and determine the corresponding solution space. Statistical analyses (e.g., Kolmogorov – Smirnov test) can subsequently be used to calculate a global sensitivity coefficient for each model parameter from these results (51).

### ***Model refinement***

Failure of experimental confirmation of model predictions can trigger a process of model refinement which may also lead to a better understanding of the associated biology. A first step in this process is to identify parameters or model components which have a significant control on the (false) model predictions. PSA provides a means to do this. In models of biological systems, typically, a large number of parameters are insensitive considering the limited number of model outputs of interest. Only a subset of parameters significantly influences the model output of interest (45). Changing model parameters or introducing new control mechanisms at insensitive parts of the model is not likely to improve predictions. On the other hand, sensitive model parameters do provide suitable candidates for further analyses. A possible next step is to investigate if re-parameterization of the sensitive parameters will improve model predictions. If unsuccessful the model is most likely missing essential regulatory mechanisms. In the latter case, the sensitive model parameters provide leads to pathway components that are most likely to be involved in the additional regulation. This information can therefore focus literature searches or the design of new experiments to identify missing control mechanisms. An alternative strategy of refining a model is to substitute phenomenological parts by more mechanistic new parts. Especially, when model predictions are sensitive to phenomenological model components, replacing these parts can contribute to an increased reliability of model predictions.

### ***Iterative cycle of model development***

Developing detailed mechanistic models that capture the full complexity of metabolic pathways involved in ATP metabolism of skeletal muscle cannot be achieved in a single step. Instead, many

steps of model testing, refining and re-testing are required; a process also referred to as the iterative cycle of systems biology (13). It is likely that in order to avoid a standstill in this cycle often computational and experimental methods have to be combined in a process known as 'experimental based modeling and model based experimental design' (39). Another characteristic of this approach is that model development and obtaining new insights in the associated biology go hand-in-hand. It will therefore be not useful to wait for the 'ultimate' model of energy metabolism in skeletal muscle to be finished before applying it to analyze e.g.,  $^{31}\text{P}$  MRS data of ATP metabolism. Instead, by testing model predictions against  $^{31}\text{P}$  MRS data it is possible to identify opportunities for model improvement while at the same time it is possible to gain a better understanding of the biological processes underlying the experimental observations. As such, a synergy is created which may advance both fields.

## MECHANISTIC MODELING OF GLYCO(GENO)LYSIS

The first detailed kinetic model of glyco(geno)lysis in skeletal muscle was developed by Lambeth and Kushmerick (38). A schematic representation of the model is provided in Figure 3. The model contains detailed kinetic descriptions of 12 pathway enzymes coupled to cellular ATP demand flux and ATP buffering (CK + adenylate kinase (AK)). The kinetic parameters, enzyme  $V_{\max}$  values and metabolite concentrations at rest were scavenged from different sources in literature. As a result, the final model could be termed a 'Frankenstein - model'; it was based on data from different species, including rabbit, mouse, pig, human rat and chicken. This demonstrates that even for this relative simple and well known pathway it is not possible to develop mechanistic models without application of practical solutions. The model was first tested against  $^{31}\text{P}$  MRS measurements of PCr and Pi dynamics in ischemic mouse skeletal muscle at rest (52). In normoxic skeletal muscle at rest, ATP demand and supply are balanced. Consequently the concentrations of PCr and Pi are stable. However during ischemia, as a result of the shutdown of ATP supply via oxidative phosphorylation, ATP demand exceeds glycolytic ATP production. As a result, PCr is consumed, which is accompanied by a complementary increase in Pi. The kinetic model could successfully reproduce these dynamics and on top, accurately predict measured lactate accumulation in the cell.

In the cytoplasm, each biochemical reaction has an associated proton stoichiometry that is generally non-integer and pH-dependent. Therefore, changes in metabolic flux can alter cellular pH. In addition, apparent equilibrium constants and maximum enzyme velocities, which are functions of pH, are also altered. Including these aspects of the pathway in the model is essential for a meaningful interpretation of pH dynamics as reporter of glycolytic flux. Vinnakota and colleagues therefore provided a vital contribution by extending the Lambeth and Kushmerick model with pH-dependent enzyme kinetics and reaction equilibria to compute the time course of pH changes (53). In addition, they verified the model against data reported by Scopes (54,55), who reconstructed the glycolytic pathway in a cell free system *in vitro*. The result showed that for such a cell free system model predictions could accurately reproduce reported dynamics of pH, lactate, PCr, Pi, ADP, AMP and ATP with only minor adjustments in parameter values; however predictions of time courses of hexose-mono-phosphate, fructose-diphosphate, glycerol-3-phosphate and

phosphoglycerates were less accurate. Vinnakota et al. speculated that these predictions could probably be improved by adjusting parameterization of phosphofructokinase and aldolase.

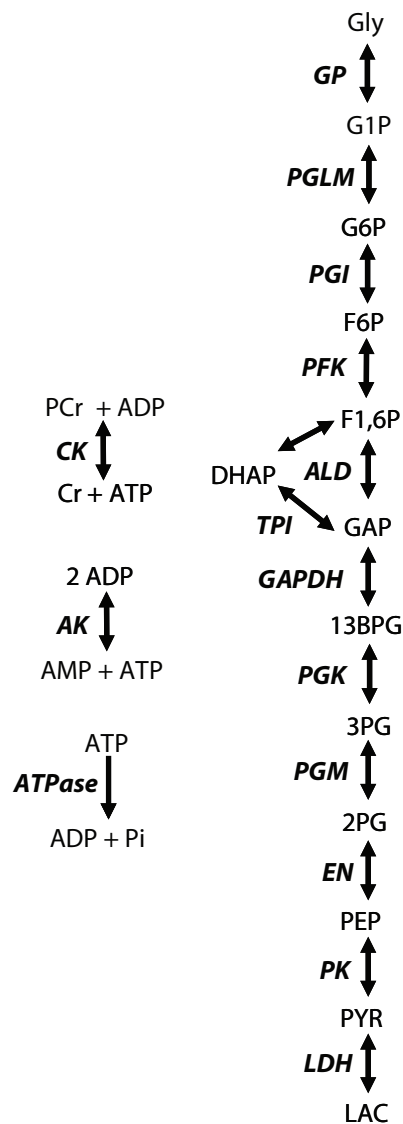


**Figure 3.** Schematic overview of the Lambeth and Kushmerick model of glyco(genol)ysis in skeletal muscle (38). Abbreviations denote: GP, glycogen phosphorylase; Gly, glycogen; PGLM, phosphoglucomutase; G1P, glucose-1-phosphate; G6P, glucose-6-phosphate; PGI, phosphoglucoisomerase; F6P, fructose 6-phosphate; PFK, phosphofructokinase; F1,6P2, fructose 1,6-bisphosphate; ALD, aldolase; DHAP, dihydroxyacetone-phosphate; TPI, triose phosphate isomerase; GAP, glyceraldehyde-3-phosphate; GADPH, glyceraldehyde-3-phosphate dehydrogenase; 13BPG, 1,3-bisphosphoglycerate; PGK, phosphoglycerate kinase; 3PG, 3-phosphoglycerate; PGM, phosphoglyceromutase; 2PG, 2-phosphoglycerate; EN, enolase; PEP, phosphoenolpyruvate; PK, pyruvate kinase; PYR, pyruvate; LDH, lactate dehydrogenase; LAC, lactate; PCr, phosphocreatine; CK, creatine kinase; ADP, adenosine diphosphate; Cr, creatine; ATP, adenosine triphosphate; AK, adenylate kinase; Pi, inorganic phosphate; AMP, adenosine monophosphate.

In a recent study, the model was tested against  $^{31}\text{P}$  MRS measurements of metabolite dynamics (PCr, Pi, pH) in ischemic muscle at rest (56). Again it was reported that the model could reproduce the experimental data fairly well. Moreover, for achieving this result only a small number

of parameters were optimized. One of the main conclusions of this study was that glycogen phosphorylase B is an important step in the regulation of glycolytic flux in resting muscle and that other enzymes play a minor role at most. Additional simulations, not reported in the original paper, revealed that predictions of intermediates downstream of glycogen phosphorylase were at unphysiologically low concentrations (up to a few orders of magnitude lower than experimentally observed). These very low concentrations may explain why the control of pathway flux was shifted to glycogen phosphorylase

## **MECHANISTIC MODELING OF OXIDATIVE PHOSPHORYLATION**

Compared to the glycolytic pathway, the scope of the complexity involved in the mitochondrial pathways is several orders of magnitude larger. For example, the current estimate of the number of proteins that make up the mitochondrial hardware is ~3000 (34-36). Consequently, at the moment, it is not feasible to model mitochondria at the same level of detail as the glycolytic model by Lambeth and Kushmerick. Modeling mitochondrial energy transduction requires therefore some inventive solutions. For example, by representing some processes, like the TCA cycle (37) or the electron transport chain (57) by single lumped equations, or clamping state variables e.g., matrix concentrations of pH or [Pi] to further reduce the complexity (57). By following these approaches several mechanistic models of oxidative phosphorylation have been developed (37,57-61). Some of these models have a similar origin, share components or apply the same parameter values (see e.g., (57) and (60), or (61) and (37)). In this chapter, we do not intend to provide a full overview of differences and similarities of all these models. Instead, we focus on the mechanistic models that have been applied recently for the analysis of <sup>31</sup>P MRS measurements of skeletal muscle bioenergetics. In particular, the Beard model (37) which was partly based on the Korzeniewski model (61), acted as foundation of the studies described in this thesis.

The basic components of the model proposed by Beard include a lumped TCA cycle, reactions at complex I, III and IV of the electron transport chain, ATP synthesis at F<sub>1</sub>F<sub>0</sub> ATPase and substrate transport including adenine nucleotide translocase (ANT) and the phosphate-hydrogen co-transporter, and cation fluxes across the inner membrane including fluxes through the K<sup>+</sup>/H<sup>+</sup> antiporter and passive H<sup>+</sup> and K<sup>+</sup> permeation. 16 parameter values were estimated on nine independent data curves of isolated cardiac mitochondria obtained from Bose et al. (62). Specifically, it was shown that incorporation of a phosphate-dependent activation of complex III is required to reproduce the observed data.

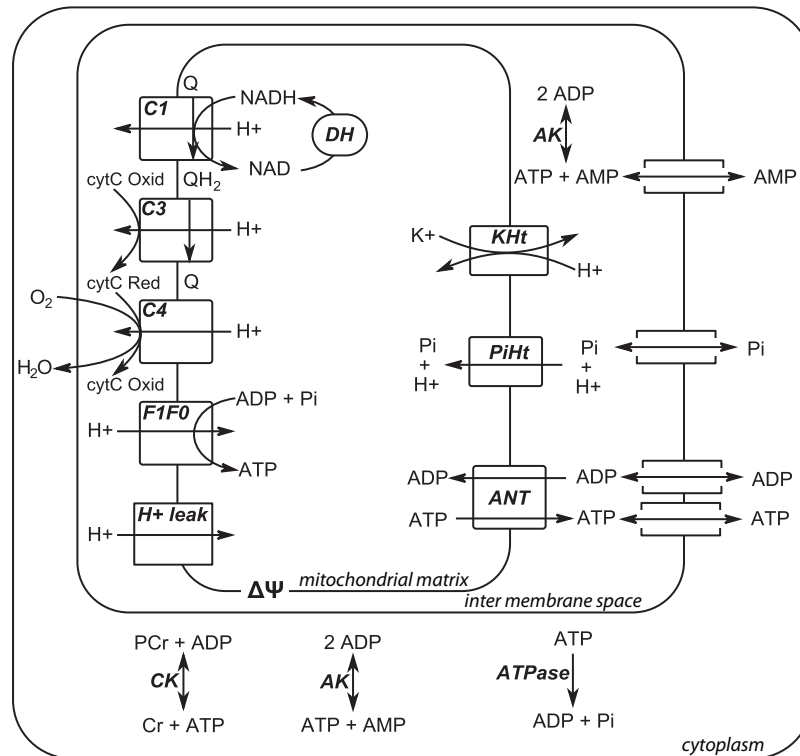


**Figure 4.** Schematic representation of the computational model of skeletal muscle energetic (63). Abbreviations denote: dehydrogenases (DH), complex I (C1), complex III (C3), complex IV (C4),  $F_1F_0$ ATPase (F1F0), proton leak (H<sup>+</sup> leak), adenine nucleotide transporter (ANT), Pi-H<sup>+</sup> co-transporter (PiHt), K<sup>+</sup>-H<sup>+</sup> exchanger (KHt), adenylate kinase (AK), creatine kinase (CK), lumped cellular ATPase fluxes (ATPase), ubiquinone (Q), ubiquinol (QH<sub>2</sub>), oxidized cytochrome C (cytC Oxid), reduced cytochrome C (cytC Red), adenosine diphosphate (ADP), inorganic phosphate (Pi), adenosine triphosphate (ATP), nicotinamide adenine dinucleotide (NAD), reduced nicotinamide adenine dinucleotide, adenosine monophosphate (AMP)

Wu et al. (63) investigated if this model could explain the mitochondrial input – output relations ( $[ADP] - J_p$ ,  $[Pi] - J_p$  and  $\Delta G_p - J_p$ ) that were previously proposed to capture the regulation of mitochondria in skeletal muscle *in vivo* (see section: 'Mitochondrial input – output relation'). To this end, the mitochondrial model component was combined with mathematical descriptions of cytoplasmic ATP buffering (CK + AK) and ATP hydrolysis flux. In addition, metabolite concentrations were set to values appropriate for skeletal muscle and mitochondrial content was adjusted to match the available morphometric data. A schematic representation of the model is provided in Figure 4. Model predictions were compared to  $[ADP] - J_p$ ,  $[Pi] - J_p$  and  $\Delta G_p - J_p$  relations obtained from <sup>31</sup>P MRS measurements human forearm flexor muscle (7). Results of these predictions (solid line) versus experimental data are shown in Figure 5. These fits were obtained by optimizing only a single model parameter, i.e., [PCr] at rest, which was set at 23.6mM. This parameter value was however not consistent with the original dataset for which a [PCr] at rest was reported of  $36.5 \pm 2.7$ mM (mean  $\pm$  SD, n=20). Adjusting the initial [PCr] to 23.6mM also changed the initial [Cr] to 19.1mM. These settings were also not consistent with the assumption that 85% of the total creatine pool was phosphorylated at rest, which was applied to calculate cellular [ADP]. The dotted lines in Figure 5 represent the simulation results when initial [PCr] was set to 36.5mM. These results clearly indicated that the model was not yet consistent with these experimentally observed transduction functions and required a more detailed analysis.

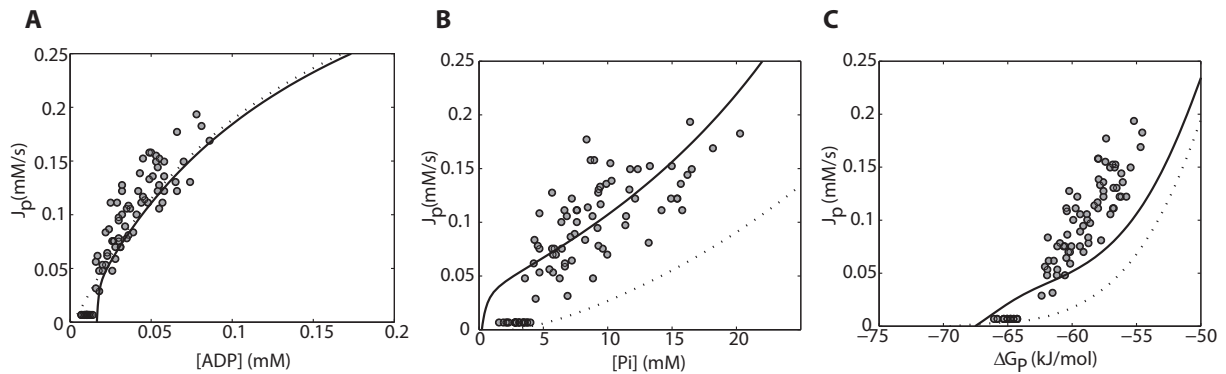


**Figure 5.** Model predictions of mitochondrial input – output relations ( $[ADP] - J_p$  (**A**),  $[Pi] - J_p$  (**B**) and  $\Delta G_p - J_p$  (**C**)). Experimental data were obtained from (7). The solid lines show model predictions for settings used in the original paper by Wu et al. (63): initial  $[PCr]$  set to 23.6mM. The dotted lines show model predictions when initial  $[PCr]$  was set according to the experimentally determined value: initial  $PCr$  set to 36.5mM (7).

## OUTLINE OF THIS THESIS

A lot of research has been conducted to investigate skeletal muscle bioenergetics by application of  $^{31}P$  magnetic resonance spectroscopy in many different subjects groups. However, still many of the experimental observations cannot be directly related to properties of the components of the underlying metabolic pathways. The aim of this thesis was to apply a systems biology based research strategy combining mechanistic computational modeling and  $^{31}P$  MRS measurements to study skeletal muscle bioenergetics. As explained in the section ‘formalisms for mechanistic modeling’ achieving this goal requires an iterative cycle of model development. Continuing this cycle is expected to improve both the predictive power of the model while at the same time new insight in the energy metabolism of skeletal muscle is obtained.

It has been shown that  $PCr$ ,  $Pi$  and  $ATP$  dynamics in ischemic skeletal muscle at rest were explained by a model which integrated known enzyme kinetics of the glycolytic pathway (52,56). However, predictions of some of the intermediate metabolites (e.g., hexose-mono-phosphate, fructose-diphosphate, glycerol-3-phosphate and phosphoglycerates) were less accurate. This indicated that the understanding of the pathway captured by the model was possibly incomplete. In **chapter 2** this was further investigated by testing model simulations against newly recorded dynamics of hexose-mono-phosphate (glucose-1P + glucose-6P + fructose-6P) during metabolic recovery following intense exercise. This study confirmed that the model indeed missed essential regulatory mechanisms. Additional numerical analyses were performed to identify possible missing mechanisms. **Chapter 3** describes a next loop in the iterative cycle. It was tested if the missing mechanism proposed in chapter 2 (i.e., calcium-calmodulin mediated activation of phosphofruktokinase (PFK)) also played an important role in the control of pathway dynamics observed in ischemic, contracting muscle for various excitation frequencies. While previous studies mainly focused on investigating pathway dynamics for skeletal muscle at rest, in this chapter a first attempt is described to investigate the mechanisms controlling glycolytic flux in contracting skeletal muscle by means of application of a mechanistic model.



The Beard model of oxidative phosphorylation (37) that was modified by Wu et al. (63) could not reproduce the regulation of skeletal muscle observed *in vivo* as captured by the ADP –  $J_p$  and  $\Delta G_p$  –  $J_p$  transduction functions (Figure 5, dotted lines). Before we could advance to the analysis of clinical data of patients, first it had to be investigated why these model predictions failed in reproducing these experimental data of healthy humans. Is it caused by a problem in the model parameterization? Or is the model missing essential regulatory mechanisms? **Chapter 4** describes an investigation of the ADP –  $J_p$  transduction function. The dataset that was available from (7) and is shown in Figure 5 is characterized by a rather wide scatter of individual data points. In an attempt to improve the quality of the computational studies a new dataset was recorded in which the noise by the scatter of individual data points was reduced and the overall number of data points was increased. Next, numerical analyses of the model were used to identify components of the molecular network that controlled the ADP sensitivity of mitochondria *in silico*. The results of this investigation were used to significantly improve the predictive power of the model. In a different study, the same dataset was used to investigate which regulatory mechanisms explained the experimentally observed  $\Delta G_p$  –  $J_p$  transduction function. This study is described in **chapter 5**. Two different control schemes were tested: (i) Pi control of respiratory chain activity and (ii) parallel activation of ATP consumption and activity of mitochondrial enzymes. In addition, these control schemes were tested against a validation dataset recorded in subjects with a sedentary lifestyle and track athletes.

*In vivo* mitochondrial capacity quantified by the rate of post exercise PCr recovery is a physiological parameters frequently derived from  $^{31}\text{P}$  MRS datasets. Sometimes, additional analyses of muscle biopsy samples are used to identify changes in the metabolic pathways responsible for observations of a decreased mitochondrial capacity *in vivo*. State-of-the-art approaches for analyses of the combined data remain typically limited to statistical and intuitive strategies. Chapters 6 and 7 describe analyses of this type of dataset from a systems biology perspective. Specifically, it is investigated to which extend the changes in the metabolic pathways determined from the muscle biopsy samples contribute to a decreased mitochondrial capacity *in vivo* by taking into account the functioning and regulation of the underlying metabolic networks captured by the mathematical model. In the first part of **chapter 6**, the extension of the modeling framework from a single uniform-cell model to a three-cell model capturing the microscopic heterogeneity of skeletal muscle tissue is described. In addition, verification tests of the model are presented. The validated model was applied for quantitative analyses of the changes in skeletal muscle physiology responsible for a decreased mitochondrial capacity in obese type 2 diabetes patients compared to healthy lean control subjects. The results were used to outline a strategy for integration of *in vivo* and *in vitro* and *in silico* methods for systems biology of mitochondrial function. In **chapter 7** this approach was tested in an animal model (8 versus 25 week old Wistar rats). An extensive dataset containing both *in vivo* ( $^{31}\text{P}$  MRS) and *in vitro* (high resolution respirometry, immunohistochemistry, western blotting, qPCR) measures of mitochondrial function was collected. *In silico* analyses were performed to test if the *in vivo* observed changes of mitochondrial function were explained by the *in vitro* recorded data taking into account control properties of underlying metabolic pathways as captured by the model.

Chapters 2 and 3 describe studies of the glycolytic pathway. Chapters 4 to 7 present studies of oxidative ATP metabolism. In these studies the pathways were investigated for conditions in which only one of them was active (ischemia versus post exercise recovery). In **chapter 8** these models are combined to investigate if the control mechanisms embedded in these models also explain the balance between glycoytic and mitochondrial ATP production during rest – exercise – recovery protocols in normoxic skeletal muscle.

The concluding **chapter 9** provides a summarizing discussion. In addition, application of the iterative cycle of model development will be discussed and possible future directions are highlighted.

## REFERENCES

1. **Wild S, Roglic G, Green A, Sicree R and King H.** Global prevalence of diabetes: estimates for the year 2000 and projections for 2030. *Diabetes Care* 27: 1047-1053, 2004
2. **Bajpeyi S, Pasarica M, Moro C, Conley K, Jubrias S, Sereda O, Burk DH, Zhang Z, Gupta A, Kjems L et al..** Skeletal muscle mitochondrial capacity and insulin resistance in type 2 diabetes. *J Clin Endocrinol Metab* 96: 1160-1168, 2011
3. **De Feyter HM, van den Broek NM, Praet SF, Nicolay K, van Loon LJ and Prompers JJ.** Early or advanced stage type 2 diabetes is not accompanied by in vivo skeletal muscle mitochondrial dysfunction. *Eur J Endocrinol* 158: 643-653, 2008
4. **Meex RC, Schrauwen-Hinderling VB, Moonen-Kornips E, Schaart G, Mensink M, Phielix E, van de Weijer T, Sels JP, Schrauwen P and Hesselink MK.** Restoration of muscle mitochondrial function and metabolic flexibility in type 2 diabetes by exercise training is paralleled by increased myocellular fat storage and improved insulin sensitivity. *Diabetes* 59: 572-579, 2010
5. **Coggan AR, Abduljalil AM, Swanson SC, Earle MS, Farris JW, Mendenhall LA and Robitaille PM.** Muscle metabolism during exercise in young and older untrained and endurance-trained men. *J Appl Physiol* 75: 2125-2133, 1993
6. **Conley KE, Jubrias SA and Esselman PC.** Oxidative capacity and ageing in human muscle. *J Physiol* 526 Pt 1: 203-210, 2000
7. **Jeneson JA, Westerhoff HV, Brown TR, Van Echteld CJ and Berger R.** Quasi-linear relationship between Gibbs free energy of ATP hydrolysis and power output in human forearm muscle. *Am J Physiol* 268: C1474-C1484, 1995
8. **Jeneson JA, Wiseman RW, Westerhoff HV and Kushmerick MJ.** The signal transduction function for oxidative phosphorylation is at least second order in ADP. *J Biol Chem* 271: 27995-27998, 1996
9. **Layec G, Bringard A, Le FY, Vilmen C, Micallef JP, Perrey S, Cozzone PJ and Bendahan D.** Comparative determination of energy production rates and mitochondrial function using different (31)P MRS quantitative methods in sedentary and trained subjects. *NMR Biomed*, 2010
10. **Meyer RA.** A linear model of muscle respiration explains monoexponential phosphocreatine changes. *Am J Physiol* 254: C548-C553, 1988
11. **Conley KE, Blei ML, Richards TL, Kushmerick MJ and Jubrias SA.** Activation of glycolysis in human muscle in vivo. *Am J Physiol* 273: C306-C315, 1997
12. **Ideker T, Galitski T and Hood L.** A new approach to decoding life: systems biology. *Annu Rev Genomics Hum Genet* 2: 343-372, 2001
13. **Kitano H.** Computational systems biology. *Nature* 420: 206-210, 2002
14. **Blei ML, Conley KE and Kushmerick MJ.** Separate measures of ATP utilization and recovery in human skeletal muscle. *J Physiol* 465: 203-222, 1993
15. **Walter G, Vandenborne K, Elliott M and Leigh JS.** In vivo ATP synthesis rates in single human muscles during high intensity exercise. *J Physiol* 519 Pt 3: 901-910, 1999
16. **Guyton AC, Hall JE.** *Textbook of Medical Physiology 10th ed.* Philadelphia: Saunders company, 2000
17. **Chance B, Eleff S, Leigh JS, Jr., Sokolow D and Sapega A.** Mitochondrial regulation of phosphocreatine/inorganic phosphate ratios in exercising human muscle: a gated 31P NMR study. *Proc Natl Acad Sci U S A* 78: 6714-6718, 1981
18. **Hoult DJ, Busby SJ, Gadian DG, Radda GK, Richards RE and Seeley PJ.** Observation of tissue metabolites using 31P nuclear magnetic resonance. *Nature* 252: 285-287, 1974
19. **Chance B, Im J, Nioka S and Kushmerick M.** Skeletal muscle energetics with PNMR: personal views and historic perspectives. *NMR Biomed* 19: 904-926, 2006
20. **Kemp GJ, Meyerspeer M and Moser E.** Absolute quantification of phosphorus metabolite concentrations in human muscle in vivo by 31P MRS: a quantitative review. *NMR Biomed* 20: 555-565, 2007
21. **Taylor DJ, Bore PJ, Styles P, Gadian DG and Radda GK.** Bioenergetics of intact human muscle. A 31P nuclear magnetic resonance study. *Mol Biol Med* 1: 77-94, 1983
22. **Quistorff B, Johansen L and Sahlin K.** Absence of phosphocreatine resynthesis in human calf muscle during ischaemic recovery. *Biochem J* 291 ( Pt 3): 681-686, 1993
23. **Kushmerick MJ.** Energy balance in muscle activity: simulations of ATPase coupled to oxidative phosphorylation and to creatine kinase. *Comp Biochem Physiol B Biochem Mol Biol* 120: 109-123, 1998
24. **Lawson JW, Veech RL.** Effects of pH and free Mg<sup>2+</sup> on the Keq of the creatine kinase reaction and other phosphate hydrolyses and phosphate transfer reactions. *J Biol Chem* 254: 6528-6537, 1979
25. **McFarland EW, Kushmerick MJ and Moerland TS.** Activity of creatine kinase in a contracting mammalian muscle of uniform fiber type. *Biophys J* 67: 1912-1924, 1994
26. **Roman BB, Meyer RA and Wiseman RW.** Phosphocreatine kinetics at the onset of contractions in skeletal muscle of MM creatine kinase knockout mice. *Am J Physiol Cell Physiol* 283: C1776-C1783, 2002
27. **Brown GC.** Control of respiration and ATP synthesis in mammalian mitochondria and cells. *Biochem J* 284 ( Pt 1): 1-13, 1992
28. **Phielix E, Schrauwen-Hinderling VB, Mensink M, Lenaers E, Meex R, Hoeks J, Kooi ME, Moonen-Kornips E, Sels JP, Hesselink MK et al..** Lower intrinsic ADP-stimulated mitochondrial respiration underlies in vivo mitochondrial dysfunction in muscle of male type 2 diabetic patients. *Diabetes* 57: 2943-2949, 2008
29. **Praet SF, De Feyter HM, Jonkers RA, Nicolay K, van PC, Kuipers H, van Loon LJ and Prompers JJ.** 31P MR spectroscopy and in vitro markers of oxidative capacity in type 2 diabetes patients. *MAGMA* 19: 321-331, 2006
30. **Kushmerick MJ.** Multiple equilibria of cations with metabolites in muscle bioenergetics. *Am J Physiol* 272: C1739-C1747, 1997
31. **Kemp GJ, Taylor DJ, Styles P and Radda GK.** The production, buffering and efflux of protons in human skeletal muscle during exercise and recovery. *NMR Biomed* 6: 73-83, 1993
32. **Kemp GJ, Thompson CH, Taylor DJ and Radda GK.** Proton efflux in human skeletal muscle during recovery from exercise. *Eur J Appl Physiol Occup Physiol* 76: 462-471, 1997

33. **Marcinek DJ, Kushmerick MJ and Conley KE.** Lactic acidosis in vivo: testing the link between lactate generation and H<sup>+</sup> accumulation in ischemic mouse muscle. *J Appl Physiol* 108: 1479-1486, 2010
34. **Mootha VK, Bunkenborg J, Olsen JV, Hjerrild M, Wisniewski JR, Stahl E, Bolouri MS, Ray HN, Sihag S, Kamal M et al..** Integrated analysis of protein composition, tissue diversity, and gene regulation in mouse mitochondria. *Cell* 115: 629-640, 2003
35. **Taylor SW, Fahy E, Zhang B, Glenn GM, Warnock DE, Wiley S, Murphy AN, Gaucher SP, Capaldi RA, Gibson BW et al..** Characterization of the human heart mitochondrial proteome. *Nat Biotechnol* 21: 281-286, 2003
36. **Westermann B, Neupert W.** 'Omics' of the mitochondrion. *Nat Biotechnol* 21: 239-240, 2003
37. **Beard DA.** A biophysical model of the mitochondrial respiratory system and oxidative phosphorylation. *PLoS Comput Biol* 1: e36, 2005
38. **Lambeth MJ, Kushmerick MJ.** A computational model for glycogenolysis in skeletal muscle. *Ann Biomed Eng* 30: 808-827, 2002
39. **van Riel NA.** Dynamic modelling and analysis of biochemical networks: mechanism-based models and model-based experiments. *Brief Bioinform* 7: 364-374, 2006
40. **Neves SR, Iyengar R.** Modeling of signaling networks. *Bioessays* 24: 1110-1117, 2002
41. **Teusink B, Passarge J, Reijenga CA, Esgalhado E, van der Weijden CC, Schepper M, Walsh MC, Bakker BM, van DK, Westerhoff HV et al..** Can yeast glycolysis be understood in terms of in vitro kinetics of the constituent enzymes? Testing biochemistry. *Eur J Biochem* 267: 5313-5329, 2000
42. **Ashyraliyev M, Fomekong-Nanfack Y, Kaandorp JA and Blom JG.** Systems biology: parameter estimation for biochemical models. *Febs Journal* 276: 886-902, 2009
43. **Raue A, Kreutz C, Maiwald T, Bachmann J, Schilling M, Klingmuller U and Timmer J.** Structural and practical identifiability analysis of partially observed dynamical models by exploiting the profile likelihood. *Bioinformatics* 25: 1923-1929, 2009
44. **Brodersen R, Nielsen F, Christiansen JC and Andersen K.** Characterization of binding equilibrium data by a variety of fitted isotherms. *Eur J Biochem* 169: 487-495, 1987
45. **Gutenkunst RN, Waterfall JJ, Casey FP, Brown KS, Myers CR and Sethna JP.** Universally sloppy parameter sensitivities in systems biology models. *PLoS Comput Biol* 3: 1871-1878, 2007
46. **Rodriguez-Fernandez M, Mendes P and Banga JR.** A hybrid approach for efficient and robust parameter estimation in biochemical pathways. *Biosystems* 83: 248-265, 2006
47. **Popper KR.** *The Logic of scientific discovery.* Hutchinson, 1959
48. **Cacuci DG, Ionescu-Bujor M.** A comparative review of sensitivity and uncertainty analysis of large-scale systems - II: Statistical methods. *Nuclear Science and Engineering* 147: 204-217, 2004
49. **Ionescu-Bujor M, Cacuci DG.** A comparative review of sensitivity and uncertainty analysis of large-scale systems - I: Deterministic methods. *Nuclear Science and Engineering* 147: 189-203, 2004
50. **Marino S, Hogue IB, Ray CJ and Kirschner DE.** A methodology for performing global uncertainty and sensitivity analysis in systems biology. *J Theor Biol* 254: 178-196, 2008
51. **Zi Z, Cho KH, Sung MH, Xia X, Zheng J and Sun Z.** In silico identification of the key components and steps in IFN-gamma induced JAK-STAT signaling pathway. *FEBS Lett* 579: 1101-1108, 2005
52. **Lambeth MJ, Kushmerick MJ, Marcinek DJ and Conley KE.** Basal glycogenolysis in mouse skeletal muscle: in vitro model predicts in vivo fluxes. *Mol Biol Rep* 29: 135-139, 2002
53. **Vinnakota K, Kemp ML and Kushmerick MJ.** Dynamics of muscle glycogenolysis modeled with pH time course computation and pH-dependent reaction equilibria and enzyme kinetics. *Biophys J* 91: 1264-1287, 2006
54. **Scopes RK.** Studies with a reconstituted muscle glycolytic system. The rate and extent of creatine phosphorylation by anaerobic glycolysis. *Biochem J* 134: 197-208, 1973
55. **Scopes RK.** Studies with a reconstituted muscle glycolytic system. The rate and extent of glycolysis in simulated post-mortem conditions. *Biochem J* 142: 79-86, 1974
56. **Vinnakota KC, Rusk J, Palmer L, Shankland E and Kushmerick MJ.** Common phenotype of resting mouse extensor digitorum longus and soleus muscles: equal ATPase and glycolytic flux during transient anoxia. *J Physiol* 588: 1961-1983, 2010
57. **Magnus G, Keizer J.** Minimal model of beta-cell mitochondrial Ca<sup>2+</sup> handling. *Am J Physiol* 273: C717-C733, 1997
58. **Bazil JN, Buzzard GT and Rundell AE.** Modeling mitochondrial bioenergetics with integrated volume dynamics. *PLoS Comput Biol* 6: e1000632, 2010
59. **Bohnensack R.** Control of energy transformation of mitochondria. Analysis by a quantitative model. *Biochim Biophys Acta* 634: 203-218, 1981
60. **Cortassa S, O'Rourke B, Winslow RL and Aon MA.** Control and regulation of mitochondrial energetics in an integrated model of cardiomyocyte function. *Biophys J* 96: 2466-2478, 2009
61. **Korzeniewski B, Zoladz JA.** A model of oxidative phosphorylation in mammalian skeletal muscle. *Biophys Chem* 92: 17-34, 2001
62. **Bose S, French S, Evans FJ, Joubert F and Balaban RS.** Metabolic network control of oxidative phosphorylation: multiple roles of inorganic phosphate. *J Biol Chem* 278: 39155-39165, 2003
63. **Wu F, Jeneson JA and Beard DA.** Oxidative ATP synthesis in skeletal muscle is controlled by substrate feedback. *Am J Physiol Cell Physiol* 292: C115-C124, 2007



# Chapter 2

## *Silencing of glycolysis in muscle: experimental observation and numerical analysis*

Adapted from

J.P.J. Schmitz, N.A.W. van Riel, K. Nicolay, P.A.J. Hilbers, J.A.L. Jeneson  
*Silencing of glycolysis in muscle: experimental observation and numerical analysis*  
Experimental Physiology, 2010, 95(2):380-397

## ABSTRACT

The longstanding problem of rapid inactivation of the glycolytic pathway in skeletal muscle after contraction was investigated using  $^{31}\text{P}$  NMR spectroscopy and computational modeling. *In vivo* dynamics of phosphorylated glycolytic intermediates (hexose-mono-phosphates) during cyclic contraction and subsequent metabolic recovery were measured by applying  $^{31}\text{P}$  NMR spectroscopy. Hexose-mono-phosphates concentration in muscle peaked 40 seconds into metabolic recovery from maximal contractile work at  $6.9 \pm 1.3$  mM (mean  $\pm$  SD;  $n=8$ ) and subsequently declined at a rate of  $0.009 \pm 0.001$  mM/s. It was next tested if current knowledge of the kinetic controls in the glycolytic pathway in muscle integrated in a computational model could explain the experimental data. The model underestimated the magnitude of deactivation of the glycolytic pathway in resting muscle resulting in depletion of glycolytic intermediates and substrate for oxidative ATP synthesis. Numerical analysis identified phosphofructokinase and pyruvate kinase as the most likely kinetic control sites involved in deactivation of the pathway. Ancillary hundred-fold inhibition of both phosphofructokinase and pyruvate kinase was necessary to correctly predict glycolytic intermediate and ADP concentrations in resting human muscle. Incorporation of this information in the model resulted in highly improved agreement between predicted and measured *in vivo* hexose-mono-phosphates dynamics in muscle following contraction. It was concluded that silencing of the glycolytic pathway in muscle following contraction is most likely mediated by phosphofructokinase and pyruvate kinase inactivation on a timescale of seconds and minutes, respectively.

## INTRODUCTION

Excitable cells like skeletal muscle fibres may undergo rapid and large (up to two orders of magnitude) transitions in ATP turnover rate upon activation (1,2). To buffer and balance this large dynamic capacity for ATP utilization, excitable cells contain multiple ATP synthetic pathways including glycolysis and mitochondrial oxidative phosphorylation (1,2). These pathways and their kinetic controls have been extensively investigated and characterized to the point that detailed *in silico* models are now available (3-8). Conversely, these computational models offer powerful quantitative tools for rigorous testing of the sufficiency and consistency of current understanding and formulation of cellular ATP synthesis and its regulation (9). A specific concern is the fact that the majority of the information captured by these models has come from *in vitro* determinations of enzyme kinetics (9,10). However, in the living cell, ancillary interactions (e.g. protein-protein interactions (11) or substrate channelling (12)) may greatly influence pathway behaviour. For example, it has been documented that the activity of phosphofructokinase (PFK), a key regulatory enzyme in the glycolytic pathway, is regulated by attachment to the cellular cytoskeletal matrix in addition to classic metabolic regulation by AMP, ADP and inorganic phosphate (Pi) (13-15). Any incorporation of this information in the available computational models of glycolysis, however, has been lacking (3-5). As such, it remains to be tested if and how much the latter type of 'physiological' metabolic regulation (as opposed to 'biochemical' regulation by metabolite concentrations) contributes to pathway flux and concentration control *in vivo*.

In the case of glycolysis, there is, in fact, a clear and pressing need for such a test. It has been long known that glycolytic flux in skeletal muscle is arrested in non-contracting muscle even in the presence of elevated concentrations of the classic metabolic regulators AMP, ADP and Pi. This observation was first made almost 30 years ago (16), and has since been independently confirmed (17-21). Hypotheses explaining this surprising finding all invoke inactivation of key glycolytic enzymes like PFK via some relaxation-related mechanism (e.g., a drop in cytoplasmic  $Ca^{2+}$ ) (16,20,21). However, biochemical details, including sites, magnitude and mechanism of pathway inactivation as well as the physiological significance for the resting skeletal muscle state all remain yet to be discovered.

Here, the kinetic controls involved in shutting down glycolysis in non-contracting skeletal muscle and its physiological significance for the resting skeletal muscle state are investigated using a combination of experimental and computational investigative approaches. First, we performed high time resolution dynamic *in vivo* measurements of the turnover of phosphorylated glycolytic metabolites (hexose monophosphates; HMP) in human leg muscle after exhaustive exercise using  $^{31}P$  NMR spectroscopy. Next, the Lambeth & Kushmerick computational model of glycolysis in muscle was used as a platform to investigate if current knowledge of glycolytic flux and concentration control incorporated in the model was sufficient to explain the measured HMP dynamics (3). Finally, computational strategies, including network analysis, were used to identify the kinetic control sites in the glycolytic pathway involved in shutting down glycogen turnover in the post-exercise state and to investigate its significance for the resting skeletal muscle state.



## METHODS

### Experimental methods

#### ***Subjects***

Eight normally active, healthy male subjects (mean age 26 yrs; range 22-45) participated in the study. The nature and the risks of the experimental procedures were explained to the subjects, and all gave their written informed consent to participate in the study, which conformed to the standards set by the Declaration of Helsinki and was approved by the local Medical Ethical Committee of the Máxima Medical Center, Veldhoven, The Netherlands.

#### ***<sup>31</sup>P MRS***

All measurements were performed on a 1.5T whole body scanner (Gyroscan S15/ACS, Philips Medical Systems, Best, The Netherlands) equipped with a custom-built non-ferrous, mechanically-braked bicycle ergometer. Details of the ergometer, its interfacing with the spectrometer for gated acquisition during bicycling exercise, subject positioning and familiarization with the exercise are described in detail elsewhere (22). A single-turn <sup>31</sup>P surface coil (diameter: 6 cm) supplied by the manufacturer was positioned over the medial head of the quadriceps muscle of the right leg and fastened with velcro strips. The magnet was shimmed using a custom-built rectangular <sup>1</sup>H surface coil (20x10 cm) positioned over the quadriceps muscle as described elsewhere (22). All <sup>31</sup>P NMR spectra were acquired using a 90° adiabatic excitation pulse. Prior to the exercise bout, two <sup>31</sup>P spectra (16 summed free induction decays (FIDs); 1024 points; sweep width 2 kHz) were obtained from the resting muscle in resting position under fully relaxed (TR 15s) and partly-saturated (TR 3s), actual experimental conditions to determine saturation correction factors for each resonance. Next, subjects performed a bicycling ramp exercise bout consisting of three incremental workloads including maximal (1, 2 and 3 kg braking load, respectively). The pedalling rate was 80 rpm set by a metronome. Each workload was maintained for 144s during which four <sup>31</sup>P NMR spectra (12 summed FIDs) were collected from the muscle. During the first 108s of metabolic recovery after completion of the exercise test, <sup>31</sup>P NMR spectra consisting of four summed FIDs were serially collected yielding a time resolution of 12s. In the second phase of recovery, the time resolution was decreased to 36s (12 summed FIDs per spectrum). The total scan time was 846s (432s during exercise and 414s during recovery, respectively). 15 minutes after exercise had ended the subjects performed a second, less intense incremental workload of which the data was not used, except for the first spectrum that provided an additional data point in the hexose-monophosphates (HMP) recovery dynamics.

#### ***Data processing***

Spectra were fitted in the time domain by using a nonlinear least-squares algorithm (AMARES) in the jMRUI software package (23). Phosphate-mono-esters (PME), Pi, PCr and ATP signals were fitted to Lorentzian line shapes. The three ATP peaks were fitted as two doublets and one triplet, with equal amplitudes and line widths and prior knowledge for the J-coupling constant (17 Hz). Maximal line widths were constrained at 30Hz. Absolute concentrations of the metabolites were calculated

after correction for partial saturation and assuming that the ATP concentration ([ATP]) is 8.2 mM at rest (24). Intracellular pH was calculated from the chemical shift difference between the P<sub>i</sub> and PCr resonances ( $\delta$ ; measured in parts per million) according to Eq. 1 (25):

$$pH = 6.75 + \log\left(\frac{\delta - 3.27}{5.63 - \delta}\right) \quad (Eq.1)$$

## **Computational methods**

### ***Model description***

The primary purpose of the computational part of this study was to investigate the mechanisms involved in the observed HMP dynamics during metabolic recovery from exercise. The analysis also required information that was obtained by performing simulations under two additional conditions: high ATP demand flux and rest, respectively. The glycolytic pathway substrate supply flux was assumed to be different for each of these three conditions: (i) under the metabolic recovery conditions, substrate for the glycolytic pathway supply was provided by glucose phosphorylation by hexokinase concomitant with net glycogen synthesis. The model for this particular condition will be referred to as the 'recovery condition model' (Figure 1A). (ii) under the condition of high ATP demand (i.e., during exercise), pathway substrate supply was assumed to be provided by net glycogen breakdown; the relative contribution of glucose phosphorylation by hexokinase was assumed to be negligible (Figure 1B). (iii) under steady state rest conditions (i.e., with respect to ATP metabolism), it was assumed as a first approximation that no net glycogen production occurred and pathway supply was provided by glucose phosphorylation through hexokinase. The pathway model under this particular condition will be referred to as the 'resting condition model' (Figure 1C).

The Lambeth and Kushmerick model of muscle glycolysis (3) was used as platform to perform the numerical analyses. This model was parameterized with data of mammalian skeletal muscle origin, except for the phosphoglycerate mutase parameters which were obtained from chicken skeletal muscle. Minor adaptations were made to model conditions (i) and (iii) described above. A schematic representation of the adapted models is shown in Figure 1. The flux equations, initial conditions and parameter values have been described previously by Lambeth and Kushmerick (3); in the sections below we restrict the description to the details of model adaptations. The computational models were implemented using Matlab 7.5.0 (the Mathworks Inc., Natick, US). Differential equations were numerically solved using ODE15s. The model did not take mitochondrial dynamics into account. The ATPase flux that was set in the model therefore corresponded only to the part that was matched by glycogenolytic ATP production.

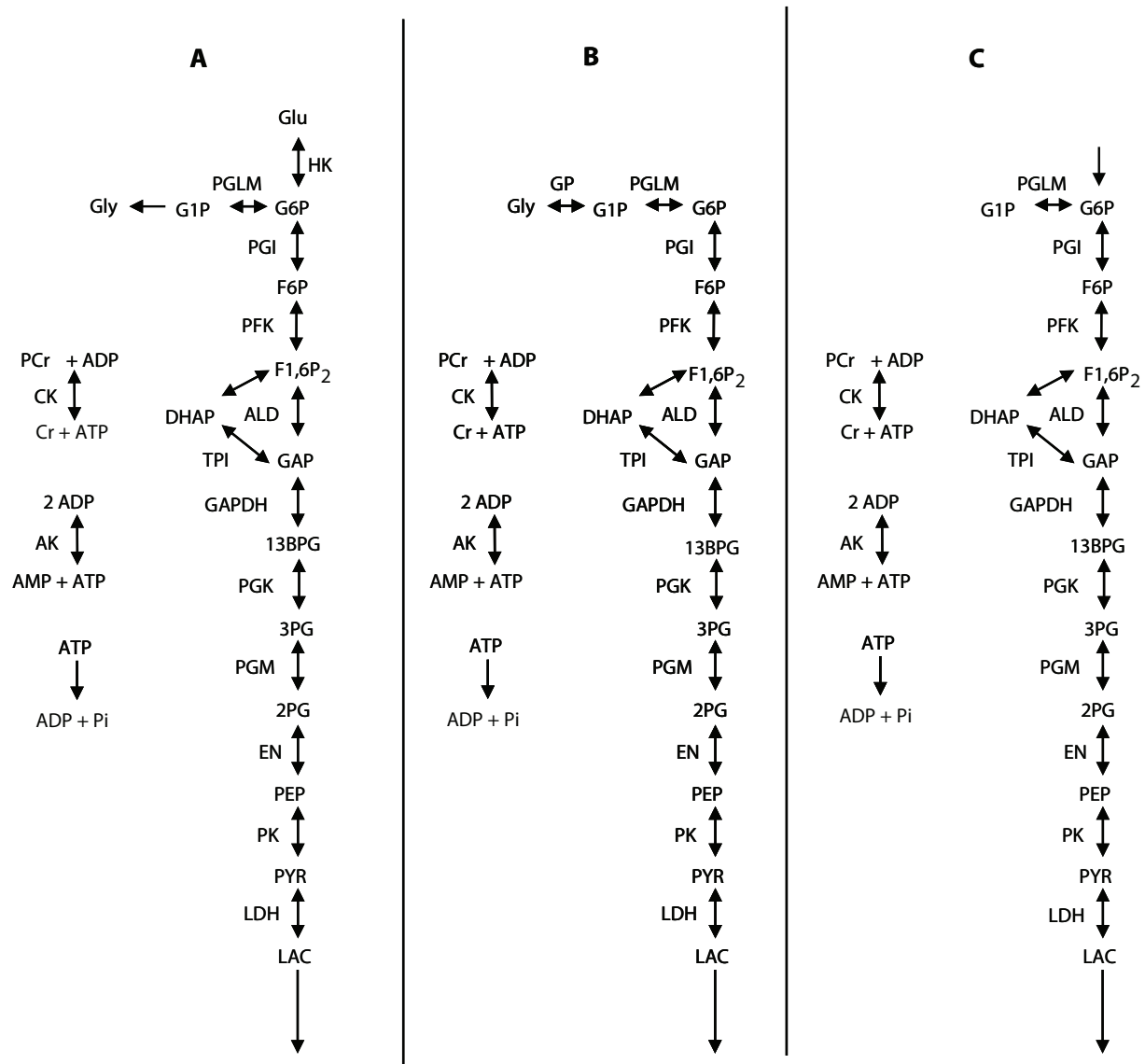


**Figure 1.** Schematic representation of the computational model. Recovery condition model (A), original Lambeth and Kushmerick model (B) and resting condition model (C). Abbreviations: Glu, glucose; HK, hexokinase; PGLM, phosphoglucomutase; Gly, glycogen; G1P, glucose-1-phosphate; G6P, glucose-6-phosphate; PGI, phosphoglucoisomerase; F6P, fructose 6-phosphate; PFK, phosphofruktokinase; F1,6P<sub>2</sub>, fructose 1,6-bisphosphate; ALD, aldolase; DHAP, dihydroxyacetone-phosphate; TPI, triose phosphate isomerase; GAP, glyceraldehyde-3-phosphate; GAPDH, glyceraldehyde-3-phosphate dehydrogenase; 13BPG, 1,3-bisphosphoglycerate; PGK, phosphoglycerate kinase; 3PG, 3-phosphoglycerate; PGM, phosphoglyceromutase; 2PG, 2-phosphoglycerate; EN, enolase; PEP, phosphoenolpyruvate; PK, pyruvate kinase; PYR, pyruvate; LDH, lactate dehydrogenase; LAC, lactate; PCr, phosphocreatine; CK, creatine kinase; ADP, adenosine diphosphate; Cr, creatine; ATP, adenosine triphosphate; AK, adenylate kinase; Pi, inorganic phosphate; AMP, adenosine monophosphate.

Under resting conditions, ATP is mainly produced by mitochondria, whereas the glycolytic pathway accounts for only a minor part of the total ATP production flux. The ATPase flux in resting human skeletal muscle tissue was reported by Blei et al.:  $8 \pm 2 \mu\text{M/s}$  ( $n=5$ ) (2). The part of the ATPase flux that was accounted for by glycolytic ATP production was calculated. Assuming mitochondria synthesize 30 moles of ATP per mole of glucose and glycolysis has a net yield of 2 moles ATP per mole glucose (27), glycolytic flux would account for 1/15 part of the total ATPase flux under the conditions mitochondria rely solely upon pyruvate as substrate. However, under resting conditions

muscle mitochondria also oxidize significant amounts of fatty acids. Reported values for the percentage of fatty acid utilization vary between 30 and 60 percent (28-30). To include this effect and take into account some additional uncertainties due to unknown fluxes through other pathway branches, the glycolytic ATP production flux at rest was estimated to be within the range of 0.1 and 0.75  $\mu\text{M/s}$ . This range is in accordance with literature values of leg glucose uptake (0.05 – 0.35mM/min per limb (31-35)), that were converted by assuming a leg has between 7-10 kg of muscle mass (35).

Blei et al. reported the ATPase rate in resting skeletal muscle; it remained however unknown to which extent these values are also valid for skeletal muscle during recovery conditions. To include this uncertainty in the analysis the ATPase during recovery was estimated to be within a range of 0.1– 10 times the normal resting muscle ATPase activity, which sets the range for ATPase during recovery conditions to 0.0001-0.01 mM/s.

### **Model analysis of recovery dynamics**

The model used to simulate recovery conditions featured a net glycogen production and glucose phosphorylation by hexokinase (recovery condition model, Figure 1A). Developing a kinetic model of the glycogen production pathways was beyond the scope of this study. Instead, net glycogen production was modelled by deleting glycogen phosphorylase flux and substituting it with a net glycogen production flux. Glucose phosphorylation is inhibited at high [G6P]. As a consequence, G6P supply flux by hexokinase could not be modelled as a constant during recovery period, therefore a kinetic model of hexokinase was included. Hexokinase was modelled according to the description of (36), Eq. 2. Although this model was developed for a different cell type, i.e. human erythrocytes, this description was used since in skeletal muscle tissue the same iso-enzyme is predominant too (37).

$$HK_{flux} = \frac{V_{max}^{HK} \frac{[ATP][Glc]}{K_{ATP}K_{ATP,Glc}}}{1 + \frac{[ATP]}{K_{ATP}} + \frac{[Glc]}{K_{Glc}} + \frac{[ATP][Glc]}{K_{ATP}K_{ATP,Glc}} + \frac{[G6P]}{K_{G6P}} + \frac{[Glc][G6P]}{K_{Glc}K_{Glc,G6P}}} \quad (\text{Eq. 2})$$

Kinetic parameter values are listed in Table 1.

The ATPase flux equation was simplified compared to the original model. The mass action equation used by Lambeth and Kushmerick was substituted by a single, parameter (unit mM/s) which effectively clamped ATPase flux at a certain, adjustable level.

**Table 1.** Kinetic parameters of hexokinase model, according to (36)

<b>Parameter</b>	<b>Value</b>	<b>Unit</b>
<b>V<sub>max</sub>HK</b>	0.0078	mM/s
<b>K<sub>ATP</sub></b>	1.76	mM
<b>K<sub>Glc</sub></b>	0.040	mM
<b>K<sub>ATP,Glc</sub></b>	0.051	mM
<b>K<sub>G6P</sub></b>	0.334	mM
<b>K<sub>Glc,G6P</sub></b>	0.069	mM

The model adaptations introduced a few new parameters: kinetic parameters of hexokinase, glycogen production flux and ATPase flux. All other parameters were left unchanged from the original paper of Lambeth and Kushmerick.

Hexokinase kinetic parameter values are listed in Table 1. Intracellular glucose concentration was clamped at 3mM, according to measurements of Katz et al, who reported glucose concentration remained stable during at least the first 10 minutes of recovery following an exhaustive bicycle exercise bout (31).  $V_{max}HK$  was calculated by assuming for [ATP], [Glucose], [G6P] and steady state  $HK_{flux,r}$  8.2mM, 3mM, 0.4mM and 2.5 $\mu$ M/s respectively.

The glycogen production flux (unit  $\mu$ M/s) after a glycogen depleting exercise bout was measured by Price et al. (38). From these results the glycogen production flux was estimated to be within a range of 0 – 0.75  $\mu$ M/s.

The ATPase during recovery was estimated to be within a range of 0.1– 10 times the normal resting ATPase activity, which sets the range for ATPase during recovery conditions to 0.0001-0.01 mM/s.

The model  $V_{max}$  parameters were set by Lambeth and Kushmerick according to the Scopes et al. data (26). As these parameters were not specifically set for human quadriceps muscle uncertainties with respect to these values were also taken into account.  $V_{max}$  values of glycolytic enzymes were assumed to be within a range of 25 – 175 percent of the value determined by Scopes et al. This range was set based upon comparison of glycolytic enzyme activities determined for multiple species: rabbit, pig, rat and human respectively (26,39,40).

Lactate efflux was modelled by a mass action flux, Eq. 3, with parameter  $K_{lac}$  set to 0.01s<sup>-1</sup>.

$$LAC_{eff} = K_{Lac} \cdot [Lac] \quad (Eq. 3)$$

During the first phase of recovery PCr was re-synthesized by mitochondrial function. These dynamics were accompanied by Pi, ADP and AMP concentrations that dropped to resting levels. Pi, ADP and AMP are important substrates and regulators of the glycolytic pathway. The mitochondria exert control on the Pi, ADP and AMP dynamics and thus indirectly on the dynamics of the glycolytic pathway. Modelling glycolysis during the full recovery period would therefore require including a model of mitochondrial function. However, instead of introducing more complexity to the model, we choose a different solution. The first 60 seconds of data were excluded, which restricted our analysis to the part of the data where PCr, Pi, ADP and AMP were close to resting levels. The part of the data analyzed with the computational model is indicated in Figure 3.

All initial conditions were left unchanged from the paper by Lambeth and Kushmerick, except for the initial conditions of [G1P], [G6P] and [F6P] which were set according to the experimental NMR data. The PME detected in the NMR spectra was used to calculate the concentration of HMP, which represent the sum of G1P, G6P and F6P (1,16). Individual G1P, G6P and F6P concentrations were calculated by assuming phosphoglucomutase and phosphoglucoisomerase were close to equilibrium (41,42). Calculated values for initial concentrations of G1P, G6P and F6P were 0.26mM, 4.37mM and 1.96mM, respectively.

For glycogen production flux, ATPase rate and glycolytic enzyme  $V_{max}$  values we determined a range rather than a precise value. A Monte Carlo approach was used to perform

simulations for these parameter distributions. Uniform distributions were assumed within the determined range. 5000 simulations were run, randomly drawing parameter values from the distributions. As a result the computational model predicted a solution space (mean±SD of 5000 simulations) indicating the influence of the width of the distributions on the accuracy of the model predictions. It was tested if 5000 simulations were enough to obtain stable predictions for the models solution space. To this end, the solution space calculated based upon 5000 simulations was compared to the result obtained with 1000 simulations. These results were similar indicating 5000 simulations were enough to provide stable predictions.

### **Maximal glycolytic ATP production capacity**

We calculated the maximal glycolytic ATP production capacity, which was defined as the maximal ATP production flux the model can generate while state variables remained within a physiological domain. During maximal activation of the glycolytic pathway, pathway substrate supply is primarily provided by glycogen breakdown. These conditions were modelled by the original Lambeth and Kushmerick model (Figure 1B). Therefore, the Lambeth and Kushmerick model was used to calculate the maximal pathway flux (pathway  $V_{max}$ ).

Maximal pathway flux was calculated by performing a series of simulations, incrementally increasing the ATPase rate with a step size of 0.01mM/s. All simulations were run until glycolytic ATP production and ATPase fluxes were balanced and steady state was reached. The free energy of cytoplasmic ATP hydrolysis ( $\Delta G_p$ ) was calculated according to Eq. 4, (43):

$$\Delta G_p = \Delta G_p^{\circ'} + RT \ln([ADP][P_i]/[ATP]) \quad (\text{Eq. 4})$$

Where,  $\Delta G_p^{\circ'}$  is -31.8kJ/mol at 37°C.

Previous studies indicated that if  $\Delta G_p$  increased beyond -48kJ/mole, excitation-contraction coupling failed (45). This information was used to constrain the computational dynamic range of the model: if  $\Delta G_p$  increased beyond -48kJ/mole, simulations went out of physiological range and the incremental increase of ATPase flux was ended. The ATPase flux at which the simulations were ended was then defined as the maximal glycolytic ATP production capacity.

### **Identification of control points**

We analyzed which enzymes exerted most of the concentration control under resting conditions. To this end, resting state model predictions (resting condition model, Figure 1C) were compared to literature data of the skeletal muscle resting concentration of a selected subset of metabolites relevant to the model: [ADP], [G6P] and [F-1,6P<sub>2</sub>].

Under resting state conditions it was assumed no net glycogen production or consumption was present. This was modelled by deleting the glycogen phosphorylase flux from the original Lambeth and Kushmerick model. The resting state ATPase flux that was met by glycogenolytic ATP production was, as described in the section 'Estimation of ATPase flux rate', estimated between 0.1 and 0.75  $\mu\text{M/s}$ . Under steady state conditions, glycolytic pathway substrate supply, glycolytic ATP production and ATPase flux are in balance. Glycolysis yields 2 moles of ATP per glucose molecule. This stoichiometry combined with the requirement of steady state conditions determine that

glucose phosphorylation flux is balanced to ATPase flux according to Eq. 5. This relation was used to set the G6P supply flux in these steady state simulations.

$$G6P_{supply} = \frac{1}{2} ATPase \quad (Eq. 5)$$

The concentration control of individual glycolytic enzymes on the concentration of selected metabolites [ADP], [G6P] and [F-1,6P<sub>2</sub>] was calculated by performing a series of simulations. For each simulation a different glycolytic enzyme was inhibited, by multiplying the  $V_{max}$  of that specific enzyme with 0.05 and differences in steady state values of glycolytic intermediates were compared.

## RESULTS

### **<sup>31</sup>P MRS**

Figure 2 shows a selection of <sup>31</sup>P NMR spectra from a large dynamic set acquired from the quadriceps muscle at rest (Figure 2A), during exercise at maximal workload (Figure 2B) and during metabolic recovery (Figures 2C and D). At the end of the incremental exercise bout, the phosphocreatine (PCr) pool was near-depleted and accompanied by complementary increase in Pi. During bicycling at the maximal workload, a significant phosphate-monoester (PME) resonance appeared up-field of the Pi resonance that was attributed to accumulating phosphorylated glycolytic intermediates (hexose-mono-phosphates; HMP) in contracting muscle fibres (1,16). During subsequent metabolic recovery, Pi and PCr returned to resting levels within 60s. The PME resonance, however, exhibited much slower dynamics and was still clearly observed 240s into recovery. The accumulation of HMP is most clearly observed during recovery due to the downfield shift of the Pi resonance as a result of rapid ancillary muscle acidification (Figures 2C and D).

The quantified, pooled results of the <sup>31</sup>P NMR measurements in eight muscles are shown in Figure 3. The PCr concentration decreased from 32.2±3.0 mM (mean±SD; n=8) at rest to 5.9±3.2 mM at the end of the high intensity exercise bout, while Pi increased from 4.8±0.8 to 26.8±3.5 mM (Figure 3A). Accumulation of HMP started during exercise at the highest workload and peaked at 6.9±1.3 mM 42s into recovery, after which a slow, but steady consumption (0.009±0.001 mM/s) was observed (Figure 3B). The HMP concentration, quantified from a spectrum obtained 15 minutes after the end of exercise had returned to resting level (1.1 ± 0.4mM; data point not shown in figure 3). ATP and total phosphate pool levels remained stable within 10% of resting values throughout the entire protocol (8.2 mM and 47 mM, respectively; Figure 3C). Intramuscular pH decreased 0.3 units during the exercise bout from 7.08±0.02 at rest to 6.75±0.05 at maximal workload (Figure 3D). This moderate drop in muscle pH during exercise indicated that the muscle remained well perfused during the entire exercise protocol and lactate and CO<sub>2</sub> were to a high extent washed out of the muscle tissue (46). During the initial phase of recovery, pH dropped another 0.3 units to 6.46±0.11 as a result of rapid consumption of proton buffer (i.e., Pi; (46)) and recovered slowly towards resting value (Figure 3D).

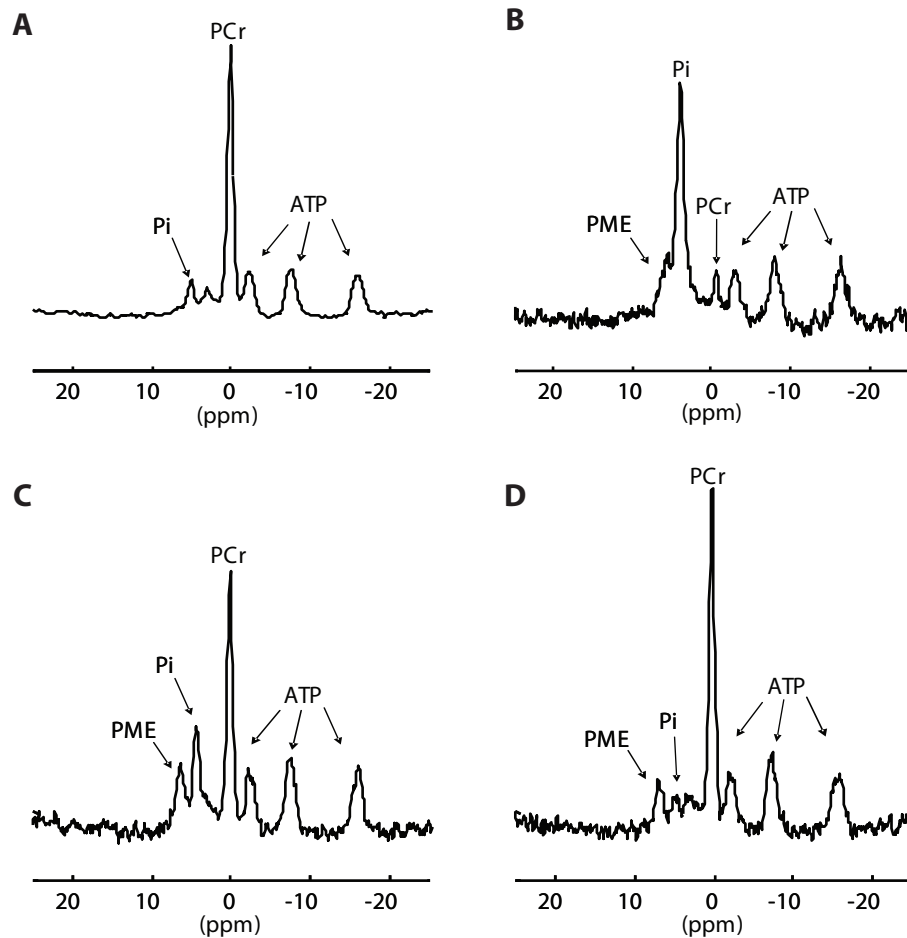


**Figure 2.** Selection of  $^{31}\text{P}$  NMR spectra recorded during the rest-exercise-recovery protocol. The spectra at rest (A), end of exercise (B), 40 s into recovery (C) and 240 s into recovery (D) are shown. Spectra were apodized with a 10 Hz Lorentzian function.

### ***Model simulations of recovery dynamics***

Model simulations of metabolite recovery dynamics were performed in a Monte Carlo approach to account for uncertainties in the model parameter values. In this approach, parameter values for the ATPase rate, the glycogen consumption and  $V_{\max}$  parameters of glycolytic enzymes were selected randomly from a uniform distribution with ranges 0.0001 mM/s – 0.01 mM/s, 0 – 0.75  $\mu\text{M/s}$  and 25% – 175% of the value reported by Scopes et al., respectively. HMP dynamics (sum of glucose-1-phosphate (G1P), G6P and fructose-6-phosphate (F6P) (1,16)) were calculated from the model simulations and compared to the experimental data (Figure 4). The predicted HMP consumption rate was two orders of magnitude faster than the experimentally determined rate (0.57 mM/s versus  $0.009 \pm 0.001$  mM/s, respectively).



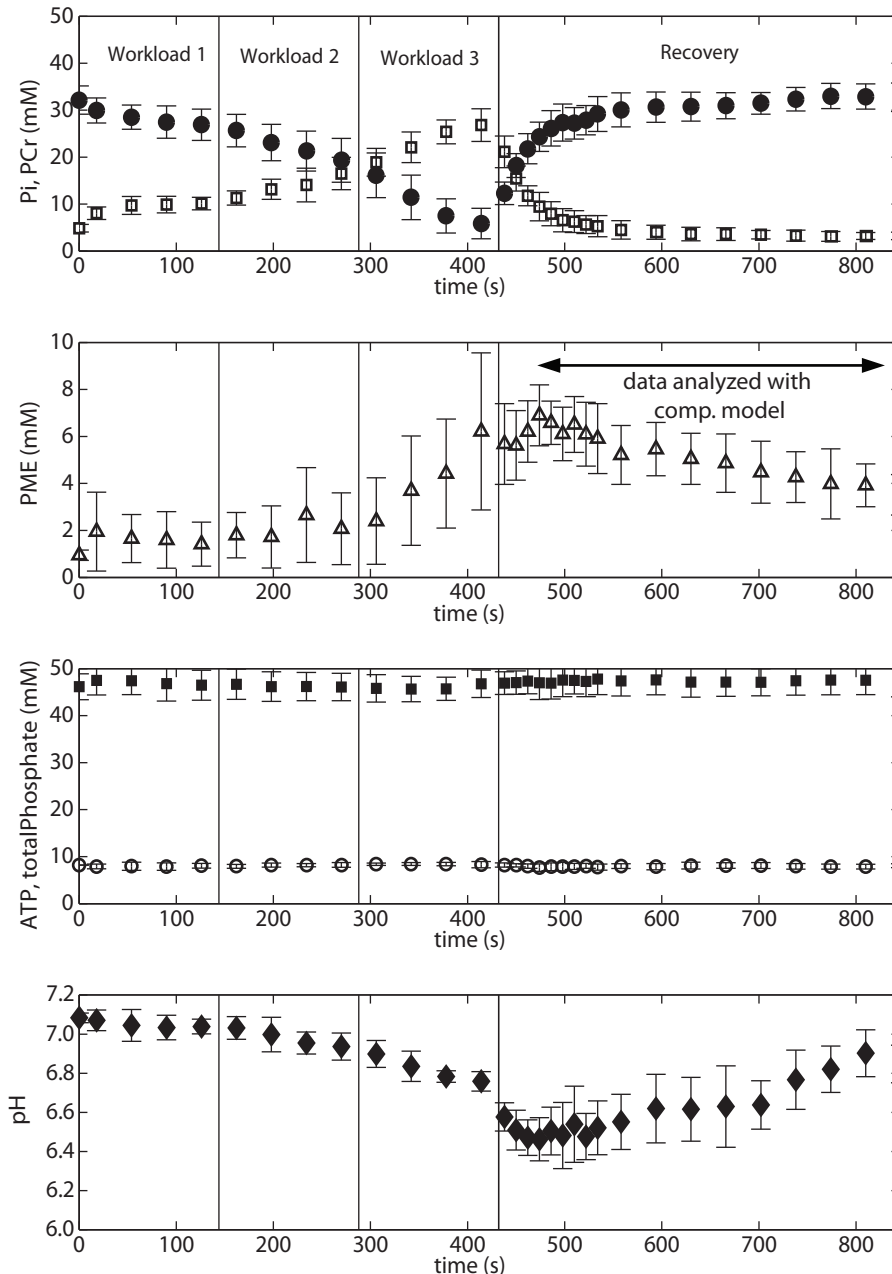


**Figure 3.** Quantified metabolite dynamics during the rest – exercise – recovery protocol. The vertical continuous black lines separate the data points of the three different workloads and the recovery period. The error bars indicate the standard deviation ( $n = 8$ ). The [PCr] (closed circles) and [Pi] (open squares), [PME] (open triangles), [ATP] (open circles) and [total phosphate pool] (closed squares) and the pH (closed diamonds) are shown. The part of the data selected for analysis using the computational model are indicated by a horizontal black bar.

### ***Maximal glycolytic ATP production capacity***

It was next tested if the overly fast kinetics of the recovery conditions model were the trivial result of the maximal glycolytic ATP production capacity of the model exceeding reported experimental values. The maximal glycolytic ATP production of the computational model was calculated to be 1.4 mM/s as described in the Methods section. This value agreed well with the rate reported for a type I muscle fibre and was about half the value reported for a type II muscle fibre (1.5 and 3.0 mM/s, respectively (47)). From these results we concluded that two orders of magnitude faster consumption of HMP predicted by the model (Figure 5) was not a trivial result.

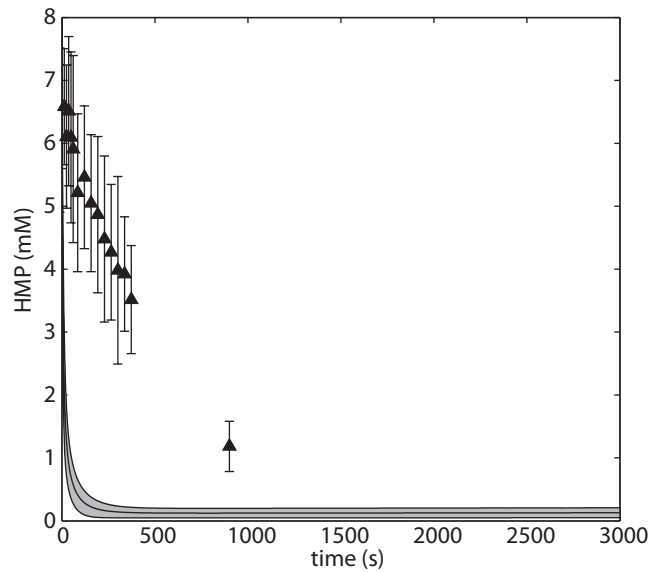


**Figure 4.** Hexose monophosphate recovery dynamics according to predictions of the original model and experimental data. Model predictions of HMP dynamics were calculated by summation of G1P, G6P and F6P dynamics. The solution space (shaded area) is indicated by the mean  $\pm$  S.D. of the 5000 simulations that were run in a Monte Carlo approach. Experimental data represent the pooled results of all eight subjects; error bars indicate standard deviation ( $n = 8$ ).

#### **Identification of control points**

It was next investigated if concentration control in the model was sufficient to reproduce reported experimental values of steady state [ADP], [G6P] and [F-1,6P<sub>2</sub>] (Table 2). Figure 5 shows the effect of inhibition of individual glycolytic enzymes by 95% (individual enzyme  $V_{max}$  value was set to 5% of original value) on steady state [ADP], [G6P] and [F-1,6P<sub>2</sub>]. Measurements of human skeletal muscle resting state metabolite concentrations reported in literature are listed in Table 2 and indicated as shaded areas in Figure 5. From these results, it followed that the model converged at a non-physiological steady state without additional enzyme inhibition, indicating inadequate concentration control. Model simulations predicted a nearly full depletion of G6P and F-1,6P<sub>2</sub> to levels of 0.0094mM and 0.00028 mM respectively, whereas reported values range between 0.24mM – 0.82mM and 0.04mM – 0.06mM, respectively (31,47-49). Likewise, [ADP] fell to a twofold lower value than the consensus value in absence of additional flux inhibition (0.005mM versus 0.01mM (1,50-52), respectively). Steady state metabolite concentrations calculated for the case of selective ancillary enzyme inhibition by 95% showed that [G6P] was increased by inhibition of PFK and [F-1,6P<sub>2</sub>] was increased by inhibition of PK. The steady state [ADP] was affected both by 95% inhibition of PFK and PK.

**Table 2.** Physiological values of metabolite concentrations in resting skeletal muscle. Mean value as well as the range are listed. The range represents the lowest and highest reported values.

State Variable	Mean value	Range	Unit	Reference
ADP	0.010	0.09 – 0.011	mM	(1,50-52)
G6P	0.40	0.24 – 0.82	mM	(31,47,48,53)
F-1,6P <sub>2</sub>	0.050	0.040 – 0.060	mM	(48,49)

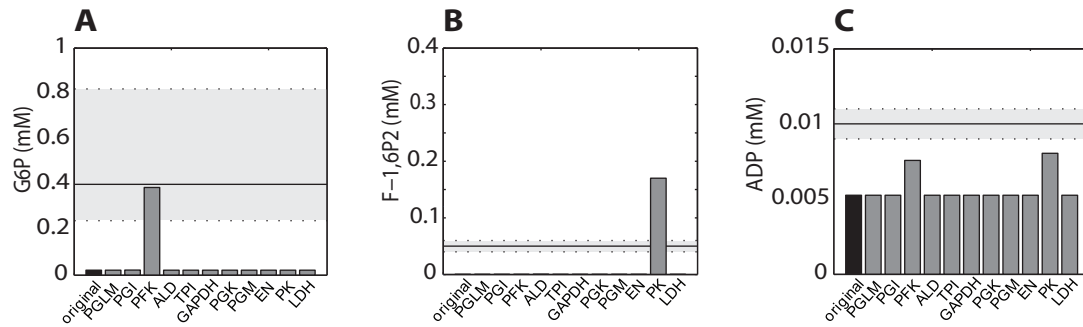


**Figure 5.** Effect of inhibition of individual enzyme activity on resting muscle steady-state [G6P] (A), [F-1,6P<sub>2</sub>] (B) and [ADP] (C). Inhibition of the enzyme activity was modelled by setting  $V_{\max}$  values to 5%. The predictions of the original model are shown as a black bar. The shaded area represents the physiological range and the horizontal continuous black line indicates the mean value, as listed in Table 2. Abbreviations: PGLM, phosphoglucomutase; PGI, phosphoglucoisomerase; PFK, phosphofructokinase; ALD, aldolase; TPI, triose phosphate isomerase; GADPH, glyceraldehyde-3-phosphate dehydrogenase; PGK, phosphoglycerate kinase; PGM, phosphoglyceromutase; EN, enolase; PK, pyruvate kinase; LDH, lactate dehydrogenase.

### Parameterization of PFK and PK inhibition factors

We hypothesized that additional inhibition of PFK and PK in electrically-silent skeletal muscle must be present. Hereto, inhibition factors in the form of  $V_{\max}$  scalars for PFK and PK were introduced into the model. Parameterization of these inhibition factors was performed based upon reported values of [G6P], [F-1,6P<sub>2</sub>] in resting skeletal muscle tissue (Table 2): first, steady state [G6P] was used to fine tune the PFK inhibition factor, next, [F-1,6P<sub>2</sub>] was used to fine tune the PK inhibition factor. [ADP] was used only for verification: for the identified inhibition factor values, steady state [ADP] was within the physiological range. The magnitude of the inhibition factors were estimated for two conditions: the upper and lower values of the estimated ATP consumption rate. This yielded an upper and lower bound on the estimate of the PFK and PK inhibition factor. The values of the inhibition factors and the corresponding steady state metabolite concentrations ([G6P], [F-1,6P<sub>2</sub>] and [ADP]) are listed in Table 3.

**Table 3.** Estimated PFK and PK inhibition factor. PFK and PK inhibition factors were estimated for two conditions: the upper and lower boundary of the ATP consumption rate at rest, 0.75  $\mu\text{M/s}$  and 0.1  $\mu\text{M/s}$ , respectively, yielding an upper and lower boundary for the estimated PFK and PK inhibition factors. Steady state metabolite concentrations ([G6P], [F-1,6P<sub>2</sub>] and [ADP]) predicted by the model that included the inhibition factors are also listed.

	PFK inhibition	PK inhibition	[G6P] [mM]	[F-1,6P <sub>2</sub> ] [mM]	[ADP] [mM]
<b>Upper bound</b>	0.030	0.021	0.38	0.056	0.009
<b>Lower bound</b>	0.0037	0.0027	0.40	0.052	0.010

It was tested if introduction of the PFK and PK inhibition factors caused other state variables to go out of their physiological range. Hereto, the steady state metabolite concentrations were calculated for four cases: (i) no additional inhibition; (ii) inhibition of PFK and PK; (iii) inhibition of PFK; (iv) inhibition of PK. Steady state metabolite concentrations were determined using a Monte Carlo approach. Parameter distributions were assumed for PFK inhibition factor (0.0037 – 0.030, Table 3), PK inhibition factor (0.0027 – 0.021, Table 3) and ATPase rate (0.1 – 0.75  $\mu\text{M/s}$ , see section Methods). The results represented by the mean  $\pm$  SD of the solution space of 5000 simulation runs and initial model conditions are listed in Table 4. Initial model conditions were set by Lambeth and Kushmerick and represent consensus literature values. Adding PFK and PK inhibition resulted in

improved predictions of steady state [G1P], [G6P], [F6P] and [F-1,6P<sub>2</sub>]. PFK inhibition was responsible for the changes observed in [G1P], [G6P], [F6P], whereas PK inhibition was responsible for the changes observed in [F-1,6P<sub>2</sub>]. Predictions of other state variables were not dramatically improved or distorted compared to model simulations without inhibition.

### ***Effect of PFK and PK deactivation on recovery dynamics***

Metabolite concentration dynamics during recovery were calculated for the adapted model featuring PFK and PK deactivation mechanisms. Simulations were run in a Monte Carlo approach. Parameter distributions were assumed for glycogen production flux (0 – 0.75 $\mu$ M/s), ATPase rate (0.01 – 0.0001mM/s), PFK inhibition factor (0.0037 – 0.030, Table 3) and PK inhibition factor (0.0027 – 0.021, Table 3). HMP dynamics were calculated for the case of both PFK + PK inhibition and PFK inhibition only and are shown in Figures 6A and B, respectively. In both cases model predictions agreed well with the experimental data. Figures 6C and D show the model predictions of steady state [G6P], [F1,6P<sub>2</sub>] and [ADP] relative to the literature value, in case of PFK and PK deactivation (Figure 6C) and only PFK inhibition (Figure 6D). The results were normalized by dividing model predictions by the reported literature value. The black line represents the target value of 1, which corresponds to ideal situation of a perfect agreement between literature value and model prediction. The results show that in case of only PFK deactivation, the model failed to correctly predict [F-1,6P<sub>2</sub>] at steady state indicating both PFK and PK deactivation must be present in resting skeletal muscle. Finally, it was investigated if inhibition of all glycolytic enzymes other than PFK and PK by 99% or reduced inhibition of PFK and PK (80%) could produce similar results. In either case, the HMP dynamics were similar to the original model and did not agree with experimental data (data not shown).

## **DISCUSSION**

The main and novel result of the present investigation of muscle glycolysis was the identification of a principal role for the regulation of PFK and PK activity in silencing of glycolytic flux in non-contracting muscle. Below, these results and possible regulatory mechanisms that may be involved in PFK and PK activity control are discussed together with several methodological aspects of the study.

### ***Experimental observations***

The dynamics observed in the PME domain of the NMR spectrum were attributed to G6P, F6P, G1P conform to previous studies (1,16). The accumulation of G6P observed during the high intensity in-magnet exercise protocol agreed with measurements based upon the analysis of muscle biopsy samples obtained after high intensity dynamical exercise (31,47,48,53). Essen and Kaijser collected five biopsy samples during the first 180 seconds of the recovery period (48) to determine the [G6P] dynamics. They also reported [G6P] peaks after about 30 seconds (48). Moreover, the measured rate of G6P consumption (0.007 $\pm$ 0.001mM/s) agreed well with the rate that we determined non-

invasively by  $^{31}\text{P}$  MRS ( $0.006\pm 0.001$  mM/s). The G6P consumption rate was obtained by applying the computational model to decompose the measured HMP consumption rate ( $0.009\pm 0.001$  mM/s) by predicting individual G6P ( $0.006\pm 0.001$  mM/s), G1P ( $0.0004\pm 0.0002$  mM/s), F6P ( $0.003\pm 0.002$  mM/s) consumption rates.

**Table 4.** Model predictions of resting steady state metabolite concentrations. Steady state metabolite concentrations calculated for four cases: (i) no additional inhibition (original model); (ii) PFK and PK inhibition; (iii) PFK inhibition; (iv) PK inhibition. \* indicates improved model prediction as a result of PFK and PK inhibition. \$ indicates improved model prediction as a result of PFK inhibition. # indicates improved model prediction as a result of PK inhibition.

State variable	Initial conditions <sup>a,b</sup> [mM]	Original model [mM] (mean±SD)	PFK and PK inhibition [mM] (mean±SD)	PFK inhibition [mM] (mean±SD)	PK inhibition [mM] (mean±SD)
G1P	0,059	0,00056± 0,00024	0,025±0,011 *	0,025±0,012 \$	0,00057±0,00025
G6P	0,75	0,0094±0,0040	0,41±0,19 *	0,41±0,20 \$	0,0094± 0,0041
F6P	0,23	0,0042±0,0018	0,18±0,086 *	0,19±0,089 \$	0,0042±0,0018
F-1,6P <sub>2</sub>	0,072	0,00028± 0,00020	0,18±0,30 *	2,46e-5±1,42e-5	0,41±0,46 #
DHAP	0,076	0,0011± 0,00045	0,020±0,022	0,00027±0,00011	0,037±0,026
GAP	0,036	0,021±,0087	0,39±0,43	0,0053± 0,0021	0,71±0,50
13BPG	0,065	0,0043± 3,97e-5	0,0032±0,00071	0,0025± 0,0005 8	0,0037±0,0010
P3G	0,052	0,13±0,00021	0,20±0,042	0,12±0,0074	0,21±0,042
P2G	0,0050	0,024±3,69e-5	0,036±0,0076	0,021±0,0013	0,039±0,0076
PEP	0,019	0,012±1,45e-5	0,018±0,0037	0,010±0,00066	0,019±0,0037
PYR	0,099	0,065±5,05e-5	0,012±0,015	0,088±0,010	0,0051±0,0096
LAC	1,3	0,84±0,36	0,84±0,36	0,84±0,36	0,84±0,36
ATP	8,2	8,20±5,0e-5	8,20±0,0046	8,21±0,0013	8,20±0,0051
ADP	0,013	0,0045±5,0e-5	0,0098±0,0046	0,0070±0,0013	0,0095±0,0051
AMP	2,0e-05	1,13e-6±2,5e-8	6,49e-6± 6,94e-6	2,82e-6±1,11e-6	6,47e-6±7,75e-6
Pi	4,1	1,82±0,022	3,79±1,35	3,02±0,60	3,36±1,43
PCr	34,7	38,26±0,037	34,85±2,56	36,49±0,89	35,09±2,89
NAD	0,50	0,50±0,00017	0,47±0,044	0,50±0,00011	0,46±0,048

<sup>a</sup>See Refs: (54-57)

<sup>b</sup>Concentration unreported for skeletal muscle. Estimated values are based upon orders of magnitude seen in other cell types.

### Model parameterization

The Lambeth and Kushmerick model of muscle glycogenolysis, like the majority of computational models of metabolism (e.g.,(4,6)), contains specific values for all model parameters. The lack of information on the exact value of the ATP consumption and glycogen synthesis rates in human quadriceps muscle during recovery following exhaustive exercise as well as the postulated PFK and PK inhibition factors, however, warranted the use of an alternative approach in the present study. Instead of single values, simulations of our adapted model of muscle glycogenolysis were performed using a range of values for this particular subset of the model parameters. This allowed

investigation of the sensitivity of the model predictions to uncertainties in the value of each of these model parameters. Indeed, the predictions of HMP dynamics by the tested adaptations of the Lambeth and Kushmerick model that included additional PFK and PK inhibition were sensitive to these uncertainties (Figure 6A, B). However, the resulting solution space was still sufficiently narrow to allow for detection of improvement of the model predictions after inclusion of the postulated additional strong PFK and PK inactivation in non-contracting muscle. Conversely, it allowed for validation of the model adaptations by comparison of the simulations to the recorded in vivo HMP dynamics. On basis of these findings, we conclude that, in this particular case, the limited incorporation of uncertainties in parameter values in a deterministic computational model of a biological network through the use of parameter value ranges instead of single parameter values was beneficial. Any generic value of this particular model parameterization strategy in computational biology remains to be established.

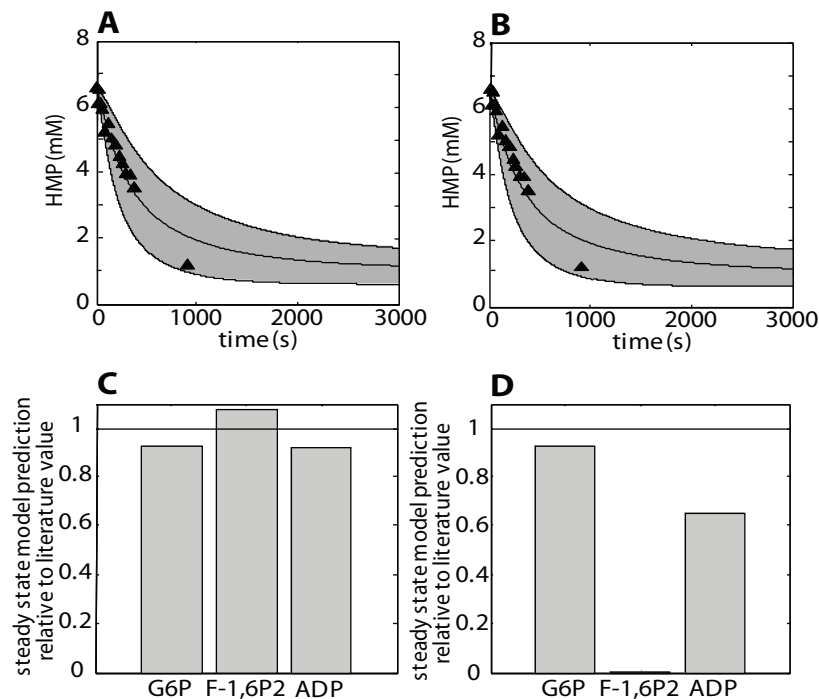


**Figure 6.** Hexose monophosphate recovery dynamics (**A** and **B**) and steady-state G6P, F-1,6P2 and ADP relative to literature values (**C** and **D**), predicted for the case of both PFK and PK inhibition (**A** and **C**) and only PFK inhibition (**B** and **D**). Model predictions of HMP dynamics were calculated by summation of G1P, G6P and F6P dynamics. The solution space (shaded area) is indicated by the mean $\pm$ SD of the 5000 simulations that were run in a Monte Carlo approach. Experimental data represent the pooled results of all eight subjects ( $n = 8$ ); error bars are omitted for clarity of presentation. The values of the steady-state G6P, F-1,6P2 and ADP relative to literature values were calculated by dividing steady-state model predictions by the mean value reported in literature as listed in Table 2.

#### **Model adaptation: PFK inhibition**

We used model predictions of steady state [ADP], [G6P] and [F-1,6P<sub>2</sub>] in combination with measurements of the concentrations of these metabolites in resting human skeletal muscle tissue to identify and parameterize the inhibition factors. As the HMP dynamics were not used in this methodology, they provided an independent dataset that could be used for testing the model adaptations. Comparison of Figures 4 and 6 shows the clear improvement of model predictions as a result of addition of the deactivation mechanisms. This improvement was attributed to the

addition of the PFK inhibition factor; not including PK inhibition did not affect predicted HMP dynamics, Figure 6A,B. The comparison of HMP model predictions and experimental data provides validation of the model adaptations with respect to PFK inhibition.

Previous studies of silencing of glycolysis in resting muscle have proposed direct or indirect (i.e., via a kinase / phosphatase network) inactivation of key glycolytic enzymes by a drop in intracellular  $\text{Ca}^{2+}$  to explain their experimental observations. Alternatively, PFK deactivation may be explained by detachment from the cytoskeleton (13-15). Yet another possible mechanism may be related to pH. Specifically, Hand and Somero measured PFK activity as a function of pH at different temperatures in *Spermophilus beecheyi* (58). They found that at pH 6.8 (temperature 37 °C), there was no inhibition of pH on PFK (PFK activity 95% of  $V_{\text{max}}$ ), whereas at pH 6.5 PFK activity was nearly fully inhibited (PFK activity 5% of  $V_{\text{max}}$ ). During the initial phase of recovery, pH dropped from 6.8 to 6.5 within seconds (Figure 3). As such, pH may have a regulatory function in the work to rest transitions. However, it can not explain the deactivation of PFK in a normal resting skeletal muscle (pH: 7.05) and therefore we concluded that a pH related mechanism of PFK deactivation cannot be the primary mechanism.

#### **Model adaptation: PK inhibition.**

Predictions of resting steady state  $[\text{F-1,6P}_2]$  according to the model with only PFK inhibition were over ten thousand times smaller than experimentally determined. Computational analysis of inhibition of individual glycolytic enzymes indicated PK inactivation must be present in resting skeletal muscle tissue to rise resting  $[\text{F-1,6P}_2]$ . However, no  $\text{Ca}^{2+}$  mediated PK inactivation mechanism has been reported. Model simulations of recovery dynamics of both PFK and PK inhibition and only PFK inhibition showed no difference in predicted HMP dynamics.  $[\text{F-1,6P}_2]$  dynamics were however more affected. These predictions provide valuable information about the mechanisms of PK inhibition. Analysis of muscle biopsy samples taken after intense exercise showed only a twofold increase in  $[\text{F-1,6P}_2]$  from 0.05mM to 0.1mM respectively (48,49). Immediate inactivation of both PFK and PK predicted a solution space of  $[\text{F-1,6P}_2]$  accumulation larger than experimentally observed, whereas only PFK inhibition predicted a solution space more consistent with experimental data. These results indicated that PK inhibition is not present at the onset of the recovery period and the deactivating mechanism is not as fast as PFK inhibition and thus probably also not  $\text{Ca}^{2+}$  mediated. Feed forward regulation of PK activity by  $[\text{F-1,6P}_2]$  is a well known mechanism (59-61) that can explain the PK inhibition at rest. All mammalian PK iso-enzymes are sensitive for allosteric regulation of F-1,6P<sub>2</sub> except for isoenzyme M1 (59-61), which is the isoenzyme found in mammalian skeletal muscle tissue (59-61). However, there is also evidence that a single amino acid substitution in the M1 isoenzyme can turn it into an allosteric regulated enzyme (62). It is not inconceivable that under *in vivo* conditions other factors, e.g. metabolites, signalling molecules, cause a small conformation change which activates the allosteric regulation in the M1 isoenzyme. This investigation indicated PK inhibition must occur in parallel to PFK inhibition, albeit at a much slower timescale. The underlying mechanism, however, remains to be determined.

***Silencing of glycolysis in muscle: hypothesis***

The present finding of a slow HMP consumption rate in muscle in the post-exercise state agreed well with the observation that in spite of high substrate (ADP, Pi) and activator (AMP) levels, glycolytic flux is silenced in non-contracting muscle (16-21). Quistorff et al. did not detect any accumulation of HMP during ischemic recovery from which they concluded glycogen phosphorylase must be regulated in concert with glycolysis (18). This hypothesis was later refuted by results reported by Crowther et al. who found that glycolytic flux was silenced despite a significant increase in HMP (>3mM) (20,21). Instead, these results indicated that the deactivation of glycolytic flux is controlled at one or more sites downstream of glycogenolysis. Our results confirm the findings of Crowther et al. (20,21). Moreover, our computational analysis of metabolite concentrations in resting skeletal muscle, validated by reproduction of the HMP dynamics, has for the first time identified the most likely sites of this regulation (i.e., PFK and PK) as well as the physiological significance of these controls for the skeletal muscle resting state. Specifically, the simulations suggest that the inactivation of PFK and PK in non-contracting muscle is necessary for cellular metabolite concentration control by preventing depletion of ADP and Pi and associated negative effects on other cellular processes including mitochondrial ATP synthesis. Furthermore, glycolytic intermediates like G1P, G6P, F6P, F-1,6P<sub>2</sub> and DHAP would also be depleted affecting fluxes through other branches of the glycolytic pathway. The precise mechanisms involved in the rapid deactivation of PFK and the slower deactivation of PK in skeletal muscle indicated by the present study to occur in the post-exercise state remain, however, to be elucidated.

***Model limitations***

All of the above should be viewed in the context of the limitations of the model simulations. In the process of developing computational models very often model parameterization is based upon data obtained from different species and or cell types (e.g. (63-65)). Here, we have dealt with this problem numerically by performing Monte Carlo simulations to probe the effect of small changes in parameter values on simulation results. A further improvement can be made by determining the glycolytic enzyme kinetic parameters of human quadriceps muscle. In addition, incorporation of knowledge on the pH dependency of these enzyme kinetics (66) would also further improve the basis for the generated hypothesis. Specifically, the NMR data provides quantitative information on *in vivo* muscle pH dynamics that can be used in the computations. With the current model we were not able to exploit this data. Finally, the numerical analysis indicated that additional PFK and PK deactivation must be present to explain the recorded HMP dynamics. The current model could not be used to reveal the precise biochemical implementation of this deactivation. As discussed above, the numerically identified hypothesis relates to the work of others indicating a potential role for Ca<sup>2+</sup> mediated binding of PFK to the cytoskeleton. It can, however, not be ruled out that other (unknown) metabolic feedback loops not included in the model, may also contribute to the predicted magnitude of PFK and PK deactivation. Experimental identification of these control loops and addition of this information into future models can be used to gain quantitative insight in relative contribution of these feedback loops to the deactivation mechanisms.



**Summary**

*In vivo* magnetic resonance spectroscopy revealed a large accumulation of hexosemono-phosphates during exercise and a subsequent slow turnover during metabolic recovery. Computational modelling was used to relate these experimental observations to the control mechanisms of the underlying metabolic pathways. Following this approach, the experimental observations were translated into a new hypothesis that silencing of glycolysis in skeletal muscle tissue involves inactivation of both PFK as well as PK.

## REFERENCES

1. **Walter G, Vandenborne K, Elliott M and Leigh JS.** In vivo ATP synthesis rates in single human muscles during high intensity exercise. *J Physiol* 519 Pt 3: 901-910, 1999
2. **Blei ML, Conley KE and Kushmerick MJ.** Separate measures of ATP utilization and recovery in human skeletal muscle. *J Physiol* 465: 203-222, 1993
3. **Lambeth MJ, Kushmerick MJ.** A computational model for glycogenolysis in skeletal muscle. *Ann Biomed Eng* 30: 808-827, 2002
4. **Dash RK, Li Y, Kim J, Beard DA, Sidel GM and Cabrera ME.** Metabolic dynamics in skeletal muscle during acute reduction in blood flow and oxygen supply to mitochondria: in-silico studies using a multi-scale, top-down integrated model. *PLoS ONE* 3: e3168, 2008
5. **Selivanov VA, de AP, Centelles JJ, Cadefau J, Parra J, Cusso R, Carreras J and Cascante M.** The changes in the energy metabolism of human muscle induced by training. *J Theor Biol* 252: 402-410, 2008
6. **Beard DA.** A biophysical model of the mitochondrial respiratory system and oxidative phosphorylation. *PLoS Comput Biol* 1: e36, 2005
7. **Magnus G, Keizer J.** Minimal model of beta-cell mitochondrial Ca<sup>2+</sup> handling. *Am J Physiol* 273: C717-C733, 1997
8. **Vicini P, Kushmerick MJ.** Cellular energetics analysis by a mathematical model of energy balance: estimation of parameters in human skeletal muscle. *Am J Physiol Cell Physiol* 279: C213-C224, 2000
9. **Beard DA, Bassingthwaite JB and Greene AS.** Computational modeling of physiological systems. *Physiol Genomics* 23: 1-3, 2005
10. **Teusink B, Passarge J, Reijenga CA, Esgalhado E, van der Weijden CC, Schepper M, Walsh MC, Bakker BM, van DK, Westerhoff HV et al..** Can yeast glycolysis be understood in terms of in vitro kinetics of the constituent enzymes? Testing biochemistry. *Eur J Biochem* 267: 5313-5329, 2000
11. **Frieden C.** Protein-protein interaction and enzymatic activity. *Annu Rev Biochem* 40: 653-696, 1971
12. **Winkel BS.** Metabolic channeling in plants. *Annu Rev Plant Biol* 55: 85-107, 2004
13. **Lilling G, Beitner R.** Altered allosteric properties of cytoskeleton-bound phosphofructokinase in muscle from mice with X chromosome-linked muscular dystrophy (mdx). *Biochem Med Metab Biol* 45: 319-325, 1991
14. **Marinho-Carvalho MM, Zancan P and Sola-Penna M.** Modulation of 6-phosphofructo-1-kinase oligomeric equilibrium by calmodulin: formation of active dimers. *Mol Genet Metab* 87: 253-261, 2006
15. **Marinho-Carvalho MM, Costa-Mattos PV, Spitz GA, Zancan P and Sola-Penna M.** Calmodulin upregulates skeletal muscle 6-phosphofructo-1-kinase reversing the inhibitory effects of allosteric modulators. *Biochim Biophys Acta*, 2009
16. **Dawson MJ, Gadian DG and Wilkie DR.** Studies of the biochemistry of contracting and relaxing muscle by the use of <sup>31</sup>P n.m.r. in conjunction with other techniques. *Philos Trans R Soc Lond B Biol Sci* 289: 445-455, 1980
17. **Taylor DJ, Bore PJ, Styles P, Gadian DG and Radda GK.** Bioenergetics of intact human muscle. A <sup>31</sup>P nuclear magnetic resonance study. *Mol Biol Med* 1: 77-94, 1983
18. **Quistorff B, Johansen L and Sahlin K.** Absence of phosphocreatine resynthesis in human calf muscle during ischaemic recovery. *Biochem J* 291 ( Pt 3): 681-686, 1993
19. **Wackerhage H, Hoffmann U, Essfeld D, Leyk D, Mueller K and Zange J.** Recovery of free ADP, Pi, and free energy of ATP hydrolysis in human skeletal muscle. *J Appl Physiol* 85: 2140-2145, 1998
20. **Crowther GJ, Carey MF, Kemper WF and Conley KE.** Control of glycolysis in contracting skeletal muscle. I. Turning it on. *Am J Physiol Endocrinol Metab* 282: E67-E73, 2002
21. **Crowther GJ, Kemper WF, Carey MF and Conley KE.** Control of glycolysis in contracting skeletal muscle. II. Turning it off. *Am J Physiol Endocrinol Metab* 282: E74-E79, 2002
22. **Jenerson JA, Schmitz JP, Hilbers PA and Nicolay K.** An MR-compatible bicycle ergometer for in-magnet whole body human exercise testing. *J Magn Reson* , 2009.
23. **Vanhamme L, van den BA and Van HS.** Improved method for accurate and efficient quantification of MRS data with use of prior knowledge. *J Magn Reson* 129: 35-43, 1997
24. **Taylor DJ, Styles P, Matthews PM, Arnold DA, Gadian DG, Bore P and Radda GK.** Energetics of human muscle: exercise-induced ATP depletion. *Magn Reson Med* 3: 44-54, 1986
25. **Tobin RB, Mackerer CR and Mehلمان MA.** pH effects on oxidative phosphorylation of rat liver mitochondria. *Am J Physiol* 223: 83-88, 1972
26. **Scopes RK.** Studies with a reconstituted muscle glycolytic system. The rate and extent of creatine phosphorylation by anaerobic glycolysis. *Biochem J* 134: 197-208, 1973
27. **Brand MD.** The efficiency and plasticity of mitochondrial energy transduction. *Biochem Soc Trans* 33: 897-904, 2005
28. **Bradley SJ, Kingwell BA and McConell GK.** Nitric oxide synthase inhibition reduces leg glucose uptake but not blood flow during dynamic exercise in humans. *Diabetes* 48: 1815-1821, 1999
29. **Jensen MD, Nguyen TT, Hernandez MA, Johnson CM and Murray MJ.** Effects of gender on resting leg blood flow: implications for measurement of regional substrate oxidation. *J Appl Physiol* 84: 141-145, 1998
30. **Bergman BC, Butterfield GE, Wolfel EE, Casazza GA, Lopaschuk GD and Brooks GA.** Evaluation of exercise and training on muscle lipid metabolism. *Am J Physiol* 276: E106-E117, 1999
31. **Katz A, Broberg S, Sahlin K and Wahren J.** Leg glucose uptake during maximal dynamic exercise in humans. *Am J Physiol* 251: E65-E70, 1986
32. **Bergman BC, Butterfield GE, Wolfel EE, Lopaschuk GD, Casazza GA, Horning MA and Brooks GA.** Muscle net glucose uptake and glucose kinetics after endurance training in men. *Am J Physiol* 277: E81-E92, 1999
33. **Enevoldsen LH, Simonsen L and Bulow J.** Postprandial triacylglycerol uptake in the legs is increased during exercise and post-exercise recovery. *J Physiol* 568: 941-950, 2005

34. **Durham WJ, Miller SL, Yeckel CW, Chinkes DL, Tipton KD, Rasmussen BB and Wolfe RR.** Leg glucose and protein metabolism during an acute bout of resistance exercise in humans. *J Appl Physiol* 97: 1379-1386, 2004
35. **Snyder WS, Cook MJ, Nasset ES, Karhausen LR, Howells GP and Tipton IH.** *Report of the Task Group on Reference Man.* Oxford, UK: Pergamon Press, 1975
36. **Gerber G, Preissler H, Heinrich R and Rapoport SM.** Hexokinase of human erythrocytes. Purification, kinetic model and its application to the conditions in the cell. *Eur J Biochem* 45: 39-52, 1974
37. **Wilson JE.** Hexokinases. *Rev Physiol Biochem Pharmacol* 126: 65-198, 1995
38. **Price TB, Rothman DL, Taylor R, Avison MJ, Shulman GI and Shulman RG.** Human muscle glycogen resynthesis after exercise: insulin-dependent and -independent phases. *J Appl Physiol* 76: 104-111, 1994
39. **Shonk CE, KOVEN BJ, Majima H and Boxer GE.** Enzyme patterns in human tissues II. Glycolytic enzyme patterns in nonmalignant human tissues. *Cancer Res* 24: 722-731, 1964
40. **Shonk CE, Boxer GE.** Enzyme patterns in human tissues I. Methods for the determination of glycolytic enzymes. *Cancer Res* 24: 709-721, 1964
41. **Rolleston FS, Newsholme EA.** Control of glycolysis in cerebral cortex slices. *Biochem J* 104: 524-533, 1967
42. **Eanes WF, Merritt TJ, Flowers JM, Kumagai S, Sezgin E and Zhu CT.** Flux control and excess capacity in the enzymes of glycolysis and their relationship to flight metabolism in *Drosophila melanogaster*. *Proc Natl Acad Sci U S A* 103: 19413-19418, 2006
43. **Jenerson JA, Wiseman RW, Westerhoff HV and Kushmerick MJ.** The signal transduction function for oxidative phosphorylation is at least second order in ADP. *J Biol Chem* 271: 27995-27998, 1996
44. **Rosing J, Slater EC.** The value of G degrees for the hydrolysis of ATP. *Biochim Biophys Acta* 267: 275-290, 1972
45. **Hancock CR, Brault JJ, Wiseman RW, Terjung RL and Meyer RA.** <sup>31</sup>P-NMR observation of free ADP during fatiguing, repetitive contractions of murine skeletal muscle lacking AK1. *Am J Physiol Cell Physiol* 288: C1298-C1304, 2005
46. **Jenerson JA, Bruggeman FJ.** Robust homeostatic control of quadriceps pH during natural locomotor activity in man. *FASEB J* 18: 1010-1012, 2004
47. **Greenhaff PL, Nevill ME, Soderlund K, Bodin K, Boobis LH, Williams C and Hultman E.** The metabolic responses of human type I and II muscle fibres during maximal treadmill sprinting. *J Physiol* 478 ( Pt 1): 149-155, 1994
48. **Essen B, Kaijser L.** Regulation of glycolysis in intermittent exercise in man. *J Physiol* 281: 499-511, 1978
49. **Katz A, Lee AD.** G-1,6-P2 in human skeletal muscle after isometric contraction. *Am J Physiol* 255: C145-C148, 1988
50. **Roef MJ, Reijngoud DJ, Jenerson JA, Berger R and de MK.** Resting oxygen consumption and in vivo ADP are increased in myopathy due to complex I deficiency. *Neurology* 58: 1088-1093, 2002
51. **Chen JT, Argov Z, Kearney RE and Arnold DL.** Fitting cytosolic ADP recovery after exercise with a step response function. *Magn Reson Med* 41: 926-932, 1999
52. **van den Broek NM, De Feyter HM, de GL, Nicolay K and Prompers JJ.** Intersubject differences in the effect of acidosis on phosphocreatine recovery kinetics in muscle after exercise are due to differences in proton efflux rates. *Am J Physiol Cell Physiol* 293: C228-C237, 2007
53. **Sahlin K, Katz A and Henriksson J.** Redox state and lactate accumulation in human skeletal muscle during dynamic exercise. *Biochem J* 245: 551-556, 1987
54. **Arnold H, Pette D.** Binding of glycolytic enzymes to structure proteins of the muscle. *Eur J Biochem* 6: 163-171, 1968
55. **Cheatham ME, Boobis LH, Brooks S and Williams C.** Human muscle metabolism during sprint running. *J Appl Physiol* 61: 54-60, 1986
56. **Harris RC, Hultman E and Nordesjo LO.** Glycogen, glycolytic intermediates and high-energy phosphates determined in biopsy samples of musculus quadriceps femoris of man at rest. Methods and variance of values. *Scand J Clin Lab Invest* 33: 109-120, 1974
57. **Sahlin K.** NADH in human skeletal muscle during short-term intense exercise. *Pflugers Arch* 403: 193-196, 1985
58. **Hand SC, Somero GN.** Phosphofructokinase of the hibernator *Citellus beecheyi*: temperature and pH regulation of activity via influences on the tetramer-dimer equilibrium. *Physiological zoology* 56: 380-388, 1983
59. **Hall ER, Cottam GL.** Isozymes of pyruvate kinase in vertebrates: their physical, chemical, kinetic and immunological properties. *Int J Biochem* 9: 785-793, 1978
60. **Valentini G, Chiarelli L, Fortin R, Speranza ML, Galizzi A and Mattevi A.** The allosteric regulation of pyruvate kinase. *J Biol Chem* 275: 18145-18152, 2000
61. **Fothergill-Gilmore LA, Michels PA.** Evolution of glycolysis. *Prog Biophys Mol Biol* 59: 105-235, 1993
62. **Ikeda Y, Tanaka T and Noguchi T.** Conversion of non-allosteric pyruvate kinase isozyme into an allosteric enzyme by a single amino acid substitution. *J Biol Chem* 272: 20495-20501, 1997
63. **Wu F, Yang F, Vinnakota KC and Beard DA.** Computer modeling of mitochondrial tricarboxylic acid cycle, oxidative phosphorylation, metabolite transport, and electrophysiology. *J Biol Chem* 282: 24525-24537, 2007
64. **Cortassa S, Aon MA, Marban E, Winslow RL and O'Rourke B.** An integrated model of cardiac mitochondrial energy metabolism and calcium dynamics. *Biophys J* 84: 2734-2755, 2003
65. **Nguyen MH, Jafri MS.** Mitochondrial calcium signaling and energy metabolism. *Ann N Y Acad Sci* 1047: 127-137, 2005
66. **Vinnakota K, Kemp ML and Kushmerick MJ.** Dynamics of muscle glycogenolysis modeled with pH time course computation and pH-dependent reaction equilibria and enzyme kinetics. *Biophys J* 91: 1264-1287, 2006





# Chapter 3

## *Combined in vivo and in silico investigations of activation of glycolysis in contracting skeletal muscle*

Adapted from

J.P.J. Schmitz, W. Groenendaal, B. Wessels, R.W. Wiseman  
P.A.J. Hilbers, K. Nicolay, J.J. Prompers, J.A.L. Jeneson, N.A.W. van Riel  
*Combined in vivo and in silico investigations of activation of glycolysis in contracting skeletal muscle*  
(submitted)

## ABSTRACT

The hypothesis was tested that the variation of *in vivo* glycolytic flux with contraction frequency in skeletal muscle can be qualitatively and quantitatively explained by calcium-calmodulin activation of phosphofructokinase (PFK). Ischemic rat tibialis anterior muscle was electrically stimulated at frequencies between 0 and 80 Hz to co-vary the ATP turnover rate and calcium concentration in the tissue. Estimates of *in vivo* glycolytic rates and cellular free energetic states were derived from dynamic changes in intramuscular pH and phosphocreatine content, respectively, determined by phosphorus magnetic resonance spectroscopy (<sup>31</sup>P MRS). Computational modeling was applied to relate these empirical observations to understanding of the biochemistry of muscle glycolysis. Hereto, the kinetic model of PFK activity in a previously reported mathematical model of the glycolytic pathway was adapted to contain a calcium-calmodulin binding sensitivity. The two main results were: introduction of regulation of PFK activity by binding of a calcium – calmodulin complex in combination with activation by increased concentrations of AMP and ADP was essential to qualitatively and quantitatively explain the experimental observations. Secondly, the model predicted that shutdown of glycolytic ATP production flux in muscle post-exercise may lag behind deactivation of PFK (timescales: 5-10 s versus 100 – 200 ms, respectively) as a result of accumulation of glycolytic intermediates downstream of PFK during contractions.

## INTRODUCTION

Glycolysis plays a central role in catabolism and anabolism for all cell types (1,2). Identification of regulatory mechanisms has been important to many areas of biomedical research, ranging from basic understanding of the biochemistry of carbohydrate utilization to applications in biotechnology (3) and drug development for cancer therapies (4). In mammalian cells, skeletal muscle has been a key experimental model to study the regulation of glycolysis and glycogenolysis. It can increase the glyco(geno)lytic ATP production flux by two orders of magnitude during rest to work transitions on a timescale of seconds (5). This exceptionally broad and dynamic operational range of glyco(geno)lytic flux puts a high duty cycle upon the control mechanism(s) of this pathway.

Several approaches have been used to elucidate the underlying regulatory mechanisms including physical isolation and *in vitro* kinetic characterization of individual enzymes from skeletal muscle providing a wealth of information on the individual components of this pathway (6). The application of non-invasive, non-destructive investigative techniques such as *in vivo* nuclear magnetic resonance spectroscopy (MRS) have since allowed studying the behavior of the intact pathway in muscle (7). For example, it has been demonstrated that glycolytic flux rapidly shuts down in the absence of muscle contraction (8-12). More recently, computational modeling approaches have been used to integrate the accumulated knowledge base at the molecular level including quantitative formulation of hypotheses on regulatory mechanisms with *in vivo* flux measurements to test this knowledge base against empirical data (6).

The precise biochemical mechanisms underlying the rapid shutdown of glycolysis in muscle upon termination of muscle contraction have remained poorly understood (6,chapter 2).In chapter 2 we showed that reproducing this particular pathway characteristic solely on the basis of known *in vitro* enzymes kinetics is not possible. Specifically, silencing of glycolysis in non-contracting muscle requires rapid deactivation of the key crossover enzymes phosphofructokinase (PFK) and pyruvate kinase (PYK) in the pathway (chapter 2). The regulation at the level of PFK was predicted to have a dominant role in glycolytic flux control, while in contrast the regulation of PYK was found to be more relevant to glycolytic metabolite concentration control particularly with respect to intermediate metabolites downstream of PFK. A mechanism that may explain the wanting additional regulation at the level of PFK is calcium - calmodulin mediated activation of this enzyme by binding of PFK to e.g. cytoskeleton and the contractile proteins (14-16). Whether or not this mechanism is qualitatively and quantitatively sufficient to reconcile the observed characteristics *in vivo* remains to be tested.

Here, this question was further investigated. Testing of the PFK calcium activation hypothesis is, however, not straightforward for practical reasons. On the one hand, the (i) complexity of muscle cell structure (e.g. cytoskeletal localization) and (ii) ancillary processes (e.g. fast calcium release and uptake and calcium – calmodulin signaling) are difficult to include in an *in vitro* experimental system. On the other hand, *in vivo* experiments likewise suffer from practical limitations. These include the fact that (i) the pathway can only be studied as an integrated system, (ii) few biochemical indicators are available to evaluate glycolytic output (for example intermediate metabolite concentrations are often unknown), (iii) there is only limited control of individual variables (metabolite levels often co-vary with changes in flux (9,10) and, (iv) pathway flux may change with negligible variations in steady state metabolite concentrations.



To overcome these limitations, the present investigation of calcium regulation of PFK activity in skeletal muscle via PFK - calmodulin interaction has employed an integrative approach of combining *in vivo* measurements of pathway behavior and the extensive database of known enzyme kinetics embedded in a computational model. The *in vivo* read-outs were acquired in rat using  $^{31}\text{P}$ -MRS of the ischemic tibialis anterior (TA) evoking contractions at different duty cycles, thereby inducing varying conditions of myocellular calcium concentration and glycolytic flux. The objective of the modeling studies was to reproduce both metabolite and pH dynamics for these different electrically-induced contraction protocols and test whether pathway regulation proposed within the computational model was consistent with the measured physiologic behavior. It is shown that introduction of regulation of PFK activity by binding of a calcium – calmodulin complex in combination with classic AMP and ADP activation was qualitatively and quantitatively necessary and sufficient for model predictions to be consistent with *in vivo* behavior.

## METHODS

### Study design

The principal aim of this study was to investigate the regulation of glycolysis in muscle *in vivo* through the use of an integrated approach of experiments and computational modeling. The experimental work involved  $^{31}\text{P}$  MR spectroscopy of the exercising rat TA muscle. To prevent complications from oxidative ATP production all experiments were performed under conditions of ischemia. Different metabolic workloads and levels of calcium were applied by varying the frequency of muscle excitation. From these data measures for the metabolic status of the muscle (PCr concentration) and the glycolytic rate (deduced from pH dynamics) were determined. The aim of the modeling effort was to test if addition of calcium – calmodulin activation of PFK allowed the model to reproduce both metabolic state of the muscle (PCr concentration) and glycolytic rate (pH dynamics). The recorded dynamics of the sugar phosphates were used as input signal of the model (for detailed description see section: *Pathway supply flux*). Therefore the model for glycogenolysis does not contain a kinetic description of glycogen phosphorylase (GP). The dynamics of GP activity, including the activation of GP by calcium (17), were included in the experimentally determined input flux.

### Experimental methods

#### **Animals**

Adult male Wistar rats (385 $\pm$  22 gram, 15 weeks old, n=28, Charles River Laboratories, France) were housed in groups at 20°C and 50% humidity, on a 12-h light dark cycle with ad libitum access to water and chow. Principles of laboratory animal care were followed and all experimental procedures were approved by the Animal Ethics Committee of Maastricht University, the Netherlands. During preparatory surgical procedures and MRS experiments, animals were anesthetized using 0.8-1.2% isoflurane (Forene, Abbot GmbH, Wiesbaden Germany) administered

via a face mask with medical air and oxygen (0.2 and 0.1 L/min respectively). Temgesic was used as analgesic (0.3mg/ml Temgesic in saline solution (1:10), 0.10 mg/kg, Schering-Plough). Body temperature was maintained at  $37\pm 1^\circ\text{C}$  using heat pads and monitored by a custom build monitoring system. In the MR scanner, respiration was monitored using a pressure sensor registering thorax movement (Rapid Biomedical, Rimpair, Germany). Ischemia was applied by means of a silicone vessel loop (Identi Loops supermaxi blue, Dispo Medical), which was applied around the thigh to restrict blood flow in the leg.

Contractions were induced by using electrical stimuli applied via acute, subcutaneously implanted platinum electrodes positioned along the distal nerve trajectory of the n. peroneus communis. Excitation of this nerve induced contraction in the TA, extensor digitorum longus (EDL), peroneus longus and brevis in the anterior compartment of the rat hind limb (18,19). Stimulation voltage ranged between 6-7 V, pulse length was 1 ms. Contractile duty cycles were varied over a range of frequencies (5, 10, 40, and 80Hz) and pulse train lengths, summarized in Table 1. For each group 4-5 successful measurements were obtained in different animals. All experiments were conducted under ischemic conditions. Successful occlusion of oxygen supply to the muscle was verified by the absence of any PCr and pH recovery in the 10 minutes after exercise.

**Table 1.** Summary experimental groups

Group	Stimulation frequency (Hz)	Pulse train length (#pulses)	Pulse train length (s)	Duration of the experiment (min)
<b>Group 1 (rest)</b>	No stimulation			120 min
<b>Group 2</b>	1	5	5	20 min*
<b>Group 3</b>	5	10	2	20 min*
<b>Group 4</b>	10	10	1	20 min*
<b>Group 5</b>	40	10	0.25	20 min*
<b>Group 6</b>	40	20	0.5	20 min*
<b>Group 7</b>	80	10	0.125	20 min*

\* protocol consisted out of 2 min rest, 8 min electrical stimulation, 10 min rest

### ***<sup>31</sup>P NMR acquisition parameters***

All MRS measurements were performed on a 6.3 T horizontal Bruker magnetic resonance spectrometer (MRS) (Bruker, Ettlingen, Germany). Phosphorus (<sup>31</sup>P) MRS was performed by using a two coil configuration. A circular <sup>1</sup>H surface coil (40 mm) was used to adjust the magnetic field homogeneity using the available proton signal from water, while a smaller elliptical surface coil (10/18 mm) was positioned over the TA to acquire phosphorus data. <sup>31</sup>P spectra were acquired applying an adiabatic excitation pulse with a flip angle of 90°. A fully relaxed spectrum (TR=20 s, 32 averages) was measured at rest. A time series of spectra (TR = 5 s, 2 averages) before, during and after electrical stimulation of ischemic TA. A time series consisted of 2 minutes rest, 8 minutes stimulation and 10 minutes after stimulation. An exception was the experiment without stimulation (group 1, Table 1), which had a duration of 120 minutes.

### ***Coil sensitivity profile***

The sensitivity profile of the <sup>31</sup>P coil was calculated from a 2D chemical shift imaging (CSI) dataset recorded in rest conditions with blood supply intact. 2D CSI acquisition parameters were: FOV, 25x25 mm<sup>2</sup>; matrix size, 16x16 (reconstruction 32x32); TR=5000 ms; hamming weighted acquisition and post processing with 1800 scans in total, and adiabatic excitation pulse with a flip angle of 90°

(identical to the time series experiments). The intensity of the PCr peak was calculated for each voxel. The intensity of the PCr peak was integrated over the voxels of the muscle in which contractions were induced (TA, EDL and peroneus longus + brevis), and the voxels in which no contractions were induced. These calculations indicated that 75% of the signal detected by the surface coil, originated from contracting muscle. The residual signal (25%) was received from the non-contracting muscle.

### Data processing

<sup>31</sup>P MR spectra were fitted in the time domain by using nonlinear least squares algorithm in the jMRUI software package (20). The PCr peak was fitted to a Lorentzian line shape. The inorganic phosphate (Pi) and phosphor-monoester (PME) peaks and α- and γ-ATP peaks were fitted to Gaussian line shapes. α- and γ-ATP peaks were fitted with equal peak areas. The β-ATP was not quantified because of concerns for the limited bandwidth of the excitation pulse. Absolute concentrations were calculated after correction for partial saturation with the assumption that the ATP concentration is 8.2 mM at rest (21,22). Intracellular pH was calculated from the chemical shift difference between the Pi and PCr resonances ( $\delta$ ; measured in part per million), according to Eq. 1 (23).

$$pH = 6.75 + \log\left(\frac{\delta - 3.27}{5.63 - \delta}\right) \quad (Eq. 1)$$

The <sup>31</sup>P coil received signal from both contracting muscle (75%) and non-contracting muscle (25%), (see paragraph on *coil sensitivity profile*). The metabolite dynamics in the contracting muscle were derived from the measured dynamics according to the following calculations. The signal received by the <sup>31</sup>P MRS coil is described by equation Eq. 2.

$$X_{observed}(t) = X_{contraction}(t) \cdot F_{contraction} + X_{non-contraction}(t) \cdot F_{non-contraction} \quad (Eq. 2)$$

Where,  $X_{observed}$ ,  $X_{contraction}$ ,  $X_{non-contraction}$ ,  $F_{contraction}$ ,  $F_{non-contraction}$  denote the measured metabolite concentration, the metabolite concentration in contracting muscle, metabolite concentration in the non-contracting muscle, the fraction of the signal originating from contracting muscle and the fraction of the signal originating from non-contracting muscle, respectively.

$F_{contraction}$  and  $F_{non-contraction}$  were set according to the values determined from the 2D-CSI dataset: 0.75 and 0.25, respectively.  $X_{non-contraction}(t)$  was determined from the ischemia experiment without electrical muscle stimulation. According to this dataset  $ATP_{non-contraction}(t)$  could be assumed constant during the first 30 minutes at 8.2mM.  $PCr_{non-contraction}(t)$ ,  $Pi_{non-contraction}(t)$  and  $PME_{non-contraction}(t)$  during the first 30 minutes are well described by equations:  $PCr_{non-contraction}(t) = PCr_{rest} - ATPase_{rest} \cdot t$ ,  $Pi_{non-contraction}(t) = Pi_{rest} + ATPase_{rest} \cdot t$  and  $PME_{non-contraction}(t) = 0.92 + 0.000564 \cdot t$ , with  $PCr_{rest}$ ,  $Pi_{rest}$  and  $ATPase_{rest}$  set to 33.5 mM, 6.2 mM and 0.01 mM/s, respectively. By adding this information to Eq. 2, the equations for calculation of metabolite dynamics in the contracting muscle compartment become:

$$\begin{aligned}
 PCr_{contracting}(t) &= \frac{PCr_{observed}(t) - (33.5 - 0.01 \cdot t) \cdot 0.25}{0.75} \\
 Pi_{contracting}(t) &= \frac{Pi_{observed}(t) - (6.2 + 0.01 \cdot t) \cdot 0.25}{0.75} \\
 ATP_{contracting}(t) &= \frac{ATP_{observed}(t) - 8.2 \cdot 0.25}{0.75} \\
 PME_{contracting}(t) &= \frac{PME_{observed}(t) - (0.92 + 0.000564 \cdot t) \cdot 0.25}{0.75}
 \end{aligned} \tag{Eq. 3}$$

### ***Selection of data included in computational analysis***

The ATP hydrolysis rate was modeled by mass action kinetics, Eq. 4. Because the [ATP] is well buffered by creatine kinase at values close to 8.2 mM, effectively the ATP hydrolysis rate is assumed constant during exercise. The experimental data included in the numerical analyses were therefore limited to the part of the dataset for which it was verified that this assumption was not violated by the onset of fatigue. The ATP hydrolysis flux during the experiment was calculated as the sum of the PCr breakdown rate and the glycolytic ATP production. Estimation of glycolytic ATP production rate was performed by application of a phenomenological model described by Conley et al. (24). From these calculations it followed that the assumption of constant ATP hydrolysis rate was not violated for conditions of pH > 6.5. Therefore, model simulations were run until pH dropped below 6.5.

## **Computational methods**

### ***Modeling glycolysis in skeletal muscle***

A previously developed detailed kinetic model of glycolysis in muscle was used as a basis of the computational analyses (25). A schematic overview of the model is shown in Figure 1. The model includes flux descriptions of the glycolytic enzymes: glycogen phosphorylase (GP), phosphoglucomutase (PGLM), phosphogluco-isomerase (PGI), phosphofructokinase (PFK), aldolase and triose phosphate isomerase (ALD and TPI), glycerol-3-phosphate dehydrogenase (G3PDH), glyceraldehyde-3-phosphate dehydrogenase (GAPDH), phosphoglycerate kinase (PGK), phosphoglyceromutase and enolase (PGM and EN), pyruvate kinase (PYK), and lactate dehydrogenase (LDH). In addition, the model contained detailed reaction kinetics of cellular ATP buffering processes: creatine kinase (CK) and adenylate kinase (AK). ATP hydrolysis was described by mass action kinetics, Eq. 4.

$$flux_{ATP\_Hydr} = k_{ATP\_Hydr} \cdot [ATP] \tag{Eq. 4}$$

During actual experimental conditions large acidifications in cytosolic pH were observed (7.2 – 6.2). The effects of varying proton concentration on enzyme kinetics, pH dependency of enzyme  $v_{max}$  and equilibrium constants were included when known. Furthermore, proton buffering by metabolites and proteins and other cell structures was modeled by assuming a constant cellular buffer capacity (proteins) and dynamical buffer capacity which was calculated from metabolite concentrations. The stoichiometry of proton production and consumption was included for all

modeled reactions in order to predict cellular proton accumulation. For further details on flux equations and kinetic parameter values we refer to the original work published by Vinnakota and co-workers (25). Ordinary differential equations (ODE's) were numerically solved using ODE15s, Matlab 7.5.0 (the Mathworks Inc., Natick, MA, USA)

Several changes to the Vinnakota model were made: First, the temperature for the model simulations was set to 35° C. Since the original framework by Vinnakota et al. used  $v_{\max}$  parameters determined at 25° C, all  $v_{\max}$  parameters were updated according to values determined at 37° C reported by Eagle and Scopes (26). Second, ATP synthesis flux by oxidative phosphorylation was removed because the current experiments were conducted under ischemic conditions. Third, the model for pathway supply of phosphorylated glucose was changed and fourth, the kinetic model description of PFK was substituted by a new rate equation. In the following sections the changes for the model for pathway supply flux and rate equations of PFK will be described in detail.

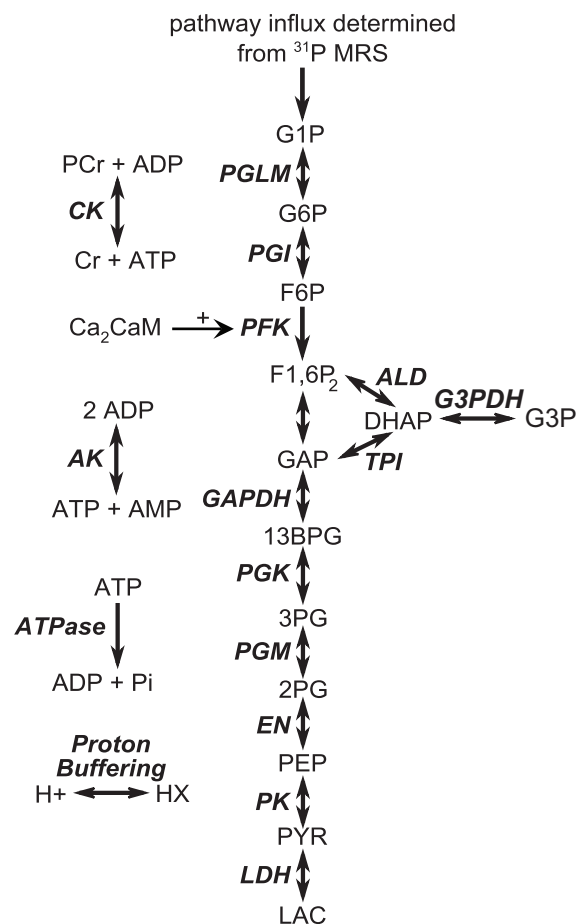


**Figure 1.** Schematic overview of the computational model. Abbreviations denote: PGLM, phosphoglucomutase; PGI, phosphoglucoisomerase; PFK, phosphofrufructokinase; ALD, aldolase; TPI, triose phosphate isomerase; GAPDH, glyceraldehydes-3-phosphate dehydrogeanse; G3PDH, glycerol-3-phosphate dehydrogenase; PGK, phosphoglycerate kinase; PGM, phosphoglyceromutase; EN, enolase; PYK, pyruvate kinase; LDH, lactate dehydrogenase; CK, creatine kinase; AK, adenylate kinase; ATPase, ATP hydrolysis; G1P, glucose-1-phosphate; G6P, glucose-6-phosphate; F6P, fructose-6-phosphate; F1,6P<sub>2</sub>, fructose-1,6-biphosphate; DHAP, dihydroxyacetone-phosphate; G3P, glycercol-3-phosphate; GAP, glyceraldehydes-3-phosphate; 13BPG, 1,3-biphosphoglycerate; 3PG, 3-phosphoglycerate; 2PG, 2-phosphoglycerate; PEP, phosphoenolpyruvate; PYR, puryvate; LAC, lactate; PCr, phosphocreatine; Cr, creatine; ADP, adenosine-diphosphate; ATP, adenosine-triphosphate; Ca<sub>2</sub>CaM, calcium-calmodulin complex; AMP, adenosine-monophosphate; Pi, inorganic phosphate; HX, protons bound to cellular proton buffer.

### Pathway supply flux

The original model described by Vinnakota et al. included glycogen phosphorylase (GP) to account for the pathway supply flux. However, model simulations revealed that the dynamic range of the GP model was insufficient to predict a realistic flux through this pathway (data not shown). This model behavior was probably due to lack of allosteric interactions of G6P in the flux descriptions and enzyme phosphorylation dynamics. At the moment, no better validated, detailed model of GP is available. Therefore it was chosen to deduce pathway influx from our own experimental data. For conditions of constant ATP, it was assumed that the PME resonance represented the summed concentration of G1P, G6P and F6P, which is in accordance with reports from other investigators (5,11). The PME dynamics were well described by a linear function (data not shown). The derivative of this linear function was used to model the G1P input flux. The coefficients of the linear relation are provided in Table 2. It was assumed that all pathway influx was due to glycogen breakdown. The contribution of hexokinase was assumed negligible due to the complete occlusion of muscle blood flow blocking glucose supply to the muscles.

**Table 2.** Linear fit to observed PME dynamics

Group	[PME] t = 0 (mM)	Slope (mM s <sup>-1</sup> )
Group 1 (rest)	0.9	0.00056
Group 2 (1 Hz)	1.5	0.010
Group 3 (5 Hz)	1.5	0.022
Group 4 (10 Hz)	1.5	0.023
Group 5 (40 Hz)	1.5	0.019
Group 6 (40 Hz)	1.5	0.019
Group 7 (80 Hz)	1.5	0.015

### Calcium- calmodulin mediated activation of PFK

The PFK model was substituted by the pseudorandom order, statistical inhibition model originally developed by Waser et al. (27) and adapted by Connett (28). In this section the adaptations of this model are described. For the full set of equations governing this model the reader is referred to the Appendix. Connett reported this model to be superior in terms of reproducing *in vitro* enzyme kinetics compared to the PFK description used by Vinnakota et al. (25). It does not include regulation by citrate or fructose -2,6 biphosphate, both of which are strong allosteric modulators of PFK *in vitro* (29). The rationale for not including them in the kinetic model was that for mammals the dynamic range of these modulators in skeletal muscle is small and therefore their contribution to the control of the enzyme *in vivo* is very limited (30,31).

The model proposed by Connett featured an ADP and AMP dependent term to account for competitive binding of ADP and AMP to the ATP inhibition site. This term will hereafter be referred to as 'deinhibition' term. The definition of this term is:

$$deinhibition = 1 + \frac{AMP}{k_{AMP}} + \frac{ADP}{k_{ADP}} \quad (Eq. 5)$$

Where,  $k_{AMP}$  and  $k_{ADP}$  are the AMP and ADP competitive binding constants respectively and  $AMP$  and  $ADP$  the AMP and ADP concentration.

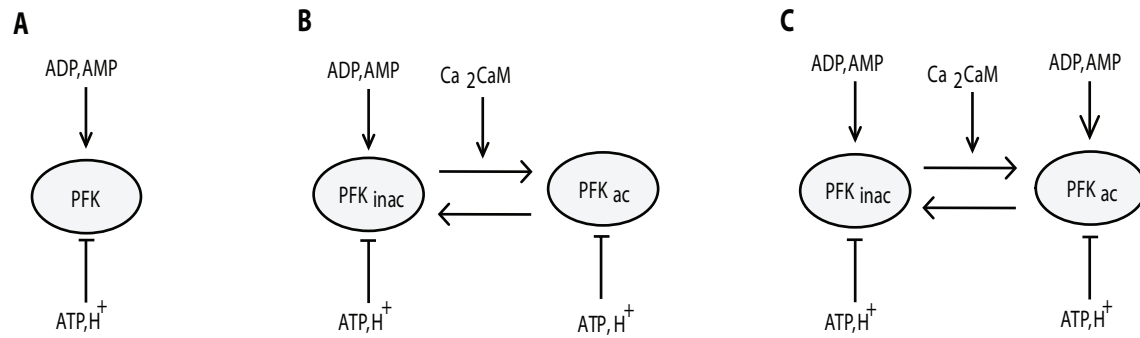


**Figure 2.** Schematic representation of the regulation of PFK as modeled in each model configuration. Model configuration *i* (A) represented the hypothesis in which no regulation of PFK by calcium – calmodulin signaling is present. Model configuration *ii* (B) represented the hypothesis in which binding of calcium – calmodulin complexes to PFK partly relieves ATP inhibition of the enzyme independent of the levels of ADP and AMP. Model configuration *iii* (C) represented the hypothesis in which binding of calcium – calmodulin complexes partly relieves ATP inhibition by enhancing the competitive binding of AMP and ADP to the inhibitory ATP site.

Effectively, an increase of the deinhibition term as a result of elevated AMP and ADP levels relieves part of the ATP inhibition thereby activating PFK flux. At physiological concentrations ( $\sim 8$  mM) ATP inhibition results in a nearly full deactivation of the enzyme ( $>95\%$ ) (16). Reversing this inhibition will therefore result in a significant increase of the enzymes catalytic activity.

In the present investigation, three different configurations of the PFK model were evaluated (Figure 2). The first configuration ('model configuration *i*') represents conditions in which no calcium – calmodulin mediated activation of PFK is present (Figure 2A). This model includes the PFK flux equation proposed by Connett (28). The parameter values of  $k_{AMP}$  and  $k_{ADP}$  were estimated from the PCr and pH time course data as described in the section '*Parameter estimation*'.

The second configuration ('model configuration *ii*') included calcium – calmodulin activation of PFK (Figure 2B). Two forms of PFK were defined: an inactive ( $PFK_{inactive}$ ) and an active ( $PFK_{active}$ ) form (15,16). The inactive PFK was described by the model proposed by Connett (28). Upon binding of two calcium – calmodulin complexes the enzymes switches from the inactive to the active isoform (16). Activation of the enzyme was suggested to occur via reversing the inhibitory effect of ATP (16). To account for this regulatory effect the deinhibition term of the active PFK enzyme was modified to a constant ( $k_{deinhib\_Act}$ ), Eq. 6:

$$deinhibition_{activePFK} = k_{deinhib\_Act} \quad (Eq. 6)$$

The value of  $k_{deinhib\_Act}$  was estimated from the PCr and pH time course data as described in the section '*Parameter estimation*'. Effectively, the value of the deinhibition term of the active PFK enzyme was larger compared to the inactive PFK enzyme. Consequently switching from inactive to active form stimulates overall PFK flux. The fractions of PFK in active and inactive form were described by differential equations Eq. 7 and 8. Switching of the enzyme from inactive to active form was stimulated by elevated cellular calcium – calmodulin concentrations, which is in accordance with observations by (14-17). The values of  $k_{on}$  and  $k_{off}$  were estimated from the PCr and pH time course data as described in the section '*Parameter estimation*'.

$$\frac{dPFK_{active}}{dt} = k_{on}Ca_2CaM^2 \cdot (1 - PFK_{active}) - k_{off}PFK_{active} \quad (Eq. 7)$$

$$PFK_{inactive} = 1 - PFK_{active} \quad (Eq. 8)$$

The deinhibition term of configuration *ii* (Eq. 6) was independent from cellular ADP and AMP levels. There are however indications that the flux through the activated PFK enzyme is dependent on both cellular calcium and ADP, AMP levels (9). This particular regulatory scheme was represented by model configuration *iii*. To this end, the deinhibition term of the activated enzyme was modeled as a function of ADP and AMP concentrations, albeit with different competitive binding constants ( $k_{AMP}^{act}$  and  $k_{ADP}^{act}$ ), Eq. 9.

$$deinhibition_{activePFK} = 1 + \frac{AMP}{k_{AMP}^{act}} + \frac{ADP}{k_{ADP}^{act}} \quad (Eq. 9)$$

The values of  $k_{AMP}^{act}$  and  $k_{ADP}^{act}$  are estimated from the PCr and pH time course data as described in the section 'Parameter estimation'. Compared to the inactive enzyme the values of the competitive binding constants  $k_{AMP}^{act}$  and  $k_{ADP}^{act}$  were lower. Consequently, the flux through the active PFK enzyme is already increased at low AMP and ADP concentrations (compared to the inactive enzyme). The calcium – calmodulin fraction of PFK in active and inactive form was modeled identical to model configuration *ii*: i.e., according to differential equations Eq. 7 and 8.

For the full set of equations governing the PFK model the reader is referred to the Appendix.

### **Calcium - calmodulin dynamics in muscle**

The differential equations of PFK (de)activation are modeled as a function of  $Ca_2CaM$  (Eq. 7 and 8). As a consequence, the PFK (de)activation kinetics are determined by the particular reaction kinetics of calcium-calmodulin binding and unbinding, respectively. The latter were derived from a previously developed temperature dependent spatio-temporal model of skeletal muscle calcium handling (32,33). The calcium handling model was extended by calcium - calmodulin reaction kinetics based on mass action kinetics. The values for the  $k_{off}$  and  $k_d$  were set to  $100s^{-1}$  and  $3.8 \mu M$ , and  $5000s^{-1}$  and  $28.9 \mu M$  for the formation of  $Ca_2CaM$  and  $Ca_4CaM$  respectively (34-37). The spatially averaged calcium – calmodulin signal ( $Ca_2CaM$ ) was calculated for  $35^\circ C$  and used as an input of the glycolysis model.

### **Parameter estimation**

The model contained several parameters for which an accurate value was either not available from any literature, or were previously estimated in a computational study and likewise had no solid experimental basis (Table 3). These parameters were (re-)estimated from the newly recorded PCr and pH time-course data using a non linear least squares optimization algorithm (*lsqnonlin*, Matlab 7.5.0 (the Mathworks Inc., Natick, MA, USA)). The algorithm adjusted parameter values during a series of model evaluations with the aim of minimizing the error (SSE) between model predictions and PCr and pH time-course data defined by Eq. 10. Because PCr and pH data are expressed in



different units, a weighting parameter is required to balance the contribution of PCr and pH time-course data to the SSE. Instead of applying arbitrary defined weighting parameters, the accuracy of the measurement data (quantified by the SD of each data point) was used as weighting value. The entire dataset was divided into two groups: i.e., (i) data for parameterization and (ii) data for verification.. The parameterization data (at 0, 5, 10, 40 (1 pulse train per 5 s, 10 pulses per pulse train) and 80Hz) was used to estimate model parameter values. These parameters, initial conditions and the optimal values are given in Table 3. As indicated in the table, the initial parameter values were calculated from the MRS data or taken from other studies. An initial guess for the values of the PFK, calcium – calmodulin binding constant, i.e.,  $k_{on}$  and  $k_{off}$  was however not available. Therefore, the initial values for these parameters were randomly taken from uniform distributions with ranges as indicated in Table 3 using a multi-start optimization approach (500 runs).

Model predictions were next tested against independent data (i.e, data not used in the parameter estimation procedure: 5 pulses per 5 s (1Hz) and 1 pulse train per 5 s, 20 pulses per pulse train (40Hz)). For these simulations all parameters were left unchanged, except for the ATP hydrolysis rate constant  $k_{ATP\_Hydr}$ . The resulting estimated values of these rate constants are provided in Table 3.

### **Quantification of model fit**

The goodness of fit of the different model configurations to the experimental data was quantified by the sum of squared errors (SSE). The SSE was summed over all data used for parameter estimation. Data points were weighted by the SD of the experimental data (n=4-5), Eq. 10.

$$SSE = \sum_{j=1}^M \left( \sum_{i=1}^N \left( \frac{\text{mean}(PCr_{observed}(i)) - PCr_{predicted}(i)}{SD(PCr_{observed}(i))} \right)^2 + \sum_{i=1}^N \left( \frac{\text{mean}(pH_{observed}(i)) - pH_{predicted}(i)}{SD(pH_{observed}(i))} \right)^2 \right) \quad (Eq. 10)$$

Where,  $PCr_{observed}(i)$  represents the mean [PCr] (across-animal) at time point  $i$ ;  $PCr_{predicted}(i)$  represents the predicted [PCr] at time point  $i$ ;  $pH_{observed}(i)$  represents the mean pH (across-animal) at time point  $i$ ;  $pH_{predicted}(i)$  represents the predicted pH at time point  $i$ ;  $SD(PCr_{observed}(i))$  represents the across-animal SD of the [PCr] at time point  $i$ ;  $SD(pH_{observed}(i))$  represents the across-animal SD of the pH at time point  $i$ ;  $j$  denotes a specific experimental groups (e.g. 0Hz, 5Hz, 10Hz, 40Hz, 80Hz).

### **Akaike information criterion**

The Akaike information criterion (AIC) (38) was calculated for each model configuration to investigate if any improvement in SSE was merely the results of additional degrees of freedom of the model. AIC was calculated according to Eq. 11:

$$AIC = n \cdot \ln(SSE/n) + 2 \cdot K \quad (Eq. 11)$$

Where,  $n$  denotes the number of datapoints (422) and  $K$  represents the number of estimated parameters (9, 12 and 13, for configuration  $i$ ,  $ii$  and  $iii$ , respectively).

The AIC provides a means to select the preferred model (lowest AIC) taking into account the reduction of SSE while penalizing the additional degrees of freedom ( $K$ ).

**Table 3.** Optimized parameter values.

Parameter	Unit	Description	Initial condition	Optimized parameter value		
				model conf <i>i</i>	model conf <i>ii</i>	model conf <i>iii</i>
$k_{ATP\_Hydr} (0Hz)$	s <sup>-1</sup>	ATPase rate constant 0Hz	0.001 <sup>a</sup>	0.0020	0.00204	0.0017
$k_{ATP\_Hydr} (5Hz)$	s <sup>-1</sup>	ATPase rate constant 5Hz	0.01 <sup>a</sup>	0.084	0.091	0.068
$k_{ATP\_Hydr} (10Hz)$	s <sup>-1</sup>	ATPase rate constant 10Hz	0.01 <sup>a</sup>	0.072	0.077	0.056
$k_{ATP\_Hydr} (40Hz)$	s <sup>-1</sup>	ATPase rate constant 40Hz	0.01 <sup>a</sup>	0.061	0.065	0.049
$k_{ATP\_Hydr} (80Hz)$	s <sup>-1</sup>	ATPase rate constant 80Hz	0.01 <sup>a</sup>	0.048	0.050	0.041
<b>BuffCapFixed</b>	M	Fixed buffer cellular proton buffer capacity	0.0142 <sup>b</sup>	0.068	0.073	0.050
$v_{max}PFK$	mM s <sup>-1</sup>	$V_{max}$ PFK	0.93 <sup>b</sup>	8.76	10.43	10.25
$k_{AMP}$	mM	PFK deinhibition constant AMP	0.002 <sup>c</sup>	0.0017	0.014	0.046
$k_{ADP}$	mM	PFK deinhibition constant ADP	0.030 <sup>c</sup>	0.31	0.16	0.24
$k_{deinhibAct}$	unitless	PFK deinhibition constant activated PFK	1 <sup>c</sup>	-	8.72*10 <sup>6</sup>	-
$k_{AMPact}$	mM	PFK deinhibition constant AMP activated PFK	0.002 <sup>c</sup>	-	-	8.97*10 <sup>-5</sup>
$k_{ADPact}$	mM	PFK deinhibition constant ADP activated PFK	0.030 <sup>c</sup>	-	-	0.020
$k_{on}$	μM <sup>-2</sup> s <sup>-1</sup>	PFK, calcium – calmodulin binding constant	1*10 <sup>4</sup> – 1*10 <sup>9</sup>	-	8.70*10 <sup>5</sup>	5.00*10 <sup>5</sup>
$k_{off}$	s <sup>-1</sup>	PFK, calcium – calmodulin binding constant	1*10 <sup>1</sup> – 1*10 <sup>4</sup>	-	4.75*10 <sup>3</sup>	106
$k_{ATP\_Hydr} (1Hz)$	s <sup>-1</sup>	ATPase rate constant 5Hz	0.005 <sup>a,d</sup>	0.036	0.038	0.032
$k_{ATP\_Hydr} (40Hz, 20 pulses)$	s <sup>-1</sup>	ATPase rate constant 40Hz 20 pulses	0.02 <sup>a,d</sup>	0.050	0.042	0.072

<sup>a</sup> estimated from initial PCr breakdown rate<sup>b</sup> values used as initial condition in (52)<sup>c</sup> values obtained from (10)<sup>d</sup> estimated for validation experiments (Figure 5)

## RESULTS

### **<sup>31</sup>P magnetic resonance spectroscopy: characterization of pathway dynamics**

The dynamics of cellular metabolites: adenosine-triphosphate (ATP), phosphocreatine (PCr), inorganic phosphate (Pi) and phospho-monoesters (PME) as well as intracellular pH were monitored by <sup>31</sup>P magnetic resonance spectroscopy in ischemic rat TA muscle, under varying muscle stimulation frequencies (0 – 80 Hz). Figure 3A shows a stack plot of the spectra recorded during the 10Hz stimulation protocol. These spectra were obtained by averaging 12 FID's and processed with 5Hz line broadening. In response to muscle contraction and corresponding elevated cellular ATP demand flux, the cellular ATP buffer, PCr, is consumed to balance energy demand and supply. PCr depletion coincides with the production of Pi, a product of ATP hydrolysis. In addition, during stimulation an increasing PME resonance was observed which was in the absence of any ATP depletion, attributed to the accumulation of sugar-phosphates (glucose-1P,

glucose-6P and fructose-6P) (5,11). Figure 3B-C shows an example (10 Hz) of the PCr and pH dynamics used for model testing (data expressed as mean  $\pm$  SEM). The part of the data used for model testing is indicated in the figure. Any PCr and, or pH recovery was not observed during the period after stimulation. This observation validated the successful occlusion of blood circulation and obstruction of O<sub>2</sub> delivery to the muscle cells.

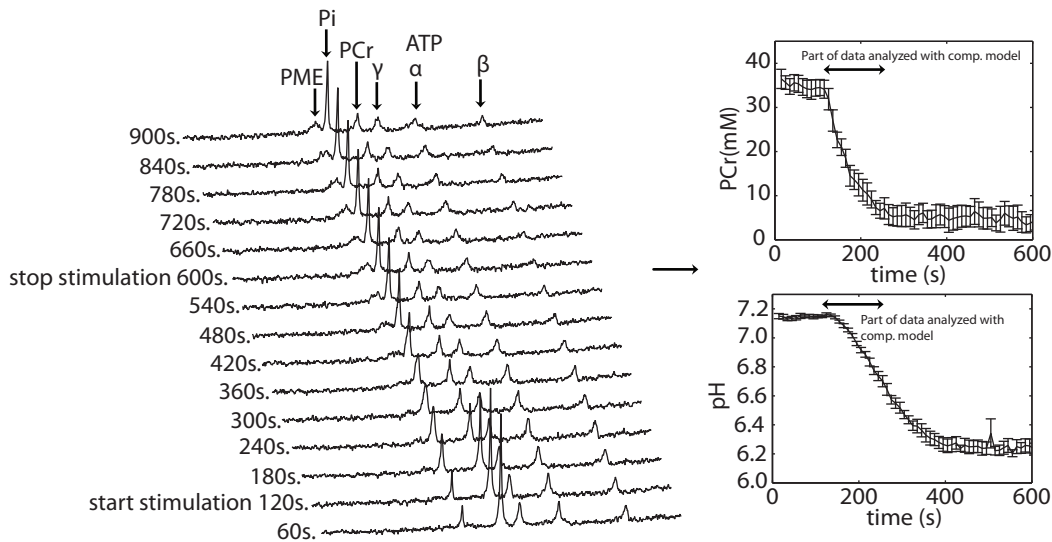


**Figure 3.** Characterization of *in vivo* pathway dynamics. Typical result of the experimental data obtained to characterize *in vivo* pathway behavior. A stack plot of spectra obtained at 10Hz stimulation is shown (A). These spectra were obtained by averaging 12 FID's and processed with 5Hz line broadening. Phospho-monoester (PME), inorganic phosphate (Pi), phosphocreatine (PCr) and adenosine-tri-phosphate (ATP) resonances are indicated. Pooled PCr (B) and pH (C) dynamics at 10Hz stimulation (n=5). Error bars indicate SEM. The part of the data analyzed by the computational model is indicated by a black arrow.

### Model simulations vs. experimental data

Model simulations according to the three different model configurations were compared to the experimental data, Figure 4. Panels A-E show the PCr dynamics for all model configurations; panels F-J show the pH dynamics for all model configurations. The goodness of fit was used to test the hypothesis represented by each model configuration. Model configuration *i* (red lines) represented conditions lacking any calcium activation of PFK, whereas configuration *ii* (green lines) and *iii* (blue lines) both include calcium activation of PFK, albeit according to a different kinetic mechanism. Both model configurations *i* and *ii* failed in reproducing the experimental data. In contrast, model configuration *iii* could successfully reproduce both the energetic state of the muscle (PCr) as well as the glycolytic flux (pH dynamics) simultaneously. Compared to the model configuration *i* and *ii* the sum of squared errors was reduced more than eightfold (386.7 and 354.6 vs. 44.8, respectively). The calculated AIC for model configuration *i* and *ii* and *iii* were: -8.1, -49.4 and -920.5 respectively. The large reduction in AIC for model configuration *iii* compared to *i* and *ii* indicates that the improvement in the model fit (reduction in SSE) was much larger than could be expected from the additional number of estimated parameter. Based on these results it was concluded that model configuration *i* and *ii* could not explain the *in vivo* sampled pathway dynamics. In contrast, these results provided evidence that calcium – calmodulin mediated activation of PFK in combination

with activation of the enzyme by increased concentrations of AMP and ADP (model configuration *iii*) can explain the recorded dynamics of glycolytic flux in skeletal muscle *in vivo*.

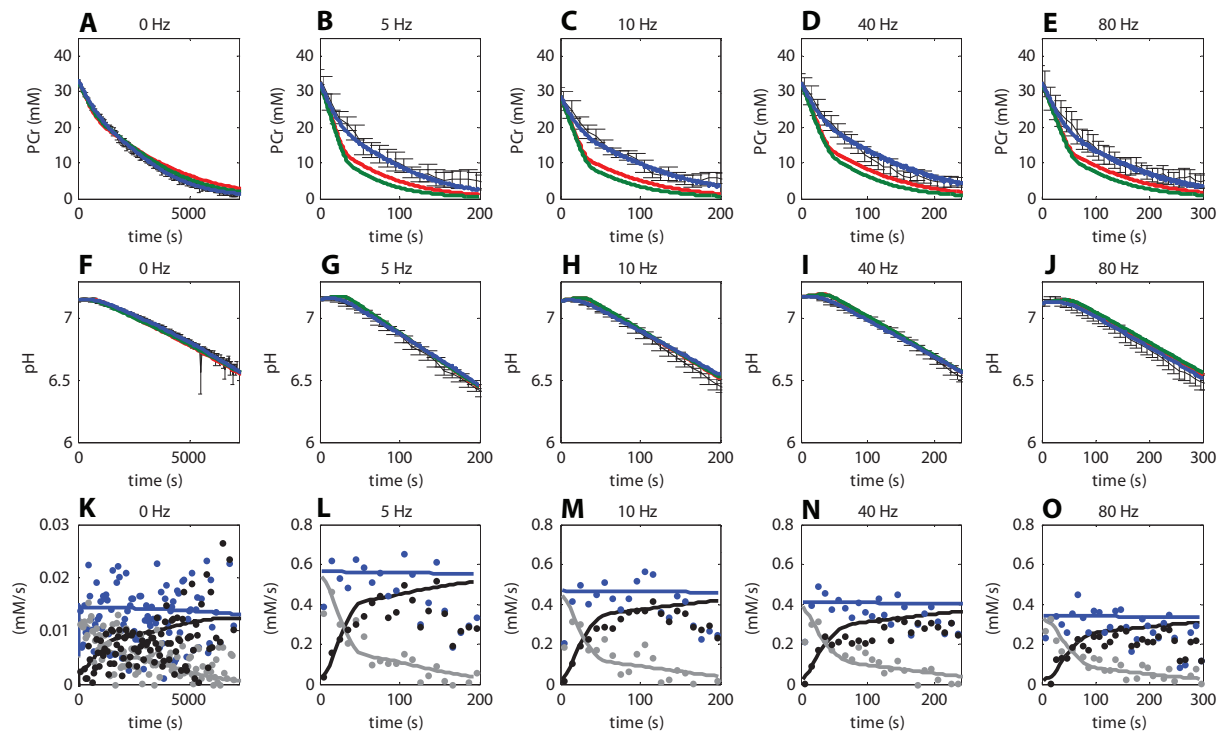


**Figure 4.** Quantitative hypotheses testing; experimental data vs. model simulations. Experimental data are indicated in black. Error bars indicate SEM ( $n=4-5$ ). Simulation results according to model configuration *i* (without calcium activation of PFK, red lines) and model configuration *ii* and *iii* (with calcium activation of PFK, green and blue, respectively) are shown. Optimized model parameter values listed in Table 3 were obtained by fitting model stimulations to these data. Panels **K-O** show predictions according to model configuration *iii* (solid lines) of ATP supply flux by PCr hydrolysis (grey lines) and, glycolysis (black lines) and ATP demand flux (blue lines), compared to values derived from the experimental data by using the phenomenological model (dots) described by Conley et al. (9).

Panels **K-O** of Figure 4 show the predicted ATP supply flux by PCr hydrolysis (grey lines) and, glycolysis (black lines) and ATP demand flux (blue lines), compared to values derived from the experimental data by using the phenomenological model described by Conley et al. (24). For clarity of presentation these predictions are only showed for the model configuration *iii*. These results demonstrate that the fluxes predicted by the mechanistic model and the phenomenological model are consistent with one another. In retrospect, the predictions of model configuration *iii* were also consistent with the calculations used to identify the part of the data at which the model assumption of constant ATP hydrolyses rates were not violated. The model predictions show that for conditions of  $\text{pH} > 6.5$  the sum of PCr breakdown rate (PCr dynamics) and glycolytic ATP production (pH dynamics) remain constant while being consistent with the experimental data.

#### **Model verification: model testing against independent data**

The veracity of the model was increased by using the algorithm on independent data sets. Experimental data of groups with a different number of excitation pulses per 5 seconds (compared to the data used for parameter estimation) was used: i.e., 1Hz continuous stimulation (5 pulses / 5 s)

and 40Hz (1 pulse train per 5 s, 20 pulses per pulse train). Experimental data versus model predictions are shown in Figure 5. These results show that the model can describe the behavior of the pathway for conditions of varying number of muscle excitation pulses. Model simulations are shown for the different configurations. The results show that only model configuration *iii* (blue lines) can reproduce the data. These results therefore act as validation of model configuration *iii* and they falsify model configuration *i* and *ii*. Panels E-F show the predicted ATP supply flux by PCR hydrolysis (grey lines) and, glycolysis (black lines) and ATP demand flux (blue lines), compared to values derived from the experimental data by using the phenomenological model described by Conley et al. (24). For clarity of presentation these predictions are only showed for the model configuration *iii*.

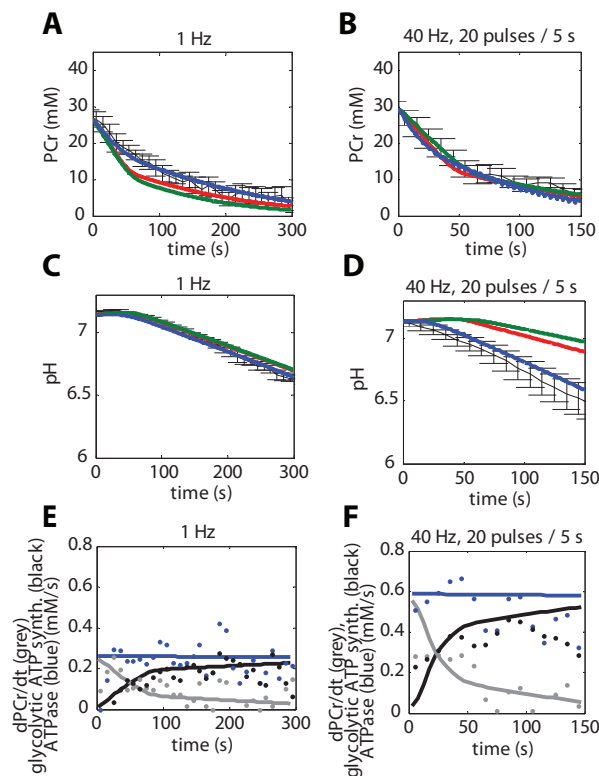


**Figure 5.** Model verification; comparison of model simulations and independent data for other stimulation frequencies than used for parameterization. Model simulations according to configuration *i*, *ii* and *iii* are indicated in red, green and blue, respectively. Experimental data are indicated in black and correspond to muscle stimulation protocols of 1 Hz continuous stimulation (**A** and **C**) and 40Hz (1 pulse train per 5 s, 20 pulses per pulse train) (**B** and **D**). Error bars indicate SEM (n=4-5). Panels **E-F** show predictions according to model configurations *iii* (solid lines) of ATP supply flux by PCR hydrolysis (grey lines) and, glycolysis (black lines) and ATP demand flux (blue lines), compared to values derived from the experimental data by using the phenomenological model (dots) described by Conley et al. (9).

### **Model predictions: deactivation of glycolysis post exercise**

It has been well documented that glycolysis is rapidly silenced after termination of muscle contraction (8-12). We tested if adding calcium regulation of PFK to the model could indeed explain this pathway characteristic. Figure 6 shows model predictions of a rest – exercise (60s, 5Hz continuous muscle stimulation) – recovery protocol. The ATP synthesis by the pathway post-exercise is reflected in the PCr dynamics. The inset of Figure 6A shows a small PCr resynthesis and thus glycolytic ATP production, post-exercise. The time constant of the PCr resynthesis is between

5 to 10 seconds and the ATP produced by the pathway during this period is  $\sim 1$  mM. These predictions are in excellent accordance with the time constant and magnitude of the PCr recovery due to glycolytic ATP production reported by Forbes et al. and Crowther et al. (10,39). This result showed that the model can reproduce transients observed in other independent datasets, providing additional model verification. Results of simulation were explored to determine the origin of this small glycolytic ATP production in the first few seconds of recovery. It was concluded that these dynamics were caused by accumulation of pathway intermediates downstream of PFK (Figure 6B). Recovery of these intermediates to baseline levels occurred in 5 - 10 s, thereby yielding  $\sim 1$  mM ATP. Figure 6C shows PFK flux, which closely tracked the rapid pulsatile  $\text{Ca}^{2+}$  release and re-uptake during exercise. As a result, PFK flux was quickly deactivated post-exercise. In addition, the sum of the fluxes through the ATP producing steps in the pathway (PGK + PK) is shown. These simulation results provided further evidence that, although PFK flux is quickly silenced (100 – 200 ms), ATP production by glycolysis lags behind by 5 – 10 s.

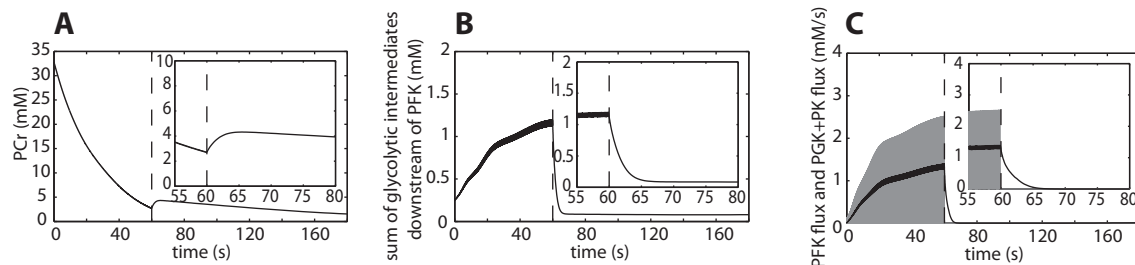


**Figure 6.** Model predictions of the silencing of glycolysis in non-contracting muscle. Simulations of exercise (5Hz continuous muscle excitation, 60s) – recovery protocol. The dotted line indicates the end of exercise (time = 60s). At the onset of recovery a small PCr resynthesis is observed (A). The PCr dynamics reflects the glycolytic ATP production at the beginning of recovery. Model simulations of the summed concentration of glycolytic intermediates downstream of PFK (F1,6P<sub>2</sub> + DHAP + G3P + GAP + 13BPG + 3PG + 2PG + PEP) are shown in (B). Panel (C) shows the PFK flux (grey) and the PGK + PK flux (black). PGK and PK are the ATP generating steps of the pathway. These predictions show that although PFK flux is quickly deactivated post-exercise, ATP production flux (PGK+PK flux) is deactivated at a slower timescale.

### Model predictions: PFK activation dynamics

The time constant of activation and deactivation of calcium - calmodulin binding to PFK have to this date remained unknown. This process was included in the model and values of kinetic  $k_{on}$  and  $k_{off}$  parameters were inferred from the *in vivo* experimental data. Simulations with the parameterized model were performed to investigate the (de)activation kinetics of PKF-1 for two stimulation frequencies, 10 and 40Hz Figure 7A-B. In addition, kinetics of calcium – calmodulin (red lines) and calcium (blue lines) are shown that were used as input of the model and drive the (de)activation of PFK are shown. For illustrative purposes the concentrations of these two molecules were scaled to the same order of magnitude as the fraction activated PFK. For calcium – calmodulin 1 unit corresponds to 0.040  $\mu\text{M}$  and for calcium 1 unit corresponds to 30  $\mu\text{M}$ .

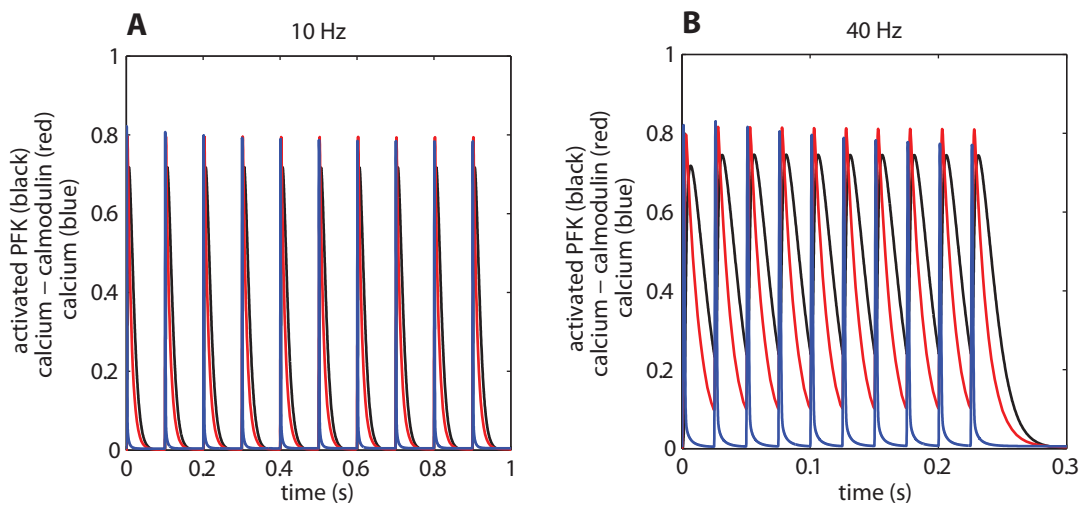


**Figure 7.** Calcium, calcium – calmodulin and PFK (de)activation kinetics. Predictions of (de)activation kinetics of PFK (black), calcium – calmodulin kinetics (red) and calcium kinetics (blue) for 10Hz (**A**) and 40Hz (**B**). For illustrative purposes the concentrations of calcium - calmodulin and calcium were scaled to the same order of magnitude as the fraction activated PFK. For calcium – calmodulin 1 unit corresponds to 0.040  $\mu\text{M}$  and for calcium 1 unit corresponds to 30  $\mu\text{M}$ .

## DISCUSSION

The principal result of this investigation was that incorporation of calcium - calmodulin mediated modulation of PFK activity combined with activation of the enzyme by increased levels of AMP and ADP into a kinetic model of glycolysis in skeletal muscle significantly improved prediction of in vivo glycolytic flux in ischemic skeletal muscle. This main result, its implications as well as several methodological considerations will be discussed.

### ***Methodological considerations: Computational Modeling***

The modeling framework developed by Vinnakota and coworkers (25) was selected as basis for this investigation. A unique property of this specific model of glycolysis in muscle is that it includes a detailed description of proton buffering by metabolites and pH dependency of the different reactions. Modeling these aspects of the pathway in detail was essential because pH dynamics were used as reporter of glycolytic flux. Moreover, during the experiments large changes in pH were observed (7.2 – 6.2) which strongly influences glycolytic flux (see e.g. (40,41)).

In this study the explanatory power of incorporation of calcium regulation of glycolytic flux at the level of PFK was investigated in detail. It is, however, well known that calcium stimulates glycogen phosphorylase (GP) flux via enzyme phosphorylation (17). This process was not explicitly modeled, but instead the dynamics of GP activity were implicitly taken into account by using the recorded dynamics of the sugar phosphates as input signal of the model. This methodology allowed simplifying the analyses while still taking the calcium changes of GP activity into account. For the modeling of the calcium – calmodulin dynamics a similar strategy was applied. These dynamics were sampled from a previously developed model of calcium handling in fast twitch

skeletal muscle. Fast twitch is also the dominant (>95%) fiber type of rat TA muscle (42). This calcium handling model was shown to have excellent performance in reproducing calcium – dye dynamical data for excitation frequencies ranging from 1 to 80Hz (33,43) and was therefore considered a good representation of this aspect of muscle physiology.

***Methodological considerations: in vivo <sup>31</sup>P MRS measurements in ischemic rat muscle.***

Electrical stimulation along the distal nerve trajectory of the n. peroneus communis induced contractions in the TA, EDL, peroneus longus and brevis, which was previously validated by functional MRI recordings (18,19). Analysis of the sensitivity profile of the <sup>31</sup>P coil by chemical shift imaging (CSI) indicated that 25% of the recorded signal originated from non-activated muscle. This problem is not unique for this specific study. For example, it is well known that MRS recordings during voluntary exercise in humans often represent the lumped dynamics of both activated and non-activated motor units (44-46). Nevertheless, to improve the quality of the analysis this partial volume problem was taken into account and corrected for by a data post-processing step described in the 'Methods' section. The percentage of signal originating from the non-contracting muscle is an influential parameter in these calculations. It was therefore verified that the outcome of the study was not sensitive to the specific value of this parameter. Specifically, all simulations (parameter optimizations and model predictions) were performed assuming the signal originating from non-contracting muscle to be 20 or 30 percent. The results of these simulations (data not shown) indicated that reported conclusions were indeed not sensitive to the specific value of this parameter.

***Calcium modulation of PFK activity***

In chapter 2, model predictions lacking any regulation by calcium previously illustrated additional regulation must be present *in vivo*. Numerical analysis indicated PFK as most likely site for the additional control (chapter 2). In addition, based on evidence provided by experimental studies (15,16,47) it was hypothesized that calcium – calmodulin activation of PFK has a dominant role in controlling the response of pathway dynamics for varying muscle stimulation frequencies. This specific mechanism was therefore tested in the computational analysis. The effects of calcium – calmodulin on PFK activity were reported to occur in a biphasic manner (15): at physiological Ca<sup>2+</sup> concentrations PFK is activated, however if the Ca<sup>2+</sup> concentration in the cells rises to pathological levels PFK is deactivated again. In the model only the activation of PFK was included. The rationale for this choice was that the analysis was restricted to the part of the data in which ATPase rate remained constant (pH>6.5). For these conditions it was not expected Ca<sup>2+</sup> concentrations rise to pathological conditions.

The kinetic model of calcium-calmodulin mediated PFK (de)activation was constructed using available information in the literature. Activation of PFK is thought to occur via binding of two calcium-calmodulin complexes to a PFK-dimer (16). This binding reduces the inhibition of the enzyme by ATP (16). At physiological concentrations (~8mM) ATP inhibition results in a nearly full deactivation of the enzyme (>95%) (16). Therefore reversing this inhibition will result in a significant increase of the enzymes catalytic activity. By competitive binding to the inhibition site AMP and ADP are able to reverse the ATP inhibition of the inactive form of PFK (28). It remains unknown whether for the activated form of the enzyme deinhibition is likewise mediated by competitive binding of ADP and AMP, albeit with a lower binding constant, or alternatively, if it is



independent of ADP and AMP levels. Irrespectively, both scenarios were evaluated using the computational model (model configuration *ii* and *iii*, respectively). A detailed analysis showed that only a model containing deinhibition mediated by competitive binding of ADP and AMP could reproduce the experimental data. A possible concern could be that comparison of the three models was biased because each model had a different number of degrees of freedom; in general, models with a greater number of free parameters tend to fit data better. This concern was quantitatively addressed using the Akaike-test. A large reduction in the value of AIC indicated that improvement of the fit of model *iii* was larger than could be expected from the few additional degrees of freedom, suggesting a biological component responsible. Although kinetic data for validation of this prediction are unavailable, it is consistent with results reported by Crowther et al. where that both elevated calcium levels and increased ADP and AMP levels were required to increase flux downstream of glycogen phosphorylase (9). Further confidence in the validity of the computational model was provided by verification against data not used for parameter estimation (see Figure 5). Finally, a corollary of the particular kinetic model for calcium control of PFK that was developed and used here, is that the kinetics of PFK activation and deactivation were almost exclusively (but see Eq. (9)) determined by the reaction kinetics of calcium-calmodulin interaction. Empirical studies have shown that the latter are extremely rapid ( $k_d$  100 s<sup>-1</sup> or faster; see *Methods*). As a result, PFK (de)activation in the model was equally rapid. No data was available in the literature to verify that this model corollary is accurate, and remains to be tested.

#### ***Silencing of glycolysis in non-contracting muscle***

It has been well documented that glycolysis is quickly silenced after termination of muscle contraction (9-12,24). In the present investigation these observations were reproduced by the absence of PCr resynthesis in the period after stimulation. Two independent studies reported a deactivation of the pathway in the order of 10 – 20 seconds (10,39). This timescale is slow compared to the rapid deactivation of PFK (100 – 200 ms), see Figure 6. However, simulations revealed that after intense muscle contractions the deactivation of the pathway is delayed as a result of accumulation of intermediates downstream of PFK. In addition, simulations indicated that glycolytic ATP production during the first seconds of recovery is dependent on the intensity of the preceding exercise (data not shown) and may explain the experimental observations that a complete absence of glycolytic flux at the onset of recovery occurs (8,12). These findings may have important implications for the analyses of PCr recovery kinetics. PCr recovery kinetics are believed to predominantly reflect oxidative ATP production rate and this rate of PCr recovery is frequently used as a measure of *in vivo* oxidative capacity and/or mitochondrial function (48). Two experimental studies already suggested that the first 10 seconds of recovery may be contaminated by glycolytic ATP production. The current simulation study provided additional support for this contention. These results therefore imply that in order to obtain PCr kinetics that truly reflect the oxidative ATP synthesis it is advisable to exclude the first 10 seconds of recovery from the data analyses.

#### ***Parallel activation of ATP consumption and glycolytic ATP production***

The results of this study indicate that to meet energetic demands parallel activation of glycolytic ATP supply flux and muscle contraction by the same signaling event, i.e., calcium release in the myoplasm, is necessary. The effect of varying calcium stimulation frequency on parallel activation

of these pathways has only been addressed in relatively few studies. Conley et al. used  $^{31}\text{P}$  MRS to determine the effect of varying muscle excitation at low frequencies (0.5 – 3 Hz) (24) and concluded that at these low stimulation frequencies glycolytic flux scales linearly with contraction frequency. A similar conclusion was inferred from the model simulations. PFK (de)activation kinetics remained pulsatile for muscle excitation frequencies < 10 Hz. For this range of stimulation frequencies PFK activation was linearly related to muscle excitation. These simulations yield results with much broader implications for glycolytic flux than previously suggested in part because reproducing these characteristics also reported by Crowther et al. also permits model predictions for much higher frequencies. Remarkably, at these frequencies, the fusing of individual PFK activation pulses was qualitatively similar to force dynamics of fast twitch muscle. These predictions also suggest that for these stimulation frequencies (>10 Hz) activation of PFK remains closely linked to muscle ATP demand flux. We speculate that the regulation of glycolysis in skeletal muscle is optimized to facilitate this parallel activation throughout the wide dynamical range of muscle excitation frequencies.

### ***Future outlook***

Recently Vinnakota and coworkers used the previous version of this computational model of glycolysis in skeletal muscle to analyze metabolite and pH dynamics in resting mouse EDL and soleus muscle (25). Although their model simulations reproduced these dynamics fairly well, the simulations failed to describe recorded dynamics during muscle excitation. A possible explanation for this model limitation was the lack of feed forward regulation downstream of glycogen phosphorylase, activated during mechanical work. This study has found that adding regulation by calcium mediated activation of PFK improves the consistency of model predictions and experimental data over a wide operational range of muscle excitation frequencies (0 – 80 Hz). We therefore concluded that the proposed model does provide an improved basis for modeling energy metabolism in skeletal muscle. In this context, relevant questions or model limitations open for future study will be discussed below.

The predictions of the current model were tested for conditions of ischemia. It will be interesting to investigate if these predictions are also accurate for conditions of normoxia. This requires adding a description of ATP production by oxidative phosphorylation to the computational model and sampling the behavior of both mitochondrial and glycolytic pathway experimentally under normoxic conditions. In the present investigation the experimental read-out of the PME resonance allowed to bypass the need for a flux equation of glycogen phosphorylase (GP). For future studies it may become relevant to add this flux description. Hereto, an improved model of GP including allosteric regulation by G6P and the effects of enzyme phosphorylation on kinetic parameters is probably required. The present analysis was based on the experimental data in which muscle fatigue had no detectable effect on cellular ATP hydrolyses rate. Acquiring an experimental read-out and modeling the effects of muscle fatigue on ATP hydrolysis rate will be a key step towards computational analyses of the remaining of the data.

With respect to extending the research on this topic, it may also be very interesting to investigate the role of calcium – calmodulin signaling on the flux control of glycolysis in tissues other than muscle. Based upon the current results it is predicted that calcium – calmodulin signaling has a very dominant flux control in skeletal muscle, but there is also evidence indicating this signaling mechanism activates glycolytic flux in nervous tissue (49,50), but also various types of

cancerous tissues (51-54). In this view, it will be of particular interest to study if calcium-calmodulin related alterations in glycolytic flux observed for these cell types will also arise from model predictions.

***In summary***

An integrative experimental and computational modeling approach was applied to test the hypothesis that calcium – calmodulin mediated activation of PFK in skeletal muscle is an important signal in flux control underlying *in vivo* pathway behavior. Model simulations revealed that incorporation of these mechanisms into a detailed model of skeletal muscle glycolysis was required for model predictions to be consistent with experimental data, thereby providing quantitative support for the hypothesis. Model predictions indicated that the (de)activation kinetics of PFK in response to different stimulation frequencies is very similar to force dynamics in fast twitch muscle. However, in spite of these very fast PFK deactivation kinetics overall shut down of glycolytic ATP production in non-contracting muscle post-exercise may be delayed by 5 – 10 seconds as a result of accumulation of glycolytic intermediates downstream of PFK.

## APPENDIX

### Model configuration i:

The PFK rate equation of model configuration *i* (obtained from Connett (10), Eq. 12).

$$\frac{V}{V_{\max}} = \frac{kNUM}{E + E_A + E_{AB} + E_{BA}}$$

$$NUM = Q_1 \cdot \left(1 + \frac{\bar{Q}}{c_1 c_2} + Q_6\right) + Q_2 \cdot \left(1 + \frac{\bar{Q}}{c_1 c_2} + Q_5\right) \cdot \left(1 + \frac{\bar{Q}}{c_1 c_2}\right)$$

$$E = \left(1 + \frac{\bar{Q}}{c_1 c_2} + Q_5\right) \cdot \left(1 + \frac{\bar{Q}}{c_1 c_2} + Q_6\right) \cdot (1 + Q_7)$$

$$E_A = Q_1 \cdot \left(1 + \frac{\bar{Q}}{c_1 c_2} + Q_6\right) \cdot Q_3 \cdot \left(1 + \frac{\bar{Q}}{c_1}\right)$$

$$E_B = Q_2 \cdot \left(1 + \frac{\bar{Q}}{c_1 c_2} + Q_5\right) \cdot Q_4 \cdot \left(1 + \frac{\bar{Q}}{c_2}\right)$$

$$E_{BA} + E_{AB} = NUM \left(1 + \frac{Q}{c_1 c_2}\right)$$

$$Q_A = \frac{[F6P]}{K_{m1}^{F6P}}$$

$$Q_B = \frac{[MgATP]}{K_{m1}^{MgATP}}$$

$$Q_1 = Q_A \left(1 + \frac{Q_7}{c_1}\right)$$

$$Q_2 = Q_B \left(1 + \frac{Q_7}{c_2}\right) \quad (\text{Eq. 12})$$

$$Q_3 = \left(1 + \frac{\bar{Q}}{c_1}\right) \cdot \left(\frac{K_{m2}^{MgATP}}{[MgATP]}\right)$$

$$Q_4 = \left(1 + \frac{\bar{Q}}{c_2}\right) \cdot \left(\frac{K_{m2}^{F6P}}{[F6P]}\right)$$

$$Q_5 = \left(\frac{K_i^{F6P}}{[F6P]}\right) \cdot (1 + \bar{Q}) \cdot Q_3 \cdot Q_A$$

$$Q_6 = \left(\frac{Q_i^{MgATP}}{[MgATP]}\right) \cdot (1 + \bar{Q}) \cdot Q_4 \cdot Q_B$$

$$Q_7 = \frac{[H^+]}{K_a} \left(1 + \left(\frac{[ATPH]}{Q_i^{ATPH}}\right)^4\right)$$

$$\bar{Q} = Q_7 \frac{\left(1 + \frac{Q_A}{c_1}\right)^3 \cdot \left(1 + \frac{Q_B}{c_2}\right)^3}{(1 + Q_A)^3 \cdot (1 + Q_B)^3}$$

$$Q_i^{MgATP} = K_i^{MgATP} \cdot \text{deinhibition}$$

$$Q_i^{ATPH} = K_i^{ATPH} \cdot \text{deinhibition}$$

$$\text{deinhibition} = 1 + \frac{ADP}{K_A^{ADP}} + \frac{AMP}{K_A^{AMP}}$$

Model parameter values are provided in Table 4.

**Table 4.** Parameter values PFK model

Parameter	Value
$K_{m1}^{F6P}$	68.49 $\mu\text{M}$ *
$K_{m2}^{F6P}$	58.70 $\mu\text{M}$ *
$K_{m1}^{MgATP}$	26.54 $\mu\text{M}$ *
$K_{m2}^{MgATP}$	37.81 $\mu\text{M}$ *
$K_i^{F6P}$	4.33 $\mu\text{M}$ *
$K_i^{MgATP}$	124.60 $\mu\text{M}$ *
$K_i^{ATPH}$	0.649 $\mu\text{M}$ *
$K_a$	0.0812 $\mu\text{M}$ *
$k$	0.990 *
$c_1$	19.09 *
$c_2$	2.63 *
$K_A^{ADP}$	Estimated (Table 3)
$K_A^{AMP}$	Estimated (Table 3)

\* value obtained from (10)

**Model configuration ii:**

Model configuration *ii* contained two PFK forms, an inactive modeled according to Eq. 11 and an active form for which the deinhibition term was described by Eq. 13.

$$deinhibition = K_{deinhib\_Act} \quad (Eq. 13)$$

Activation and deactivation of PFK by binding of calcium – calmodulin was modeled by differential equations Eq. 14 and 15:

$$\frac{dPFK_{active}}{dt} = k_{on} Ca_2 CaM^2 \cdot (1 - PFK_{active}) - k_{off} PFK_{active} \quad (Eq. 14)$$

$$PFK_{inactive} = 1 - PFK_{active} \quad (Eq. 15)$$

Parameter values of model configuration *ii* are listed in Table 3 and 4.

**Model configuration iii:**

Model configuration *iii* contained two PFK forms, an inactive modeled according to Eq. 11 and an active form for which the deinhibition term was described by Eq. 16.

$$deinhibition = 1 + \frac{AMP}{K_{AMP}^{act}} + \frac{ADP}{K_{ADP}^{act}} \quad (Eq. 16)$$

Activation and deactivation of PFK by binding of calcium – calmodulin was modeled by differential equations Eq. 14 and 15.

Parameter values of model configuration *iii* are listed in Table 3 and 4.

## REFERENCES

1. **Romano AH, Conway T.** Evolution of carbohydrate metabolic pathways. *Research in Microbiology* 147: 448-455, 1996
2. **Fothergill-Gilmore LA, Michels PA.** Evolution of glycolysis. *Prog Biophys Mol Biol* 59: 105-235, 1993
3. **Schuster S, Fell DA and Dandekar T.** A general definition of metabolic pathways useful for systematic organization and analysis of complex metabolic networks. *Nat Biotechnol* 18: 326-332, 2000
4. **Pelicano H, Martin DS, Xu RH and Huang P.** Glycolysis inhibition for anticancer treatment. *Oncogene* 25: 4633-4646, 2006
5. **Walter G, Vandeborne K, Elliott M and Leigh JS.** In vivo ATP synthesis rates in single human muscles during high intensity exercise. *J Physiol* 519 Pt 3: 901-910, 1999
6. **Bakker BM, van EK, Jeneson JA, van Riel NA, Bruggeman FJ and Teusink B.** Systems biology from micro-organisms to human metabolic diseases: the role of detailed kinetic models. *Biochem Soc Trans* 38: 1294-1301, 2010
7. **Chance B, Im J, Nioka S and Kushmerick M.** Skeletal muscle energetics with PNMR: personal views and historic perspectives. *NMR Biomed* 19: 904-926, 2006
8. **Blei ML, Conley KE and Kushmerick MJ.** Separate measures of ATP utilization and recovery in human skeletal muscle. *J Physiol* 465: 203-222, 1993
9. **Crowther GJ, Carey MF, Kemper WF and Conley KE.** Control of glycolysis in contracting skeletal muscle. I. Turning it on. *Am J Physiol Endocrinol Metab* 282: E67-E73, 2002
10. **Crowther GJ, Kemper WF, Carey MF and Conley KE.** Control of glycolysis in contracting skeletal muscle. II. Turning it off. *Am J Physiol Endocrinol Metab* 282: E74-E79, 2002
11. **Dawson MJ, Gadian DG and Wilkie DR.** Studies of the biochemistry of contracting and relaxing muscle by the use of <sup>31</sup>P n.m.r. in conjunction with other techniques. *Philos Trans R Soc Lond B Biol Sci* 289: 445-455, 1980
12. **Quistorff B, Johansen L and Sahlin K.** Absence of phosphocreatine resynthesis in human calf muscle during ischaemic recovery. *Biochem J* 291 ( Pt 3): 681-686, 1993
13. **Schmitz JP, van Riel NA, Nicolay K, Hilbers PA and Jeneson JA.** Silencing of glycolysis in muscle: experimental observation and numerical analysis. *Exp Physiol* 95: 380-397, 2010
14. **Lilling G, Beitner R.** Altered allosteric properties of cytoskeleton-bound phosphofructokinase in muscle from mice with X chromosome-linked muscular dystrophy (mdx). *Biochem Med Metab Biol* 45: 319-325, 1991
15. **Marinho-Carvalho MM, Zancan P and Sola-Penna M.** Modulation of 6-phosphofructo-1-kinase oligomeric equilibrium by calmodulin: formation of active dimers. *Mol Genet Metab* 87: 253-261, 2006
16. **Marinho-Carvalho MM, Costa-Mattos PV, Spitz GA, Zancan P and Sola-Penna M.** Calmodulin upregulates skeletal muscle 6-phosphofructo-1-kinase reversing the inhibitory effects of allosteric modulators. *Biochim Biophys Acta*, 2009
17. **Brostrom CO, Hunkeler FL and Krebs EG.** The regulation of skeletal muscle phosphorylase kinase by Ca<sup>2+</sup>. *J Biol Chem* 246: 1961-1967, 1971
18. **De Feyter HM, Lenaers E, Houten SM, Schrauwen P, Hesselink MK, Wanders RJ, Nicolay K and Prompers JJ.** Increased intramyocellular lipid content but normal skeletal muscle mitochondrial oxidative capacity throughout the pathogenesis of type 2 diabetes. *FASEB J* 22: 3947-3955, 2008
19. **De Feyter HM.** Lipids & Mitochondria in Diabetic Muscle. *PhD Thesis*. Eindhoven University of Technology; 2007.
20. **Vanhamme L, van den BA and Van HS.** Improved method for accurate and efficient quantification of MRS data with use of prior knowledge. *J Magn Reson* 129: 35-43, 1997
21. **Taylor DJ, Styles P, Matthews PM, Arnold DA, Gadian DG, Bore P and Radda GK.** Energetics of human muscle: exercise-induced ATP depletion. *Magn Reson Med* 3: 44-54, 1986
22. **Veech RL, Lawson JW, Cornell NW and Krebs HA.** Cytosolic phosphorylation potential. *J Biol Chem* 254: 6538-6547, 1979
23. **Tobin RB, Mackerer CR and Mehlman MA.** pH effects on oxidative phosphorylation of rat liver mitochondria. *Am J Physiol* 223: 83-88, 1972
24. **Conley KE, Blei ML, Richards TL, Kushmerick MJ and Jubrias SA.** Activation of glycolysis in human muscle in vivo. *Am J Physiol* 273: C306-C315, 1997
25. **Vinnakota KC, Rusk J, Palmer L, Shankland E and Kushmerick MJ.** Common phenotype of resting mouse extensor digitorum longus and soleus muscles: equal ATPase and glycolytic flux during transient anoxia. *J Physiol* 588: 1961-1983, 2010
26. **Eagle GR, Scopes RK.** Control of substrate cycling at fructose phosphates in a reconstituted muscle glycolytic system. *Arch Biochem Biophys* 208: 593-601, 1981
27. **Waser MR, Garfinkel L, Kohn MC and Garfinkel D.** Computer modeling of muscle phosphofructokinase kinetics. *J Theor Biol* 103: 295-312, 1983
28. **Connett RJ.** Glycolytic regulation during an aerobic rest-to-work transition in dog gracilis muscle. *J Appl Physiol* 63: 2366-2374, 1987
29. **Moreno-Sanchez R, Marin-Hernandez A, Gallardo-Perez JC, Quezada H, Encalada R, Rodriguez-Enriquez S and Saavedra E.** Phosphofructokinase type 1 kinetics, isoform expression, and gene polymorphisms in cancer cells. *J Cell Biochem* 113: 1692-1703, 2012
30. **Krause U, Wegener G.** Control of glycolysis in vertebrate skeletal muscle during exercise. *Am J Physiol* 270: R821-R829, 1996
31. **Peters SJ, Spriet LL.** Skeletal muscle phosphofructokinase activity examined under physiological conditions in vitro. *J Appl Physiol* 78: 1853-1858, 1995
32. **Baylor SM, Hollingworth S.** Simulation of Ca<sup>2+</sup> movements within the sarcomere of fast-twitch mouse fibers stimulated by action potentials. *J Gen Physiol* 130: 283-302, 2007
33. **Groenendaal W, Jeneson JA, Verhoog PJ, van Riel NA, Ten Eikelder HM, Nicolay K and Hilbers PA.** Computational modelling identifies the impact of subtle anatomical variations between amphibian and mammalian skeletal muscle on spatiotemporal calcium dynamics. *IET Syst Biol* 2: 411-422, 2008

34. **Andersson T, Drakenberg T, Forsen S and Thulin E.** Characterization of the Ca<sup>2+</sup> binding sites of calmodulin from bovine testis using <sup>43</sup>Ca and <sup>113</sup>Cd NMR. *Eur J Biochem* 126: 501-505, 1982
35. **Gaertner TR, Putkey JA and Waxham MN.** RC3/Neurogranin and Ca<sup>2+</sup>/calmodulin-dependent protein kinase II produce opposing effects on the affinity of calmodulin for calcium. *J Biol Chem* 279: 39374-39382, 2004
36. **Johnson JD, Snyder C, Walsh M and Flynn M.** Effects of myosin light chain kinase and peptides on Ca<sup>2+</sup> exchange with the N- and C-terminal Ca<sup>2+</sup> binding sites of calmodulin. *J Biol Chem* 271: 761-767, 1996
37. **Saucerman JJ, Bers DM.** Calmodulin mediates differential sensitivity of CaMKII and calcineurin to local Ca<sup>2+</sup> in cardiac myocytes. *Biophys J* 95: 4597-4612, 2008
38. **Akaike H.** New Look at Statistical-Model Identification. *Ieee Transactions on Automatic Control* AC19: 716-723, 1974
39. **Forbes SC, Paganini AT, Slade JM, Towse TF and Meyer RA.** Phosphocreatine recovery kinetics following low- and high-intensity exercise in human triceps surae and rat posterior hindlimb muscles. *Am J Physiol Regul Integr Comp Physiol* 296: R161-R170, 2009
40. **Gevers W, Dowdle E.** The effect of pH on glycolysis in vitro. *Clin Sci* 25: 343-349, 1963
41. **Trivedi B, Danforth WH.** Effect of pH on the kinetics of frog muscle phosphofructokinase. *J Biol Chem* 241: 4110-4112, 1966
42. **Maltin CA, Delday MI, Baillie AG, Grubb DA and Garlick PJ.** Fiber-type composition of nine rat muscles. I. Changes during the first year of life. *Am J Physiol* 257: E823-E827, 1989
43. **Groenendaal W.** Spatiotemporal skeletal muscle dynamics; Experimental observations and numerical analyses. *PhD Thesis.* Eindhoven University of Technology; 2011.
44. **Crowther GJ, Gronka RK.** Fiber recruitment affects oxidative recovery measurements of human muscle in vivo. *Med Sci Sports Exerc* 34: 1733-1737, 2002
45. **Houtman CJ, Heerschap A, Zwarts MJ and Stegeman DF.** pH heterogeneity in tibial anterior muscle during isometric activity studied by (<sup>31</sup>P)-NMR spectroscopy. *J Appl Physiol* 91: 191-200, 2001
46. **Houtman CJ, Heerschap A, Zwarts MJ and Stegeman DF.** An additional phase in PCr use during sustained isometric exercise at 30% MVC in the tibialis anterior muscle. *NMR Biomed* 15: 270-277, 2002
47. **Beitner R.** Control of glycolytic enzymes through binding to cell structures and by glucose-1,6-bisphosphate under different conditions. The role of Ca<sup>2+</sup> and calmodulin. *Int J Biochem* 25: 297-305, 1993
48. **Prompers JJ, Jeneson JA, Drost MR, Oomens CC, Strijkers GJ and Nicolay K.** Dynamic MRS and MRI of skeletal muscle function and biomechanics. *NMR Biomed* 19: 927-953, 2006
49. **Koren-Schwartz N, Chen-Zion M, Ben-Porat H and Beitner R.** Serotonin-induced decrease in brain ATP, stimulation of brain anaerobic glycolysis and elevation of plasma hemoglobin; the protective action of calmodulin antagonists. *Gen Pharmacol* 25: 1257-1262, 1994
50. **Landowne D, Ritchie JM.** On the control of glycogenolysis in mammalian nervous tissue by calcium. *J Physiol* 212: 503-517, 1971
51. **Glass-Marmor L, Beitner R.** Detachment of glycolytic enzymes from cytoskeleton of melanoma cells induced by calmodulin antagonists. *Eur J Pharmacol* 328: 241-248, 1997
52. **Glass-Marmor L, Penso J and Beitner R.** Ca<sup>2+</sup>-induced changes in energy metabolism and viability of melanoma cells. *Br J Cancer* 81: 219-224, 1999
53. **Penso J, Beitner R.** Detachment of glycolytic enzymes from cytoskeleton of Lewis lung carcinoma and colon adenocarcinoma cells induced by clotrimazole and its correlation to cell viability and morphology. *Mol Genet Metab* 76: 181-188, 2002
54. **Ashkenazy-Shahar M, Beitner R.** Effects of Ca(2+)-ionophore A23187 and calmodulin antagonists on regulatory mechanisms of glycolysis and cell viability of NIH-3T3 fibroblasts. *Mol Genet Metab* 67: 334-342, 1999







# Chapter 4

## *Magnitude and control of mitochondrial sensitivity to ADP*

Adapted from

J.A.L. Jeneson, J.P.J. Schmitz, N.M.A. van den Broek, N.A.W. van Riel, P.A.J. Hilbers, K. Nicolay, J.J. Prompers  
*Magnitude and control of mitochondrial sensitivity to ADP*  
American Journal of Physiology Endocrinology and Metabolism, 2009, 297(3):E774-784

## ABSTRACT

The transduction function for ADP stimulation of mitochondrial ATP synthesis in skeletal muscle was reconstructed *in vivo* and *in silico* to investigate the magnitude and origin of mitochondrial sensitivity to cytoplasmic ADP concentration changes. Dynamic *in vivo* measurements of human leg muscle phosphocreatine (PCr) content during metabolic recovery from contractions were performed by  $^{31}\text{P}$ -NMR spectroscopy. The cytoplasmic ADP concentration ( $[\text{ADP}]_p$ ) and rate of oxidative ATP synthesis ( $J_p$ ) at each time point were calculated from creatine kinase equilibrium and the derivative of a mono-exponential fit to the PCr recovery data, respectively. Reconstructed  $[\text{ADP}]_p$ - $J_p$  relations for individual muscles containing more than 100 data points were kinetically characterized by nonlinear curve fitting yielding an apparent kinetic order and ADP affinity of  $1.9 \pm 0.2$  and  $0.022 \pm 0.003$  mM, respectively (means  $\pm$  SD;  $n = 6$ ). Next, *in silico*  $[\text{ADP}]_p$ - $J_p$  relations for skeletal muscle were generated using a computational model of muscle oxidative ATP metabolism whereby model parameters corresponding to mitochondrial enzymes were randomly changed by 50-150% to determine control of mitochondrial ADP sensitivity. The multiparametric sensitivity analysis showed that mitochondrial ADP ultrasensitivity is an emergent property of the integrated mitochondrial enzyme network controlled primarily by kinetic properties of the adenine nucleotide translocator.

## INTRODUCTION

The metabolic regulation underlying energy balance in mammalian cells has long been subject of investigation, in particular regulation of mitochondrial ATP synthesis (1). At first, a relatively straightforward picture emerged from studies in isolated mitochondria: a feedback control loop involving transduction of changes in the extramitochondrial concentrations of the ATP hydrolysis products ADP and  $P_i$  to the intramitochondrial ATP synthetic network during cellular work explained energy balance (2,3).  $^{31}\text{P}$  NMR spectroscopy (4) and computational modeling (5) later showed that mitochondrial sensing of concentration changes in ADP alone sufficed to explain energy balance in skeletal muscle. In cardiac muscle, however, near-constant phosphocreatine (PCr), and thereby ADP, concentrations were measured during work jumps (6). This observation led to the proposition of a second, if not alternative, mitochondrial metabolic control mechanism in excitable cells such as cardiac muscle – i.e., a feedforward control loop involving direct or indirect transduction of intracellular calcium concentration changes to the mitochondrial ATP synthetic network (1). More recently, yet another alternative respiratory control mechanism of particular relevance to energy balance in the heart has been identified (7). It involves a mix of feedforward and feedback kinetic effects of  $P_i$  on multiple reactions in the oxidative ADP phosphorylation pathway (8).

What has been relatively lacking for each of the postulated respiratory control signals, in particular calcium, is a thorough kinetic characterization of the corresponding mitochondrial transduction function  $f([X], J_p)$ , where  $[X]$  is the extra-mitochondrial concentration of signal molecule  $X$  and  $J_p$  equals the rate of mitochondrial ATP synthesis. The need for explicit knowledge of these transduction functions in respiratory control model validation has recently become all the more pressing due to a surge in availability of computational models of mitochondrial oxidative metabolism that require proper validation criteria (9-14). Of these wanting kinetic functions, the transduction function  $f([\text{ADP}], J_p)$  has been most thoroughly investigated (2,3,15-18). Characterized initially as ‘approximately hyperbolic’ with a ‘ $K_m$ ’ in the range of 20-30  $\mu\text{M}$  (2,3), it was later reported that this function is in fact sigmoidal with an apparent kinetic order of at least two (17). Two independent studies have since, albeit indirectly, confirmed the non-Michaelis-Menten (non-MM) nature of the ADP stimulation of mitochondrial ATP synthesis (19,20).

According to Koshland’s classification of biological sensory systems, a sigmoidal ADP transduction function with a Hill coefficient greater than 1 would indicate that mitochondria are ultrasensitive to variations in extramitochondrial ADP concentration changes (21). Normal sensitivity was defined as the sensitivity corresponding to a hyperbolic input-output function such as in MM kinetics (i.e., Hill coefficient equals 1) (21). Importantly, mitochondrial ultrasensitivity, but not normal sensitivity to ADP was shown to explain energy balance by feedback respiratory control for a range of mammalian cell types including skeletal and cardiac muscle (17). The hypothesis of mitochondrial ADP ultrasensitivity has, however, not been generally embraced. Quantitative formalisms based on MM kinetics of ADP stimulation of mitochondrial ATP synthesis have continued to be used in the field of muscle energetics to evaluate mitochondrial function on basis of  $^{31}\text{P}$  NMR spectroscopy measurements (22). A possible explanation may be the lack of any verified mechanistic basis for second order kinetic behavior of ADP stimulation of mitochondria. Non-MM kinetics of ATP-ADP exchange across the inner membrane catalyzed by the adenine nucleotide

translocator (ANT) has been proposed but not confirmed as origin of mitochondrial ADP ultrasensitivity (17).

Here, the magnitude and control of mitochondrial ADP sensitivity are further investigated. We collected multiple high time resolution  $^{31}\text{P}$  NMR spectroscopy data sets on PCr concentration dynamics in human muscle during recovery from exercise to reconstruct the *in vivo* mitochondrial ADP transduction function with a high number of data points for accurate kinetic characterization. The result confirmed second order kinetics of ADP stimulation of mitochondrial respiration. Next, we investigated the control of mitochondrial ADP sensitivity by conducting a network analysis of a computational model of mitochondrial oxidative ADP phosphorylation in muscle (14). Hereto, a multi-parametric sensitivity analysis (MPSA) was performed involving generation of multiple random sets of parameter values for all mitochondrial enzymes in the model followed by reconstruction and characterization of the mitochondrial ADP transduction function for each set. The results indicated that mitochondrial ADP ultrasensitivity is an emergent property of the integrated mitochondrial metabolic network determined primarily by the kinetic properties of the ANT.

## METHODS

### **Subjects**

Six healthy, normally active subjects (four male, two female; mean age  $\pm$  SD:  $31 \pm 12$  years) participated in the study. The nature and the risks of the experimental procedures were explained to the subjects and all gave their written informed consent to participate in the study, which was approved by the local Medical Ethical Committee of the Máxima Medical Center, Veldhoven, The Netherlands.

### **$^{31}\text{P}$ Magnetic resonance spectroscopy**

$^{31}\text{P}$  MRS was performed at 1.5 Tesla (Gyrosan S15/ACS, Philips Medical Systems, Best, The Netherlands) as described previously (41). Briefly, after localized shimming  $^{31}\text{P}$  signals were collected using a 6-cm diameter surface coil placed over the *M. vastus lateralis* (spectral width, 2000 Hz; number of data points, 1024). From the dimension of the coil and the size and geometry of a typical upper leg, it was estimated that the majority of the signal in the unlocalized  $^{31}\text{P}$  MRS measurements originated from the *M. vastus lateralis*, with minimal contaminations from the adjacent *M. rectus femoris* and underlying *M. vastus intermedius*. Spectra were acquired during a rest-exercise-recovery protocol with a repetition time of 3 s and 2 scans yielding a time resolution of 6 s. The first 20 spectra (2 min) were measured at rest, after which the subjects started the exercise. Exercise consisted of dynamic, single-leg extensions every 1.5 s in the supine position using a home-built MR compatible ergometer (23). The initial workload varied per subject and ranged between 7.5 and 12.5 W. This level was maintained for the first min and the workload was then increased by 5 W each min. Subjects performed exercises of different durations and 8-12 data sets were collected per subject during 4-8 different sessions, with at least 15 min rest between different protocols within one session. The position of the  $^{31}\text{P}$  surface coil was marked on the leg during the first session and the coil was placed at the same location in subsequent sessions.

**<sup>31</sup>P MRS data analysis**

Spectra were fitted in the time domain by using a nonlinear least squares algorithm (AMARES) (24) in the jMRUI software package (25) as described previously (23). PCr, P<sub>i</sub> and ATP signals were fitted to Lorentzian line shapes. Absolute concentrations of the phosphorylated metabolites were calculated after correction for partial saturation and assuming that [ATP] is 8.2 mM at rest (26). Intracellular pH was calculated from the chemical shift difference between the P<sub>i</sub> and PCr resonances (27). All data sets had an end-exercise pH ≥ 6.7. The free cytosolic ADP concentration ([ADP]) was calculated from pH and [PCr] using a creatine kinase equilibrium constant ( $K_{eq}$ ) of  $1.66 \times 10^9 \text{ M}^{-1}$  (28) and assuming that 15% of the total creatine is unphosphorylated at rest (29), using the equation (Eq. 1):

$$[ADP] = \frac{[ATP][Cr]}{[PCr][H^+]K_{eq}} \quad (\text{Eq. 1})$$

The molar free energy of cytosolic ATP hydrolysis was calculated according to (Eq. 2):

$$\Delta G_p = \Delta G_p^{\circ} + RT \ln([ADP][P_i] / [ATP]) \quad (\text{Eq. 2})$$

Where,  $\Delta G_p^{\circ}$  is -31.8 kJ/mol at 37°C (30).

The PCr recovery time course, PCr(*t*), was fitted to a mono-exponential function (Eq. 3):

$$PCr(t) = PCr_e - \Delta PCr_e \cdot e^{(-t/\tau_{PCr})} \quad (\text{Eq. 3})$$

Where PCr<sub>e</sub> is the PCr level after recovery,  $\Delta PCr_e$  is the difference between the PCr levels after recovery and at the end of exercise, and  $\tau_{PCr}$  is the time constant for PCr resynthesis.

The PCr resynthesis rate at time *t* ( $V_{PCr}(t)$ ) was calculated from the derivative of the fitted PCr recovery time course (Eq. 3). During recovery from exercise, PCr is resynthesized purely as a consequence of oxidative ATP synthesis (27,31,32). Because the creatine kinase reaction is much faster than oxidative ATP production(20),  $V_{PCr}(t)$  reflects mitochondrial oxidative phosphorylation flux. Covariations of  $V_{PCr}(t)$  with thermodynamic ( $\Delta G_p$ ) and kinetic ([ADP]) adenine nucleotide concentration functions were analyzed by nonlinear curve fitting of a Hill function of the form (Eq. 4):

$$V_{PCr}(t) = (Q_{max} - Q_{min}) \cdot \frac{(x(t) / x_{0.5})^{n_H}}{1 + (x(t) / x_{0.5})^{n_H}} + Q_{min} \quad (\text{Eq. 4})$$

Where,  $Q_{max}$  and  $Q_{min}$  the maximal and minimal net ADP phosphorylation fluxes<sup>1</sup>,  $x_{0.5}$  the  $\Delta G_p$  or [ADP] value at half-maximal  $V_{PCr}$ , and  $n_H$  the Hill coefficient (17).

This analysis was performed for each subject separately, using the pooled data from all the exercise protocols of that subject (8-12 data sets per subject). Only data points with  $V_{PCr}(t) > 0.02 \text{ mM/s}$  were included in the analysis. All nonlinear curve fitting was performed using MATLAB (version 7.3, Mathworks, Natick, Massachusetts, USA).

### **Statistical analysis**

All data are expressed as means  $\pm$  SD. Statistical analyses were performed using the SPSS 15.0 software package (SPSS Inc, Chicago, IL, USA). Because of the small number of subjects, the non-parametric Wilcoxon Signed Ranks test was used for paired comparisons of the data. The level of significance was set at  $P < 0.05$ .

### **Simulation and analysis of *in silico* mitochondrial ADP transduction functions in muscle**

The computational model of skeletal muscle oxidative ATP metabolism featuring a detailed biophysical model of mitochondrial oxidative ADP phosphorylation by Wu and co-workers (14) was used as platform for all *in silico* investigations of the origin of mitochondrial ADP ultrasensitivity. First, an analysis was performed of the sensitivity of the macroscopic parameters  $Q_{\max}$ ,  $K_{50}$  and  $n_H$  of *in silico* reconstructed [ADP]- $J_p$  relations for muscle towards 19 mitochondrial parameters in the Wu model (Table 1). This particular set consisted of 15 mitochondrial parameters of which the value had been previously estimated by model fitting (denoted by reference '5' in Table 2 of ref. (14)) and 4 mitochondrial parameters ( $k_{O_2}$ ,  $K_{m,ADP}$ ,  $\theta$  and  $\beta$ , respectively) of which the value had been taken from a computational model by Aliev and co-workers (denoted by reference '26' in Table 2 of ref. (14)). The design of this multi-parametric sensitivity analysis (MPSA) was based on methods described elsewhere (33) including statistical analysis (34). Next, the MPSA results were used to investigate if any set of model parameter values existed that would give rise *in silico* to mitochondrial ADP ultrasensitivity. Hereto, the model was fitted to an *in vivo* [ADP]- $J_p$  data set from an individual muscle whereby only model parameters with a significant Kolmogorov-Smirnov test score in the MPSA (see below) were varied.

### **MPSA**

Multiple random samples were taken from a 50-150% range of the default value for each of the 19 kinetic parameters of the mitochondrial enzymes in the model (Table 1) plus 5 dummy parameters yielding multiple random sets of parameter values for simulation and analysis of *in silico* [ADP]- $J_p$  relations for muscle. An optimized Monte Carlo sampling scheme was used to sample from the multidimensional distribution while guaranteeing that individual parameter ranges were evenly covered. In this case the parameters were sampled from a logarithmic uniform distribution within the defined range. The vectors containing the parameter samples were combined to obtain  $N$  parameter combinations. It was verified that the number of Monte Carlo runs  $N$  was sufficiently large to guarantee a good representation of all possible parameter value combinations (see below). The sampling and combination process was done with Latin Hypercube Sampling whereby each parameter range is divided into  $N$  equally probable intervals from which only one sample is drawn. These samples are permuted and stored in a vector (with  $N$  samples for each parameter). Subsequently, these permuted vectors of all  $p$  parameters are combined in an  $N$ -by- $p$  matrix. After the initial combination process, the minimum distance between the sample points is maximized. The Latin hypercube was generated using the function *lhsdesign* of the Statistics Toolbox of MATLAB. The number of Monte Carlo runs  $N$  was 5000.

The model was simulated for each set of parameter values and characterized with respect to the particular  $Q_{\max}$ ,  $K_{50}$  and  $n_H$  of the corresponding *in silico* [ADP]- $J_p$  relation by fitting of a 3 parameter Hill function (Eq. 4 with  $Q_{\min}$  set at 0; in this case,  $x_{0.5} = [ADP]_{0.5} = K_{50}$ ). This particular Hill function rather than Eq. 4 was used for computational ease on grounds that  $Q_{\min}$  was very small

compared to  $Q_{\max}$  and not significantly different from 0 (see *Results*; Table 2). To quantify the similarity of each of the simulations with respect to the reference simulation the sum of squared differences was calculated as criterion function. Each set of parameter values was then classified as either 'unacceptable' or 'acceptable' by comparing the value of the criterion function to a certain threshold. Specifically, the set of parameter values was scored 'unacceptable' if the criterion function value was greater than the threshold, and 'acceptable' in all other cases. The average value of the criterion function for the total ensemble of simulations was used as threshold value (34).

**Table 1.** Overview of the mitochondrial model parameters tested in the multi-parametric sensitivity analysis.

Parameter number	Model parameter	Description
1	$r$	Dehydrogenase parameter
2	$k_{Pi, 1}$	Dehydrogenase parameter
3	$k_{Pi, 2}$	Dehydrogenase parameter
4	$X_{DH}$	Dehydrogenase parameter
5	$X_{C1}$	Complex I activity
6	$X_{C3}$	Complex III activity
7	$k_{Pi, 3}$	Complex III parameter
8	$k_{Pi, 4}$	Complex III parameter
9	$X_{C4}$	Complex IV activity
10	$K_{O2}$	Complex IV parameter
11	$X_{F1}$	$F_0F_1$ -ATPase activity
12	$X_{ANT}$	ANT activity
13	$K_{m, ADP}$	Michaelis constant ANT
14	$\theta$	ANT parameter
15	$k_{PiHt}$	$H^+/Pi^-$ co-transporter parameter
16	$X_{PiHt}$	$H^+/Pi^-$ co-transport activity
17	$X_{KH}$	$K^+/H^+$ antiporter activity
18	$X_{Hle}$	$H^+$ leak activity
19	$\beta$	Mitochondrial matrix buffering capacity

The influence of each parameter on the model output was evaluated statistically using the Kolmogorov-Smirnov (K-S) test (34). Hereto, the distributions of the individual parameter values associated with the 'unacceptable' and the 'acceptable' cases were compared. For each parameter, the cumulative frequency was calculated for all 'unacceptable' and 'acceptable' cases. The sensitivity is evaluated by a measure of the separation of the two cumulative frequency distributions. The K-S test for the  $i^{\text{th}}$  parameter is represented as (Eq. 5):

$$K - S_i = \sup |S_{>}(\theta_i) - S_{<}(\theta_i)| \quad (\text{Eq. 5})$$

Where,  $S_{>}$  and  $S_{<}$  are the cumulative frequency functions corresponding to 'unacceptable' cases and 'acceptable' cases, respectively, and  $\theta_i$  is the parameter.

The value of K-S is determined as the maximum vertical distance between the cumulative frequency distribution curves for  $n$  'unacceptable' and  $m$  'acceptable' cases,  $n + m = N$ . A larger K-S score indicates that the model is sensitive to variation in that parameter. The highest K-S score of the dummy parameters was used as threshold for statistical significance – i.e., parameters with a K-



S score above the threshold were classified as sensitive. Finally, the K-S scores were summarized in a ranking of the sensitive parameters. This ranking was also used to verify that the number of Monte Carlo runs  $N$  was sufficiently large to guarantee a good representation of all possible parameter value combinations. For sufficiently large  $N$  the ranking of the sensitive parameters is independent of the exact number of samples (33).

### **Model fitting**

To test if any set of model parameter values existed that would give rise *in silico* to mitochondrial ADP ultrasensitivity, the model was fitted to an *in vivo* [ADP]- $J_p$  data set from an individual muscle (subject #2) whereby only model parameters with a significant K-S score were adjusted. Model fitting was performed using a nonlinear least-squares optimization method employing the *lsqnonlin* algorithm in the parameter estimation toolbox in MATLAB. Subsequently, *in silico* [ADP]- $J_p$  covariations were computed for the model with the fitted parameter values and kinetically characterized by curve fitting of Eq. 4.

## **RESULTS**

### ***In vivo* mitochondrial ADP transduction function in muscle**

Figure 1 shows typical examples of  $^{31}\text{P}$  MR spectra obtained from the *vastus lateralis* muscle of an individual subject (i) at rest (Fig. 1A), (ii) at the end of exercise (Fig. 1B) and (iii) at two time points during recovery (Figs 1C and 1D). Figure 2 shows the corresponding plot of the PCr concentration against recovery time together with the mono-exponential fit of the recovery data (solid line). The PCr resynthesis rate was calculated from the derivative of the fitted PCr recovery time course for each time point sampled during recovery. For this particular population of 6 subjects, the maximal PCr resynthesis rate was  $0.73 \pm 0.05$  mM/s. End-exercise (maximal) ADP concentration and (lowest) molar Gibbs free energy of cytosolic ATP hydrolysis were  $86 \pm 8$   $\mu\text{M}$  and  $-52.8 \pm 0.4$  kJ/mol, respectively.

**Table 2.** Results of the unconstrained curve fitting of Eq. 4 to the ( $\Delta G_p$ ,  $V_{\text{PCr}}$ ) data for the 6 subjects.

<b>subject</b>	<b><math>Q_{\text{max}}</math> (mM/s)</b>	<b><math>Q_{\text{min}}</math> (mM/s)</b>	<b><math>\Delta G_{p,0.5}</math> (kJ/mol)</b>	<b><math>n_H</math></b>
1	0.81	-0.04	-58.1	24.9
2	0.76	-0.02	-58.9	25.9
3	0.69	-0.09	-58.8	21.8
4	0.70	-0.04	-57.9	23.5
5	0.86	-0.03	-57.8	23.8
6	0.65	-0.03	-57.9	22.7
<b>mean</b>	0.74	-0.04	-58.2	23.8
<b>SD</b>	0.08	0.02	0.5	1.5

Where,  $Q_{\text{max}}$ , represents maximal net PCr resynthesis flux;  $Q_{\text{min}}$ , minimal net PCr resynthesis flux;  $\Delta G_{p,0.5}$ , molar free energy of cytosolic ATP hydrolysis at half-maximal  $V_{\text{PCr}}$ ;  $n_H$ , Hill coefficient.

To estimate the PCr resynthesis rate asymptotes  $Q_{\text{max}}$  and  $Q_{\text{min}}$  in the muscle cells, we analyzed the thermodynamic flow-force relation of PCr resynthesis (35,36). This relation was characterized by

unconstrained fitting of Eq. 4 to the ( $\Delta G_p$ ,  $V_{PCr}$ ) data (Figure 3). Almost the full range of sustainable energy balance states was covered by the experimental data points, resulting in accurate estimation of the flux asymptotes  $Q_{max}$  and  $Q_{min}$  (Table 2). The group mean value for  $\Delta G_p$  at half-maximal  $V_{PCr}$  was  $-58.2 \pm 0.5$  kJ/mol.

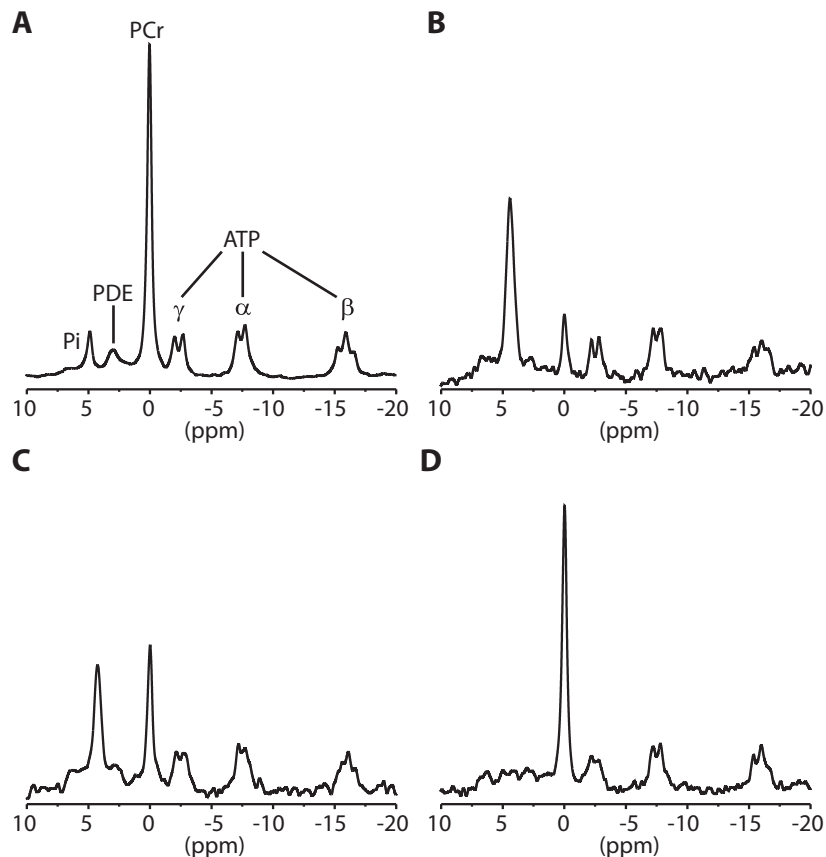


**Figure 1.** Typical *M. vastus lateralis*  $^{31}\text{P}$  MR spectra for one subject at rest (panel **A**, number of scans = 60), at the end of exercise (panel **B**, number of scans = 2) and at 15 and 117 s of recovery (panels **C** and **D**, respectively, number of scans = 2). Spectra were processed with 5 Hz line broadening.  $\text{P}_i$  indicates inorganic phosphate; PDE, phosphodiester; PCr, phosphocreatine; and  $\alpha$ ,  $\beta$  and  $\gamma$  indicate the three phosphate groups of ATP. For this subject the PCr depletion at the end of exercise (panel **B**) was 81% and the corresponding end-exercise pH was 6.72.

The values for  $Q_{max}$  and  $Q_{min}$  determined from the thermodynamic flow-force relation were next imposed as constraints on the fit of Eq. 4 to the ( $[\text{ADP}]$ ,  $V_{PCr}$ ) data (Figure 4, solid line) to determine the apparent affinity and kinetic order of mitochondrial ADP sensing. The results of the analysis for each of the subjects studied are summarized in Table 3. Group mean values for  $[\text{ADP}]_{0.5}$  and  $n_H$  were  $22 \pm 3$   $\mu\text{M}$  and  $1.9 \pm 0.2$ , respectively. Eq. 4 was also fitted to the ( $[\text{ADP}]$ ,  $V_{PCr}$ ) data without imposing any constraints on the flux asymptotes (Figure 4, dotted line; Table 4). The fitted values for  $Q_{max}$  and  $Q_{min}$  were similar to the values obtained from the thermodynamic flow-force relation (Table 2), except for one muscle (subject #3). Fitted estimates of  $[\text{ADP}]_{0.5}$  and  $n_H$  were not different from the values obtained from the constrained fit (Table 3).

Lastly, the PCr resynthesis rate,  $V_{PCr}(t)$ , was also correlated with the ADP concentration at each measurement point using a hyperbolic function ( $n_H=1$  in Eq. 4) corresponding to the classic MM ADP respiratory control model (37). The result for a single muscle is shown in Figure 4 (dashed line). The MM ADP control model was incompatible with the experimental data at high flux values

causing overestimation of the maximal net PCr resynthesis flux  $Q_{\max}$  ( $0.98 \pm 0.13$  mM/s versus  $0.74 \pm 0.08$  mM/s (Table 2);  $p < 0.05$ ). In addition, the MM ADP control model predicted a 7-fold higher net mitochondrial ATP hydrolysis rate at low ADP concentrations than the second order control model ( $Q_{\min} -0.27 \pm 0.04$  mM/s versus  $-0.04 \pm 0.02$  mM/s (Table 2);  $P < 0.05$ ).

**Table 3.** Results of the curve fitting of Eq. 4 to the  $([ADP], V_{PCr})$  data for the 6 subjects with  $Q_{\max}$  and  $Q_{\min}$  constrained to the values obtained from the thermodynamic flow-force relation (Table 2).

subject	$[ADP]_{0.5}$ ( $\mu\text{M}$ )	$n_H$
1	25	1.9
2	19	2.1
3	18	1.7
4	23	1.9
5	24	1.8
6	22	1.7
<b>mean</b>	22	1.9
<b>SD</b>	3	0.2

Where,  $[ADP]_{0.5}$  denotes the ADP concentration at half-maximal  $V_{PCr}$ ; and  $n_H$ , represents the Hill coefficient.

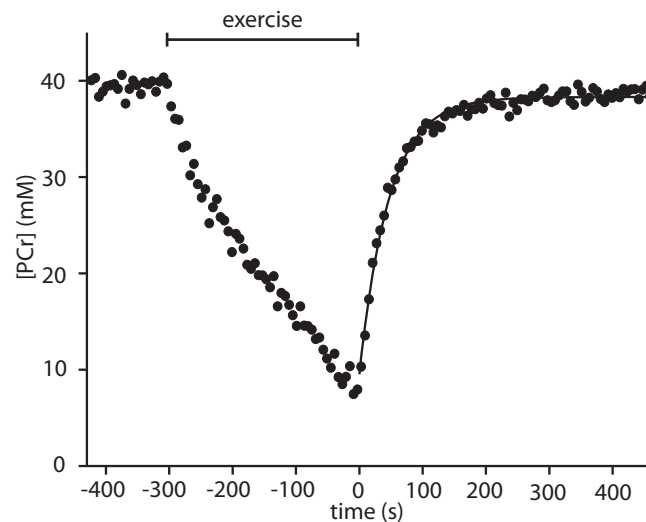


**Figure 2.** PCr concentration during rest, exercise and recovery obtained from the corresponding data set shown in Figure 1 (time resolution 6 s). The recovery of PCr (starting at  $t = 0$ ) was fitted to a mono-exponential function (solid line). The time constant for PCr recovery was 46.8 s.

### **Multi parameter sensitivity analysis**

The results of the MPSA are summarized in Figure 5. The K-S scores with respect to the  $Q_{\max}$ , ADP affinity ( $K_{50}$ ) and Hill coefficient ( $n_H$ ) of the mitochondrial ADP transduction function for each of the 19 mitochondrial kinetic parameters and 5 dummy parameters (parameters 20-24; Table 1) are shown in Figures 5A, B and C, respectively. The threshold score for significant sensitivity determined by the dummy parameters K-S scores (34) was 0.03-0.04 (Figure 5A-C). On this basis, all three macroscopic kinetic parameters of the mitochondrial ADP transduction function were found to exhibit significant sensitivity to the particular kinetic properties of three mitochondrial enzymes in the model – i.e., the lumped tricarboxylic acid dehydrogenase activity (TCA-DH; parameters 1-4), respiratory chain Complex III (CIII; parameters 6-8) and the adenine nucleotide transporter (ANT; parameters 12-14), respectively (Figure 5A-C). Within this subset, the ANT parameter sensitivity was

dominant (Figure 5A-C). Specifically, the  $Q_{\max}$  of the mitochondrial ADP transduction function exhibited significant sensitivity to model parameters 1-4, 7, 12 and 14 corresponding to TCA-DH parameters  $k_{\text{Pi},1}$ ,  $k_{\text{Pi},2}$ ,  $r$  and  $X_{\text{DH}}$ , Complex III parameter  $k_{\text{Pi},3}$  and ANT parameters  $X_{\text{ANT}}$  and  $\theta$ , respectively (Table 1) whereby the sensitivity to the ANT parameter  $X_{\text{ANT}}$  was dominant (K-S score 0.46 versus 0.05-0.07 for TCA-DH and Complex III parameters, respectively) (Figure 5A). Likewise, the apparent kinetic order of the ADP transduction function ( $n_{\text{H}}$ ) exhibited significant sensitivity only to all TCA-DH parameters (model parameters 1-4, Table 1) and all ANT parameters (model parameters 12-14, Table 1) whereby the sensitivity to ANT parameter  $\theta$  was dominant (K-S score 0.63 versus 0.09-0.13 for all other ANT and TCA-DH parameters, respectively) (Figure 5B). Finally, the overall mitochondrial ADP affinity  $K_{50}$  exhibited significant sensitivity to the TCA-DH parameters  $k_{\text{Pi},1}$ ,  $r$  and  $X_{\text{DH}}$  (model parameters 1, 3 and 4, respectively; Table 1), Complex III parameters  $X_{\text{C3}}$  and  $k_{\text{Pi},3}$  (model parameters 6 and 7, respectively) and ANT parameters  $K_{\text{m-ANT}}$  and  $\theta$  (model parameters 13 and 14, respectively) whereby the sensitivity to  $\theta$  was again dominant (K-S score 0.47 versus 0.04-0.07 for all other significant parameters, respectively) (Figure 5C).

**Table 4.** Results of the unconstrained curve fitting of Eq. 4 to the ([ADP],  $V_{\text{PCr}}$ ) data for the 6 subjects.

subject	$Q_{\max}$ (mM/s)	$Q_{\min}$ (mM/s)	[ADP] <sub>0.5</sub> ( $\mu\text{M}$ )	$n_{\text{H}}$
1	0.78	-0.03	24	2.1
2	0.72	-0.03	18	2.3
3	0.62	-0.01	18	2.3
4	0.65	-0.05	21	2.0
5	0.83	-0.07	22	1.7
6	0.64	-0.05	21	1.7
<b>mean</b>	0.71	-0.04	21	2.0
<b>SD</b>	0.09	0.02	2	0.3

Where  $Q_{\max}$ , denotes the maximal net PCr resynthesis flux;  $Q_{\min}$ , minimal net PCr resynthesis flux; [ADP]<sub>0.5</sub>, ADP concentration at half-maximal  $V_{\text{PCr}}$ ;  $n_{\text{H}}$ , Hill coefficient.

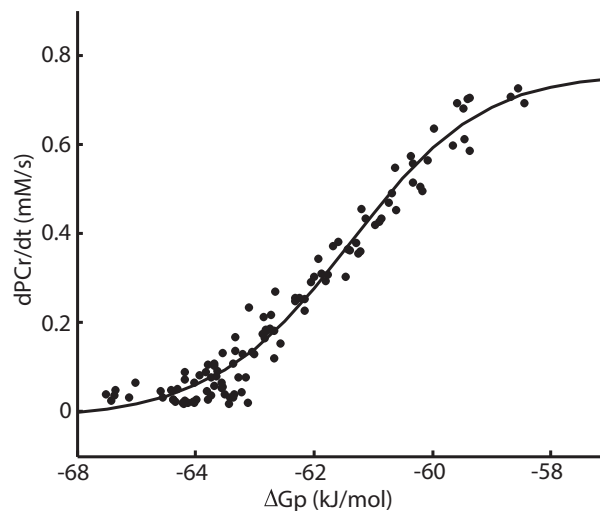


**Figure 3.** PCr resynthesis rate as a function of the molar free energy of cytosolic ATP hydrolysis (filled circles) for an individual muscle (subject 2). The unconstrained, 4-parameter fit of Eq. 4 to the data is shown by the solid line.

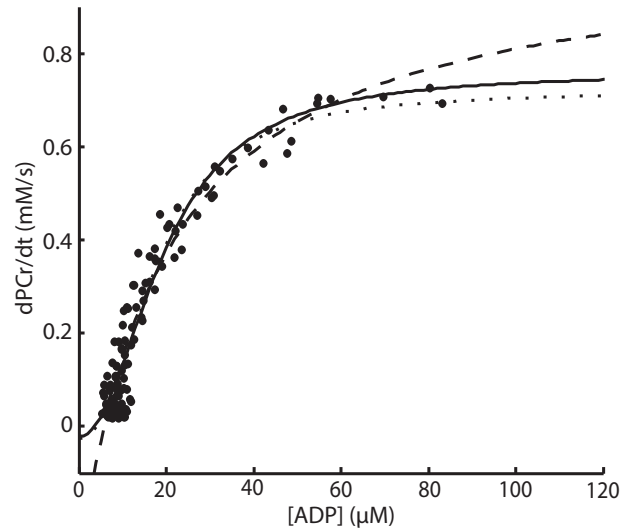


**Figure 4.** PCr resynthesis rate as a function of ADP concentration (filled circles) for an individual muscle (subject 2). Eq. 2 was fitted to the data: 2-parameter fit with  $Q_{\max}$  and  $Q_{\min}$  constrained to the values obtained from the thermodynamic flow-force relation (solid line), unconstrained, 4-parameter fit (dotted line), and 3-parameter fit with  $n_H$  constrained to 1 (dashed line).

### Model fitting

The MPSA results were next used to investigate if any set of model parameter values existed that would give rise to *in silico* mitochondrial ADP ultrasensitivity. First, the transduction function for the default parameterization of the model (14) was characterized. Figure 6A shows the  $[\text{ADP}]-J_p$  covariation computed for the default set of model parameter values together with a set of experimental  $[\text{ADP}]-J_p$  data points obtained in an individual muscle. By scaling  $X_{\text{ANT}}$  and  $X_{\text{DH}}$ , the *in silico*  $Q_{\max}$  of oxidative phosphorylation was adjusted to 0.8 mM/s corresponding to the *in vivo* estimate for this particular muscle (Table 2; subject #2). This required a twofold increase of  $X_{\text{ANT}}$  and a threefold increase of  $X_{\text{DH}}$  to 0.016 mM/s and 0.260 mM/s, respectively. Curve-fitting of Eq. 4 to the simulated data showed that the ADP transduction function for the default parameterization of the model was hyperbolic ( $n_H$  1.06) with  $Q_{\max}$  and  $Q_{\min}$  of 0.80 and -0.02 mM/s, respectively, and a  $K_{50}$  of 0.16 mM. Clearly, the first-order *in silico* mitochondrial ADP sensitivity for the default model parameterization was incompatible with the measured *in vivo* response of  $J_p$  to  $[\text{ADP}]$  changes in muscle (Figure 6A). Figures 6B and 6C show the computed variations of the mitochondrial membrane potential ( $\Delta\psi_m$ ) and redox potential ( $([\text{NADH}]/[\text{NAD}])_m$ ) with  $[\text{ADP}]$ , respectively, for the default parameterization. Both potentials were predicted first to rapidly increase at very low  $[\text{ADP}]$  and subsequently gradually drop towards limit values of 170 mV and 1.3, respectively (Figures 6B and C).

Figures 6D-I show the results of the model fitting to the same *in vivo*  $[\text{ADP}]-J_p$  data set for two cases. In the first case, only the model parameters with the highest MPSA K-S score (i.e., ANT parameters  $X_{\text{ANT}}$  and  $\theta$ ; Figure 5A-C) were adjustable parameters in the fitting yielding  $X_{\text{ANT}} = 0.041$  mM/s and  $\theta = 1.0$  (versus 0.016 mM/s and 0.35 in the default case, respectively). Figure 6D shows the corresponding fit of Eq. 4 to the computed  $[\text{ADP}]-J_p$  covariation for this particular model parameterization in comparison to the measured  $[\text{ADP}]-J_p$  covariation in the individual muscle. The *in silico* ADP transduction function in this case was sigmoidal with a Hill coefficient of 1.5 and a  $K_{50}$  of 0.025 mM corresponding to ADP ultrasensitivity (21). The fitted estimates for  $Q_{\max}$  and  $Q_{\min}$  were

0.82 and -0.02 mM/s, respectively. Figures 6E and 6F show the computed variations with [ADP] of  $\Delta\psi_m$  and  $([NADH]/[NAD])_m$  for this particular model parameterization. Both potentials exhibited a steeper drop over the physiological range of ADP concentration changes in muscle compared to the default model parameterization (but without any initial rise at low [ADP]) followed by a more rapid stabilization at 165 mV and 1.1, respectively, at ADP concentrations above 0.2 mM. Figures 6G-I show the results for an alternative model fitting. In this case, all model parameters with a significant K-S score except  $\theta$  were adjustable parameters in the fitting, yielding  $X_{ANT} = 0.32$  mM/s,  $X_{DH} = 0.12$  mM/s and  $r = 3.1$  (versus 0.016 mM/s, 0.26 mM/s and 4.6 for the default case in Figure 6A, respectively). The ADP transduction function for this model parameterization was likewise sigmoidal with fitted estimates of  $Q_{max}$ ,  $Q_{min}$  and  $K_{50}$  of 0.81 mM/s, -0.02 mM/s and 0.023 mM, respectively (Figure 6G). The Hill coefficient was in this case even higher than in the former case (i.e., 2.1 versus 1.5, respectively). However, for this particular model parameterization  $([NADH]/[NAD])_m$  collapsed over the physiological range of ADP concentration changes in muscle accompanied by  $\Delta\psi_m$  falling below 150 mV (Figure 6H and I).

## DISCUSSION

The present *in vivo* and *in silico* investigations of the magnitude and origin of mitochondrial sensitivity to cytoplasmic ADP concentration changes in human skeletal muscle has yielded two main results. First, it was found by  $^{31}\text{P}$  MRS that the *in vivo* affinity and kinetic order of ADP stimulation of mitochondrial oxidative ADP phosphorylation in human skeletal muscle were  $0.022 \pm 0.003$  mM and  $1.9 \pm 0.2$ , respectively. Secondly, it was found by computational analysis that these kinetic characteristics of mitochondrial ADP sensing and transduction, respectively, are primarily determined by the kinetic properties of the mitochondrial adenine nucleotide transporter. Below, these results and aspects of the underlying analysis are discussed.

### ***In vivo mitochondrial ADP transduction function: analysis.***

The previous investigation of the mitochondrial ADP transduction function used, amongst others, *in vivo* data sets on the covariations of the mitochondrial ATP synthesis rate  $J_p$  with cytosolic  $\Delta G_p$  and [ADP] in contracting forearm muscle (17). Hereto, muscle PCr,  $P_i$  and ATP concentrations and pH were measured in individual subjects typically at six electrical nerve stimulation frequencies (17). As such, the  $(\Delta G_p, J_p)$  and  $([ADP], J_p)$  relations in individual subjects were only sparsely sampled (7 points in each data set). As a consequence, adequate sampling of the underlying physiological relationship to determine the Hill coefficient was achieved only by pooling data sets of six subjects yielding 42 data points ((17); Figure 2). This introduced additional scatter as a result of intersubject variation in muscle fiber type composition giving rise to a 3-fold range in ATPase activity at a particular twitch contraction frequency (38). In the present study, this problem was circumvented by taking an alternative approach: the relationship between mitochondrial ATP synthesis flux and  $\Delta G_p$  and [ADP], respectively, was reconstructed from the densely sampled (6 s time resolution) PCr recovery time course following muscle contractions (Figures 3 and 4). Moreover, multiple data sets were obtained from each subject. As a result, single subject data sets therefore typically contained 100+ (range: 109-206) data points (Figures 3 and 4) compared to 7 data points in the previous

study (17). In particular, much improved sampling of the  $\Delta G_p$ - $J_p$  covariation was obtained at very low fluxes (Figure 3). As a result, accurate estimation of the mitochondrial flux asymptotes (and thereby  $n_H$ ) was achieved in individual subjects (Tables 2 and 3). In fact, fully unconstrained fitting of a sigmoidal relation to individual ( $[ADP]$ ,  $J_p$ ) data sets yielded the same results as two-parameter fits with flux asymptotes fixed at values obtained from the thermodynamic flow-force analysis ( $n_H$ :  $2.0 \pm 0.3$  versus  $1.9 \pm 0.2$ , respectively; Tables 3 and 4). These values were not different from the value previously obtained for skeletal muscle (i.e., 2.1 (17)).

A second methodological difference with the previous investigation of the mitochondrial ADP transduction function regarded the calculation of the mitochondrial ATP synthesis rate  $J_p$  corresponding to each  $[ADP]$  data point. In both cases, the derivative of the exponential fit to the time course of PCr was used to compute the net ATP turnover flux at each time point. However, in the previous study, a subsequent subtraction step was necessary to correct for any non-oxidative ATP synthesis flux evidenced from progressive acidification of the contracting muscle fibers (17). The magnitude of this flux was estimated from the pH time course (17). In the present study, no such correction was necessary because the muscle was electrically silent during recovery. It has been previously shown that anaerobic ATP synthesis flux is negligible under these conditions (27,31,32,39,40). Indeed, fitting of a bi-exponential function to the PCr time course during recovery failed to detect any significant second source of ATP synthesis (data not shown). If any, only the first PCr concentration time point at 3 s into metabolic recovery may have had a contribution from non-mitochondrial ATP synthesis (41). In that case, the data points in Figure 4 at the highest ADP concentrations would need to be correlated with lower mitochondrial  $J_p$  values. If anything, this would render the fitted transduction function even more, not less sigmoidal.

#### ***In vivo mitochondrial ADP transduction function: magnitude of the kinetic order***

The first main result of the present investigation of the magnitude and origin of mitochondrial ADP ultrasensitivity is that the apparent kinetic order of the *in vivo* mitochondrial transduction function  $f([ADP], J_p)$  in skeletal muscle is  $1.9 \pm 0.02$  (range: 1.7 – 2.1; Table 3). This value is in close agreement with the outcome of a previous investigation of the precise value of this macroscopic kinetic parameter in isolated mitochondria and human forearm muscle (2.4 and 2.1, respectively) (17). As such, the present investigation constitutes the first direct *in vivo* confirmation of the previously formulated hypothesis that mitochondria are ultrasensitive to extramitochondrial ADP concentration changes (17). Previous confirmations had come only from indirect evidence (19,20).

This result impacts the field of bioenergetics in two ways. Firstly, after having been previously dismissed as an irrelevant regulatory mechanism in cardiac energetic (6), feedback control of mitochondrial ATP synthesis has recently returned to the center of attention (7). This renewed interest has been spurred by the discovery of multiple stimulatory effects of  $P_i$  on the mitochondrial metabolic network involved in oxidative ADP phosphorylation in cardiac and skeletal muscle (8). Indeed, a recent review of contemporary knowledge of cardiac energetic elaborately discuss the impact of this discovery on understanding energy balance in the heart (7).

No mentioning was made, however, of the other ATP hydrolysis product, ADP and its particular role in feedback control of ATP synthesis in the heart (7). Yet, it was previously shown that mitochondrial ADP ultrasensitivity may for a large part explain the measured covariation of  $[ADP]$  and myocardial oxygen consumption (17). Therefore, the present affirmation of the hypothesis of mitochondrial ADP ultrasensitivity suggests that both this particular mechanism as well as the

multiple stimulatory roles of  $P_i$  both contribute to the efficacy of feedback respiratory control in striated muscle energetics. Importantly, the apparent allosteric stimulatory effects of ADP and  $P_i$  on mitochondrial ATP synthesis appear to operate independently. This conclusion is based on the finding that the magnitude of mitochondrial ADP ultrasensitivity quantified by the Hill coefficient of the transduction function (21) was sensitive only to a subset of the parameters in the mitochondrial metabolic network model whereby the multiple stimulatory roles of  $P_i$  were mathematically implemented (Figure 5B). Secondly, the result impacts computational modeling of mammalian cell energetic. Specifically, the affirmation of second order for the mitochondrial ADP transduction function provides a firm and tractable validation criterion for evaluation of past (9-14) and future computational models of mitochondrial oxidative metabolism.

#### ***In vivo mitochondrial ADP sensing and transduction: origin of ADP ultrasensitivity***

Koshland identified three distinct generic biochemical mechanisms that may endow a biological network with ultrasensitivity (21). For the particular case of mitochondrial ultrasensitivity to cytoplasmic ADP concentration changes, concrete indications exist for the possible involvement of two of these mechanisms – i.e., the presence of allosteric network elements and multi-site network activation, respectively (21). Specifically, three alternative biochemical implementations of multi-site activation have been demonstrated in mitochondria – i.e., multi-site kinetic activation by calcium (1), by inorganic phosphate (8), and multi-site phosphorylation (42). Likewise, *in vitro* evidence has been obtained for non-MM kinetics of ADP-ATP exchange catalyzed by the ANT (43,44). The latter mechanism was previously invoked to explain mitochondrial ADP ultrasensitivity in the original communication (17). However, that particular hypothesis for the origin of mitochondrial ADP ultrasensitivity has awaited validation. The present investigation has yielded new evidence that the kinetic properties of ANT indeed principally determine the macroscopic mitochondrial property of ADP sensitivity. This is the second main result of the investigation.

The evidence for this conclusion that was obtained in this study was twofold. Firstly, the MPSA of the computational model of skeletal muscle oxidative ATP metabolism including a detailed biophysical model of mitochondrial oxidative ADP phosphorylation (14) identified an ANT parameter as the primary determinant of mitochondrial ADP sensitivity both with respect to ADP sensing ( $K_{50}$ ) as well as transduction ( $n_H$ ) (Figures 5B and C). This particular parameter,  $\theta$ , is a phenomenological parameter in the rate equation for the ADP-ATP exchange reaction catalyzed by ANT of the model that was analyzed ((14); see Appendix). The K-S scores for this parameter only were one order of magnitude higher than the statistical threshold and 5 to 10-fold higher than any other model parameter (Figures 5B and C). Secondly, the results of the model fitting to an *in vivo* [ADP]- $J_p$  data set from an individual muscle showed that mitochondrial ultrasensitivity to ADP concomitant with homeostasis of the mitochondrial membrane and redox potentials could be obtained *in silico* if, and only if the ANT parameter  $\theta$  was included in the set of adjustable parameters in the model fitting (Figure 6).



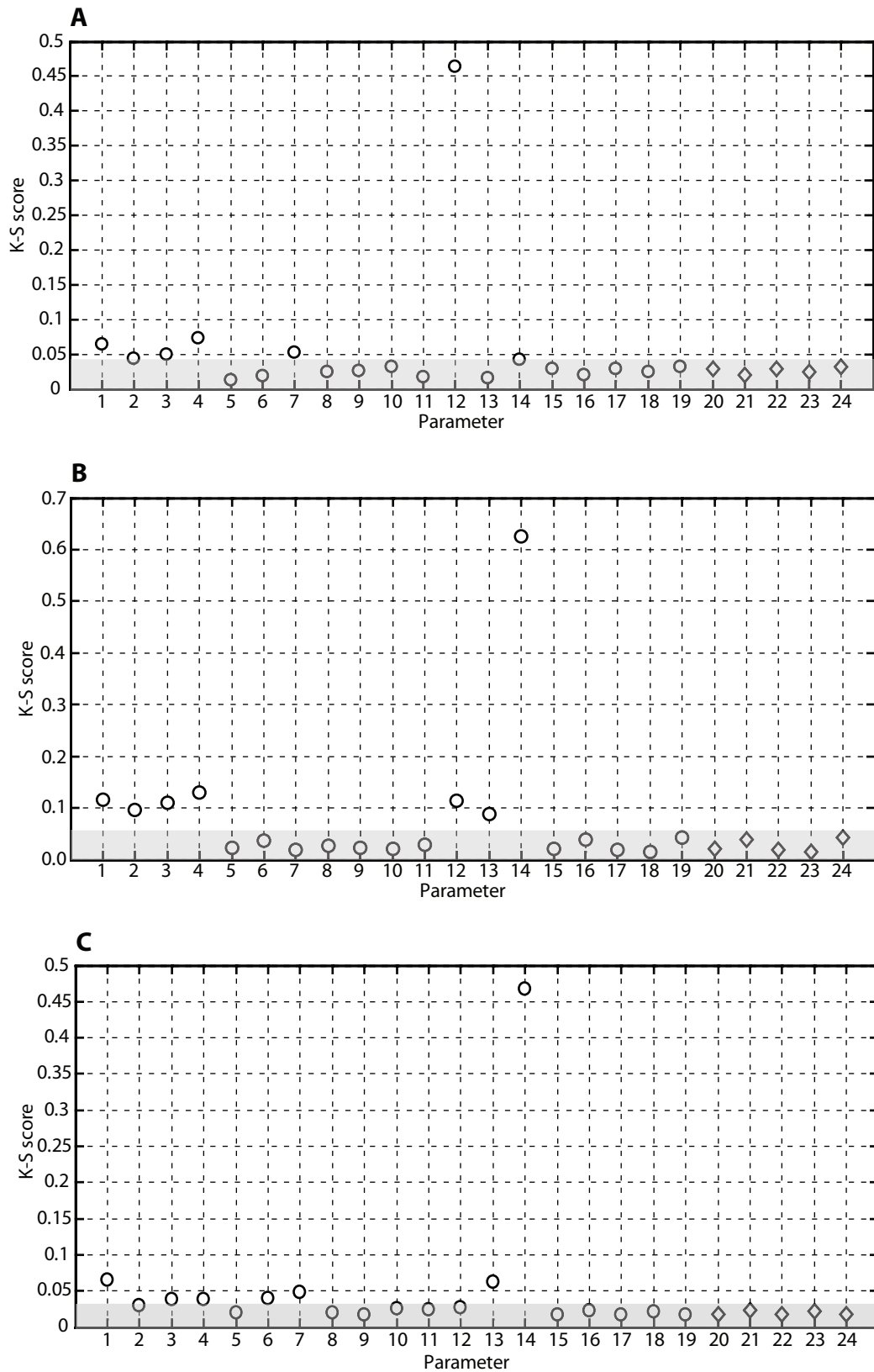


**Figure 5.** K-S scores of the 19 model parameters (o) and 5 dummy parameters (◊) from the multi-parametric sensitivity analysis of the model for each of the three macroscopic kinetic parameters of the mitochondrial transduction function: (A)  $Q_{max}$ , (B)  $n_H$  and (C)  $K_{50}$ . Shaded areas indicate the threshold of significance set by the K-S scores of the 5 dummy parameters in each graph.

The default ADP sensitivity of the mitochondrial network in the model was insufficient, as indicated by the hyperbolic nature of the simulated [ADP]-Jp relation for the default model parameterization (Figure 6A). Changing  $\theta$  from its default value of 0.35 to the fitted optimum of 1.0 concomitant with a 2.5-fold increase of the  $V_{\max}$  of ANT resulted in an almost 5-fold increase in mitochondrial ADP sensitivity compared to the default parameterization of the model ( $n_H$  1.5 versus 1.06 and  $K_{50}$  0.025 versus 0.16 mM, respectively; Figures 6A and 6D). Importantly, these specific values of *in silico* mitochondrial ADP affinity and transduction closely agreed with the experimentally determined values of these macroscopic mitochondrial kinetic parameters in muscle (Table 3). Furthermore, simulation showed that homeostasis of the mitochondrial membrane and redox potential at high ADP concentrations was superior compared to the default model parameterization (Figures 6B and C versus 6E and F, respectively). In contrast,  $\Delta\psi_m$  and particularly  $([NADH]/[NAD])_m$  collapsed at physiological ADP concentrations in muscle for the alternative combination of fitted model parameters (including the  $V_{\max}$  of ANT but not  $\theta$ ) that yielded mitochondrial ADP ultrasensitivity (Figure 6H and I, respectively). Specifically, simulation showed that  $([NADH]/[NAD])_m$  in this case near-instantaneously collapsed to almost zero when mitochondria were activated by cytoplasmic accumulation of ADP and  $\Delta\psi_m$  dropped below the critical value of 150 mV at a, for muscle, only moderately elevated cytoplasmic ADP concentration of 0.07 mM (Figures 6H and I). It has been well established that the reaction catalyzed by mitochondrial F1-ATPase reverses from net ATP synthesis to ATP hydrolysis for  $\Delta\psi_m$  values below 150 mV (11).

Finally, it could perhaps be argued that the maximal Hill coefficient for *in silico* mitochondrial ADP transduction that was obtained by fitting of  $\theta$  and  $X_{ANT}$  falls short of reproducing the *in vivo* estimate of this macroscopic parameter (1.5 versus  $1.9 \pm 0.02$  (range: 1.7 – 2.1), respectively; Table 3). In that case, there would maximally be need for another twofold increase in sensitivity by some kinetic mechanism that remained unidentified in the present computational studies likely because it was not included in the particular mitochondrial computational model that was analyzed. Since multi-site kinetic activation of the mitochondrial network by  $P_i$  has been explicitly incorporated in the model (14), it is more likely another kinetic mechanism must be involved. In that case, some form of kinetic regulation by calcium may appear a tenable first hypothesis for several reasons. First of all, the computational mitochondrial model platform for our computational studies did not yet include implementation of calcium balance (nor of any metabolic regulatory effect of calcium; (14)). Secondly, it has been well established that calcium can modify TCA-DH activity in mitochondria (1). Thirdly, the kinetic parameters of the TCA-DH were found to have significant control, albeit small compared to  $\theta$ , of the Hill coefficient of the mitochondrial ADP transduction function (Figure 5B). However, we were unable to further increase  $n_H$  above 1.5 by additionally changing any of the TCA-DH parameter values within a 10-fold range (data not shown) indicating that, if any, none of the known calcium effects on TCA-DH activity (1) would be involved. Any significant contribution of calcium activation of other enzymes in the mitochondrial network (e.g., direct activation of ATP synthase (1) or indirect activation of the redox proton pumps via covalent modification by kinases (42)) also appears unlikely since none of these mitochondrial enzymes had any significant MPSA K-S score (Figure 5B). As such, it may well prove difficult to identify any ancillary kinetic mechanisms and their biochemical implementation in the mitochondrial metabolic network that may further increase the macroscopic kinetic order of ADP

transduction from 1.5 to 1.9. However, the present study illustrates that computational modeling and network analysis provide powerful tools to conduct such an investigation.

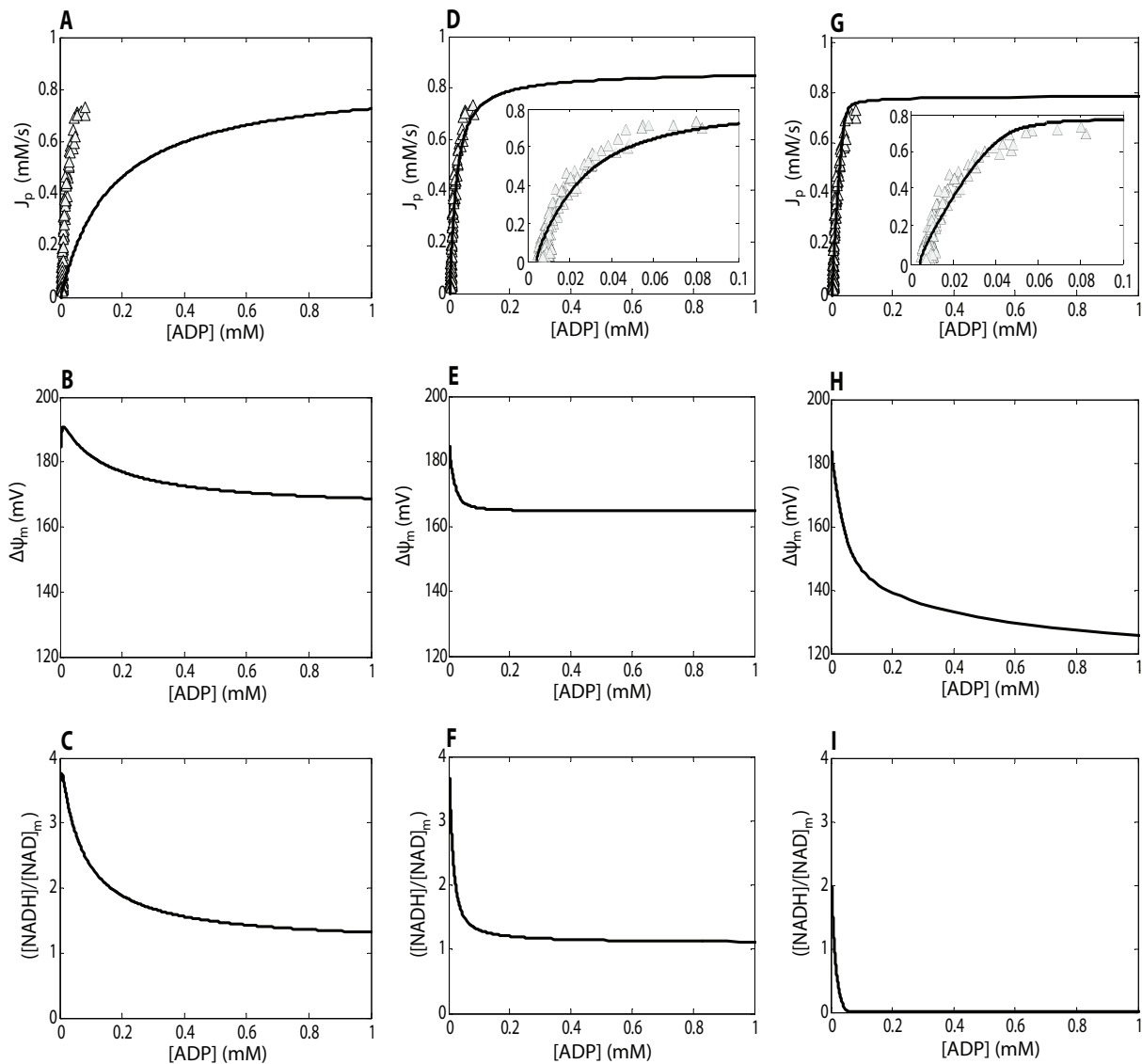


**Figure 6.** Simulations of the covariation of  $J_p$  (in mM/s),  $\Delta\psi_m$  (in mV) and  $([NADH]/[NAD])_m$  with cytoplasmic ADP concentration (in mM) for three different model parameterizations. Open symbols correspond to measured *in vivo* [ADP]- $J_p$  covariation in an individual muscle (subject 2). **(A)-(C)**: default model parameterization with  $X_{ANT}$  and  $X_{DH}$  0.41 and 0.269 mM/s, respectively. In (A), the simulated relation was kinetically characterized by unconstrained, 4-parameter curve-fitting of Eq. 4 yielding fitted estimates for with  $Q_{max}$ ,  $Q_{min}$ ,  $n_H$  and  $K_{50}$  of 0.80 mM/s, -0.02 mM/s, 1.06 and 0.16 mM, respectively. **(D)-(F)**: fitted model parameterization I with  $X_{ANT} = 0.41$  mM/s and  $\theta = 1.0$ .  $X_{DH}$  was kept at 0.269 mM/s. In (D), the simulated relation was kinetically characterized by unconstrained, 4-parameter curve-fitting of Eq. 4 yielding fitted estimates for with  $Q_{max}$ ,  $Q_{min}$ ,  $n_H$  and  $K_{50}$  of 0.82 mM/s, -0.02 mM/s, 1.50 and 0.025 mM, respectively. **(G)-(I)**: fitted model parameterization II with  $X_{ANT} = 0.32$  mM/s,  $X_{DH} = 0.12$  mM/s and  $r = 3.1$ . In (G), the simulated relation was kinetically characterized by unconstrained, 4-parameter curve-fitting of Eq. 4 yielding fitted estimates for with  $Q_{max}$ ,  $Q_{min}$ ,  $n_H$  and  $K_{50}$  of 0.81 mM/s, -0.02 mM/s, 2.10 and 0.023 mM, respectively.

**Implications for kinetic modeling of ANT**

The adjustment of the value of ANT parameter  $\theta$  from 0.35 to 1.0 that, together with a 2.5-fold increase in  $V_{\max}$  of ATP-ADP exchange, transforms the ADP sensitivity of the mitochondrial metabolic network in the Wu model (14) from normal to ultrasensitivity represents not merely an arbitrary model optimization. Instead, it has a significant mechanistic implication. In the Wu model (14),  $\theta$  is a phenomenological partition coefficient that determines the magnitude of the effective  $\Delta\psi_m$  components on the intermembrane space and matrix sides of the inner membrane ( $\Delta\psi_{m-i}$  and  $\Delta\psi_{m-x}$ , respectively) with respect to the transport of ADP and ATP across the inner membrane (Appendix). The phenomenological partitioning of  $\Delta\psi_m$  into  $\Delta\psi_{m-i} = \theta \cdot \Delta\psi_m$  and  $\Delta\psi_{m-x} = (1-\theta) \cdot \Delta\psi_m$ , respectively, was originally introduced in the kinetic modeling of the ATP-ADP exchange reaction catalyzed by the ANT by Korzeniewski and Froncisz (45) and later parameterized by fitting of *in vitro* mitochondrial adenine nucleotide uptake data yielding  $\theta = 0.35$  (46). It has since been used in other computational models of mitochondrial ATP synthesis including the model analyzed here (14,47).

The results of the present investigation invalidate this particular kinetic model of mitochondrial ATP-ADP exchange as a suitable component of any computational model that seeks to simulate the behavior of mitochondria in living cells. Specifically, the result of the model fitting that  $\theta$  should be 1 rather than 0.35 to adequately simulate ATP metabolism in muscle indicated that the partitioning of  $\Delta\psi_m$  into any cytoplasmic and matrix component introduced on basis of *in vitro* data is not appropriate *in vivo* and should be omitted. The adjusted ANT rate equation is shown in the Appendix (Eq. 8). The mechanistic implication of this conclusion is that the transport rate of the cytoplasmic adenine nucleotides into the mitochondria remains sensitive both to mass action as well as the electrochemical potential over the inner mitochondrial membrane, whereas the transport rate of adenine nucleotides from inside the mitochondria to the outside *in vivo* is apparently sensitive to mass action only (Appendix; Eq. 8).

## APPENDIX

The rate equation for ATP-ADP exchange across the inner mitochondrial membrane catalyzed by the ANT in the model of Wu et al. (14) is (Eq. 5):

$$J_{\text{ANT}} = X_{\text{ANT}} \left( \frac{[\text{fADP}]_i}{[\text{fADP}]_i + [\text{fATP}]_i e^{-\theta F \Delta \Psi_m / RT}} - \frac{[\text{fADP}]_x}{[\text{fADP}]_x + [\text{fATP}]_x e^{-(1-\theta) F \Delta \Psi_m / RT}} \right) \cdot \left( \frac{1}{1 + (K_{\text{m,ADP}} / [\text{fADP}]_i)} \right) \quad (\text{Eq. 5})$$

where  $[\text{fX}]_i$  and  $[\text{fX}]_x$  are the magnesium-unbound species of ATP and ADP in the mitochondrial intermembrane space and matrix, respectively, and  $\Delta \Psi_m$  is the mitochondrial membrane potential (14). The kinetic parameters  $X_{\text{ANT}}$  and  $K_{\text{m,ADP}}$  (parameters 12 and 13 in Table 1, respectively) correspond to the ANT activity (in mol/s/l mito) and the ANT Michaelis constant (in M), respectively (14). Parameter  $\theta$  is a phenomenological coefficient introduced by Korzeniewski and Froncisz (45) that determines the magnitude of the effective  $\Delta \Psi_m$  components on the intermembrane space and matrix sides of the inner membrane ( $\Delta \Psi_{m-i}$  and  $\Delta \Psi_{m-x}$ , respectively) with respect to the transport of ADP and ATP across the inner membrane according to (Eq. 6 and 7):

$$\Delta \Psi_{m-i} = \theta \cdot \Delta \Psi_m \quad (\text{Eq. 6})$$

$$\Delta \Psi_{m-x} = (1 - \theta) \cdot \Delta \Psi_m \quad (\text{Eq. 7})$$

The default value of  $\theta$  in the Wu model was 0.35 (14) and identical to the value previously derived by Korzeniewski on basis of model fitting to *in vitro* data of adenine nucleotide uptake in isolated mitochondria (46).

For the case  $\theta = 1$ , Eq. 5, reduces to (Eq. 8):

$$J_{\text{ANT}} = X_{\text{ANT}} \left( \frac{[\text{fADP}]_i}{[\text{fADP}]_i + [\text{fATP}]_i e^{-F \Delta \Psi_m / RT}} - \frac{[\text{fADP}]_x}{[\text{fADP}]_x + [\text{fATP}]_x} \right) \cdot \left( \frac{1}{1 + (K_{\text{m,ADP}} / [\text{fADP}]_i)} \right) \quad (\text{Eq. 8})$$

## REFERENCES

1. **Balaban RS.** Cardiac energy metabolism homeostasis: role of cytosolic calcium. *J Mol Cell Cardiol* 34: 1259-1271, 2002
2. **Chance B.** Reaction of oxygen with the respiratory chain in cells and tissues. *J Gen Physiol* 49: Suppl-95, 1965
3. **Chance B, WILLIAMS GR.** Respiratory enzymes in oxidative phosphorylation. I. Kinetics of oxygen utilization. *J Biol Chem* 217: 383-393, 1955
4. **Chance B, Eleff S, Bank W, Leigh JS, Jr. and Warnell R.** 31P NMR studies of control of mitochondrial function in phosphofructokinase-deficient human skeletal muscle. *Proc Natl Acad Sci U S A* 79: 7714-7718, 1982
5. **Kushmerick MJ.** Energy balance in muscle activity: simulations of ATPase coupled to oxidative phosphorylation and to creatine kinase. *Comp Biochem Physiol B Biochem Mol Biol* 120: 109-123, 1998
6. **Balaban RS, Kantor HL, Katz LA and Briggs RW.** Relation between work and phosphate metabolite in the in vivo paced mammalian heart. *Science* 232: 1121-1123, 1986
7. **Balaban RS.** Domestication of the cardiac mitochondrion for energy conversion. *J Mol Cell Cardiol* 46: 832-841, 2009
8. **Bose S, French S, Evans FJ, Joubert F and Balaban RS.** Metabolic network control of oxidative phosphorylation: multiple roles of inorganic phosphate. *J Biol Chem* 278: 39155-39165, 2003
9. **Beard DA.** A biophysical model of the mitochondrial respiratory system and oxidative phosphorylation. *PLoS Comput Biol* 1: e36, 2005
10. **Cortassa S, Aon MA, Marban E, Winslow RL and O'Rourke B.** An integrated model of cardiac mitochondrial energy metabolism and calcium dynamics. *Biophys J* 84: 2734-2755, 2003
11. **Magnus G, Keizer J.** Minimal model of beta-cell mitochondrial Ca<sup>2+</sup> handling. *Am J Physiol* 273: C717-C733, 1997
12. **Nguyen MH, Dudycha SJ and Jafri MS.** Effect of Ca<sup>2+</sup> on cardiac mitochondrial energy production is modulated by Na<sup>+</sup> and H<sup>+</sup> dynamics. *Am J Physiol Cell Physiol* 292: C2004-C2020, 2007
13. **van Stiphout RG, van Riel NA, Verhoog PJ, Hilbers PA, Nicolay K and Jeneson JA.** Computational model of excitable cell indicates ATP free energy dynamics in response to calcium oscillations are undamped by cytosolic ATP buffers. *Syst Biol (Stevenage)* 153: 405-408, 2006
14. **Wu F, Jeneson JA and Beard DA.** Oxidative ATP synthesis in skeletal muscle is controlled by substrate feedback. *Am J Physiol Cell Physiol* 292: C115-C124, 2007
15. **De Martino C, Floridi A, Marcante ML, Malorni W, Scorza BP, Bellocchi M and Silvestrini B.** Morphological, histochemical and biochemical studies on germ cell mitochondria of normal rats. *Cell Tissue Res* 196: 1-22, 1979
16. **Jacobus WE, Moreadith RW and Vandegaer KM.** Mitochondrial respiratory control. Evidence against the regulation of respiration by extramitochondrial phosphorylation potentials or by [ATP]/[ADP] ratios. *J Biol Chem* 257: 2397-2402, 1982
17. **Jeneson JA, Wiseman RW, Westerhoff HV and Kushmerick MJ.** The signal transduction function for oxidative phosphorylation is at least second order in ADP. *J Biol Chem* 271: 27995-27998, 1996
18. **Kushmerick MJ, Meyer RA and Brown TR.** Regulation of oxygen consumption in fast- and slow-twitch muscle. *Am J Physiol* 263: C598-C606, 1992
19. **Cieslar JH, Dobson GP.** Free [ADP] and aerobic muscle work follow at least second order kinetics in rat gastrocnemius in vivo. *J Biol Chem* 275: 6129-6134, 2000
20. **Vicini P, Kushmerick MJ.** Cellular energetics analysis by a mathematical model of energy balance: estimation of parameters in human skeletal muscle. *Am J Physiol Cell Physiol* 279: C213-C224, 2000
21. **Koshland DE, Jr., Goldbeter A and Stock JB.** Amplification and adaptation in regulatory and sensory systems. *Science* 217: 220-225, 1982
22. **Prompers JJ, Jeneson JA, Drost MR, Oomens CC, Strijkers GJ and Nicolay K.** Dynamic MRS and MRI of skeletal muscle function and biomechanics. *NMR Biomed* 19: 927-953, 2006
23. **van den Broek NM, De Feyter HM, de GL, Nicolay K and Prompers JJ.** Intersubject differences in the effect of acidosis on phosphocreatine recovery kinetics in muscle after exercise are due to differences in proton efflux rates. *Am J Physiol Cell Physiol* 293: C228-C237, 2007
24. **Vanhamme L, van den Boogaart A and Van HS.** Improved method for accurate and efficient quantification of MRS data with use of prior knowledge. *J Magn Reson* 129: 35-43, 1997
25. **Narressi A, Couturier C, Devos JM, Janssen M, Mangeat C, de BR and Graveron-Demilly D.** Java-based graphical user interface for the MRUI quantitation package. *MAGMA* 12: 141-152, 2001
26. **Taylor DJ, Styles P, Matthews PM, Arnold DA, Gadian DG, Bore P and Radda GK.** Energetics of human muscle: exercise-induced ATP depletion. *Magn Reson Med* 3: 44-54, 1986
27. **Taylor DJ, Bore PJ, Styles P, Gadian DG and Radda GK.** Bioenergetics of intact human muscle. A 31P nuclear magnetic resonance study. *Mol Biol Med* 1: 77-94, 1983
28. **Lawson JW, Veech RL.** Effects of pH and free Mg<sup>2+</sup> on the K<sub>eq</sub> of the creatine kinase reaction and other phosphate hydrolyses and phosphate transfer reactions. *J Biol Chem* 254: 6528-6537, 1979
29. **Boska M.** ATP production rates as a function of force level in the human gastrocnemius/soleus using 31P MRS. *Magn Reson Med* 32: 1-10, 1994
30. **Guynn RW, Veech RL.** The equilibrium constants of the adenosine triphosphate hydrolysis and the adenosine triphosphate-citrate lyase reactions. *J Biol Chem* 248: 6966-6972, 1973
31. **Quistorff B, Johansen L and Sahlin K.** Absence of phosphocreatine resynthesis in human calf muscle during ischaemic recovery. *Biochem J* 291 ( Pt 3): 681-686, 1993
32. **Sahlin K.** Intracellular pH and energy metabolism in skeletal muscle of man. With special reference to exercise. *Acta Physiol Scand Suppl* 455: 1-56, 1978
33. **Zi Z, Cho KH, Sung MH, Xia X, Zheng J and Sun Z.** In silico identification of the key components and steps in IFN-gamma induced JAK-STAT signaling pathway. *FEBS Lett* 579: 1101-1108, 2005

34. **Groenendaal W, Jeneson JA, Verhoog PJ, van Riel NA, Ten Eikelder HM, Nicolay K and Hilbers PA.** Computational modelling identifies the impact of subtle anatomical variations between amphibian and mammalian skeletal muscle on spatiotemporal calcium dynamics. *JET Syst Biol* 2: 411-422, 2008
35. **Rottenberg H.** The thermodynamic description of enzyme-catalyzed reactions. The linear relation between the reaction rate and the affinity. *Biophys J* 13: 503-511, 1973
36. **van Dam K, Westerhoff HV.** *Thermodynamics and control of biological free energy transduction.* Amsterdam: Elsevier, 1987
37. **Chance B, Leigh JS, Jr., Clark BJ, Maris J, Kent J, Nioka S and Smith D.** Control of oxidative metabolism and oxygen delivery in human skeletal muscle: a steady-state analysis of the work/energy cost transfer function. *Proc Natl Acad Sci U S A* 82: 8384-8388, 1985
38. **Blei ML, Conley KE, Odderson IB, Esselman PC and Kushmerick MJ.** Individual variation in contractile cost and recovery in a human skeletal muscle. *Proc Natl Acad Sci U S A* 90: 7396-7400, 1993
39. **Blei ML, Conley KE and Kushmerick MJ.** Separate measures of ATP utilization and recovery in human skeletal muscle. *J Physiol* 465: 203-222, 1993
40. **Crowther GJ, Kemper WF, Carey MF and Conley KE.** Control of glycolysis in contracting skeletal muscle. II. Turning it off. *Am J Physiol Endocrinol Metab* 282: E74-E79, 2002
41. **Forbes SC, Paganini AT, Slade JM, Towse TF and Meyer RA.** Phosphocreatine recovery kinetics following low- and high-intensity exercise in human triceps surae and rat posterior hindlimb muscles. *Am J Physiol Regul Integr Comp Physiol* 296: R161-R170, 2009
42. **Hopper RK, Carroll S, Aponte AM, Johnson DT, French S, Shen RF, Witzmann FA, Harris RA and Balaban RS.** Mitochondrial matrix phosphoproteome: effect of extra mitochondrial calcium. *Biochemistry* 45: 2524-2536, 2006
43. **Brandolin G, Le SA, Trezeguet V, Lauquin GJ and Vignais PV.** Chemical, immunological, enzymatic, and genetic approaches to studying the arrangement of the peptide chain of the ADP/ATP carrier in the mitochondrial membrane. *J Bioenerg Biomembr* 25: 459-472, 1993
44. **Duyckaerts C, Sluse-Goffart CM, Fux JP, Sluse FE and Liebecq C.** Kinetic mechanism of the exchanges catalysed by the adenine-nucleotide carrier. *Eur J Biochem* 106: 1-6, 1980
45. **Korzeniewski B, Froncisz W.** An extended dynamic model of oxidative phosphorylation. *Biochim Biophys Acta* 1060: 210-223, 1991
46. **Korzeniewski B.** Simulation of oxidative phosphorylation in hepatocytes. *Biophys Chem* 58: 215-224, 1996
47. **Vendelin M, Kongas O and Saks V.** Regulation of mitochondrial respiration in heart cells analyzed by reaction-diffusion model of energy transfer. *Am J Physiol Cell Physiol* 278: C747-C764, 2000







# Chapter 5

## Prediction of muscle energy states at low metabolic rates requires feedback control of mitochondrial respiratory chain activity by inorganic phosphate

Adapted from

J.P.J. Schmitz, J.A.L. Jeneson, J.W.M. van Oorschot, J.J. Prompers, K. Nicolay, P.A.J. Hilbers, N.A.W. van Riel  
*Prediction of muscle energy states at low metabolic rates requires feedback control of mitochondrial respiratory chain activity by inorganic phosphate*  
PloS ONE, 2012, 7(3): e34118

## ABSTRACT

The regulation of the 100-fold dynamic range of mitochondrial ATP synthesis flux in skeletal muscle was investigated. Hypotheses of key control mechanisms were included in a biophysical model of oxidative phosphorylation and tested against metabolite dynamics recorded by  $^{31}\text{P}$  nuclear magnetic resonance spectroscopy ( $^{31}\text{P}$  MRS). Simulations of the initial model featuring only ADP and Pi feedback control of flux failed in reproducing the experimentally sampled relation between myoplasmic free energy of ATP hydrolysis ( $\Delta G_p = \Delta G_p^{\circ} + RT \ln ([\text{ADP}][\text{Pi}]/[\text{ATP}])$ ) and the rate of mitochondrial ATP synthesis at low fluxes ( $<0.2\text{mM/s}$ ). Model analyses including Monte Carlo simulation approaches and metabolic control analysis (MCA) showed that this problem could not be amended by model re-parameterization, but instead required reformulation of ADP and Pi feedback control or introduction of additional control mechanisms (feed forward activation), specifically at respiratory Complex III. Both hypotheses were implemented and tested against time course data of phosphocreatine (PCr), Pi and ATP dynamics during post-exercise recovery and validation data obtained by  $^{31}\text{P}$  MRS of sedentary subjects and track athletes. The results rejected the hypothesis of regulation by feed forward activation. Instead, it was concluded that feedback control of respiratory chain complexes by inorganic phosphate is essential to explain the regulation of mitochondrial ATP synthesis flux in skeletal muscle throughout its full dynamic range.

## INTRODUCTION

The means by which oxidative ATP synthesis is controlled has remained an intensively studied topic during the past decades (1). The first control scheme that was proposed involved a feedback signal of cellular ATP hydrolysis products, i.e. ADP and Pi (2). More recently, a second control mechanism was proposed: i.e. parallel activation of cellular ATP demand and production (feed forward activation). It was hypothesized that parallel activation (feed forward regulation) of cellular ATP demand and production was essential to explain energy homeostasis (1,3). Since then, several sites of Ca<sup>2+</sup> stimulation present in the mitochondrial network as well as a vast protein phosphorylation network controlled by Ca<sup>2+</sup> signaling have been discovered (4). These data provided further support of the parallel activation hypothesis. However, although both control mechanisms have a firm basis in literature, it is still unclear to which extent each of these mechanisms contributes to the cellular energy homeostasis of the intact system (see e.g. (5,6) versus (1) and (7)). In addition, related questions, like e.g., the role of these control mechanisms in the development and progression of metabolic diseases, are considered important topics for future research (8).

Answering these questions requires a thorough understanding of the integrated system (9,10). Computational modeling has been proposed as an important research tool for keeping track of biological complexity and developing such 'systems - level' understanding (11,12). Although most models are constructed by integration of information obtained under *in vitro* experimental conditions, the goal of these models remains to represent *in vivo* conditions. It is therefore essential to test and improve them with *in vivo* data.

<sup>31</sup>P magnetic resonance spectroscopy (MRS) provides a non-invasive method for measuring metabolite dynamics (PCr, Pi, ATP) during rest, exercise and recovery conditions in human skeletal muscle (13). In chapter 4, <sup>31</sup>P MRS was used to sample the transduction functions between regulatory metabolites (ADP, Pi) or thermodynamic potential ( $\Delta G_p = \Delta G_p^{\circ} + RT \ln [ADP][Pi]/[ATP]$ ) and the oxidative ATP synthesis flux ( $J_p$ ). These transduction functions capture important characteristics of the regulation of oxidative phosphorylation *in vivo* and can therefore be applied for testing and validation of computational models of oxidative ATP metabolism.

The computational model of oxidative energy metabolism developed by Beard and coworkers (14) is among the most advanced models currently available. At first, it was developed to describe oxidative ATP metabolism in cardiac myocytes. At the moment, it has excellent performance in reproducing <sup>31</sup>P MRS observed metabolite dynamics in cardiac cells (5,6). In addition, we showed that the model reproduced the transduction function between ADP and  $J_p$  recorded in skeletal muscle fairly well (chapter 4). However, it has also been reported that at low respiration rates and corresponding ATPase fluxes (ATPase < 0.2mM/s) the model systematically underestimates ADP and Pi concentrations (15,16), which is most evident in predictions of the  $\Delta G_p - J_p$  relation. These limitations are probably not a severe shortcoming for modeling of cardiac energetics. The normal physiological ATPase range of cardiac myocytes does not include these low fluxes. However, in case of skeletal muscle, or other excitable cell types, like neurons, the problem is considerably more significant, as these cells often experience low flux conditions.

It was studied if the observed model limitations are a result of inadequate parameterization; or alternatively, if the model is lacking essential control mechanisms. The latter will also have important physiological implications. Specifically, three hypotheses were tested: (i),

the model is not missing control mechanisms, but merely requires parameter optimization; (ii), the missing control can be explained by addition of a substrate feedback mechanisms (by e.g. Pi) acting on a subset of model components; or (iii), the missing control can be explained by addition of feed forward regulation (by e.g. Ca<sup>2+</sup> signaling and protein phosphorylation) acting on a subset of model components.

To test these hypotheses, first, the relation between  $\Delta G_p$  and  $J_p$  was obtained from high time resolution <sup>31</sup>P MRS recordings of metabolite dynamics (PCr, Pi, ATP, ADP, pH) during recovery from exercise. The relation was determined for healthy human subjects (control group; data were obtained from chapter 4) and two other populations, i.e., subjects with sedentary lifestyle and track athletes (validation datasets). Next, numerical analysis and model simulations were applied to test which of the three hypotheses could explain both control and validation datasets. The results rejected the solution of model re-parameterization or addition of regulation by a feed forward control mechanism. Instead, our findings provide new evidence in support of a substrate feedback related control mechanism that acts on the respiratory chain complexes, and at Complex III in particular, which regulates  $\Delta G_p$  at low respiration rates in skeletal muscle.

## METHODS

### **Experimental data**

Healthy, normally active control subjects - The experimentally sampled  $\Delta G_p - J_p$  relation was obtained from human quadriceps muscle of healthy, normally active subjects using *in vivo* <sup>31</sup>P NMR spectroscopy. These data were already presented in chapter 4. Full details regarding the methods of these experiments are described in chapter 4.

Subjects with sedentary lifestyle - The data of sedentary humans used for model validation were obtained from de Feyter et al. (17). This dataset was recorded using the same methodology as described in chapter 4. The inter - subject difference in mitochondrial capacity in the study by de Feyter et al. was rather large (range: 0.31 – 0.82 mM/s). It was chosen to select the data of 2 subjects with the lowest mitochondrial capacity. As a result the scatter of data points decreased, making the dataset more appropriate for rigorous model testing, while the  $\Delta G_p - J_p$  relation was still sufficiently sampled (> 300 samples). Analysis of muscle biopsy samples taken from the same subjects (18) showed that the decreased mitochondrial capacity correlated well with *in vitro* measures of mitochondrial content (CS and SDH activity). These results provided additional verification that the selected sedentary subjects had a decreased mitochondrial content.

Athletes - The data recorded in athletes has not been published before. For all experiments, the nature and risks of the experimental procedures were explained to the subject. All gave their written informed consent to participate to the study, which conformed the standards set by the Declaration of Helsinki and was approved by the local Medical Ethics Committee of the Máxima Medical Centre, Veldhoven, The Netherlands.

The applied methodology was identical to the two other datasets (normally active, sedentary), with the only exception being that for this study a bicycle ergometer was used and the

sample time of the measurements was decreased from 6 to 3s. Details of the ergometer can be found elsewhere (19). The track athletes (age: 22 $\pm$ 2 mean $\pm$ SD, n=3) participated in national and international level competition and trained for more than 8 hours a week.

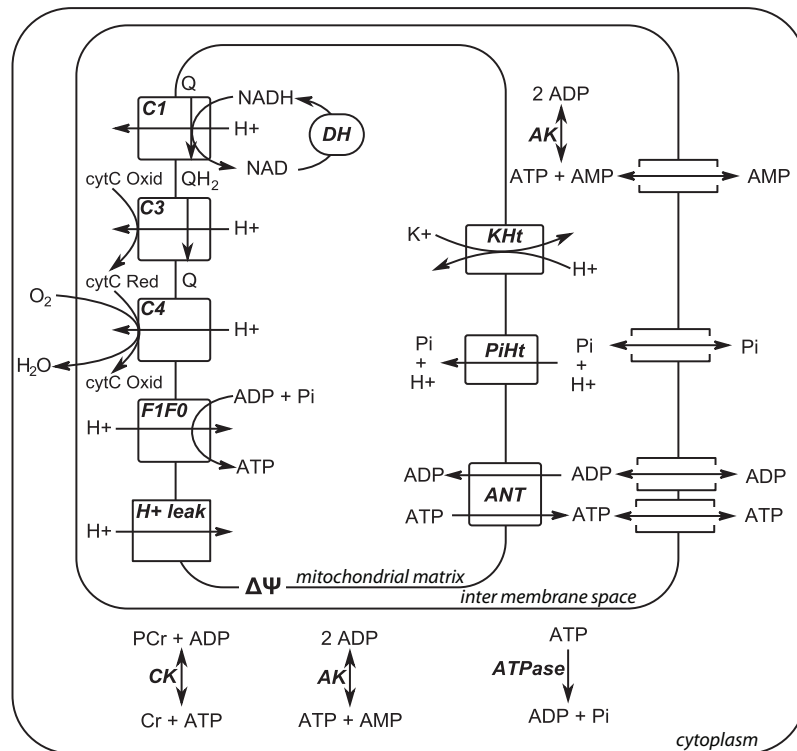


**Figure 1.** Schematic representation of the computational model of skeletal muscle energetics. Abbreviations denote: dehydrogenases (DH), complex I (C1), complex III (C3), complex IV (C4), F<sub>1</sub>F<sub>0</sub>ATPase (F1F0), proton leak (H<sup>+</sup> leak), adenine nucleotide transporter (ANT), Pi-H<sup>+</sup> co-transporter (PiHt), K<sup>+</sup> - H<sup>+</sup> exchanger (KHt), adenylate kinase (AK), creatine kinase (CK), lumped cellular ATPase fluxes (ATPase), ubiquinone (Q), ubiquinol (QH<sub>2</sub>), oxidized cytochrome C (cytC Oxid), reduced cytochrome C (cytC Red), adenosine diphosphate (ADP), inorganic phosphate (Pi), adenosine triphosphate (ATP), nicotinamide adenine dinucleotide (NAD), reduced nicotinamide adenine dinucleotide, adenosine monophosphate (AMP)

### Model description

A detailed biophysical model of mitochondrial oxidative ADP phosphorylation previously described by Wu et al. (16) was used as the basis for the present computational study. The model distinguished three cellular compartments: mitochondrial matrix, mitochondrial inter membrane space and cell cytoplasm. A schematic representation of the model is provided in Figure 1.

Model parameterization was updated according to the results presented in chapter 4: dehydrogenase activity ( $X_{DH}$ ), ANT activity ( $X_{ANT}$ ) and ANT parameter ( $\theta$ ) were set to 0.269 mol s<sup>-1</sup> M<sup>-1</sup> (L mito)<sup>-1</sup>, 0.041 mol s<sup>-1</sup> (L mito)<sup>-1</sup> and 1, respectively. In addition, proton leak activity ( $X_{Hle}$ ) was adjusted from 200 mol s<sup>-1</sup> M<sup>-1</sup> mV<sup>-1</sup> (L mito)<sup>-1</sup> to 33 mol s<sup>-1</sup> M<sup>-1</sup> mV<sup>-1</sup> (L mito)<sup>-1</sup>. The rationale behind this adjustment was to decrease the fraction of protons entering the matrix through the leak in resting skeletal muscle (ATPase=0.01mM/s) to values within the range observed experimentally (35-50%) (20). Adjusting the value of  $X_{Hle}$  decreased this fraction from 92% in the original parameterization to 50% according to the new parameterization.

Ordinary differential equations were implemented in Matlab (version 7.5.0; Mathworks, Natick, MA) and numerically solved using ODE15s with relative and absolute tolerance set to  $10^{-8}$  and  $10^{-8}$  respectively. Details of the simulation and parameter estimation protocols are provided in the Appendix.

## RESULTS

### ***Model testing: analysis of model parameterization***

Model predictions of the  $\Delta G_p - J_p$  relation were employed to test the hypothesis that the model harbors all essential control mechanisms, but requires parameter optimization. The experimentally sampled  $\Delta G_p - J_p$  data were identical to the data presented in chapter 4. It was investigated which part of this dataset could be reproduced by the models' original parameterization. Predictions according to the model are shown in Figure 2A (red line). While for ATPase  $> 0.2\text{mM/s}$ , model predictions and experimental data match well, for ATPase  $< 0.2\text{mM/s}$  the results show a clear discrepancy between predictions and data. These results confirmed that the original model failed to adequately describe rest and low exercise conditions.

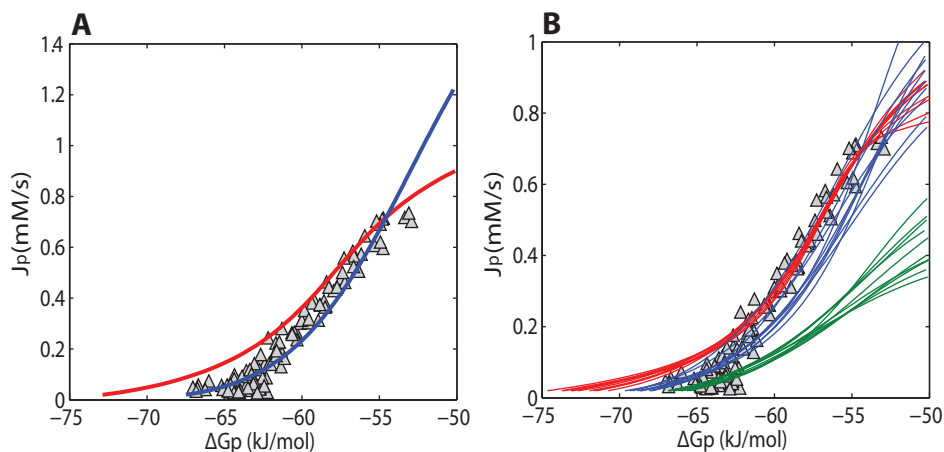


**Figure 2.** Model predictions of the  $\Delta G_p - J_p$  relation according to the initial model parameterization (red line) and after parameter optimization (blue line) (A). (B) shows the results of sampling of the model solution space by a Monte Carlo simulation approach. The 10 simulations with the best fit to all experimental data (blue lines), to high flux data points ( $J_p > 0.4\text{mM/s}$ , red lines) and to low flux data points ( $J_p < 0.1\text{mM/s}$ , green lines) are shown. Experimental data points are indicated by  $\triangle$ .

Next, it was investigated if adjusting the model parameterization could improve model predictions. To this end, two different methods were applied. The first involved application of a parameter estimation algorithm (Levenberg – Marquardt minimization). 27 adjustable parameters were included in this procedure. For more details of the parameter estimation procedure, a description of the parameters and the optimized values, the reader is referred to the Appendix (Table 3). Figure 2A (blue line) shows model predictions vs. experimental data after optimization of parameter values. Although from a purely mathematical point of view these model predictions represent an

improved fit of the model (the sum of squared errors decreased from 4396.5 kJ<sup>2</sup>/mol<sup>2</sup> to 530.3 kJ<sup>2</sup>/mol<sup>2</sup>), additional simulations with the re-parameterized model predicted non – physiological behavior. Specifically, the predicted  $\Delta G_p - J_p$  relation is expected to follow a sigmoidal relation in which the upper asymptote reflects maximal mitochondrial ATP synthetic flux ( $V_{max}$ ) (21,22). Model predictions show that the reparameterized model (Figure 2A, blue line) did not approach an asymptote in the high flux domain, but instead continued to rise. Consequently, the predicted  $V_{max}$  (~2.5 mM/s) significantly overestimated previously reported values, which ranged between 0.62 and 0.83 mM/s (chapter 4). Furthermore, the model failed in predictions of the experimentally observed ADP –  $J_p$  transduction function. For example, the predicted [ADP] at half maximal flux ( $K_{50ADP}$ ), was ~0.2mM, which is about tenfold larger than calculated from the experimentally sampled ADP –  $J_p$  relation (chapter 4). It was also tested if including both the  $\Delta G_p - J_p$  and ADP –  $J_p$  data in the parameter optimization procedure could improve the performance of the model. However, in this case, the transduction function of the reparameterized model became very similar to the initial model and was rejected because it failed to describe rest and low exercise conditions (data not shown). In the previous approach large changes of model parameter values were allowed (Appendix Table 3). As a result of these changes in parameter values non – physiological model behavior was observed. In an attempt to study model predictions which were more constrained to the physiological domain, model behavior was sampled for a large number of parameter sets around the initial parameterization. A Monte Carlo simulation approach (10,000 simulations) was applied to randomly select parameter values within the range of 0.1 – 2 times the values of the initial model parameterization (uniform distribution). Figure 2B, shows the 10 simulations with the best fit to all experimental data (blue lines), to the high flux data points (ATPase > 0.4mM/s, red lines) and to the low flux data points (ATPase < 0.1mM/s, green lines). These results indicated that the model can either fit the high flux domain experimental data (red lines) or the low flux domain experimental data (green lines), but cannot reproduce all data points with a single set of parameters (blue lines).

On the basis of the results above it was concluded that reparameterization of the model did not suffice to reproduce the experimental data. An alternative explanation would be that the model was lacking essential regulatory control mechanisms. This possibility was investigated in the remainder of the study.

### ***Mathematical analysis of model control points: metabolic control analysis***

A first essential step in testing hypotheses of additional control was to identify the subset of model components that were most likely involved. Metabolic control analysis (MCA) was applied to identify components influencing  $\Delta G_p$  at low flux conditions. MCA has been described in multiple review papers (see e.g., (23)). In brief, MCA is a quantitative framework for relating steady state fluxes or concentrations in a biochemical network to properties (control coefficients) of the networks individual components. The control coefficients reflect the sensitivity of model predictions (steady state flux or concentrations) to a change in the activity ( $V_{max}$ ) of an individual network component. The model parameters that were included in the MCA are listed in the Appendix (Table 4). The list was constructed by selecting all model parameters representing enzyme activities ( $V_{max}$ ). Enzyme activity parameters of creatine kinase, adenylate kinase, the mitochondrial  $K^+/H^+$  exchanger and magnesium binding fluxes were excluded from the analysis since at steady state the fluxes through these enzymes were zero and consequently, control



coefficients could not be calculated. The control coefficients were calculated for resting skeletal muscle (ATP demand: 0.01mM/s (24)) because for this condition model predictions failed most dramatically (Figure 1). In this section only the results relevant for the present investigation are described.

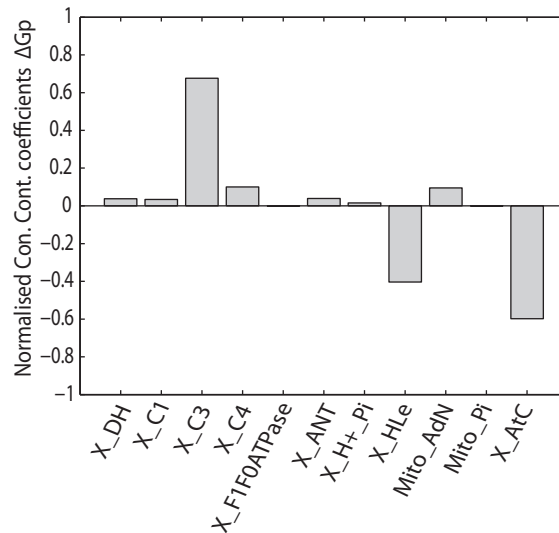


**Figure 3.** Normalized concentration control coefficients for cellular phosphate potential ( $\Delta G_p$ ). Concentration control coefficients were calculated for cellular ATPase rate 0.01mM/s. The model parameters that were included in the MCA are listed in the Appendix (Table 4).

According to the theory of metabolic control analysis, the concentration control coefficients sum to 0 (23). Normalized concentration control coefficients were calculated for  $\Delta G_p$ , Figure 3. The concentration control coefficients were normalized by scaling the sum of positive control coefficients to 1. Consequently, the sum of negative concentration control coefficients summed to -1. The positive concentration control of  $\Delta G_p$  was for 60% located at complex III, whereas the remaining part of the positive control was distributed among the other components of the network. The negative control was shared between proton leak (control coefficient -0.35) and cellular ATP demand (control coefficient -0.65). Complex III, the proton leak and cellular ATP demand were therefore proposed as possible candidates for additional regulation. Additional simulations revealed that by adjusting the proton leak flux it was indeed possible to predict the experimentally observed  $\Delta G_p$  at rest. However, it required increasing the proton leak flux until over 99 percent of all protons entered the matrix through the leak. The physiological range of the proton leak in skeletal muscle is between 35 and 50% (20). Since the proton leak at rest accounted already for 50% of the proton flux into the mitochondrial matrix, this network component was ruled out as a potential site of additional regulation. Simulations also confirmed that by increasing cellular ATP demand it was possible to reproduce the experimentally observed  $\Delta G_p$  at rest (-64 kJ/mol). However, this could only be achieved when the cellular ATP demand at rest was increased 15-fold, from 0.01mM/s to 0.15mM/s. The cellular ATP demand flux in human skeletal muscle at rest has however been measured accurately by a variety of experimental methods (25). The reported values range from 0.002 to 0.02mM/s, median value: 0.01mM/s. Increasing basal ATP demand to 0.15mM/s corresponded to unphysiological conditions. It was therefore chosen to set the basal ATP consumption flux to the experimentally observed value (0.01mM/s). Consequently, in addition to

the proton leak flux, also basal ATP demand flux was ruled out as possible solution for improving model predictions. It was therefore chosen to focus on complex III as the primary site of additional control.

### ***Hypotheses of additional regulation***

The original model provided insufficient control to capture the regulation present in skeletal muscle *in vivo*. In this section two alternative model configurations are defined, according to the two currently leading hypotheses: i.e. (i) substrate feedback regulation (6), and (ii) feed forward activation (parallel activation) mediated by protein phosphorylation (1). For both configurations, complex III was selected as the site of the additional control.

***Substrate feedback regulation*** - The original model already included substrate feedback regulation of the dehydrogenases and complex III, which was described by a phenomenological hyperbolic activation term as a function of matrix Pi concentration. In the new model this term was substituted by a Hill equation which can describe both a hyperbolic relation ( $nH = 1$ ) as well as a sigmoidal relation ( $nH > 1$ ). The Hill equation captured a wider range of regulatory functions and thus a wider range of potential control mechanisms. The new flux equation for complex III was defined as follows:

$$F_{C3} = X_{C3} \left( \frac{[Pi]_x^{nH}}{K_{50Pi}^{nH} + [Pi]_x^{nH}} \right) \left( e^{\frac{-\Delta G_{0,c3} - 4\Delta G_H + 2F\Delta\psi}{2RT}} [cyt(ox)^{3+}]_j [QH_2]_j^{\frac{1}{2}} - [cytC(red)^{2+}]_j [Q]_j^{\frac{1}{2}} \right) \quad (Eq 1)$$

***Feed forward activation (parallel activation)*** - In the feed forward activation model two states of complex III were defined; a phosphorylated active state ( $X_{phos}$ ) and dephosphorylated inactive state ( $X_{dephos}$ ). The flux through these model components (complex III, Eq. 2) was calculated as the weighted sum of the fluxes through the phosphorylated active (weighting parameter  $F_A$ ) and the dephosphorylated inactive states (weighting parameter  $F_{IA}$ ) of complex III. *kineticEq<sub>C3</sub>* denotes the kinetic description of the flux through complex III according to the original model.

$$F_{C3} = F_A X_{phos} \text{kineticEq}_{C3} + F_{IA} X_{dephos} \text{kineticEq}_{C3} \quad (Eq. 2)$$

$$\text{Where, } \text{kineticEq}_{C3} = X_{C3} \left( \frac{1 + \frac{[Pi]_x}{k_{Pi,3}}}{1 + \frac{[Pi]_x}{k_{Pi,4}}} \right) \left( e^{\frac{-\Delta G_{0,c3} - 4\Delta G_H + 2F\Delta\psi}{2RT}} [cyt(ox)^{3+}]_j [QH_2]_j^{\frac{1}{2}} - [cytC(red)^{2+}]_j [Q]_j^{\frac{1}{2}} \right)$$

The activity of the regulatory kinase-phosphatase system controlling the fraction of complex III in the phosphorylated and the dephosphorylated state was modeled with parameters  $K_{on}$  and  $K_{off}$  yielding differential equations Eq. 3 and Eq. 4. According to the parallel activation hypothesis, the equilibrium between the phosphorylated and dephosphorylated states ( $K_{on}/K_{off}$ ) was modeled as a function of cell energy demand. Hereto  $K_{off}$  was described by Eq. 5, in which the energy demand of the cell was expressed by the cytoplasmic ATPase flux  $J_{ATC}$

$$\frac{dF_A}{dt} = -F_A K_{on} + F_{IA} K_{off} \quad (Eq\ 3)$$

$$\frac{dF_{IA}}{dt} = F_A K_{on} - F_{IA} K_{off} \quad (Eq\ 4)$$

$$K_{off} = K'_{off} \frac{J_{AtC}^{nH}}{K_{50AtC}^{nH} + J_{AtC}^{nH}} \quad (Eq\ 5)$$

Newly introduced model parameters were estimated based upon the experimental data of the  $\Delta G_p - J_p$  transduction function recorded in healthy, normally active human subjects (Table 1 and 2). Full details of the parameterization procedure are provided in the Appendix.

**Table 1.** Parameter values model configuration *i*, substrate feedback at complex III

Parameter name	Value (mean +/- SD)	Unit
$X_{CIII}$	54.24 +/- 4.28	$\text{mol s}^{-1} \text{M}^{-3/2} (\text{L mito})^{-1}$
$nH$	4.02 +/- 0.35	unitless
$K_{SOPI}$	6.43 +/- 0.52	mM

**Table 2.** Parameter values model configuration *ii*, parallel activation at complex III

Parameter name	Value (mean +/- SD)	Unit
$X_A$	1.46 +/- 0.21	unitless
$X_{IA}$	0.030 +/- 0.010	unitless
$nH$	1.35 +/- 0.11	unitless
$K_{50AtC}$	0.094 +/- 0.015	$\text{mmol (L cell water)}^{-1} \text{s}^{-1}$
$K_{on}$	0.033 +/- 0.006	$\text{s}^{-1}$
$K_{off}$	52.64 +/- 17.4	$\text{s}^{-1}$

It was tested if the two model configurations could reproduce the  $\Delta G_p - J_p$  relation after parameter optimization. These simulations were run in a Monte Carlo simulation approach to probe the effect of the uncertainty in the newly introduced model parameter values on model predictions. 1000 simulations were run and parameter values were randomly selected from the 95.4% confidence interval (mean $\pm$ 2SD) of normal distributions with mean and SD as reported in Tables 1 and 2. The selected parameters were limited to  $\pm$  2SD to ensure no negative parameter values were drawn. The calculations were performed for both model configurations and results are shown in Figure 4A,B. The solution space of the model was represented by the mean (solid blue line) and standard deviation (dashed blue line) of the 1000 simulations obtained in the Monte Carlo approach. In each sub-figure the simulation of the original model lacking additional regulation is indicated in red. The solution space of the substrate feedback model (configuration *i*) was more constraint compared to the parallel activation model (configuration *ii*), which is probably a result of the smaller number of parameters included in the substrate feedback model configuration. Nevertheless, the mean of the solution space was for both model configurations consistent with the experimentally observed  $\Delta G_p - J_p$  relation.

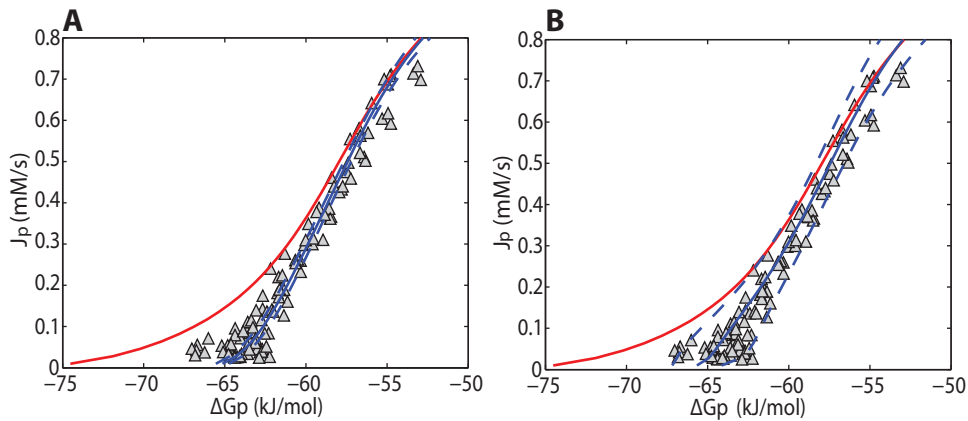


**Figure 4.** Model predictions of the relation between cellular phosphate potential ( $\Delta G_p$ ) and mitochondrial ATP synthetic flux ( $J_p$ ) according to model configuration *i* (metabolic feedback regulation) (**A**), model configuration *ii* (regulation by parallel activation) (**B**). Model predictions are indicated as the mean (solid blue line) and SD (dotted blue line) of the 1000 simulations that were run in a Monte Carlo approach. Predictions of the original model are shown in red. Experimental data points are indicated by  $\triangle$ .

#### **Mitochondrial redox state, inner membrane potential and mitochondrial ADP sensitivity**

Because both model configurations could reproduce the control dataset, it was next investigated if model predictions of important mitochondrial state variables were within physiological range. Figures 5A-D show model predictions of the mitochondrial redox state ( $J_p - \text{NADH/NAD}$ ) and membrane potential ( $J_p - \Delta\Psi$ ) at different cellular ATP demand fluxes. These simulations were also run in a Monte Carlo approach to probe the effect of uncertainty in model parameterization (SD reported in Table 1,2). Results of the original model lacking any additional regulation are indicated in red (Figure 5). Compared to the original model, the newly added regulatory elements decreased the inner membrane potential ( $\Delta\Psi$ ) at low flux conditions. For both model configurations predictions of  $\Delta\Psi$  and NADH/NAD remained within their physiological range (150 - 200mV, 0.3 - 100 respectively). Model predictions of  $J_p - \text{NADH/NAD}$  were very similar for both model configurations (blue) as well as the original model (red). The predictions of  $J_p - \text{NADH/NAD}$  relation are in good correspondence with experimental observations in isolated mitochondria (26). The experimental data indicate an NADH/NAD ratio at State 3 respiration of about 1. NADH/NAD ratio was found to increase at lower ATP turnover fluxes eventually approaching a value of 100 at State 4 respiration. In addition, it was tested if predictions according to the two model configurations reproduced a sigmoidal  $\Delta G_p - J_p$  relation, physiological  $V_{\max}$  value and experimentally observed ADP -  $J_p$  relation. It was concluded that both model configurations successfully reproduced these physiological characteristics and data (data not shown).

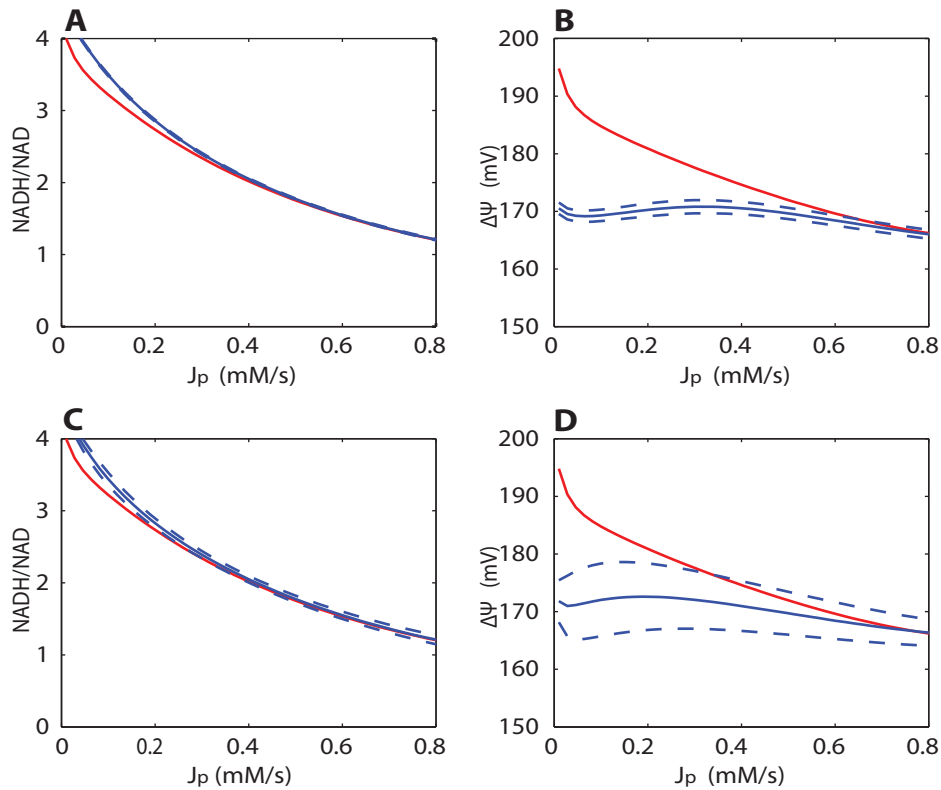


**Figure 5.** Model predictions of mitochondrial redox state (NADH/NAD) and membrane potential ( $\Delta\Psi$ ) at different mitochondrial ATP synthesis rates ( $J_p$ ) according to model configuration *i* (A-B) and model configuration *ii* (C-D). Model predictions are indicated as the mean (solid blue line) and SD (dotted blue line) of the 1000 simulations that were run in a Monte Carlo approach. Predictions of the original model are shown in red.

### Model testing against independent data

Based on predictions of physiological end-points (NADH/NAD,  $\Delta\Psi$ ) it was not possible to discriminate between the model configurations. Furthermore, steady state model predictions of both configurations were consistent with the experimentally observed  $\Delta G_p - J_p$  relation (Figure 4). The experimental data was however recorded during post exercise recovery period. It was therefore also tested if model predictions derived from simulations of post exercise recovery were consistent with the data. In addition, also independent data of athletes and obese sedentary subjects was used. A well known difference in phenotype between these groups is the mitochondrial density in skeletal muscle; the athletes having more mitochondria, the sedentary subjects having less. It was tested if the model could reproduce the data for all these phenotypes by adjusting only the mitochondrial volume density. All other parameters, included the ones of the newly introduced regulatory mechanisms were left unchanged. The results of these simulations are shown in Figure 6A-C. The substrate feedback model (red lines) could reproduce the experimental data for all three phenotypes. In contrast, the parallel activation model (blue lines) could only reproduce the experimental data of the healthy, normally active human subjects and failed in reproducing any of the two independent datasets.

In addition, it was also investigated if the parallel activation model could reproduce the two independent datasets by adjusting its parameterization. In fact, this was indeed possible, but only in the specific cases that parameters  $K_{on}$  and  $K_{off}$  were tuned to make the time constant of deactivation of the mitochondria (transition of phosphorylated, activated complex III into the non-

phosphorylated inactive state,  $A \rightarrow IA$ ) similar to the time constant of metabolic recovery (PCr, Pi recovery). The experimentally observed time constant of metabolic recovery was quantified by a mono-exponential fit to the PCr recovery data. The corresponding time constant was  $82 \pm 6.4s$ ,  $15 \pm 6.5s$  and  $28 \pm 5.4s$  for the sedentary, athletes and healthy control subjects, respectively (mean $\pm$ SD). The predicted time constant of mitochondrial deactivation ( $A \rightarrow IA$ ) was  $29.5s$  (mono-exponential fit), which matches the experimentally observed time constant of metabolic recovery of the healthy control subjects well ( $28 \pm 5.4s$ ). After adjusting the values  $K_{on}$  and  $K_{off}$  to fit the data of sedentary subjects or athletes, the predicted time constant of deactivation was  $91.6s$  and  $14.7s$ , respectively. These values are again similar to the time constant of metabolic recovery measured for these subjects ( $82 \pm 6.4s$  and  $15 \pm 6.5s$ , respectively). It was concluded that the model could only reproduce the  $\Delta G_p - J_p$  relation of a dataset if the time constant of metabolic recovery matched the time constant of deactivation of the mitochondria. However, in these cases, the model failed in reproducing the other two datasets. The substrate feedback model could predict all datasets without re-parameterization of the regulatory mechanism. The substrate feedback model was therefore defined as the most robust and selected as best model configuration and thus the most likely hypothesis.

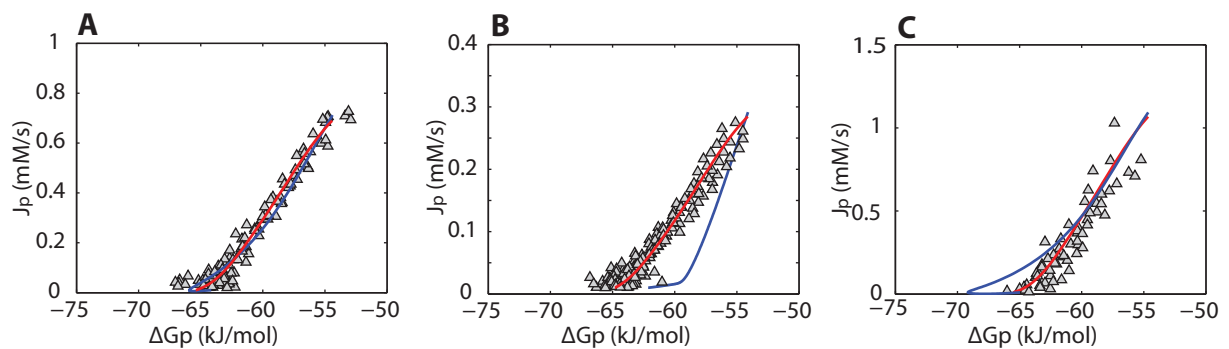


**Figure 6.** Model predictions of the  $\Delta G_p - J_p$  relation during post exercise recovery. Results are shown for normally active healthy subjects (A), sedentary subjects (B), athletes (C). Experimental data are indicated by  $\triangle$ . Model predictions according to the substrate feedback model (model configuration *i*) are indicated by a red line. Model predictions according to the parallel activation model (model configuration *ii*) are indicated by a blue line.

### Model testing against $^{31}P$ MRS observed metabolite recovery dynamics

Model simulations were tested against  $^{31}P$  MRS observed recovery dynamics (PCr, Pi, ATP, pH). For each population (control subjects, athletes, subjects with sedentary lifestyle) an individual dataset was selected. It was necessary to test model simulations against an individual data instead of the mean $\pm$ SD of all recorded data, because these datasets were characterized by differences in end-exercise pH and level of PCr depletion. In Figure 7, model simulations for the original model (red lines), model configuration *i* (blue lines) and model configuration *ii* (green lines) are compared to PCr (open circles), Pi (grey triangles), ATP (closed diamonds), and pH (open diamonds) recovery dynamics. Full details of the simulation protocol are provided in the Appendix. Model predictions according to the original model failed in predicting the correct PCr and Pi levels at fully recovered state for the control subject and the athlete dataset. The parallel activation model (model configuration *ii*) could not reproduce metabolite dynamics for the control subject and the subject with sedentary lifestyle. Remarkably, model configuration *ii* reproduced the  $\Delta G_p - J_p$  relation of the

control data well (Figure 6), but it failed in reproducing the metabolite (PCr, Pi) dynamics of the same dataset (Figure 7). This result is explained by the effect of end - exercise pH. The calculations for the  $\Delta G_p - J_p$  relation were performed for resting pH (7.05) because the relation was insensitive to changes in pH. The calculations of the metabolite dynamics (PCr and Pi recovery) are however sensitive for end - exercise pH, which was therefore taken into account in the simulations. The substrate feedback model (model configuration *i*) could reproduce the dynamics of all datasets. The results show this model configuration can also reproduce the time constant of metabolic (PCr, Pi) recovery for the different datasets. These simulations therefore provide again further evidence that the substrate feedback model is the best model configuration.

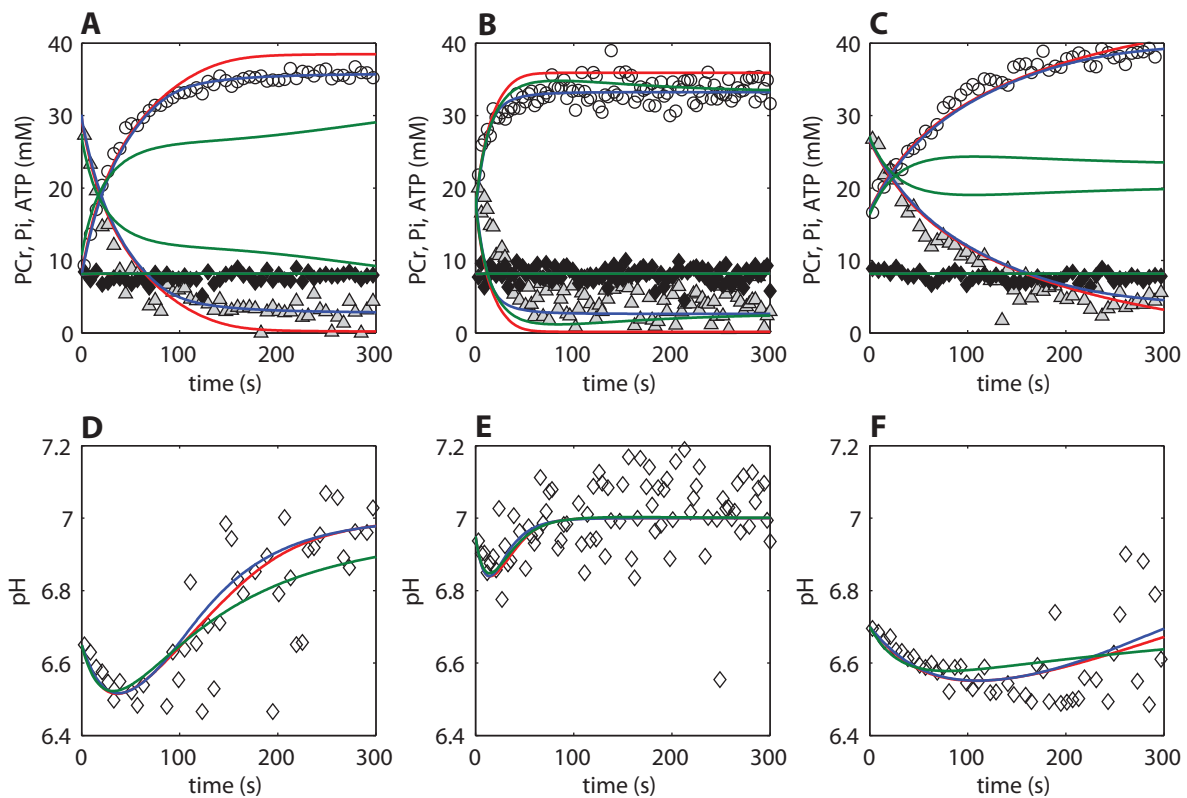


**Figure 7.** Model predictions versus  $^{31}\text{P}$  MRS observed metabolite dynamics during post exercise recovery period. Experimental data and model simulations of a healthy control subject (**A,D**), athlete (**B,E**) and subject with a sedentary lifestyle (**C,F**) are shown. Model simulations according to the original model, model configuration *i* and model configuration *ii* are indicated by red, blue and green lines respectively. Experimental data of PCr, Pi, ATP and pH are indicated by open circles, grey triangles, closed diamonds and open diamonds respectively.

## DISCUSSION

The main result of this investigation was twofold. First, it was identified that the control mechanisms captured by a detailed biophysical model of oxidative phosphorylation in human skeletal muscle could not explain the empirically observed  $\Delta G_p - J_p$  relation, even not after parameter optimization. Second, the results support the hypothesis that substrate feedback control of the respiratory protein complexes plays an important role in the regulation of

mitochondrial ATP synthesis in skeletal muscle by controlling  $\Delta G_p$  at low ATPase rates in muscle. These main results as well as several methodological considerations are discussed.

### ***Methodological considerations***

The computational model that was used as a basis for this investigation builds on a series of previously published models (14,16). A possible concern for applying this model could be the use of a homogenous unit to represent skeletal muscle tissue. It is well known that skeletal muscle is a heterogeneous tissue in which distinct cell types are present (27). These cell types differ in size, force generating capacity, but also mitochondrial density. In the current model this was not taken into account; skeletal muscle tissue was modeled by a single cell in which an averaged mitochondrial density was represented. It was therefore investigated in more detail if this choice affected the study outcome. Three different cells were defined, each with a different mitochondrial density. The mean density was equal to the value used in the single cell model. Predictions of the  $\Delta G_p - J_p$  relation were identical when comparing the average of the three cells and the single cell model. From these results it was concluded that this specific model assumption did not affect the overall outcome of this study.

Another important model assumption was that ATP was produced purely through oxidative processes. This choice was justified by limiting the analyses to data recorded during post exercise recovery period. For this period it is well established that the PCr dynamics reflect almost purely oxidative ATP synthesis (24,28-30).

The current analysis was conducted under the assumption that changes in cellular pH as a result of e.g. lactate acidosis did not significantly affect the  $\Delta G_p - J_p$  relation. This assumption was verified by analysis of the experimental data. The data of healthy normally active subjects was obtained during multiple exercise bouts of varying length and intensity. As a result, the  $\Delta G_p - J_p$  relation was sampled for varying conditions of end - exercise pH. It was investigated if varying conditions of cellular pH influenced the observed  $\Delta G_p - J_p$  relation (data not shown). The results indicated that the  $\Delta G_p - J_p$  relation was insensitive to cellular pH, which validated the model assumption.

The model of oxidative phosphorylation that was chosen as a basis for the analysis was previously derived from a model parameterized based upon data of cardiac mitochondria (14). The conversion to a skeletal muscle model mainly comprised adjusting metabolite pool sizes and structural parameters (e.g., mitochondrial volume percentage). In contrast, the kinetic parameters of oxidative phosphorylation remained unchanged. An assumption underlying these studies therefore is that the parameterization derived from the cardiac mitochondria is also representative for skeletal muscle. The experimental data used to parameterize the original model were taken from Bose et al. (31). Bose et al. also reported that they conducted the experiments with mitochondria collected from skeletal muscle. It was reported that the results of the skeletal muscle mitochondria were very similar to that of cardiac mitochondria. In addition, the assumption is further supported by proteomics studies, which show that cardiac and skeletal muscle mitochondria are very similar (32). Furthermore, it was tested if failure of model predictions at low ATP turnover rates could be a result of one or more of the parameter values to be incorrect for skeletal muscle. Optimizing model parameters could however not solve the problem. Next, the results of the metabolic control analysis were used to investigate which model parameters influenced predictions of  $\Delta G_p$ . These results showed that the majority of the concentration control



was located at complex III. Conversely, they indicated that model predictions were insensitive to changes in other parameters. It was therefore concluded that possible small deviations in parameter values as a result of the cardiac origin of the model did not affect the overall outcome of the study. Nevertheless, these results do not rule out the possibility that in future studies other model predictions actually are sensitive to multiple (other) kinetic parameters. Analysis of the differences in behavior of skeletal muscle and cardiac mitochondria and translation of these differences to models' parameterization may therefore become an important topic of future research.

Some physiological parameters that were not modeled in detail were taken into account in the analysis implicitly. For example, nutrient supply was captured by the lumped dehydrogenase flux ( $X_{DH}$ ) and oxygen availability will affect mitochondrial dynamics through complex IV flux ( $X_{C4}$ ). The control coefficients determined for  $X_{DH}$  and  $X_{C4}$  therefore also implicitly reflect control of these physiological parameters.

The two models used to describe the additional regulation are of phenomenological nature. For testing and evaluating of these concepts the models were found very insightful. However, one should remain careful with the deduction of statements related to the molecular mechanisms of the regulation. For example, although the results clearly indicate the signal modulating respiratory chain activity to be related to cellular substrate levels, it cannot be ruled out that molecular implementation of this regulation involves e.g. protein (de)phosphorylations or other post translational modifications. The results of this study therefore do not contradict with recent evidence of the vast mitochondrial protein phosphorylation network (1).

### ***Regulation of oxidative ATP production in skeletal muscle***

It was concluded that a substrate feedback related control signal provided the best explanation for the additional regulation. The evidence supporting this conclusion was twofold: the model configuration representing the substrate feedback control mechanism could reproduce both the control dataset (healthy volunteers) and the validation datasets (subjects with sedentary lifestyle and track athletes) without re-parameterization, whereas the parallel activation model could not. Secondly, the parallel activation model could reproduce the data of humans with a sedentary lifestyle or track athletes if re-parameterized. However, this occurred only in the specific case that parameter settings caused the time constant of deactivation (transition of phosphorylated, activated complex III into the non-phosphorylated inactive state) to match the time constant of metabolic recovery. This result indicated that the regulatory mechanisms could still involve post translational modifications (e.g. protein phosphorylation) but that the key control signal is probably closely linked to substrate levels (e.g. Pi, ADP, ADP/ATP). In chapter 4 we proposed that the order of the ADP sensitivity provides a tractable validation criterion for evaluation of computational models of oxidative ATP metabolism. Experimentally a second order Hill - coefficient was observed (1.9+/-0.2). Analysis of the computational model revealed that the mitochondrial ultra-sensitivity to ADP was primarily controlled by the kinetic parameters of the adenine nucleotide transporter (ANT). Reformulation of the ANT kinetics increased the Hill - coefficient of the model from 1 to 1.5. Although this was an important step forward, the computational model still underestimated the experimentally observed Hill - coefficient (1.5 vs. 1.9, respectively). It was concluded that the kinetic mechanisms required for the remainder of the difference in Hill - coefficient were not yet included in the model and remained to be identified.

Specifically, multisite Pi activation of the mitochondrial network was ruled out as mechanism because it was already explicitly incorporated in the model. However, in the new model, the Pi activation term of the Complex III flux description was updated. The modification of the Pi activation term could also affect the models corresponding Hill – coefficient. In fact, model simulations revealed that the changes applied in the new model increased the Hill - coefficient to 1.8, which is close to the experimental observations (1.9+/-0.2). On this basis, it was concluded that in addition to the kinetic parameters of ANT, Pi modulation of respiratory chain activity contributes to the model predictions of second order kinetics of mitochondrial sensitivity to ADP.

The regulation of skeletal muscle oxidative ATP metabolism has also been investigated extensively by Korzeniewski and colleagues (see e.g. (33-35)). The model that was developed and updated in these studies overlaps in part with the model used in the current investigation: i.e., part of the models topology and some flux equations and parameter values are identical. Interestingly, the studies by Korzeniewski and colleagues point towards a principal role for parallel activation in the regulation of oxidative phosphorylation in skeletal muscle (35). Although, at first, this result seems conflicting, Korzeniewski and colleagues evaluated many other quantitative but also qualitative characteristics of skeletal muscle energy metabolism (like e.g., PCr overshoot behavior or asymmetry between PCr on - off kinetics). In the present study we focused on <sup>31</sup>P MRS observed metabolite dynamics, and, in particular the  $\Delta G_p - J_p$  relation. Our results however do not rule out the possibility that regulation by parallel activation is essential to explain other characteristics of energy metabolism in muscle. At the moment, these models share the same ANT flux equation. In chapter 4 we concluded that this particular component has a dominant role in controlling the model sensitivity to ADP. Moreover, it was concluded that the  $K_{50ADP}$  (i.e., [ADP] at half maximal velocity) derived from predictions of the ADP –  $J_p$  relation should be decreased about tenfold (from ~0.2mM to 0.021mM) by adjusting ANT parameter  $\theta$  to match the experimentally observed ADP –  $J_p$  relation. Adjusting the ADP sensing of the model increased the models' sensitivity to control by substrate feedback regulation (ADP, Pi). This step in model development provides an explanation for why the current model did not require multi step parallel activation for reproducing the experimentally observed  $\Delta G_p - J_p$  relation.

The physiological implications of the added regulation on e.g., membrane potential and mitochondrial redox state were also explored. The model predicted a decreased inner membrane potential at low flux conditions. For instance, under resting conditions, the membrane potential dropped by 25mV as a result of the added regulation. These predictions may provide a clue about the functionality of the regulation. A high mitochondrial membrane potential is believed to be a major source of cellular ROS production (36) and corresponding cellular damage. There is an increasing amount of evidence that mitochondria regulate membrane potential by e.g., the concentration of uncoupling proteins in the inner membrane (37,38). We speculate that the proposed Pi regulation of respiratory chain activity has a similar function: it prevents high membrane potentials under low flux conditions protecting the cells against excessive ROS production.

### ***Significance and future prospective***

It is concluded that explaining the experimentally observed relation between  $\Delta G_p$  and  $J_p$  in skeletal muscle *in vivo* requires increasing the control of the Pi activation term of complex III in a detailed model of oxidative ATP metabolism. The significance of this result is twofold. First, it provides new

evidence supporting a dominant role for substrate feedback regulation in the control of mitochondrial ATP synthesis in skeletal muscle. Second, the proposed adaptations provide an important step towards developing a computational model of ATP metabolism in skeletal muscle representing *in vivo* conditions. The updated model was shown to reproduce  $^{31}\text{P}$  MRS observed metabolite dynamics throughout the entire dynamical range of ATPase fluxes in skeletal muscle *in vivo*. To the best of our knowledge, this is the first detailed computational model that is quantitatively consistent with  $^{31}\text{P}$  observed metabolite dynamics throughout this full range. Hence, it provides an improved basis for future studies of energy metabolism in muscle. From this viewpoint, application of the model may not remain limited to healthy subjects, but may also include analysis of for example mitochondrial (dys)function related to obesity, type 2 diabetes or aging. Specifically, model simulations can quantify the contribution of changes in specific physiological parameters (e.g., mitochondrial content, enzyme activities) observed in these patients to  $^{31}\text{P}$  MRS recordings of mitochondrial function *in vivo* (time constant of post exercise PCr recovery). This study can test the relevance of the current model for the analysis of metabolic diseases in humans.

## APPENDIX

## Simulation and parameter estimation protocols

**Testing of initial model, Figure 2A**

The  $\Delta G_p - J_p$  relation was calculated from a series of steady state simulations, hereto the ATP consumption in the cytoplasm was incrementally increased (starting value: 0.01mM/s, step size: 0.01mM/s) until the steady state cytoplasmic ADP concentration exceeded a level of 0.1mM. Simulations were run for 10<sup>8</sup>s to ensure a steady state was reached. Next, ATP consumption was decreased to 0.01mM/s in order to simulate post exercise recovery conditions.

Parameter estimation was performed using Matlab routine *lsqnonlin* (Levenberg - Marquardt algorithm) with option *DiffminChange* set to 10<sup>-6</sup>. All other options were set to default values. The error between experimental data and model predictions of steady state behavior as well as post exercise recovery conditions were used as objective function. The parameter estimation procedure was run 100 times, every time randomly perturbing the initial parameter values by +/-10 percent. The model fit with the overall lowest mean squared error was selected as final parameter set (Table 3).

**Table 3.** Adjustable model parameters

Parameter name	Description	Value original model	Value optimized model (Figure 1A)	Unit
$R$	Dehydrogenase parameter	4.559	7.61	unitless
$k_{Pi,1}$	Dehydrogenase parameter	0.1553	0.317	mM
$k_{Pi,2}$	Dehydrogenase parameter	0.8222	3.70	mM
$X_{DH}$	Dehydrogenase activity	0.16	0.735	mol s <sup>-1</sup> M <sup>-1</sup> (L mito) <sup>-1</sup>
$X_{C1}$	Complex I activity	4405	14057	mol s <sup>-1</sup> M <sup>-2</sup> (L mito) <sup>-1</sup>
$X_{C3}$	Complex III activity	4.887	4.10	mol s <sup>-1</sup> M <sup>-3/2</sup> (L mito) <sup>-1</sup>
$k_{Pi,3}$	Complex III parameter	0.3601	0.560	mM
$k_{Pi,4}$	Complex III parameter	5.651	0.334	mM
$X_{C4}$	Complex IV activity	6.766×10 <sup>-5</sup>	10.6×10 <sup>-5</sup>	mol s <sup>-1</sup> M <sup>-1</sup> (L mito) <sup>-1</sup>
$k_{O2}$	Complex IV parameter	0.12	0.11	mM
$X_{F1}$	F <sub>o</sub> F <sub>1</sub> -ATPase activity	1000.0	699.8	mol s <sup>-1</sup> M <sup>-1</sup> (L mito) <sup>-1</sup>
$X_{ANT}$	ANT activity	0.041	0.112	mol s <sup>-1</sup> (L mito) <sup>-1</sup>
$K_{m,ADP}$	Michaelis constant ANT	3.5 ×10 <sup>-3</sup>	13.0×10 <sup>-3</sup>	mM
$k_{PiHt}$	H <sup>+</sup> /Pi <sup>-</sup> cotransporter parameter	0.2542	0.270	mM
$X_{PiHt}$	H <sup>+</sup> /Pi <sup>-</sup> cotransporter activity	3.850 ×10 <sup>-5</sup>	18.9×10 <sup>-5</sup>	mol s <sup>-1</sup> M <sup>-1</sup> (L mito) <sup>-1</sup>
$X_{KH}$	K <sup>+</sup> /H <sup>+</sup> antiporter activity	5.651 ×10 <sup>7</sup>	11.9×10 <sup>7</sup>	mol s <sup>-1</sup> M <sup>-2</sup> (L mito) <sup>-1</sup>
$P_{pi}$	Mitochondrial membrane permeability to inorganic phosphate	327	796.5	μm s <sup>-1</sup>
$P_A$	Mitochondrial outer membrane permeability to nucleotides	85.0	117.2	μm s <sup>-1</sup>
$C_{tot}$	total cytochrom C concentration	2.7	3.97	mmol (L IM water) <sup>-1</sup>
$Q_{tot}$	total ubiquinol concentration - Q+QH2	1.35	1.26	mmol (L matrix water) <sup>-1</sup>
$NAD_{tot}$	total matrix NAD(H) concentration - NAD+NADH	2.97	2.59	mmol (L matrix water) <sup>-1</sup>
$X_{buff}$	matrix buffering coefficient	100	118.64	M <sup>-1</sup>
$K_{DT}$	Mg-ATP binding constant	24×10 <sup>-6</sup>	231.9×10 <sup>-6</sup>	M
$K_{DD}$	Mg-ADP binding constant	347×10 <sup>-6</sup>	309.1×10 <sup>-6</sup>	M
gamma	mito membrane area per cell volume	5.99	15.1	μm <sup>-1</sup>
$\theta$	ANT parameter	1	0.960	unitless
Total matrix ADP+ATP	Total matrix ADP+ATP	10	8.66	mmol (L matrix water) <sup>-1</sup>

**Testing of initial model, Figure 2B**

The  $\Delta G_p - J_p$  relation was calculated as described in 'Testing of initial model, Figure 2A'. 10 000 simulations were performed in a Monte Carlo simulation approach randomly selecting parameter values within the range of 0.1 – 2 times the values of the initial model parameterization. A few parameter sets caused numerical problems when solving the ODE system. These were automatically stopped by the algorithm, excluded from further analyses and substituted by a new simulation. Overall less than 5 percent of the simulations required such substitution. The goodness of fit was quantified by calculating the mean squared error between model simulations and experimental data.

**Metabolic control analysis, Figure 3**

The model parameters included in the metabolic control analysis are listed in Table 4. This list was constructed by selecting all parameters representing enzyme activities ( $V_{max}$ ). Enzyme activity parameters of creatine kinase, adenylate kinase, the mitochondrial  $K^+/H^+$  exchanger and magnesium binding fluxes were excluded from the analysis since at steady state the fluxes through these enzymes were zero and consequently, control coefficients could not be calculated. The flux and concentration control coefficients were calculated for an increase in enzyme activity of one percent.

**Table 4.** Overview of mitochondrial model parameters included in the metabolic control analysis

Parameter name	Description
$X_{DH}$	Dehydrogenase activity
$X_{C1}$	Complex I activity
$X_{C3}$	Complex III activity
$X_{C4}$	Complex IV activity
$X_{F1}$	$F_0F_1$ -ATPase activity
$X_{ANT}$	ANT activity
$X_{PiHt}$	$H^+/Pi^-$ cotransporter activity
$X_{Hle}$	$H^+$ leak activity
$Mito_{Adn}$	Mito. outer membrane permeability to nucleotides
$Mito_{Pi}$	Mito. outer membrane permeability to Pi
$X_{AtC}$	Cytoplasm ATPase activity

Flux control coefficients were calculated according to Eq. 8 (23).  $C_{E_{xase}}^{J_{ydh}}$ ,  $J_{ydh}$  and  $E_{xase}$ , denote the flux control coefficient, a flux through a particular reaction ( $ydh$ ), and an enzyme concentration ( $xase$ ), respectively.

$$C_{E_{xase}}^{J_{ydh}} = \frac{\partial \ln |J_{ydh}|}{\partial \ln E_{xase}} \quad (Eq. 8)$$

Concentration control coefficients were calculated according to Eq. 9 (23).  $C_{E_{xase}}^S$ ,  $S$  and  $E_{xase}$ , denote the concentration control coefficient, the concentration of a particular metabolite, and an enzyme concentration ( $xase$ ), respectively.

$$C_{E_{xase}}^S = \frac{\partial \ln S}{\partial \ln E_{xase}} \quad (Eq. 9)$$

It has been verified that all flux control coefficients summed to 1 and all concentration control coefficients summed to 0.

**Parameter estimation substrate feedback and parallel activation models**

Model parameters were estimated in a two step approach. The first step was selection of initial model parameter values. A wide range of parameter values was explored in a Monte Carlo simulation approach randomly drawing parameter values within selected ranges. For each model configurations, in total, 50 000 simulations were run.

The  $\Delta G_p - J_p$  relation was calculated as described in 'Testing of initial model, Figure 1A'. The set of parameters that yielded the best fit to the experimental  $\Delta G_p - J_p$  relation, quantified by the mean least square error was then selected as starting point for the second step in the parameter estimation procedure. In this next step, model parameter values were optimized by applying a non linear least square optimization algorithm: i.e., Matlab routine *lsqnonlin*

(Levenberg - Marquardt algorithm) with option *DiffminChange* set to  $10^{-6}$ . All other options were set to default values. The error between experimental data and model predictions of steady state behavior as well as post exercise recovery conditions were used as objective function. The optimization algorithm was started 100 times, every time adding +/-25% of random noise to the parameter values obtained in step one. The optimal parameter values obtained in this second step are listed in Tables 1 and 2 as the mean and standard deviation of the 100 optimization runs.

#### **Model testing, Figure 4**

The  $\Delta G_p - J_p$  relation was calculated as described in 'Testing of initial model, Figure 2A'. 1000 simulations were run and parameter values were randomly selected from the 95% confidence interval (mean  $\pm$  2SD) of a normal distributions with mean and SD as reported in Tables 1 and 2. The selected parameters were limited to  $\pm$  2SD, to ensure no negative parameter values were drawn. The solution space of the model was represented by the mean and standard deviation of the 1000 simulations. It was verified that 1000 simulations were enough to obtain a stable solution.

#### **Predictions of mitochondrial redox state and membrane potential, Figure 5**

The relations between mitochondrial redox potential and ATPase rate and membrane potential and ATPase rate were calculated for steady state conditions. Different steady states were obtained by incrementally increasing the cytoplasmic ATPase rate (starting value: 0.01mM/s, step size: 0.01mM/s). Simulations were run for  $10^8$ s to ensure a steady state was reached. The simulations were run in a Monte Carlo simulation approach as described in 'Model testing, Figure 4'.

#### **Model testing, Figure 6**

The  $\Delta G_p - J_p$  relation was calculated for post exercise recovery conditions. The ATP consumption in the cytoplasm was incrementally increased (starting value: 0.01mM/s, step size: 0.01mM/s) until the steady state cytoplasmic ADP concentration exceeded a level of 0.065mM. Simulations were run for  $10^8$ s to ensure a steady state was reached. Next, ATP consumption was decreased to 0.01mM/s in order to simulate post exercise recovery conditions.

The mitochondrial density for simulations of sedentary subjects was set to 0.0235 percent and 0.030 percent for model configuration *i* and *ii*, respectively. The mitochondrial density for simulations of athletes was set to 0.085 percent and 0.080 percent for model configuration *i* and *ii*, respectively.

#### **Prediction of $^{31}P$ observed metabolite dynamics during post – exercise recovery period, Figure 7**

PCr and Pi recovery are sensitive to cellular pH. Simulations of these metabolite dynamics therefore required to take pH dynamics into account. pH was modeled as described by Kemp et al. (39,40), Eq. 10.

$$\frac{dpH}{dt} = \frac{1}{\beta} (\lambda \cdot (7.05 - pH) + (m + \varphi) \cdot J_{CK}) \quad (Eq. 10)$$

$$m = \frac{0.16}{1 + 10^{6.1 - pH}}, \varphi = \frac{1}{1 + 10^{pH - 6.75}}, \beta = buffCap + 2.3 \cdot [Pi] \cdot \varphi \cdot (1 - \varphi)$$

Where,  $\lambda$  denotes the apparent proton efflux rate parameter,  $J_{CK}$  the flux through creatine kinase and *buffCap* the cytosolic buffer capacity (20 slykes (i.e. mmol·L<sup>-1</sup>·pH<sup>-1</sup>)).

The simulations comprised two parts: i.e., initialization and recovery. The mitochondrial volume percent was set to the values also used to determine the  $\Delta G_p - J_p$  in Figure 6. During the initialization of the model the pH was clamped at the experimentally observed end – exercise pH. ATPase demand flux was adjusted to obtain steady state predictions of [PCr] and [Pi] which matched the experimentally observed end – exercise conditions. The steady state values were used as initial conditions of the recovery simulations. During recovery ATPase demand flux was set to resting values (0.01mM/s). pH dynamics were modeled by Eq. 10. The proton efflux parameter,  $\lambda$ , was adjusted to reproduce the experimentally observed pH dynamics. Simulations were performed for the original model and model configuration *i* and *ii* and compared to an individual dataset of a control subject, athlete and subject with sedentary lifestyle. The total creatine concentration was calculated from experimentally observed resting PCr concentration assuming that 15% of the total creatine is unphosphorylated at rest (41).

## REFERENCES

1. **Balaban RS.** Domestication of the cardiac mitochondrion for energy conversion. *J Mol Cell Cardiol* 46: 832-841, 2009
2. **Chance B.** Reaction of oxygen with the respiratory chain in cells and tissues. *J Gen Physiol* 49: Suppl-95, 1965
3. **Balaban RS, Kantor HL, Katz LA and Briggs RW.** Relation between work and phosphate metabolite in the in vivo paced mammalian heart. *Science* 232: 1121-1123, 1986
4. **Balaban RS.** Cardiac energy metabolism homeostasis: role of cytosolic calcium. *J Mol Cell Cardiol* 34: 1259-1271, 2002
5. **Wu F, Zhang EY, Zhang J, Bache RJ and Beard DA.** Phosphate metabolite concentrations and ATP hydrolysis potential in normal and ischaemic hearts. *J Physiol* 586: 4193-4208, 2008
6. **Wu F, Zhang J and Beard DA.** Experimentally observed phenomena on cardiac energetics in heart failure emerge from simulations of cardiac metabolism. *Proc Natl Acad Sci U S A* 106: 7143-7148, 2009
7. **Wust RC, Grassi B, Hogan MC, Howlett RA, Gladden LB and Rossiter HB.** Kinetic control of oxygen consumption during contractions in self-perfused skeletal muscle. *J Physiol* 589: 3995-4009, 2011
8. **Balaban RS.** The mitochondrial proteome: a dynamic functional program in tissues and disease states. *Environ Mol Mutagen* 51: 352-359, 2010
9. **Balaban RS.** Modeling mitochondrial function. *Am J Physiol Cell Physiol* 291: C1107-C1113, 2006
10. **Kitano H.** Systems biology: a brief overview. *Science* 295: 1662-1664, 2002
11. **Beard DA, Bassingthwaite JB and Greene AS.** Computational modeling of physiological systems. *Physiological Genomics* 23: 1-3, 2005
12. **Kitano H.** Computational systems biology. *Nature* 420: 206-210, 2002
13. **Prompers JJ, Jeneson JA, Drost MR, Oomens CC, Strijkers GJ and Nicolay K.** Dynamic MRS and MRI of skeletal muscle function and biomechanics. *NMR Biomed* 19: 927-953, 2006
14. **Beard DA.** A biophysical model of the mitochondrial respiratory system and oxidative phosphorylation. *PLoS Comput Biol* 1: e36, 2005
15. **Jeneson JA, Ter VF, Schmitz JP, Meyer RA, Hilbers PA and Nicolay K.** Similar mitochondrial activation kinetics in wild-type and creatine kinase-deficient fast-twitch muscle indicate significant Pi control of respiration. *Am J Physiol Regul Integr Comp Physiol* 300: R1316-R1325, 2011
16. **Wu F, Jeneson JA and Beard DA.** Oxidative ATP synthesis in skeletal muscle is controlled by substrate feedback. *Am J Physiol Cell Physiol* 292: C115-C124, 2007
17. **De Feyter HM, van den Broek NM, Praet SF, Nicolay K, van Loon LJ and Prompers JJ.** Early or advanced stage type 2 diabetes is not accompanied by in vivo skeletal muscle mitochondrial dysfunction. *Eur J Endocrinol* 158: 643-653, 2008
18. **Praet SF, De Feyter HM, Jonkers RA, Nicolay K, van PC, Kuipers H, van Loon LJ and Prompers JJ.** 31P MR spectroscopy and in vitro markers of oxidative capacity in type 2 diabetes patients. *MAGMA* 19: 321-331, 2006
19. **Jeneson JA, Schmitz JP, Hilbers PA and Nicolay K.** An MR-compatible bicycle ergometer for in-magnet whole-body human exercise testing. *Magn Reson Med* 63: 257-261, 2010
20. **Brand MD.** The efficiency and plasticity of mitochondrial energy transduction. *Biochem Soc Trans* 33: 897-904, 2005
21. **Jeneson JA, Westerhoff HV, Brown TR, Van Echteld CJ and Berger R.** Quasi-linear relationship between Gibbs free energy of ATP hydrolysis and power output in human forearm muscle. *Am J Physiol* 268: C1474-C1484, 1995
22. **Westerhoff HV, Van Echteld CJ and Jeneson JA.** On the expected relationship between Gibbs energy of ATP hydrolysis and muscle performance. *Biophys Chem* 54: 137-142, 1995
23. **Fell DA.** Metabolic control analysis: a survey of its theoretical and experimental development. *Biochem J* 286 ( Pt 2): 313-330, 1992
24. **Blei ML, Conley KE and Kushmerick MJ.** Separate Measures of Atp Utilization and Recovery in Human Skeletal-Muscle. *Journal of Physiology-London* 465: 203-222, 1993
25. **Kemp GJ.** The interpretation of abnormal 31P magnetic resonance saturation transfer measurements of Pi/ATP exchange in insulin-resistant skeletal muscle. *Am J Physiol Endocrinol Metab* 294: E640-E642, 2008
26. **Mayevsky A, Chance B.** Oxidation-reduction states of NADH in vivo: from animals to clinical use. *Mitochondrion* 7: 330-339, 2007
27. **Bottinelli R, Reggiani C.** Human skeletal muscle fibres: molecular and functional diversity. *Prog Biophys Mol Biol* 73: 195-262, 2000
28. **Conley KE, Blei ML, Richards TL, Kushmerick MJ and Jubrias SA.** Activation of glycolysis in human muscle in vivo. *Am J Physiol* 273: C306-C315, 1997
29. **Crowther GJ, Kemper WF, Carey MF and Conley KE.** Control of glycolysis in contracting skeletal muscle. II. Turning it off. *Am J Physiol Endocrinol Metab* 282: E74-E79, 2002
30. **Quistorff B, Johansen L and Sahlin K.** Absence of phosphocreatine resynthesis in human calf muscle during ischaemic recovery. *Biochem J* 291 ( Pt 3): 681-686, 1993
31. **Bose S, French S, Evans FJ, Joubert F and Balaban RS.** Metabolic network control of oxidative phosphorylation: multiple roles of inorganic phosphate. *J Biol Chem* 278: 39155-39165, 2003
32. **Benard G, Faustin B, Passerieux E, Galinier A, Rocher C, Bellance N, Delage JP, Casteilla L, Letellier T and Rossignol R.** Physiological diversity of mitochondrial oxidative phosphorylation. *Am J Physiol Cell Physiol* 291: C1172-C1182, 2006
33. **Korzeniewski B.** Regulation of ATP supply in mammalian skeletal muscle during resting state-->intensive work transition. *Biophys Chem* 83: 19-34, 2000
34. **Korzeniewski B.** Regulation of oxidative phosphorylation in different muscles and various experimental conditions. *Biochem J* 375: 799-804, 2003
35. **Korzeniewski B.** Regulation of oxidative phosphorylation through parallel activation. *Biophys Chem* 129: 93-110, 2007

36. **Poyton RO, Ball KA and Castello PR.** Mitochondrial generation of free radicals and hypoxic signaling. *Trends Endocrinol Metab* 20: 332-340, 2009
37. **Azzu V, Parker N and Brand MD.** High membrane potential promotes alkenal-induced mitochondrial uncoupling and influences adenine nucleotide translocase conformation. *Biochem J* 413: 323-332, 2008
38. **Azzu V, Brand MD.** The on-off switches of the mitochondrial uncoupling proteins. *Trends Biochem Sci* 35: 298-307, 2010
39. **Kemp GJ, Taylor DJ, Styles P and Radda GK.** The production, buffering and efflux of protons in human skeletal muscle during exercise and recovery. *NMR Biomed* 6: 73-83, 1993
40. **Kemp GJ, Thompson CH, Taylor DJ and Radda GK.** Proton efflux in human skeletal muscle during recovery from exercise. *Eur J Appl Physiol Occup Physiol* 76: 462-471, 1997
41. **Boska M.** ATP production rates as a function of force level in the human gastrocnemius/soleus using <sup>31</sup>P MRS. *Magn Reson Med* 32: 1-10, 1994





# Chapter 6

## *Mitochondrial function in skeletal muscle: Numerical dissection of a multi – factorial process*

Adapted from:

J.P.J. Schmitz, J.A.L. Jeneson, J.J. Prompers, K. Nicolay, P.A.J. Hilbers, N.A.W. van Riel,  
*Mitochondrial function in skeletal muscle: Numerical dissection of a multi– factorial process*  
(submitted)

## ABSTRACT

A decreased mitochondrial function is associated with many different diseases or aging. For design of therapies it is essential to understand which factors contribute to the decreased oxidative capacity *in vivo*. At the moment, this information cannot be obtained from *in vivo* methods. Analysis of muscle biopsy samples allows identifying changes in muscle physiology. It remains however very challenging to relate these *in vitro* observed changes to the functioning of the systems *in vivo*. We propose to apply mechanistic mathematical modeling to connect these *in vitro* measures of oxidative capacity to *in vivo* mitochondrial function. To this end, first our previously developed model of skeletal muscle bioenergetics was extended from a single-fiber to a three-fiber model (type I, IIA, IIX). In addition, several essential model verification tests were conducted. It was shown that: (i) the model could reproduce the effect of progressive inhibition of individual OXPHOS components on mitochondrial respiration rate, (ii) the three cell model could reproduce the ADP- $J_p$  and  $\Delta G_p$ - $J_p$  mitochondrial input - output functions, (iii) the mechanistic model reproduced the PCr recovery time course data just as accurate as the current gold-standard, i.e., the mono-exponential function. Subsequently, as a case study, the model was applied to investigate to which extent different adaptations in muscle physiology contributed to a decreased mitochondrial function documented for type 2 diabetes patients with a sedentary lifestyle compared to healthy lean control subjects. These results were used to outline a possible strategy for applying the mechanistic models in future studies of mitochondrial (dys)function.

## INTRODUCTION

Skeletal muscle mass represents about 30 – 40 percent of the human body weight (1). This tissue is a major site for carbohydrate and fatty acid utilization. As such, it plays a significant role in whole body metabolism. Within skeletal muscle cells the majority of the processes involved in the conversion of carbohydrates and fatty acids to energy accessible by other cellular processes occur in mitochondria. Normal function of mitochondria is essential for a healthy metabolism. Conversely, a decreased mitochondrial function has been associated with many diseases, like e.g., mitochondrial myopathies (2), chronic heart failure (3), type 2 diabetes (4) or the aging process (5). For design of therapies it is essential to understand which factors (e.g., a reduced mitochondrial density, change in muscle fiber type composition, altered mitochondrial protein content or an intrinsic dysfunction) contribute to the decreased oxidative capacity *in vivo*.

*In vivo* mitochondrial function can be measured non – invasively by  $^{31}\text{P}$  magnetic resonance spectroscopy (MRS) (6). During exercise phosphocreatine (PCr) and ADP are converted into creatine (Cr) and ATP in order to balance ATP demand and supply fluxes. During recovery following exercise, the PCr pool is resynthesized almost purely oxidatively (7-10). The rate of PCr recovery therefore reflects *in vivo* mitochondrial function (6). Although  $^{31}\text{P}$  MRS provides a measure of the functioning of the intact system under physiological conditions, the origin of a delayed PCr recovery cannot be deduced from these data. A prolonged PCr recovery time can originate from several factors, for example, a reduced mitochondrial density, change in muscle fiber type composition, altered mitochondrial protein content or an intrinsic dysfunction (i.e. a lower mitochondrial ATP synthesis flux per mitochondrion). Therefore, sometimes, additional analyses of muscle biopsy samples are performed to identify changes in muscle physiology that are possible responsible for the decreased mitochondrial function (see: e.g. (11,12)). It remains however very difficult to determine the contribution of these changes to the functioning of mitochondria *in vivo*. Moreover, often, multiple changes are observed. As a result, identifying the factors responsible for the changed mitochondrial function *in vivo* requires dissecting a multi-factorial process.

The main difficulty for relating *in vivo* and *in vitro* measures of mitochondrial capacity is that it requires taking into account the regulation and functioning of a complex molecular interaction network present in the mitochondria. A possible strategy to overcome this problem is to develop mechanistic mathematical models that capture the key complexity of the molecular interaction network. Subsequently, model simulations provide a means to explore how changes observed at the molecular level influence predictions of the functioning of the mitochondria as observed *in vivo*. In chapters 4 and 5 we demonstrated that our current model has advanced to the point it can reproduce the mitochondrial input – output relations ( $\text{ADP} - J_p$  and  $\Delta G_p - J_p$ ) that characterize the regulation of mitochondria *in vivo*. This model represents a single (uniform-type) muscle fiber. It is however well known that skeletal muscle tissue contains distinct fiber types with different oxidative capacities (6.0, 4.5 and 2.3 volume percent for type I, IIA and IIX fibers respectively (13)). A change in muscle fiber composition can therefore also affect the *in vivo* measured mitochondrial capacity. In addition, predictions of the inhibition of individual OXPHOS components (intrinsic mitochondrial dysfunction) on the rate of respiration are not yet verified.

Thus, before the model can be applied for relating *in vivo* and *in vitro* measures of oxidative capacity it is important to include the fiber-type heterogeneity in the model and conduct additional model verification tests. To this end, the mathematical framework was extended from a

uniform-fiber model to a three-fiber model (type I, IIA, IIX). In addition several key model verification experiments were conducted: (i) model predictions of progressive inhibition of individual OXPHOS components on the rate of respiration were tested; (ii) predictions of the three-fiber model were compared to previously recorded mitochondrial input – output relations (chapter 4 and 5); (iii) the accuracy of the mechanistic model for reproducing PCr recovery kinetics was compared to the current gold-standard for analysis of these data, i.e., fitting of a mono-exponential function.

The second part of the chapter describes a case study to illustrate how the validated model can be applied to study changed mitochondrial function in skeletal muscle. Hereto, we selected an intensively studied population with a decreased mitochondrial function, i.e., the comparison of healthy lean control subjects and type 2 diabetes patients (see e.g. review: (14)). Changes in muscle physiology that were proposed to underlie the *in vivo* observed decreased mitochondrial capacity were obtained from literature and translated to the mathematical model by adjusting the corresponding model parameters. Next, model simulations were compared to experimentally determined PCr recovery halftimes in type 2 diabetes patients to quantitatively evaluate the contribution of different factors to the decreased mitochondrial capacity *in vivo*. These analyses revealed that the model could reproduce the prolonged PCr recovery period observed in these patients based on changes in *in vitro* markers of mitochondrial function. These results were used to outline a strategy for applying the mechanistic models in future studies of mitochondrial (dys)function in skeletal muscle.

## METHODS

### **Description cell model**

The computational model of skeletal muscle oxidative ATP metabolism that was used as a basis for this study was described in (15) and updated according to modifications proposed in chapters 4 and 5. A schematic representation of the model is provided in Figure 1A. The model contains a detailed biophysical description of the electron transport chain, oxidative phosphorylation, adenine nucleotides and Pi transport across the mitochondrial membranes and cellular ATP buffering (creatine kinase and adenylate kinase). pH dynamics during post exercise recovery were modeled (Eq. 1) as described by Kemp et al. (16,17).

$$\frac{dpH}{dt} = \frac{1}{\beta} (\lambda \cdot (7.05 - pH) + (m + \varphi) \cdot J_{CK}), \text{ and}$$

$$m = \frac{0.16}{1 + 10^{6.1 - pH}}, \varphi = \frac{1}{1 + 10^{pH - 6.75}}, \beta = buffCap + 2.3 \cdot [Pi] \cdot \varphi \cdot (1 - \varphi) \quad (\text{Eq. 1})$$

Where,  $\lambda$  denotes the apparent proton efflux rate parameter,  $J_{CK}$  the flux through creatine kinase and  $buffCap$  the cytosolic buffer capacity (20 slykes (i.e.,  $\text{mmol} \cdot \text{L}^{-1} \cdot \text{pH}^{-1}$ )).

A new parameter ( $MitoV_{max}$ ) was introduced to adjust the apparent mitochondrial  $V_{max}$  while keeping all other parameter values fixed. To this end, all flux descriptions of the mitochondrial part of the model were multiplied by  $MitoV_{max}$ . This parameter allowed accounting for small subject

specific differences in the mitochondrial capacity by scaling all mitochondrial fluxes (see Table 4). The model was implemented in Matlab 7.5.0 (The Mathworks, Natick, MA, USA). Ordinary differential equations were solved numerically by using ODE15s with absolute and relative tolerances set to  $10^{-8}$ .

### Description three-fiber model

Metabolite dynamics of the three fiber model were calculated as the weighted average of three cell models (Eq. 2), each representing a specific fiber type: i.e., type I, IIA and IIX respectively. A schematic representation of the three-fiber model is provided in Figure 1B.

$$M_{average} = X_{typeI} \cdot M_{typeI} + X_{typeIIA} \cdot M_{typeIIA} + X_{typeIIX} \cdot M_{typeIIX} \quad (Eq. 2)$$

Where,  $X_{typeI}$ ,  $X_{typeIIA}$ ,  $X_{typeIIX}$  denote the fraction of the muscle composed of type I, type IIA and type IIX cells respectively.  $M_{typeI}$ ,  $M_{typeIIA}$ ,  $M_{typeIIX}$  denote the dynamics of a metabolite according to the fiber type specific model.

The values of for  $X_{typeI}$ ,  $X_{typeIIA}$ ,  $X_{typeIIX}$  were set according to experimental data obtained for human vastus lateralis (18) (0.5, 0.4 and 0.1, respectively). The three fiber type specific models were defined by a set of fiber type specific parameters, Table 1. In chapter 5 we reported that model predictions of the Pi concentration at rest are determined by Pi activation of the respiratory chain. To predict the fiber type specific Pi concentration listed in Table 1, the complex III parameter  $K_{50Pi}$  was set to 4.0mM for slow (type I) and 11.0mM for fast twitch (type IIA, IIX) fibers.

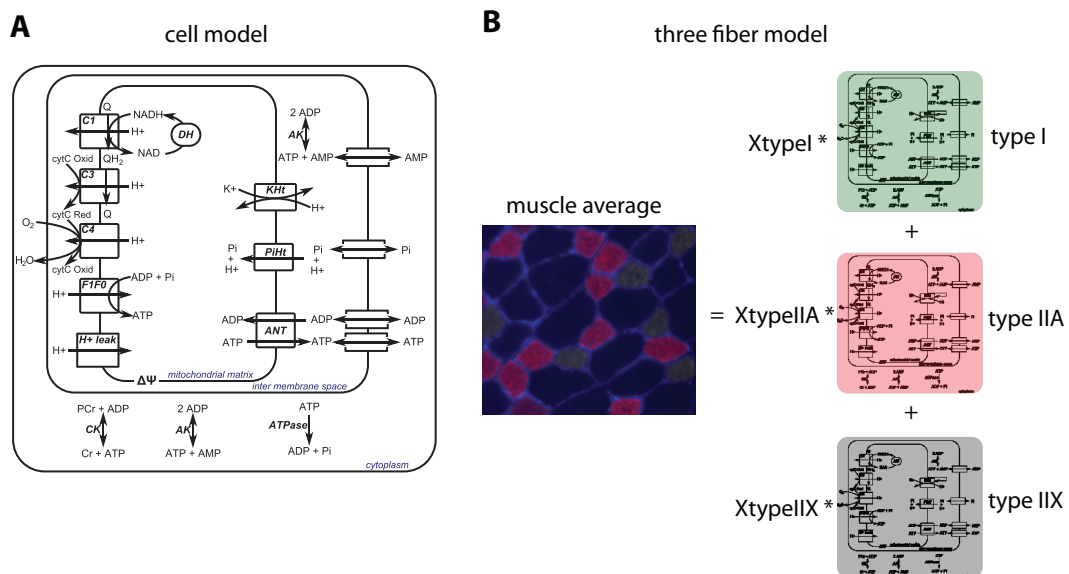


**Figure 1.** Schematic representation of the cell model (A) and three fiber model (B) of skeletal muscle energetics. Abbreviations denote: dehydrogenases (DH), complex I (C1), complex III (C3), complex IV (C4), F<sub>1</sub>F<sub>0</sub>ATPase (F1F0), proton leak (H<sup>+</sup> leak), adenine nucleotide transporter (ANT), Pi-H<sup>+</sup> transporter (PiHt), K<sup>+</sup> - H<sup>+</sup> transport (KHt), adenylate kinase (AK), creatine kinase (CK), lumped cellular ATPase fluxes (ATPase), ubiquinone (Q), ubiquinol (QH<sub>2</sub>), oxidized cytochrome C (cytC Oxid), reduced cytochrome C (cytC Red), adenosine diphosphate (ADP), inorganic phosphate (Pi), adenosine triphosphate (ATP), nicotinamide adenine dinucleotide (NAD), reduced nicotinamide adenine dinucleotide (NADH), adenosine monophosphate (AMP).

**Table 1.** Fiber type specific parameter values

Parameter	Type I	Type IIA	Type IIX	References
Mitochondrial volume percentage	6.0%	4.5%	2.3%	(19)
[PCr] rest	$(PCr_{average}) \times 0.9$	$(PCr_{average}) \times 1.1$	$(PCr_{average}) \times 1.1$	(20,21)
[Cr] total	$[PCr_{typeI}]rest / 0.85$	$[PCr_{typeIIA}]rest / 0.85$	$[PCr_{typeIIX}]rest / 0.85$	(22)
[Pi] rest	4mM	2mM	2mM	(13)
Contribution to muscle average	50%	40%	10%	(18,23)

### Parameter estimation

The models' parameterization was left unchanged except for the parameters listed in Table 2 and the newly introduced parameter  $MitoV_{max}$ . The rationale for re-estimating these parameter values was to improve the flux control exerted by the individual steps in the model; increasing the  $V_{max}$  value decreases the flux control, decreasing the  $V_{max}$  value increases the flux control. These parameters were re-estimated on the basis of the experimentally sampled relation between individual enzyme inhibition and the maximal rate of respiration (state 3 respiration) reported by Lettelier et al. (24). The newly introduced parameter  $MitoV_{max}$  could not be optimized on the inhibition - respiration curves because these data were normalized. Therefore the data sampling the transduction function between  $ADP - J_p$  and  $\Delta G_p - J_p$  were used to estimate  $MitoV_{max}$ . These data were identical to the data presented in chapters 4 and 5.

Details of the simulation protocols used to reproduce these experimental observed relations are described in the Appendix. The parameter values (Table 2) were optimized by applying a non linear parameter optimization algorithm implemented in Matlab (*Isqnonlin*), using manually pre-tuned values as initial conditions. *Isqnonlin* options *TolFun* and *TolX* were set to  $10^{-6}$ , all other options were set to default values. The difference between model simulations and experimental data was used as objective function.

**Table 2.** Re-estimated parameter values

Parameter	Description	Value	Unit
$X_{C1}$	Complex I activity	671.7	$\text{mol s}^{-1} \text{M}^{-2} (\text{L mito})^{-1}$
$X_{C3}$	Complex III activity	254.7	$\text{mol s}^{-1} \text{M}^{-3/2} (\text{L mito})^{-1}$
$X_{C4}$	Complex IV activity	$1.23 \times 10^{-5}$	$\text{mol s}^{-1} \text{M}^{-1} (\text{L mito})^{-1}$
$X_{F1F0}$	F1F0ATPase activity	2.0	$\text{mol s}^{-1} \text{M}^{-1} (\text{L mito})^{-1}$
$X_{ANT}$	ANT activity	0.097	$\text{mol s}^{-1} (\text{L mito})^{-1}$
$X_{PiTransporter}$	Pi - H+ cotransport activity	$1.76 \times 10^6$	$\text{mol s}^{-1} \text{M}^{-1} (\text{L mito})^{-1}$
$X_A$	Permeability of mitochondrial outer membrane to nucleotides	506.3	$\mu\text{m s}^{-1}$
$X_{Pi}$	Permeability of mitochondrial outer membrane to Pi	840.3	$\mu\text{m s}^{-1}$
$V_{maxmito}$	Mitochondrial $V_{max}$ scaling parameter	0.50	Unitless

### Model predictions of prolonged PCr recovery in T2D patients

It was investigated if the prolonged PCr recovery period in T2D patients could be predicted by adjusting model parameters according to experimental data obtained from the analyses of muscle biopsy samples. The model of oxidative ATP metabolism in healthy lean control subjects was used as a basis for these simulations. Model parameters  $MitoV_{max}$  and  $\lambda$  were set to the mean of the 6 subject specific values (Table 4): i.e., 0.50 and  $0.50 \text{mM s}^{-1} (\text{U pH})^{-1}$ , respectively. Available data was translated into three different hypotheses of the mechanisms underlying the prolonged PCr recovery period in type 2 diabetes patients: *i* shift in muscle fiber type composition, *ii* decreased mitochondrial content in all muscle cell types and *iii* decreased mitochondrial content in

combination with a decreased intrinsic mitochondrial function due to a decreased capacity of the ETC and TCA. These hypotheses were in good accordance with recent review papers (e.g.: (14,25-27)).

Each hypothesis was translated to the model by adjusting parameter values as listed in Table 3. For each parameter a range of values was defined, which reflected the variation in results of different studies. The shift in muscle fiber type (hypothesis *i*) was based on data of (28-30). The fiber type shift was implemented according to the relation:  $Percentage_{typeI}=50\%-X$ ,  $Percentage_{typeIIA}=40\%+\frac{1}{2}X$ ,  $Percentage_{typeIIX}=10\%+\frac{1}{2}X$ , in which  $X$  denotes a value between 0 and 20%. The decrease in mitochondrial content in all muscle cells (hypothesis *ii*) was implemented by multiplying the mitochondrial volume percentage with a factor between 0.65 and 0.73, which corresponds to observations of (31-33). The additional decrease in capacity of TCA cycle + ETC (hypothesis *iii*) was implemented by multiplying dehydrogenase, complex I, complex III and complex IV activities ( $X_{DH}$ ,  $X_{C1}$ ,  $X_{CIII}$ ,  $X_{IV}$ , respectively) by a factor between 0.45 and 0.90 (31,32).

Model simulations of PCr recovery kinetics were performed as described in the Appendix (section: *PCr recovery kinetic in individual fiber types*). The only difference was that according to the experimental studies with diabetes patients (11,34-36), cellular pH and the level of PCr depletion was set to 7.05 and 30%, respectively. The rate of PCr recovery was quantified similar to the experimental studies, i.e. by fitting of a mono exponential function. A Monte Carlo simulation approach was applied to sample the range of parameter values: simulations were performed 100 times, each time randomly drawing parameter values from a uniform distribution with boundaries set according to ranges defined in Table 3. The results were presented as a scatter plot of all individual simulation results as well as the mean PCr recovery halftime calculated from the ensemble. Comparison of predictions of PCr recovery halftimes with experimental observations in T2D patients were used to test each hypothesis.

**Table 3.** Parameter settings for quantitative hypotheses testing

<b>Hypothesis <i>i</i></b>		
<b>Parameter</b>	<b>Range</b>	<b>References</b>
Percentage type I muscle cells	50 - 30%*	(28-30)
Percentage type IIA muscle cells	40 - 50%*	(28-30)
Percentage type IIX muscle cells	10 - 20%*	(28-30)
<b>Hypothesis <i>ii</i></b>		
<b>Parameter</b>	<b>Range</b>	<b>References</b>
Mitochondrial content	65 - 73 % of reference model (healthy conditions)	(31-33)
<b>Hypothesis <i>iii</i></b>		
<b>Parameter</b>	<b>Range</b>	<b>References</b>
Mitochondrial content	65 - 73 % of reference model (healthy conditions)	(31-33)
Capacity of TCA cycle and ETC <sup>#</sup>	40 - 90 % of reference model (healthy conditions)	(31,32)

<sup>#</sup>the decreased capacity of TCA and ETC was implemented by decreasing the  $X_{DH}$ ,  $X_{C1}$ ,  $X_{C3}$  and  $X_{C4}$  according to the listed values.

\* The first numbers of the range represent the healthy condition; parameter values were constraint according to the relation:  $Percentage_{typeI} = 50\% - X$ ,  $Percentage_{typeIIA} = 40\% + \frac{1}{2}X$ ,  $Percentage_{typeIIX} = 10\% + \frac{1}{2}X$ , in which  $X$  denotes a percentage between 0 and 20%



## RESULTS

### Model verification

Model simulations of enzyme inhibition – respiration curves according to the parameter values listed in Table 1 and experimental data obtained from (24) are shown in Figure 2A-F. Inhibition - respiration curves are shown for complex I (A), complex III (B), complex IV (C),  $F_1F_0$ ATPase (D), ANT (E) and phosphate carrier (F). These results demonstrate that the single cell model is consistent with these experimental data thereby providing important verification of the distribution of the flux control exerted by different steps in the single cell model. In previous studies, the relation between  $[ADP] - J_p$  ( $dPCr/dt$ ) and  $\Delta G_p - J_p$  ( $dPCr/dt$ ) were used as important physiological endpoints for testing the *in vivo* relevance of the single-fiber model (chapters 4 and 5). It was investigated if the new multi - fiber model could still reproduce these datasets, Figure 3. The present results show that although predictions of individual fiber type kinetics are clearly distinct, the calculated muscle average matches well with the experimental data. These results therefore confirmed that after updating the model parameterization according to values listed in Table 1 and extension of the model from a uniform-fiber to a three-fiber model, the predictions of these transduction functions remained consistent with these *in vivo* data.

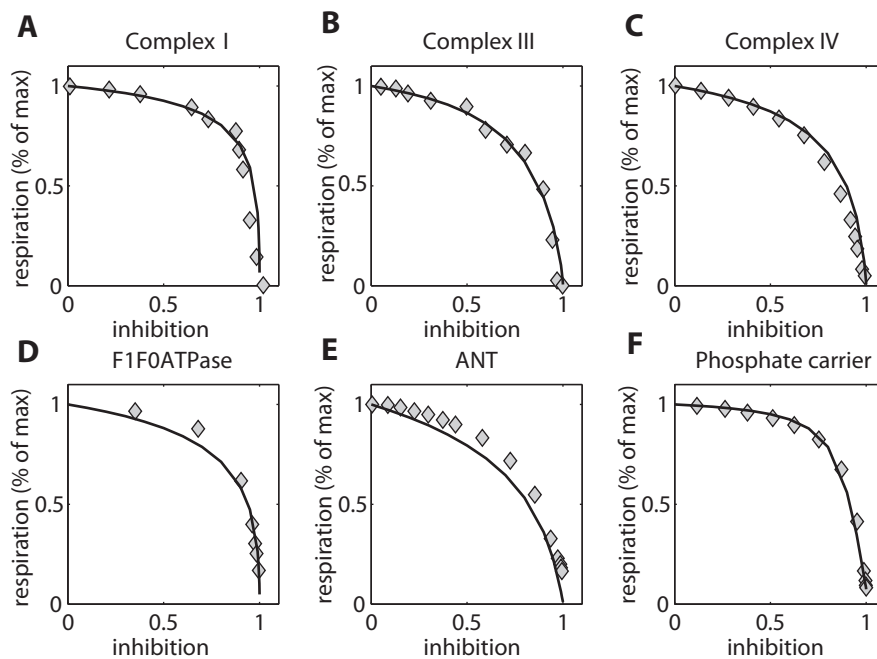


**Figure 2.** Predictions (black lines) of the relation between enzyme inhibition and state 3 respiration compared to experimental data (grey diamonds). Inhibition – respiration curves are shown for specific inhibition of complex I (A), complex III (B), complex IV (C),  $F_1F_0$ ATPase (D), ANT (E) and the phosphate carrier (F). Experimental data was obtained from Lettelier et al. (24).

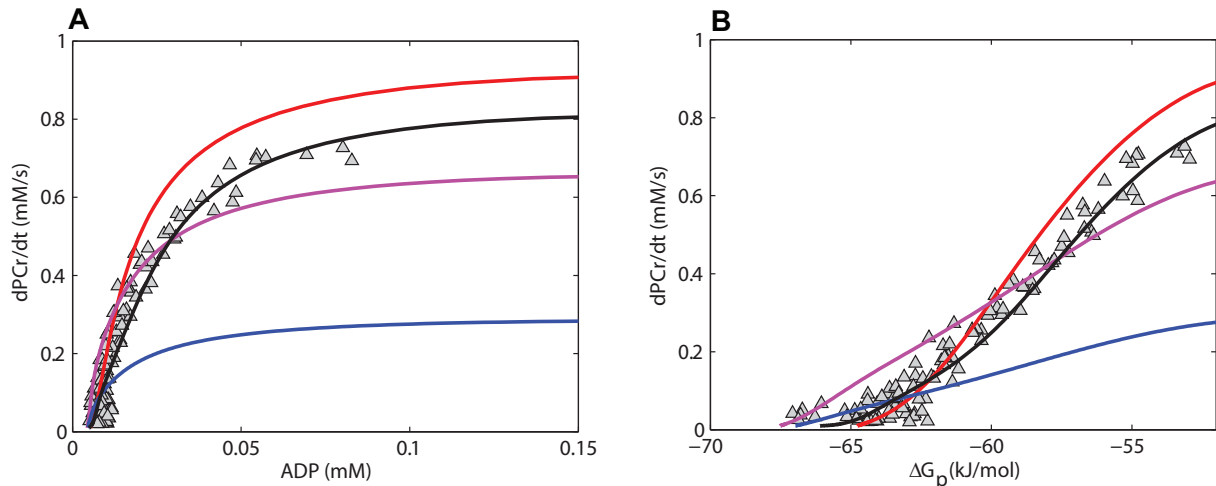


**Figure 3.** Predictions of ADP –  $J_p$  (A) and  $\Delta G_p$  –  $J_p$  (B) transduction functions compared to experimental data. Dynamics of type I, type IIA and type IIX muscle fibers are indicated by red, magenta and blue lines respectively. The calculated muscle average is indicated by a black line. Experimental data (grey diamonds) were identical to the data presented in chapters 4 and 5

### **Predictions of PCr recovery kinetics in healthy lean control subjects**

Simulations were run to test if the biophysical model could reproduce the PCr recovery kinetics dynamics recorded in vastus lateralis of healthy human subjects (chapter 4). Simulations were compared to data of six individual subjects. For each subject multiple (8 - 12) experiments were available (with varying end exercise [PCr] and pH). The performance of the model was evaluated by comparing simulation results to the gold-standard for the analysis of PCr recovery kinetics: i.e., fitting of a mono – exponential function. In Table 4 the goodness of fit ( $R^2$ ) is listed for both the biophysical model and the mono-exponential function. These results demonstrate that the biophysical model accurately reproduced the time course data ( $R^2$  is very close to 1 for all datasets), similar to the golden – standard method. Figure 4 shows a typical example of model predictions vs. data of an individual subject. These results show that the predicted individual fiber type dynamics (type I, red; type IIA, magenta; type IIX, blue) are different from the experimentally observed kinetics. In contrast, the weighted average of the individual fiber types (black lines) matches well with the experimental data. The PCr recovery halftime predicted by the biophysical model was compared to the halftime obtained by fitting of a mono-exponential function, Figure 5. These results further confirmed that the model can reproduce PCr recovery halftimes throughout the investigated range of end exercise PCr depletion (32 - 77%) and pH (6.6 – 7.0).

**Table 4.** Goodness of fit biophysical model and mono exponential model.

Subject	$V_{\max\text{mito}}$ (unitless)	$\lambda$ ( $\text{mM s}^{-1} (\text{U pH})^{-1}$ )	$R^2$ biophysical model	$R^2$ mono exponential function
1	0.50	0.38	0.99+/-0.0044	0.99 +/- 0.0039
2	0.53	0.42	0.99 +/- 0.0051	0.99 +/- 0.0055
3	0.50	0.47	0.99 +/- 0.0049	0.99+/-0.0048
4	0.53	0.75	0.98 +/- 0.0084	0.99+/-0.0089
5	0.50	0.51	0.97+/-0.024	0.98+/-0.023
6	0.43	0.33	0.99+/-0.0040	0.99+/-0.0033
<b>Mean +/- SD</b>	0.50+/-0.037	0.50+/-0.15		

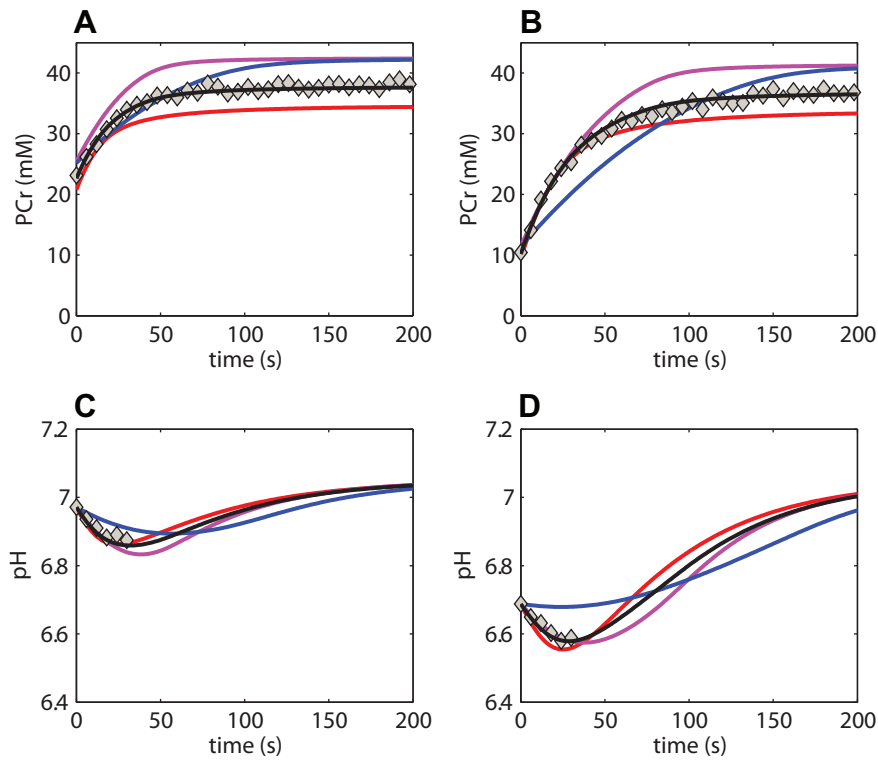


**Figure 4.** Example of predicted PCr and pH recovery dynamics. Results of an individual subject (subject 2) are provided for conditions of a relative small (**A** and **C**) and high (**B** and **D**) degree of PCr depletion. Experimental data are indicated by grey triangles. Predicted dynamics of fiber type I, IIA and IIX are indicated by red, magenta and blue lines, respectively. The calculated muscle average is indicated by a black line.

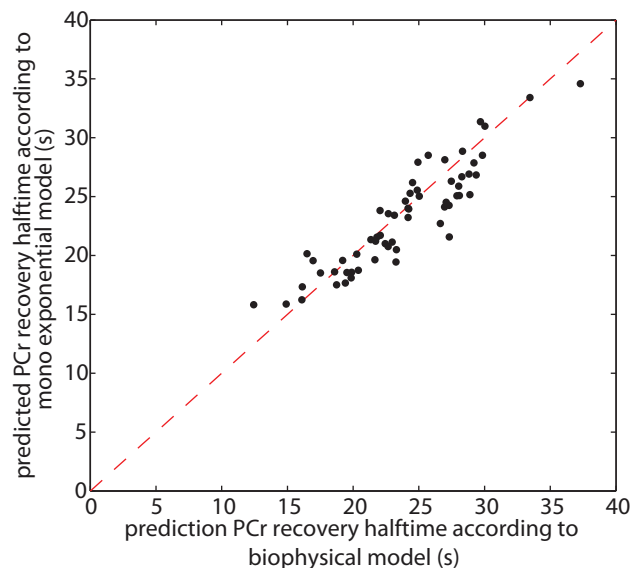


**Figure 5.** Predicted PCr recovery halftime according to biophysical model compared to the PCr recovery halftime determined by fitting of a mono-exponential function. Data points were obtained from simulations of 6 individual subjects. For each subject multiple datasets (8 - 12) were available with varying end exercise PCr depletion (32 - 77%) and pH (6.6 - 7.0). The dotted line represents the  $x = y$  diagonal.

### Predictions of prolonged PCr recovery period in T2D patients

Available data obtained from the analyses of muscle biopsy samples was summarized by three hypotheses of mechanisms underlying the prolonged PCr recovery in T2D patients. Each hypothesis was incorporated in the model by adjusting model parameterization as listed in Table 3. Model predictions of the effect of these parameter changes on predicted PCr recovery halftime were used to test these hypotheses against PCr recovery halftimes observed in obese T2D patients, Figure 6. The error bars of the experimental observations indicate the SEM reported in these studies. The dotted line indicates predicted PCr recovery halftime of healthy lean control subjects (16.6s). 100 model simulations were run in a Monte Carlo simulation approach randomly drawing parameter values from uniform distributions with upper and lower boundaries set to the values listed in Table 3. Each simulation result is shown as individual points. In addition, the mean PCr recovery halftime of the ensemble was calculated and is indicated by a black line. These results reveal that hypothesis *i* (shift in muscle fiber type) even in an extreme case (-20% type I, + 10% type IIA, +10% type IIX) can explain only part of the increase in PCr halftime. In contrast, hypothesis *ii* (~30% decrease in mitochondrial content) is quantitatively consistent with the studies reporting a relative mild decrease in mitochondrial capacity (PCr recovery halftimes < 24s) (11,35). The estimate of PCr half-time corresponding to hypothesis *iii* (~30% decrease in mitochondrial content + 10 - 65% decrease in ETC + TCA cycle capacity) is in good accordance with studies reporting the most severe decrease in mitochondrial capacity (PCr recovery halftimes > 24s) (34,36).

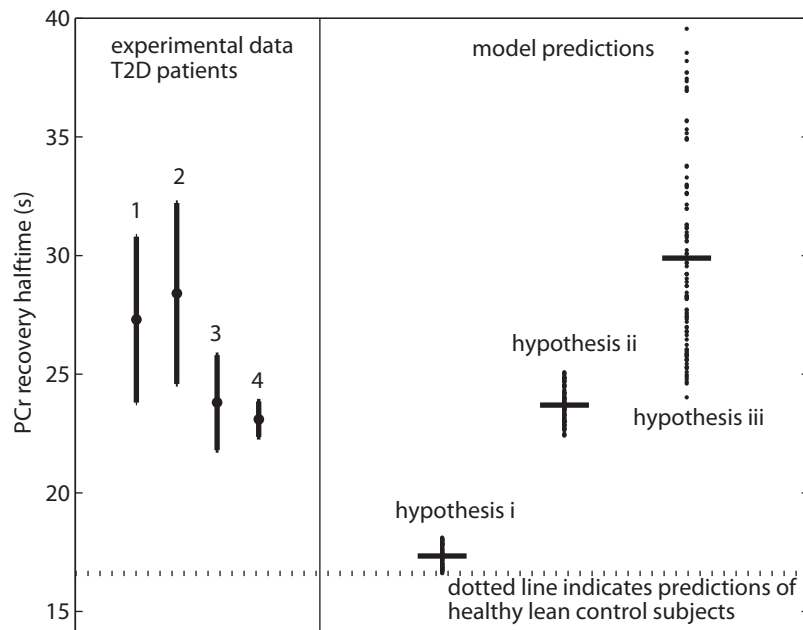


**Figure 6.** Experimental observations of prolonged PCr recovery in type 2 diabetes patients compared to predictions according to different hypotheses. The mean  $\pm$  SEM of the PCr halftime reported by: 1.) Schrauwen – Hinderling et al. (36), 2.) de Feyter et al. (34), 3.) Phielix et al. (11) and 4.) Meex et al. (35) are shown. PCr halftime representing healthy conditions (16.6s) is indicated by a dotted line. Predictions according to hypothesis *i* (shift in fiber type composition), *ii* (decrease in mitochondrial content) and *iii* (decrease in mitochondrial content + decrease in enzyme activity of ETC and TCA) are represented by individual results of the simulations run in a Monte Carlo simulation approach (black dots) as well as the mean of the ensemble (black line).

## DISCUSSION

In this chapter two main results are presented. First, the mathematical model of oxidative ATP metabolism in skeletal muscle was further improved and extended from a uniform-fiber model to a three-fiber model. Second, the model was applied for the analyses of literature data of type 2 diabetes patients to illustrate the potential of its application in future studies of mitochondrial (dys)function in skeletal muscle.

### ***Methodological considerations***

We propose to apply a biophysical model to relate *in vitro* markers of oxidative capacity to measurements of mitochondrial function *in vivo*, i.e., PCr recovery kinetics. In order to enhance the significance of these model predictions, first, several key verification test of the model were performed. It was shown that the model is consistent with experimental data on the effect of inhibition of key steps in the mitochondrial pathway on overall rate of respiration (Figure 2). The rate of respiration is closely linked to the rate of mitochondrial ATP production and thus also to the time constant of PCr recovery. Therefore, these results enhance the significance of predictions of a change in  $V_{\max}$  of individual model components or a subset of components (e.g. decrease in ETC capacity according to hypothesis *iii*) on the PCr recovery time constant. In addition, the model was shown to reproduce PCr recovery dynamics of lean healthy subjects over a range of end-exercise PCr and pH levels, (Table 3, Figure 3, 4 and 5) as well as  $\Delta G_p - J_p$  and  $[ADP] - J_p$  transduction functions. On this basis it was concluded that the model represents oxidative ATP metabolism in skeletal muscle of healthy lean subjects well and can act as a reference for evaluating the effect of changes in oxidative ATP metabolism in other patient or subjects groups (e.g. T2D) compared to healthy lean control subjects.

Some aspects of muscle physiology were not included in the model. For example, regulation by calcium signaling was not considered, because it was previously concluded that this regulation has not a dominant role in the control of  $^{31}\text{P}$  MRS observed metabolite dynamics (Pi, PCr, ATP) in skeletal muscle *in vivo* (chapters 4 and 5). In addition, in the current model ATP production by glycolysis was not included. The rationale behind this choice was that the analysis was limited to post exercise PCr recovery dynamics, for which it is well established that these dynamics almost purely reflect oxidative ATP synthesis (7,8,10). In addition, oxygen supply to muscle cells was not modelled in detail. Instead, the present analyses were performed under the assumption that oxygen supply was not limiting (37).

### ***Predictions of individual fiber type dynamics***

The multi - fiber model predicted metabolite dynamics in individual fiber types. The significance of these predictions is enhanced by the lack of robust experimental methods to determine individual fiber type kinetics in human quadriceps muscle. Non - invasive methods like  $^{31}\text{P}$  MRS are limited to recordings of metabolite dynamics averaged over all muscle cell types. Dissection and analysis of single muscle fibers from biopsy samples obtained at multiple time points provides an alternative (21,38). However, this invasive method has a low time resolution and, due to the complex assay, available data are sparse and characterized by a relative large coefficient of variation (21,38). In good accordance with the qualitative trends observed from these data, the predicted rate of PCr recovery was fastest in type I and slowest in type IIX fibers, with type IIA fibers being intermediate

(Figure 4). In addition, model predictions provided new insight in the behavior of individual fibers. For example, the predicted  $\Delta G_p - J_p$  relation was clearly distinct between fibers: type I fibers followed a sigmoidal relation, whereas for type IIA and IIX fibers a linear trend was observed.

### ***Numerical analyses of mitochondrial function***

We proposed that the mathematical model can be used as a tool for future studies of mitochondrial function in skeletal muscle. To illustrate this concept, data comparing type 2 diabetes patients and healthy lean control subjects were analyzed. The rationale for selecting these two populations is that already a large database of experimental studies comparing these populations is available in literature (see e.g., review (14)). It is however important to note that the reported differences between healthy lean control subjects and obese T2D patients are not necessarily related to insulin resistance of the muscle cells, but represent the combined effect of the difference in age, BMI, lifestyle and insulin sensitivity. The current study therefore provides no answers to the question if the decrease in mitochondrial function in these patients is (partly) caused by insulin resistance (11,35,36) or is a result of the age and sedentary lifestyle of the patients (34). Nevertheless, it still provides a relevant case for illustrating the potential of mathematical modeling for analyses of this type of data.

To the best of our knowledge the hypotheses represented by the three model configurations represent the corollary of available data well and are in good accordance with recent review papers (14,25-27). Multiple studies reported a fiber type shift with a general trend towards less oxidative fiber types (28,30,39,40), but, a similar number of studies reported no effect (29,41-43). Our analysis shows that even for an extreme case of fiber type shift only a part (<50%) of the prolonged rate of PCr recovery can be explained. In the other two hypotheses the fiber type shift was not included. These hypotheses were based on the data obtained from muscle homogenates which represent an average of all muscle fibers. The decrease in mitochondrial content considered in hypotheses *ii* and *iii* can thus still be a result of a fiber type shift, a decrease in mitochondrial content per fiber type or a combination of both. The calculations for hypotheses *ii* and *iii* show that each is consistent with part of the experimentally observed range of PCr recovery halftime (range: 23.1 - 28.4s). It was calculated that a ~30% decrease in mitochondrial content is sufficient to explain a prolongation of PCr recovery halftime up to 24s (11,35). However, for the studies reporting cases of even more severe mitochondrial dysfunction (PCr recovery halftime > 24s) (34,36) additional factors are likely to be involved. The calculations revealed that for these cases a ~30% decrease in mitochondrial content is most likely also accompanied by an additional 10 - 60% decrease in TCA cycle and ETC capacity. These results illustrate how model predictions can provide quantitative insight in effect of the changes in muscle physiology on functioning of the mitochondria observed *in vivo*.

### ***Significance and future perspective***

It was concluded that the novel three-fiber model of oxidative ATP metabolism could accurately reproduce measurements of the influence of inhibition of individual steps in oxidative phosphorylation on the rate of oxygen consumption,  $\Delta G_p - J_p$  and  $[ADP] - J_p$  transduction functions recorded *in vivo* and PCr recovery kinetics. These successful model verification experiments significantly improved the basis of the model for application in future studies. Developing and applying mathematical models has been considered an essential step for obtaining a thorough

understanding of biological systems. The extension and validation of the model obtained in this study therefore contribute to the ongoing effort of obtaining a 'systems - level' understanding of the regulation and functioning of energy metabolism in health and disease. In addition, application of the algorithm on literature data of type 2 diabetes patients illustrated how such model can be applied to analyze the contribution of different factors to the functioning of the mitochondria as observed *in vivo*. For this specific case study, the input data was obtained by integration of data from different studies. A next step for testing the model and approach will be to acquire all necessary data (*in vivo* + *in vitro*) in a single study and subsequently apply the model to analyze these data. Such a combined experimental and computational study is essential to further confirm the generic value of the approach.

## APPENDIX

### *Simulation protocols*

#### **Enzyme inhibition - respiration curves**

Enzyme inhibition - respiration curves were obtained from Lettelier et al. (24). Details on the experimental protocols are described elsewhere (24). In brief, mitochondria were isolated from rat skeletal muscle. Maximal mitochondrial respiration rate (State 3 respiration) was obtained by addition of 10mM Pi, 2mM ADP and 10mM pyruvate + 10 mM malate as oxidizable substrates. Progressive inhibition of specific steps in the mitochondrial oxidative phosphorylation pathway was induced by rotenone (complex I), antimycin (complex III), KCN (complex IV), carboxyatractylate (ANT), mersalyl (phosphate carrier) and oligomycin (ATP synthase).

Simulations of the enzyme inhibition – respiration relations were performed with the single-cell model. Simulations of state 3 respiration were performed by setting  $V_{max}$  parameters of cytoplasmic enzymes which were removed in the isolation procedure to zero (creatine kinase, adenylate kinase and ATPase). Initial metabolite concentrations were set according to experimental conditions: Pi 10mM; adenine nucleotides (AMP, ADP, ATP) in cytoplasm and inter membrane space 0mM. Model simulations were run until steady state was reached (1000s). Subsequently, state 3 respiration experiments were simulated by increasing the cytoplasmic ADP concentration to 2mM and continuing the simulation for 180s. State 3 respiration was defined as the maximal rate of  $O_2$  consumption following the addition of ADP.

Enzyme inhibition respiration curves for specific steps in the mitochondrial pathway were calculated by running multiple state 3 respiration experiments while progressively decreasing the  $V_{max}$  value of the specific process.

#### **PCr recovery dynamics**

Experimental data of PCr recovery dynamics of individual subjects ( $n=6$ ) were recorded in the study described in chapter 4. Each subject participated in multiple (8 - 12) rest – exercise – recovery experiments with varying end-exercise PCr and pH levels. The PCr and pH recovery dynamics were used for model testing.

The PCr recovery simulations were performed with the three-cell model. The simulation protocol consisted of two steps. First, initial conditions for the simulations of the post exercise recovery dynamics were determined. Hereto pH was clamped at the experimentally observed end-exercise value. Next, ATPase rate was progressively increased until predicted steady state [PCr] matched the experimentally observed value. Subsequently metabolic recovery was simulated. To this end, cellular ATPase demand was decreased to resting values (0.01mM/s (7)) and the pH clamp was removed. The end exercise pH was assumed similar for the three fiber types. This assumption was supported by the narrow peak width of the Pi resonance in the  $^{31}P$  spectra obtained at the end of exercise. The percentage of end – exercise PCr depletion was assumed similar for all fiber types. This assumption corresponds to a recruitment scheme of ballistic contractions. Although any heterogeneity in PCr concentration between muscle fibers certainly cannot be ruled out, it was found that this assumption allowed reproducing PCr recovery times constants for the entire range (32 – 77%) of investigated PCr depletion levels (see Figure 3). Therefore, in retrospect, it was concluded that this assumption did not conflict with available data. These simulations were performed for individual subjects. To account for differences in oxidative capacity and apparent proton efflux between subjects  $MitoV_{max}$  and  $\lambda$  were optimized based on the PCr and pH recovery dynamics (optimized parameter values provided in Table 3). The pH data included in the parameter estimation procedure was limited to the first 5 points during recovery. The rationale for this choice was that during the remainder of the recovery period the Pi resonance became difficult to distinguish from the noise and consequently yielded inaccurate and unreliable pH estimates.

#### **ADP - $J_p$ and $\Delta G_p$ - $J_p$ transduction functions**

The transduction functions between cellular ADP concentration and the mitochondrial ATP synthesis flux ( $ADP - J_p$ ) and cellular phosphate potential and the mitochondrial ATP synthesis flux ( $\Delta G_p - J_p$ ) characterize the regulation of mitochondrial flux ( $J_p$ ) *in vivo* (chapter 4). Experimental data sampling these transduction functions was identical to the data presented in chapter 4. Simulations of these transduction functions were performed with the three – fiber model. To sample the entire flux range, model predictions of the transduction functions were derived from simulations of an intense exercise protocol (end – exercise ADP = 0.15mM and pH = 6.7). Simulations were performed as described in section: 'PCr recovery dynamics'. Predictions of metabolic recovery were used to reconstruct the transduction functions.



Mitochondrial ATP synthetic rate ( $J_p$ ) was calculated from derivative of PCr dynamics ( $dPCr/dt$ ).  $\Delta G_p$  was calculated according to Eq. 3.

$$\Delta G_p = \Delta G_p^{\circ'} + RT \ln([ADP][P_i]/[ATP]) \quad (\text{Eq. 3})$$

Where,  $\Delta G_p^{\circ'}$  is -31.8kJ/mol at 37°C.

## REFERENCES

1. **Janssen I, Heymsfield SB, Wang ZM and Ross R.** Skeletal muscle mass and distribution in 468 men and women aged 18-88 yr. *J Appl Physiol* 89: 81-88, 2000
2. **Wallace DC.** Mitochondrial diseases in man and mouse. *Science* 283: 1482-1488, 1999
3. **Drexler H, Riede U, Munzel T, Konig H, Funke E and Just H.** Alterations of skeletal muscle in chronic heart failure. *Circulation* 85: 1751-1759, 1992
4. **Lowell BB, Shulman GI.** Mitochondrial dysfunction and type 2 diabetes. *Science* 307: 384-387, 2005
5. **Trounce I, Byrne E and Marzuki S.** Decline in skeletal muscle mitochondrial respiratory chain function: possible factor in ageing. *Lancet* 1: 637-639, 1989
6. **Prompers JJ, Jeneson JA, Drost MR, Oomens CC, Strijkers GJ and Nicolay K.** Dynamic MRS and MRI of skeletal muscle function and biomechanics. *NMR Biomed* 19: 927-953, 2006
7. **Blei ML, Conley KE and Kushmerick MJ.** Separate measures of ATP utilization and recovery in human skeletal muscle. *J Physiol* 465: 203-222, 1993
8. **Conley KE, Blei ML, Richards TL, Kushmerick MJ and Jubrias SA.** Activation of glycolysis in human muscle in vivo. *Am J Physiol* 273: C306-C315, 1997
9. **Dawson MJ, Gadian DG and Wilkie DR.** Studies of the biochemistry of contracting and relaxing muscle by the use of <sup>31</sup>P n.m.r. in conjunction with other techniques. *Philos Trans R Soc Lond B Biol Sci* 289: 445-455, 1980
10. **Quistorff B, Johansen L and Sahlin K.** Absence of phosphocreatine resynthesis in human calf muscle during ischaemic recovery. *Biochem J* 291 ( Pt 3): 681-686, 1993
11. **Phielix E, Schrauwen-Hinderling VB, Mensink M, Lenaers E, Meex R, Hoeks J, Kooi ME, Moonen-Kornips E, Sels JP, Hesselink MK et al..** Lower intrinsic ADP-stimulated mitochondrial respiration underlies in vivo mitochondrial dysfunction in muscle of male type 2 diabetic patients. *Diabetes* 57: 2943-2949, 2008
12. **Praet SF, De Feyter HM, Jonkers RA, Nicolay K, van PC, Kuipers H, van Loon LJ and Prompers JJ.** <sup>31</sup>P MR spectroscopy and in vitro markers of oxidative capacity in type 2 diabetes patients. *MAGMA* 19: 321-331, 2006
13. **Bottinelli R, Reggiani C.** Human skeletal muscle fibres: molecular and functional diversity. *Prog Biophys Mol Biol* 73: 195-262, 2000
14. **Rabol R, Boushel R and Dela F.** Mitochondrial oxidative function and type 2 diabetes. *Appl Physiol Nutr Metab* 31: 675-683, 2006
15. **Wu F, Jeneson JA and Beard DA.** Oxidative ATP synthesis in skeletal muscle is controlled by substrate feedback. *Am J Physiol Cell Physiol* 292: C115-C124, 2007
16. **Kemp GJ, Taylor DJ, Styles P and Radda GK.** The production, buffering and efflux of protons in human skeletal muscle during exercise and recovery. *NMR Biomed* 6: 73-83, 1993
17. **Kemp GJ, Thompson CH, Taylor DJ and Radda GK.** Proton efflux in human skeletal muscle during recovery from exercise. *Eur J Appl Physiol Occup Physiol* 76: 462-471, 1997
18. **Staron RS, Hagerman FC, Hikida RS, Murray TF, Hostler DP, Crill MT, Ragg KE and Toma K.** Fiber type composition of the vastus lateralis muscle of young men and women. *J Histochem Cytochem* 48: 623-629, 2000
19. **Howald H, Hoppeler H, Claassen H, Mathieu O and Straub R.** Influences of endurance training on the ultrastructural composition of the different muscle fiber types in humans. *Pflugers Arch* 403: 369-376, 1985
20. **Sahlin K, Soderlund K, Tonkonogi M and Hiraoka K.** Phosphocreatine content in single fibers of human muscle after sustained submaximal exercise. *Am J Physiol* 273: C172-C178, 1997
21. **Soderlund K, Hultman E.** ATP and phosphocreatine changes in single human muscle fibers after intense electrical stimulation. *Am J Physiol* 261: E737-E741, 1991
22. **Boska M.** ATP production rates as a function of force level in the human gastrocnemius/soleus using <sup>31</sup>P MRS. *Magn Reson Med* 32: 1-10, 1994
23. **Travnik L, Pernus F and Erzen I.** Histochemical and morphometric characteristics of the normal human vastus medialis longus and vastus medialis obliquus muscles. *J Anat* 187 ( Pt 2): 403-411, 1995
24. **Letellier T, Malgat M and Mazat JP.** Control of oxidative phosphorylation in rat muscle mitochondria: implications for mitochondrial myopathies. *Biochim Biophys Acta* 1141: 58-64, 1993
25. **Dumas JF, Simard G, Flamment M, Ducluzeau PH and Ritz P.** Is skeletal muscle mitochondrial dysfunction a cause or an indirect consequence of insulin resistance in humans? *Diabetes Metab* 35: 159-167, 2009
26. **Phielix E, Mensink M.** Type 2 diabetes mellitus and skeletal muscle metabolic function. *Physiol Behav* 94: 252-258, 2008
27. **Schrauwen-Hinderling VB, Roden M, Kooi ME, Hesselink MK and Schrauwen P.** Muscular mitochondrial dysfunction and type 2 diabetes mellitus. *Curr Opin Clin Nutr Metab Care* 10: 698-703, 2007
28. **Gaster M, Staehr P, Beck-Nielsen H, Schroder HD and Handberg A.** GLUT4 is reduced in slow muscle fibers of type 2 diabetic patients: is insulin resistance in type 2 diabetes a slow, type 1 fiber disease? *Diabetes* 50: 1324-1329, 2001
29. **He J, Watkins S and Kelley DE.** Skeletal muscle lipid content and oxidative enzyme activity in relation to muscle fiber type in type 2 diabetes and obesity. *Diabetes* 50: 817-823, 2001
30. **Hickey MS, Carey JO, Azevedo JL, Houmard JA, Pories WJ, Israel RG and Dohm GL.** Skeletal muscle fiber composition is related to adiposity and in vitro glucose transport rate in humans. *Am J Physiol* 268: E453-E457, 1995
31. **Ritov VB, Menshikova EV, He J, Ferrell RE, Goodpaster BH and Kelley DE.** Deficiency of subsarcolemmal mitochondria in obesity and type 2 diabetes. *Diabetes* 54: 8-14, 2005
32. **Kelley DE, He J, Menshikova EV and Ritov VB.** Dysfunction of mitochondria in human skeletal muscle in type 2 diabetes. *Diabetes* 51: 2944-2950, 2002

33. **Morino K, Petersen KF, Dufour S, Befroy D, Frattini J, Shatzkes N, Neschen S, White MF, Bilz S, Sono S et al.** Reduced mitochondrial density and increased IRS-1 serine phosphorylation in muscle of insulin-resistant offspring of type 2 diabetic parents. *J Clin Invest* 115: 3587-3593, 2005
34. **De Feyter HM, van den Broek NM, Praet SF, Nicolay K, van Loon LJ and Prompers JJ.** Early or advanced stage type 2 diabetes is not accompanied by in vivo skeletal muscle mitochondrial dysfunction. *Eur J Endocrinol* 158: 643-653, 2008
35. **Meex RC, Schrauwen-Hinderling VB, Moonen-Kornips E, Schaart G, Mensink M, Phielix E, van de WT, Sels JP, Schrauwen P and Hesselink MK.** Restoration of muscle mitochondrial function and metabolic flexibility in type 2 diabetes by exercise training is paralleled by increased myocellular fat storage and improved insulin sensitivity. *Diabetes* 59: 572-579, 2010
36. **Schrauwen-Hinderling VB, Kooi ME, Hesselink MK, Jeneson JA, Backes WH, van Echteld CJ, van Engelshoven JM, Mensink M and Schrauwen P.** Impaired in vivo mitochondrial function but similar intramyocellular lipid content in patients with type 2 diabetes mellitus and BMI-matched control subjects. *Diabetologia* 50: 113-120, 2007
37. **Haseler LJ, Lin A, Hoff J and Richardson RS.** Oxygen availability and PCr recovery rate in untrained human calf muscle: evidence of metabolic limitation in normoxia. *Am J Physiol Regul Integr Comp Physiol* 293: R2046-R2051, 2007
38. **Karatzafieri C, de HA, Ferguson RA, van MW and Sargeant AJ.** Phosphocreatine and ATP content in human single muscle fibres before and after maximum dynamic exercise. *Pflugers Arch* 442: 467-474, 2001
39. **Marin P, Andersson B, Krotkiewski M and Bjorntorp P.** Muscle fiber composition and capillary density in women and men with NIDDM. *Diabetes Care* 17: 382-386, 1994
40. **Nyholm B, Qu Z, Kaal A, Pedersen SB, Gravholt CH, Andersen JL, Saltin B and Schmitz O.** Evidence of an increased number of type IIb muscle fibers in insulin-resistant first-degree relatives of patients with NIDDM. *Diabetes* 46: 1822-1828, 1997
41. **Holten MK, Zacho M, Gaster M, Juel C, Wojtaszewski JF and Dela F.** Strength training increases insulin-mediated glucose uptake, GLUT4 content, and insulin signaling in skeletal muscle in patients with type 2 diabetes. *Diabetes* 53: 294-305, 2004
42. **van Loon LJ, Koopman R, Manders R, van der WW, van Kranenburg GP and Keizer HA.** Intramyocellular lipid content in type 2 diabetes patients compared with overweight sedentary men and highly trained endurance athletes. *Am J Physiol Endocrinol Metab* 287: E558-E565, 2004
43. **Zierath JR, He L, Guma A, Odegaard WE, Klip A and Wallberg-Henriksson H.** Insulin action on glucose transport and plasma membrane GLUT4 content in skeletal muscle from patients with NIDDM. *Diabetologia* 39: 1180-1189, 1996





# Chapter 7

## *Integration of in vivo, in vitro and in silico methods for systems biology of mitochondrial function*

Adapted from:

J.P.J. Schmitz, J. Ciapaite, N.M.A. van den Broek, R.A.M. Jonkers,  
K. Nicolay, P.A.J. Hilbers, J.J. Prompers., J.A.L. Jeneson, N.A.W. van Riel  
*Integration of in vivo, in vitro and in silico methods for systems biology of mitochondrial function*  
(In preparation)

## ABSTRACT

Mitochondrial ATP synthesis capacity in skeletal muscle is studied by a variety of methods, including *in vivo*, *in vitro* and *in silico* approaches. We investigated if the insight obtained by these methods can be enlarged by combining them in a systems biology research approach. The strategy was tested in an animal model of decreased mitochondrial function: 8 versus 25 week old Wistar rats.  $^{31}\text{P}$  magnetic resonance spectroscopy revealed a decreased mitochondrial capacity *in vivo* in the older animals (PCr recovery rate constant decreased from  $0.013\pm 0.00082\text{s}^{-1}$  to  $0.0082\pm 0.000021\text{s}^{-1}$ ). End-exercise pH varied between groups ( $6.91\pm 0.04$  and  $6.79\pm 0.03$ , at 8 and 25 weeks, respectively). *In vitro* analyses of tissue samples identified several differences in muscle physiology: mitochondrial content was decreased by  $17\pm 5\%$  and the capacity of electron transport chain and TCA cycle was decreased  $22\pm 2\%$ . Simulations of a mechanistic mathematical model accurately reproduced the prolongation of PCr recovery period based on the observed differences in muscle physiology. Model analyses quantified that a major part of the decreased oxidative capacity was due to the decreased mitochondrial content ( $\sim 54\%$ ). The remaining part was a result of the difference in end exercise pH ( $\sim 12\%$ ) and decreased capacity of ETC and TCA cycle ( $\sim 32\%$ ). These results demonstrate the feasibility of applying *in silico* analyses for integration of *in vivo* and *in vitro* markers of mitochondrial dysfunction.

## INTRODUCTION

Mitochondria are versatile organelles involved in many different cellular processes, e.g., signaling events (1), heat generation (2), and apoptosis (3). Re-synthesis of ATP from its hydrolyses products ADP + Pi is, however, considered its primary task. Normal function of these organelles is considered essential to life. In fact, an increasing number of studies place mitochondrial dysfunction at the center of several diseases. For example, dysfunction of mitochondria in skeletal muscle has been associated with type 2 diabetes (4), chronic heart failure (5) or the aging process (6).

A variety of methods has become available to investigate mitochondrial function in skeletal muscle including *in vivo*, *in vitro* and *in silico* techniques. The gold-standard to determine the mitochondrial ATP generating capacity *in vivo* is  $^{31}\text{P}$  magnetic resonance spectroscopy (MRS) (7). This method can accurately determine the rate of post exercise phosphocreatine (PCr) recovery, which reflects the rate of oxidative ATP synthesis (7). Although  $^{31}\text{P}$  MRS can thus diagnose the functioning of the intact system, it cannot be used to identify the origin of any observed mitochondrial dysfunction. This knowledge is however key for design of therapeutic strategies. Therefore, in diagnostic studies of mitochondrial diseases, typically, additional analyses of muscle tissue samples are performed. Isolation of mitochondria from these tissue samples allows to determine *in vitro* respiration rates for varying substrate conditions using high-resolution respirometry (8). Additional biochemical and histological analyses of tissue samples provides information at the level of the metabolic pathways, e.g.: protein content / enzyme activity, mitochondrial content. At the same time, integration of available biochemical information on the mitochondrial pathways has yielded computational models of mitochondrial oxidative phosphorylation (9). These models offer unique opportunities for *in silico* studies of questions that cannot be addressed experimentally.

In and by itself, each of the available methods provides valuable information. Thus far however, (personalized) pharmaceutical therapy has been predominantly designed on the basis of *in vitro* data. Examples of studies reporting such treatments are riboflavin therapy for complex I deficiencies (10), menadione + ascorbate treatment of a complex III deficiency (11), or vitamin E treatment in case of an ANT defect (12,13). Treatments however are often effective in only a subset of patients (14). Moreover, it remains in many cases unclear why some patients respond well to treatment while others do not respond at all (14). Even well-defined mitochondrial disorders (caused by a single gene mutation) can cause a complex pattern of adaptations in muscle metabolism. These adaptations include for example compensatory mechanisms (up-regulation of alternative enzymes or pathways) or are a result of lack of physical activity caused by (severe) exercise intolerance. For an improved design of (personalized) treatment it is crucial to answer questions like: (i) which changes in muscle physiology contribute the most to the decreased mitochondrial capacity?, (ii) which potential targets allow for the largest gain in overall mitochondrial function?, and (iii) what are the risks for possible side effects of therapies? Answering these questions requires to combine all available pieces of information (*in vivo*, *in vitro* and *in silico*) in an integrative approach (15). Such an integrative research strategy is also referred to as a 'systems biology' or 'systems medicine' approach (15). Mathematical modeling provides a powerful tool for data integration and is therefore considered a cornerstone of such an approach (15).

We propose to apply mathematical modeling to integrate *in vivo* and *in vitro* measurements of mitochondrial function. The ultimate aim of this effort is to design a method by



which the best therapeutic targets and corresponding therapies can be predicted by applying models that comprise patient specific parameters (based on *in vitro* data). However, before such model can be applied for medical purposes, first, multiple steps of thorough model testing are required. Chapters 4 to 6 already describe several studies that contribute to this process. The model described in these chapters accurately reproduced key characteristics of mitochondria *in vivo* (i.e., transduction functions, PCr recovery kinetics) as well as the effect of inhibition of individual steps in OXPHOS on the respiration rate *in vitro*. It remains however to be tested if the quality of this model is indeed at a level at which it can be applied to integrate different experimental measurements of mitochondrial function and yield reliable predictions and new insight that may eventually be used for improving therapies or design of new (pharmaceutical) treatments.

The aim of the current study was to perform such a test. The approach was tested in an animal model: 8 versus 25 week old Wistar rats. A schematic overview of the study design is provided in Figure 1. The functioning of mitochondria *in vivo* was determined by  $^{31}\text{P}$  MRS. Biochemical analyses of muscle samples were performed to identify adaptations of the mitochondrial pathway (e.g. enzyme activities, protein content, mitochondrial content). The two main questions that followed from the combined *in vivo* and *in vitro* datasets were: (i) can the set of pathway adaptations (*in vitro* data) explain the functioning of the integrated pathway *in vivo*?, (ii) what is the contribution of individual pathway changes to the *in vivo* functioning of the mitochondria? To answer these questions *in silico* analyses were performed. The changes in muscle physiology observed *in vitro* were translated to the model by adjusting corresponding parameter values. Model predictions were then compared to *in vivo* data to test if the pathway adaptations could explain the *in vivo* recorded decreased mitochondrial function.

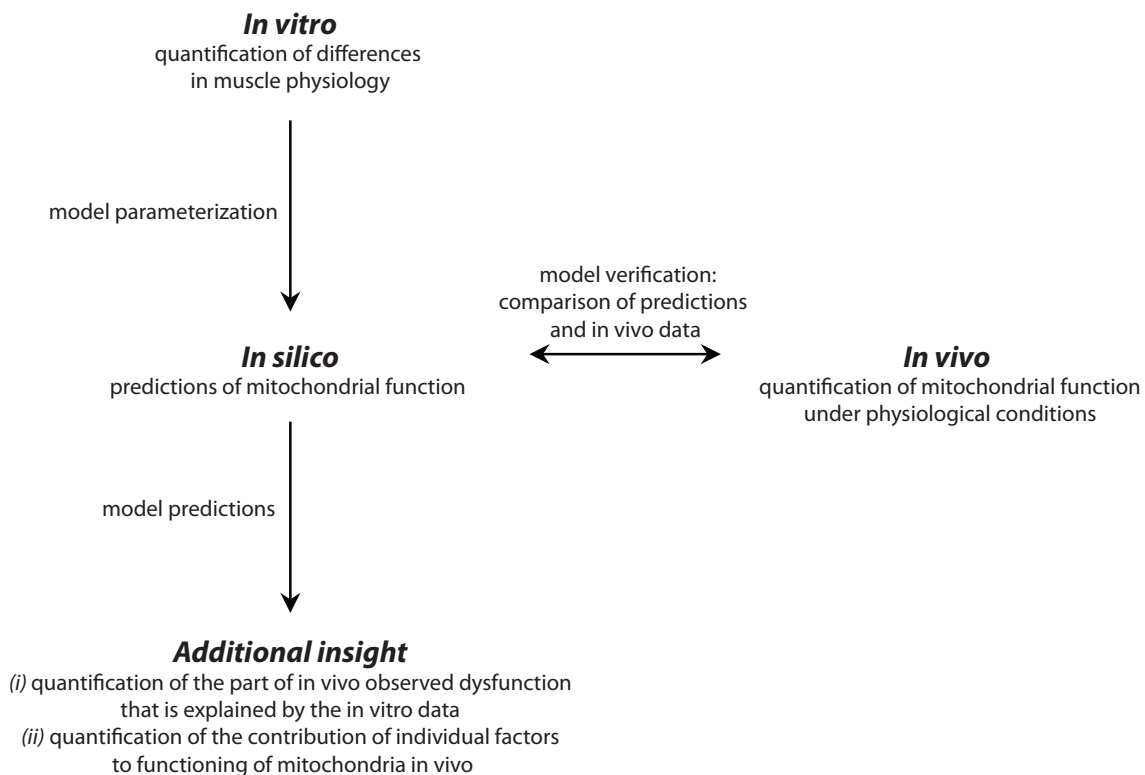


**Figure 1.** Schematic overview of the study design.

## METHODS

### **Animals**

10 male Wistar rats age 8 weeks and 10 male Wistar rats age 25 weeks (248±12 and 460±21 gram, respectively, Charles River Laboratories, France) were housed in groups at 20°C and 50% humidity, on a 12-h light dark cycle with ad libitum access to water and chow. Principles of laboratory animal care were followed and all experimental procedures were approved by the Animal Ethics Committee of Maastricht University, the Netherlands. During preparatory surgical procedures and MRS experiments, animals were anesthetized using 0.8-1.2% isoflurane (Forene, Abbot GmbH, Wiesbaden Germany) administered via a face mask with medical air and oxygen (0.2 and 0.1 L/min respectively). Body temperature was maintained at 37±1°C using heat pads and monitored by a custom build monitoring system. In the MR scanner, respiration was monitored using a pressure sensor registering thorax movement (Rapid Biomedical, Rimpär, Germany). Contractions in the Tibialis Anterior muscle (TA) of the right leg were induced by using electrical stimuli applied via acute, subcutaneously implanted platinum electrodes positioned along the distal nerve trajectory of the n. peroneus communis. Stimulation voltage ranged between 5-10 V, pulse length was 6 ms. A short pulse train of 10 muscle excitations at 80Hz was applied every second. After the <sup>31</sup>P MRS measurements the animals were allowed to recover. On the next day the animals were sacrificed. The TA muscle of the left leg was collected for high resolution respirometry experiments. The TA muscle of the left leg was collected and cut into three equally sized pieces; two were immediately frozen in liquid nitrogen and the third piece was embedded in Tissue-Tek (Sakura, Alphen aan de Rijn, The Netherlands) and frozen in liquid nitrogen cooled isopentane.

### **<sup>31</sup>P NMR acquisition parameters**

All MRS measurements were performed on a 6.3 T horizontal Bruker magnetic resonance spectrometer (MRS) (Bruker, Ettlingen, Germany). Phosphorus (<sup>31</sup>P) MRS was performed by using a two coil configuration. A circular <sup>1</sup>H surface coil (40 mm) was used to adjust the magnetic field homogeneity using the available proton signal from water, while a smaller elliptical surface coil (10/18 mm) was positioned over the TA to acquire phosphorus data. <sup>31</sup>P spectra were acquired applying an adiabatic excitation pulse with a flip angle of 90°. A fully relaxed spectrum (TR=20 s, 32 averages) was measured at rest. A time series of spectra (TR = 5 s, 2 averages) before, during and after electrical stimulation of TA. A time series consisted of 3 minutes rest, 2 minutes stimulation and 10 minutes after stimulation.

Intracellular pH was calculated from the chemical shift difference between the Pi and PCr resonances ( $\delta$ ; measured in part per million), according to Eq. 2 (16).

$$pH = 6.75 + \log\left(\frac{\delta - 3.27}{5.63 - \delta}\right) \quad (\text{Eq. 2})$$

Mitochondrial function was quantified by fitting of a mono-exponential function:

$$PCr(t) = PCr_e - \Delta PCr \cdot e^{-t \cdot kPCr} \quad (\text{Eq. 3})$$

Where,  $PCr_e$  is the PCr level after recovery,  $\Delta PCr$  is the difference between the PCr levels after recovery and at the end of exercise, and  $kPCr$  is the rate constant for PCr resynthesis.

**Isolation of mitochondria**

Mitochondria were isolated from one whole TA muscle through a differential centrifugation procedure (17). Briefly, TA muscle was excised, washed in ice-cold 0.9% KCl, freed of connective and adipose tissue, weighed, and minced with scissors in ice-cold medium A (5 ml for 1 g tissue) containing 150 mM sucrose, 75 mM KCl, 50 mM MOPS, 1 mM  $\text{KH}_2\text{PO}_4$ , 5 mM  $\text{MgCl}_2$ , 1 mM EGTA, and 0.4 mg/mL bacterial proteinase type XXIV (pH 7.4). Next, 20 mL of medium B containing 250 mM sucrose, 0.1 mM EGTA, 20 mM MOPS, and 2 mg/ml BSA (pH 7.4) was added, and the mixture was homogenized using a Potter-Elvehjem homogenizer. The homogenate was centrifuged at 800 *g* for 10 min, 4°C. The resulting supernatant was centrifuged at 10,000 *g* for 10 min, 4°C. The pellet was resuspended in 15 mL of fresh ice-cold medium B and centrifuged at 10,000 *g* for 10 min, 4°C. Mitochondrial pellet was resuspended in 100  $\mu\text{L}$  of medium B. Protein content was determined using the BCA protein assay kit (Pierce, Thermo Fisher Scientific Inc., Rockford, IL, USA).

**High resolution respirometry**

Oxygen consumption rate was measured at 37°C using a 2-channel high-resolution Oroboros oxygraph-2 k (Oroboros, Innsbruck, Austria). Mitochondria (0.15 mg/mL) were incubated in 1 mL of assay medium containing 110 mM KCl, 20 mM Tris, 2.3 mM  $\text{MgCl}_2$ , 5 mM  $\text{KH}_2\text{PO}_4$ , and 1 mg/mL BSA (pH 7.3), and supplemented with either 5 mM pyruvate plus 5 mM malate as the oxidizable substrate. An ADP-regenerating system consisting of excess hexokinase (4.8 U/mL) and glucose (12.5 mM) was used to maintain steady-state oxygen consumption rates. ATP (1 mM) was added to initiate state 3 respiration. Oxygen consumption in resting state (state 4) and uncoupled state (state U) was determined after the addition of 1.25  $\mu\text{M}$  carboxyatractyloside and 1  $\mu\text{M}$  carbonyl cyanide 3-chlorophenyl hydrazone, respectively. The signals from the oxygen electrode were recorded at 0.5s intervals. Data acquisition and analysis were performed using Oxygraph-2k-DatLab 4.2 software (Oroboros, Innsbruck, Austria).

**Determination of the relative mitochondrial copy number**

Genomic DNA was isolated from a 25-mg transversal slice of midbelly TA using the GenElute Mammalian Genomic DNA Miniprep Kit (Sigma-Aldrich). Mitochondrial DNA (mtDNA) content relative to peroxisome proliferator-activated receptor- $\gamma$  coactivator 1 $\alpha$  (PGC1 $\alpha$ ) gene was measured using real-time PCR as described previously (18). Primers for mtDNA were as follow: forward 5'-ACACCAAAGGACGAACCTG-3' and reverse 5'-ATGGGGAAGAAGCCCTAGAA-3'; and for PGC1 $\alpha$ , forward 5'-ATGAATGCAGCGGTCTTAGC-3' and reverse 5'-ACAATGGCAGGGTTTGTTC-3'. The relative mtDNA copy number was calculated using the  $\Delta\Delta C_t$  method (19).

**Western blot analysis**

Frozen transversal sections of midbelly TA (100–150 mg) were homogenized in 10 vol of cold RIPA buffer (1% Nonidet P40 substitute; 0.5% Na deoxycholate; 0.1% Na dodecyl sulfate; 150 mM NaCl; and 50 mM Tris, pH 8) supplemented with protease inhibitor cocktail (dilution 1:200; SigmaAldrich). Homogenates were solubilized for 2 h at 4°C and centrifuged at 12000 *g* for 15 min at 4°C. Supernatants (10  $\mu\text{g}$  of total protein) were resolved by SDS-PAGE.

After electrophoresis, proteins were transferred to polyvinylidene difluoride membranes (Millipore, Bedford, MA, USA). After blocking, membranes were incubated with MitoProfile® Total OXPHOS Rodent WB Antibody Cocktail (1:2000, MitoSciences, Eugene, OR, USA) containing

monoclonal antibodies against Complex I, II, III, IV and ATP synthase subunits, rabbit anti-adenine nucleotide translocase antibody (ANT; 1:200) or or goat anti-GAPDH antibody (both from Santa Cruz Biotechnology, Santa Cruz, CA, USA) overnight at 4°C. After washing with PBS containing 0.1% Tween, membranes were treated with horseradish peroxidase-conjugated goat anti-rabbit IgG (Pierce; Thermo Fisher Scientific, Rockford, IL, USA) for 1 h at room temperature. The immunocomplexes were detected using SuperSignal West Dura Extended Duration Substrate (Pierce) and quantified using Quantity One 1-D 4.4.0 analysis software (Bio-Rad Laboratories, Hercules, CA, USA).

### ***Statistical analysis***

Data are presented as means  $\pm$  SEM unless otherwise stated. The listed  $n$  values represent the number of animals used for a particular experiment. Statistical significance of the differences was assessed using two-sided unpaired Student's  $t$ -tests in PASW statistics 18.0 statistical package (SPSS, Chicago, IL). Level of statistical significance was set at  $P$  0.05.

### ***Description of the mathematical model***

The computational model of skeletal muscle oxidative ATP metabolism described in chapter 6 (uniform-fiber model) was used as a basis for this study. The single-fiber model was applied because immunohistochemical analysis of the muscle samples revealed no differences in fiber type composition between animal groups (data not shown). The model contains a detailed biophysical description of the electron transport chain, oxidative phosphorylation, adenine nucleotides and Pi transport across the mitochondrial membranes and cellular ATP buffering (creatine kinase and adenylate kinase). The model was implemented in Matlab 7.5.0 (The Mathworks, Natick, MA, USA). Ordinary differential equations were solved numerically by using ODE15s with absolute and relative tolerances set to  $10^{-8}$ .

### ***Predictions of PCr dynamics at 8 weeks (reference model)***

The mitochondrial content in the original model was set to values corresponding to human quadriceps muscle. TA muscle of Wistar rats contains predominantly (>95%) fast twitch fibers which have a low mitochondrial content. It was therefore required to re-estimate the mitochondrial volume fraction. This parameter was decreased manually to 0.0165 in order to reproduce the observed PCr recovery rate constant in 8 week old rats.

The simulations of PCr dynamics consisted out of 2 steps. First, initial conditions for the simulations of the post exercise recovery dynamics were determined. Hereto pH was clamped at the experimentally observed end-exercise value (6.91). ATPase rate was progressively increased until the initial steady state [PCr] matched the experimentally observed value (10mM). Next metabolic recovery was simulation, by decreasing cellular ATPase demand to resting value (0.01mM/s, chapter 3). Identical to the experimental data, mitochondrial function was quantified by the rate constant of a mono exponential recovery function fitted to the simulation PCr recovery kinetics (Eq. 3).

### ***Predictions of PCr dynamics at 25 weeks***

The model fitted to the recovery rate constant at 8 weeks was used as a reference for predictions of mitochondrial function at 25 weeks. Model parameterization was changed according to the

experimentally observed differences in muscle physiology: i.e., difference in end exercise pH, mitochondrial content and capacity of the TCA cycle and ETC. Parameter values were changed according to the relative difference, see Table 2. Each parameter change was represented by a normal distribution representing the uncertainty of the mean of the experimental observations ( $\sigma = \text{SEM}$ ). Simulations were performed by following a Monte Carlo approach. 100 simulations were performed randomly drawing parameter values from the normal distributions defined in Table 2. Simulations results were represented by the mean  $\pm$  SD of the ensemble.

## RESULTS

### *In vivo mitochondrial function*

Figure 2A shows a stack-plot of  $^{31}\text{P}$  MRS spectra recorded during a rest-exercise-recovery protocol of tibialis anterior (TA) muscle of Wistar rats. During exercise PCr is consumed by creatine kinase to buffer the transient mismatch between ATP demand and production by glycolysis and mitochondria. During exercise pH dropped from  $7.16 \pm 0.02$  and  $7.11 \pm 0.04$  at rest to  $6.91 \pm 0.04$  and  $6.79 \pm 0.03$  at the end of exercise. The rate of PCr recovery, quantified by rate constant of a mono – exponential function ( $k_{\text{PCr}}$ ), was used as measure of *in vivo* mitochondrial function (7). The rate constant of PCr recovery ( $k_{\text{PCr}}$ ) were  $0.013 \pm 0.00082 \text{ s}^{-1}$  and  $0.0082 \pm 0.00021 \text{ s}^{-1}$  (mean  $\pm$  SEM,  $n=10$ ) for 8 and 25 week old rats respectively, Figure 2B. The statistically significant differences between the two groups ( $p < 0.001$ ) confirmed the reduced mitochondrial capacity *in vivo* in this animal model.

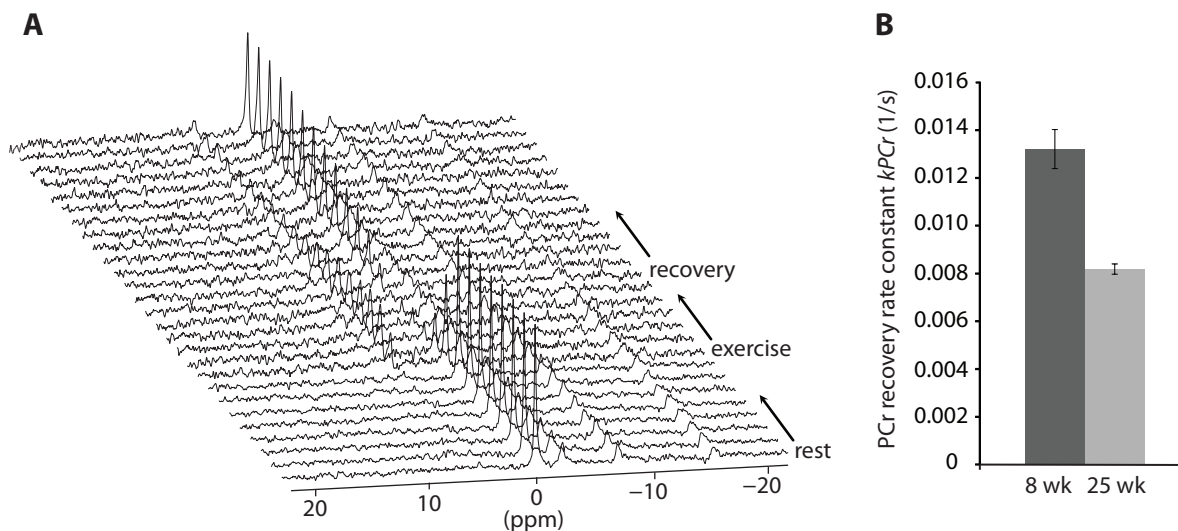


**Figure 2.** Stack plot of a representative time series of spectra recorded at age 25 weeks (A). Spectra were obtained by averaging 4 FID's (time resolution 20s) and processed with 15Hz line broadening. PCr rate constant ( $k_{\text{PCr}}$ ) of animals at age 8 and 25 weeks (B). Error bars denote SEM.

**State 3, 4, U respiration of isolated mitochondria**

Mitochondria were isolated from the TA muscle and state 3, 4 and uncoupled state (state – U) respiration experiments were performed with malate and pyruvate as oxidizable substrates (Figure 3 and Table 1). State 4 respiration was non – significantly different between the two groups ( $p = 0.15$ ,  $n=10$ ). In contrast, state 3 and state U were significantly lower in 25 week old rats ( $p < 0.001$ ,  $n=10$ ). The decrease in state 3 and state U was rather similar ( $22\pm 2\%$  and  $17\pm 2\%$ , respectively), indicating that the difference in intrinsic mitochondrial function could be attributed to decreased capacity of TCA cycle and electron transport chain (ETC).

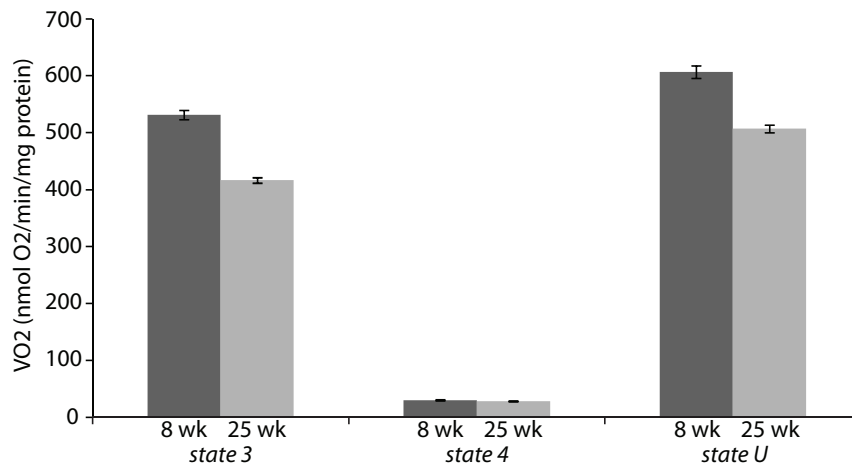


**Figure 3.** State 3, 4, U respiration of isolated mitochondria. Error bars denote SEM.

**Table 1.** State 3, 4, U respiration of isolated mitochondria (nmol O<sub>2</sub>/min/mg protein)

	State 3 respiration	State 4 respiration	State U respiration
<b>8 weeks</b>	531.4±8.3	30.1±0.9	606.7±11.0
<b>25 weeks</b>	416.4±4.8	28.4±0.7	507.9±6.6

**mtDNA copy number and Western Blotting analysis**

mtDNA copy number was measured to determine if on top of the difference in intrinsic mitochondrial function also the number of mitochondria was changed, Figure 4A. Relative mtDNA copy number was significantly decreased from  $2483\pm 90$  (mean±SEM,  $n=10$ ) to  $2056\pm 88$  (mean±SEM,  $n=10$ ), which was statistically significant ( $p=0.004$ ). These data indicate a decrease in mtDNA copy number in TA muscle of 25 week old rats of about  $17\pm 5\%$ . Western blotting analyses was applied to determine protein levels of complex I through IV,  $F_1F_0$ ATPase, ANT and GAPDH. The latter was used as housekeeping enzyme (Figure 4B). The decreased protein content of OXPHOS complexes in the Western Blotting results represents the combined effect of the decrease in mitochondrial content (mtDNA copy number) and the decrease in intrinsic mitochondrial function (state 3, U respiration). After correction for the decrease in number of mitochondria (mtDNA copy number) of  $17\pm 5\%$ , the remaining difference in protein expression of OXPHOS complexes agrees quite well with the respiration measurements indicating a  $\sim 20\%$  decrease in the capacity of OXPHOS.

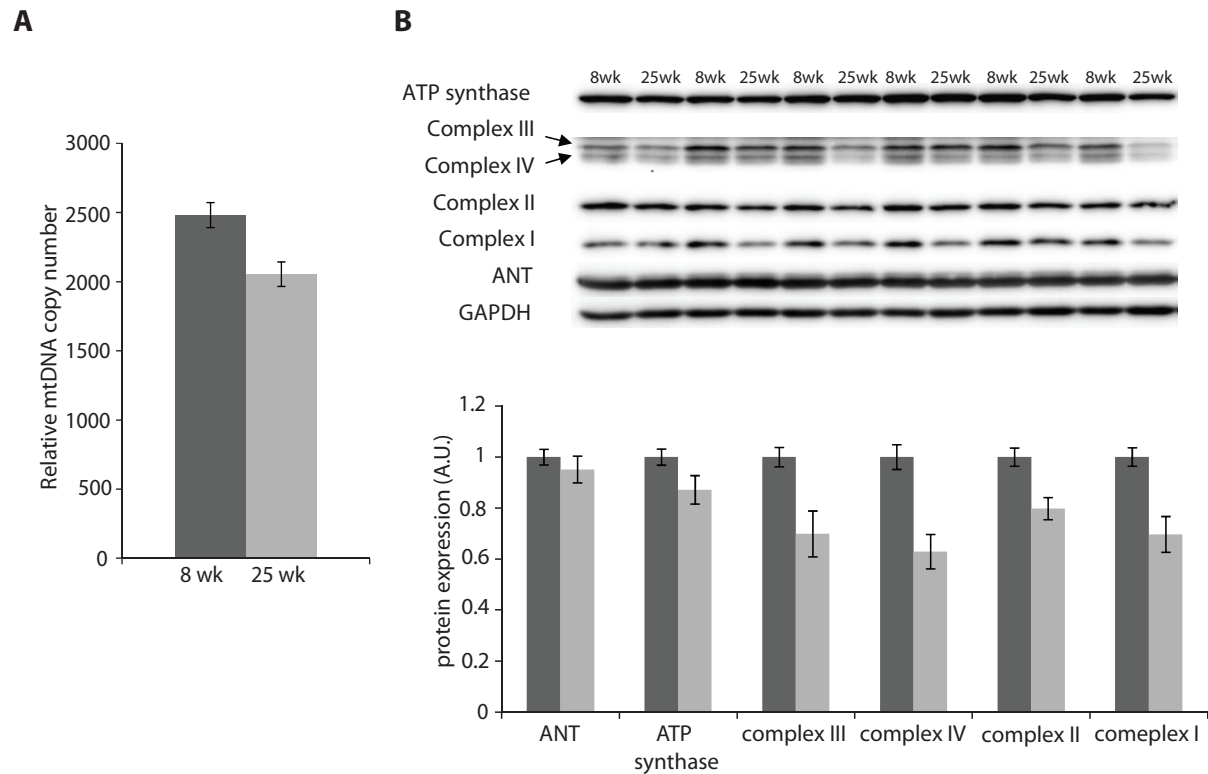


**Figure 4.** mtDNA copy number (**A**) and protein content of OXPHOS complexes determined by western blotting analysis (**B**). Errorbars indicate SEM.

### *In silico analyses*

The experimental data revealed 3 differences between the 8 and 25 week old rats that could contribute to the decrease in mitochondrial function *in vivo* (Table 2): i.e.,  $17\pm 5\%$  decrease in mitochondrial content,  $22\pm 2\%$  decrease in the capacity of the ETC + TCA cycle and a lower end exercise pH ( $6.91\pm 0.04$  vs.  $6.79\pm 0.03$ , respectively). Model simulations were used to: (i) test if these *in vitro* observations could quantitatively explain the measured prolongation of PCr recovery period and (ii) to dissect the contribution of each individual factor.

**Table 2.** Parameter changes for model of 25 weeks

Parameter	Value in reference model (8 weeks)	Value for 25 weeks (mean $\pm\sigma$ )	Difference 8 and 25 weeks (mean $\pm\sigma$ )
End exercise pH	6.91	6.79 $\pm$ 0.03	- 0.12 $\pm$ 0.03
Mitochondrial volume fraction	0.0165%	0.0137 $\pm$ 0.0007%	- 17 $\pm$ 5%
Capacity of TCA cycle and ETC #	1	0.78 $\pm$ 0.02	- 22 $\pm$ 2%

# the decreased capacity of TCA and ETC was implemented by decreasing the  $V_{\max}$  parameters of dehydrogenase, complex I, complex III and complex IV flux according to the listed values.

First, it was verified that the reference model could accurately reproduce the PCr recovery rate constant of 8 week old rats (control group), Figure 5A. Parameterization of the reference model was then changed according to the experimental data summarized in Table 2 in order to yield a model of the oxidative metabolism in 25 week old rats. The predicted PCr recovery rate constant according to this model was  $0.0082\pm 0.0008s^{-1}$  (Figure 5A), which is identical to the experimentally

observed value in 25 week old rats ( $0.0082 \pm 0.00021 \text{ s}^{-1}$ ). Additional model simulations allowed decomposing the contribution of individual factors to the decrease in mitochondrial function *in vivo*. The predicted PCr recovery rate constants were  $0.0122 \pm 0.0003 \text{ s}^{-1}$ ,  $0.0103 \pm 0.0009 \text{ s}^{-1}$  and  $0.0113 \pm 0.0003 \text{ s}^{-1}$  for the difference in end-exercise pH, mitochondrial content and intrinsic mitochondrial function, respectively. This corresponds to 12, 54 and 32% of the decreased mitochondrial capacity observed in 25 weeks old rats (Figure 5B), respectively.

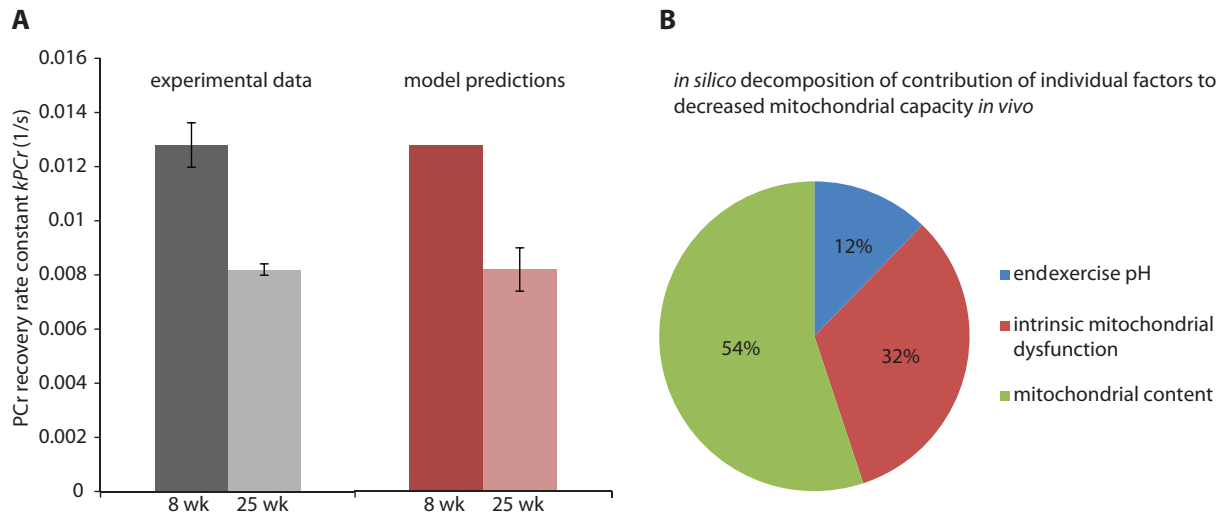


**Figure 5.** Comparison of experimentally observed and predicted mitochondrial function (PCr recovery rate constant) of animals at age 8 and 25 weeks (**A**) and, *in silico* decomposition of contribution of individual factors to decreased mitochondrial capacity *in vivo* (**B**). Error bars on experimental data denote SEM. Error bars on model predictions represent SD of the ensemble.

## DISCUSSION

In the present investigation a novel, systems biology based research strategy for studying mitochondrial (dys)function was successfully tested. The key advantages of the approach, its generic value as well as several methodological considerations will be discussed.

State-of-the-art approaches to study mitochondrial dysfunction typically involve a combination of *in vivo* and *in vitro* measurements of markers of mitochondrial function (see e.g. (20,21)). These methods are very complimentary: *in vivo* data provide a read-out of the functioning of the intact system and *in vitro* markers identify changes in muscle physiology possible related to the observed behavior. Analyses of these data are usually restricted to a combination of statistical and intuitive approaches (see: e.g. (20,22)). A promise of the current era of systems biology is to understand the integrated function of complex biological systems in order to predict and rationally manipulate their behavior, with the ultimate aim of improving human health (23). In order to obtain such understanding, the analyses of available data have to be advanced beyond the level of statistical and intuitive methods.



We propose to perform such a more insightful and predictive analysis by application of mathematical models of pathway biochemistry. An important aim in the design of the study was to combine the *in vivo* and *in vitro* recorded datasets in such a way they become the most informative. It was chosen to use the *in vitro* data to parameterize the model and apply the *in vivo* data for model testing. Specifically, we did not apply parameter estimation to fit the PCr recovery period of 25 week old animals. The rationale for this was that many model parameters influenced the rate of PCr recovery (e.g. mitochondrial volume content, enzyme  $V_{\max}$  parameters). Consequently, a parameter estimation algorithm would identify an infinite number of solutions to fit the prolongation of PCr recovery period. These results would be unreliable and inconclusive. It was therefore decided that the *in vivo* data would be most valuable when used purely for model testing.

A topic that is receiving increasingly more attention in the field of computational systems biology is how to account for measurement uncertainty in numerical analyses (24-27). Measurements of physical quantities always have a limited accuracy. In general, experiments are therefore repeated multiple times to empirically determine the coefficient of variation which reflects the measurement uncertainty. We exploited this information to estimate the uncertainty in predictions of PCr recovery rate constants by means of a numerical Monte Carlo approach. This method is already applied for quantification of uncertainty propagation in many different fields of science and engineering (see e.g., (28)). However, application of this strategy is not yet common practice in systems biology. In this particular investigation, the results of this method were considered very insightful. They provide quantitative information which allows assessing the robustness of predictions.

In chapter 6 mathematical modeling was applied to integrate literature data of type 2 diabetes patients obtained from multiple studies. Although this study already illustrated part of the benefits of a systems biology approach, it did not yet act as proof-of-concept. An important limitation of the previous study was that the data had to be collected from several different studies. As a result, the variance in data and associated uncertainty which had to be taken into account was rather large. Therefore model predictions could not be tested rigorously. The design of the current study overcomes these limitations: (i) all data were collected in a single study and (ii) selection of an animal model prevented variation due to genetic variability or lifestyle differences present in humans.

The first striking outcome of the study was that the mathematical model accurately predicted the prolongation of the PCr recovery period based on experimentally observed changes in muscle physiology. Because this result was achieved without the need of any additional parameter estimation it acts as strong validation of the model and research strategy. A promise of systems biology is that the knowledge captured by the model will yield new insight or predictions. In the current investigation additional insight was obtained from predictions of the individual contribution of differences in muscle physiology to the decreased capacity of mitochondria *in vivo*. These predictions revealed that a major part (54%) of the mitochondrial dysfunction was a result of the decrease in mitochondrial content, whereas the remaining part was a result of a decreased capacity in TCA cycle and ETC (32%) and the difference in end exercise pH (12%). These results demonstrate a major benefit of the proposed systems biology based data analyses method: i.e., it allows dissecting the individual contribution of changes in muscle physiology to the functioning of the integrated system based on contemporary knowledge of pathway biochemistry. This type of

information is crucial to obtain a more effective understanding of the impact of possible therapies aimed at improving mitochondrial function. For example, for this animal model it was predicted that the biggest gain in mitochondrial function can be achieved by reversing the decrease in mitochondrial content. Stimulation of mitochondrial biogenesis by exercise training (29,30) is therefore likely to be more effective than pharmaceutical stimulation of electron transport chain activity (31). These results illustrate how the proposed approach can eventually provide guidance for designing therapeutic strategies.

Mitochondrial disorders are characterized by a wide variety in phenotypes (32), therefore (pharmaceutical) treatments are often effective in only a subset of patients (14). Moreover, it remains in many cases unclear why some patients respond well to treatment while others do not respond at all (14). Especially for this group of metabolic disorders, there is thus an obvious need for predictive tools to design personalized treatments. The current study demonstrates the feasibility of obtaining a predictive model based on information that is also typically obtained from diagnostic muscle biopsies in patients. Further development and testing of the model for application in such a clinical context is considered a very relevant topic for future studies.

The work presented in this paper contributes to the ongoing effort of unraveling the complexity and regulation of mitochondrial function. This field has a rich history of application of mathematical modeling to identify the regulation of oxidative ATP synthesis (see e.g.: (9)). An important motivation for these past studies was that the understanding captured by the mathematical models could eventually be used to investigate the role of mitochondrial function in human health. As a result of many iterative steps the models have advanced considerably throughout the years. The current study demonstrates the feasibility of a translational step towards application of the newest generation models for (diagnostic) studies of mitochondrial function. As such this investigation provides a starting point for extension of the applied systems biology based strategy to (pre-)clinical studies of mitochondrial function in for example mitochondrial diseases (32), type 2 diabetes (4), chronic heart failure (5) or aging (6). These future studies are essential to further confirm the generic value of the method and may contribute to a more widespread application of systems biology in (clinical) biomedical research.

## REFERENCES

1. **Butow RA, Avadhani NG.** Mitochondrial signaling: the retrograde response. *Mol Cell* 14: 1-15, 2004
2. **Nicholls DG, Locke RM.** Thermogenic mechanisms in brown fat. *Physiol Rev* 64: 1-64, 1984
3. **Green DR, Reed JC.** Mitochondria and apoptosis. *Science* 281: 1309-1312, 1998
4. **Lowell BB, Shulman GI.** Mitochondrial dysfunction and type 2 diabetes. *Science* 307: 384-387, 2005
5. **Drexler H, Riede U, Munzel T, Konig H, Funke E and Just H.** Alterations of skeletal muscle in chronic heart failure. *Circulation* 85: 1751-1759, 1992
6. **Trounce I, Byrne E and Marzuki S.** Decline in skeletal muscle mitochondrial respiratory chain function: possible factor in ageing. *Lancet* 1: 637-639, 1989
7. **Prompers JJ, Jeneson JA, Drost MR, Oomens CC, Strijkers GJ and Nicolay K.** Dynamic MRS and MRI of skeletal muscle function and biomechanics. *NMR Biomed* 19: 927-953, 2006
8. **Hutter E, Unterluggauer H, Garedew A, Jansen-Durr P and Gnaiger E.** High-resolution respirometry--a modern tool in aging research. *Exp Gerontol* 41: 103-109, 2006
9. **Schmitz JP, Vanlier J, van Riel NA and Jeneson JA.** Computational modeling of mitochondrial energy transduction. *Crit Rev Biomed Eng* 39: 363-377, 2011
10. **Bakker HD, Scholte HR, Jeneson JA, Busch HF, Abeling NG and van Gennip AH.** Vitamin-responsive complex I deficiency in a myopathic patient with increased activity of the terminal respiratory chain and lactic acidosis. *J Inherit Metab Dis* 17: 196-204, 1994
11. **Eleff S, Kennaway NG, Buist NR, Darley-Usmar VM, Capaldi RA, Bank WJ and Chance B.** 31P NMR study of improvement in oxidative phosphorylation by vitamins K3 and C in a patient with a defect in electron transport at complex III in skeletal muscle. *Proc Natl Acad Sci U S A* 81: 3529-3533, 1984
12. **Bakker HD, Scholte HR and Jeneson JA.** Vitamin E in a mitochondrial myopathy with proliferating mitochondria. *Lancet* 342: 175-176, 1993
13. **Bakker HD, Scholte HR, Van den Bogert C, Jeneson JA, Ruitenbeek W, Wanders RJ, Abeling NG and van Gennip AH.** Adenine nucleotide translocator deficiency in muscle: potential therapeutic value of vitamin E. *J Inherit Metab Dis* 16: 548-552, 1993
14. **Bresolin N, Doriguzzi C, Ponzetto C, Angelini C, Moroni I, Castelli E, Cossutta E, Binda A, Gallanti A, Gabellini S et al..** Ubidecarenone in the treatment of mitochondrial myopathies: a multi-center double-blind trial. *J Neurol Sci* 100: 70-78, 1990
15. **Balaban RS.** Modeling mitochondrial function. *Am J Physiol Cell Physiol* 291: C1107-C1113, 2006
16. **Tobin RB, Mackerer CR and Mehlman MA.** pH effects on oxidative phosphorylation of rat liver mitochondria. *Am J Physiol* 223: 83-88, 1972
17. **Reichert M, Schaller H, Kunz W and Gerber G.** The dependence on the extramitochondrial ATP/ADP-ratio of the oxidative phosphorylation in mitochondria isolated by a new procedure from rat skeletal muscle. *Acta Biol Med Ger* 37: 1167-1176, 1978
18. **Ciapaite J, Bakker SJ, van EG, Wagner MJ, Teerlink T, Schalkwijk CG, Fodor M, Ouwens DM, Diamant M, Heine RJ et al..** Functioning of oxidative phosphorylation in liver mitochondria of high-fat diet fed rats. *Biochim Biophys Acta* 1772: 307-316, 2007
19. **Szuhai K, Ouweland J, Dirks R, Lemaitre M, Truffert J, Janssen G, Tanke H, Holme E, Maassen J and Raap A.** Simultaneous A8344G heteroplasmy and mitochondrial DNA copy number quantification in myoclonus epilepsy and ragged-red fibers (MERRF) syndrome by a multiplex molecular beacon based real-time fluorescence PCR. *Nucleic Acids Res* 29: E13, 2001
20. **Phielix E, Schrauwen-Hinderling VB, Mensink M, Lenaers E, Meex R, Hoeks J, Kooi ME, Moonen-Kornips E, Sels JP, Hesselink MK et al..** Lower intrinsic ADP-stimulated mitochondrial respiration underlies in vivo mitochondrial dysfunction in muscle of male type 2 diabetic patients. *Diabetes* 57: 2943-2949, 2008
21. **van den Broek NM, Ciapaite J, De Feyter HM, Houten SM, Wanders RJ, Jeneson JA, Nicolay K and Prompers JJ.** Increased mitochondrial content rescues in vivo muscle oxidative capacity in long-term high-fat-diet-fed rats. *FASEB J* 24: 1354-1364, 2010
22. **Praet SF, De Feyter HM, Jonkers RA, Nicolay K, van PC, Kuipers H, van Loon LJ and Prompers JJ.** 31P MR spectroscopy and in vitro markers of oxidative capacity in type 2 diabetes patients. *MAGMA* 19: 321-331, 2006
23. **Beard DA, Vendelin M.** Systems biology of the mitochondrion. *Am J Physiol Cell Physiol* 291: C1101-C1103, 2006
24. **Cedersund G, Roll J.** Systems biology: model based evaluation and comparison of potential explanations for given biological data. *FEBS J* 276: 903-922, 2009
25. **Gutenkunst RN, Casey FP, Waterfall JJ, Myers CR and Sethna JP.** Extracting falsifiable predictions from sloppy models. *Ann N Y Acad Sci* 1115: 203-211, 2007
26. **Nyman E, Brannmark C, Palmer R, Brugard J, Nystrom FH, Stralfors P and Cedersund G.** A hierarchical whole-body modeling approach elucidates the link between in Vitro insulin signaling and in Vivo glucose homeostasis. *J Biol Chem* 286: 26028-26041, 2011
27. **Vanlier J, Tiemann CA, Hilbers PA and van Riel NA.** An integrated strategy for prediction uncertainty analysis. *Bioinformatics* 28: 1130-1135, 2012
28. **Coleman HW, Steele WG.** *Experimentation, validation, and Uncertainty Analysis for Engineers.* Hoboken, New Jersey: John Wiley & Sons, Inc., 2009
29. **Adhihetty PJ, Irrcher I, Joseph AM, Ljubicic V and Hood DA.** Plasticity of skeletal muscle mitochondria in response to contractile activity. *Exp Physiol* 88: 99-107, 2003
30. **Irrcher I, Adhihetty PJ, Joseph AM, Ljubicic V and Hood DA.** Regulation of mitochondrial biogenesis in muscle by endurance exercise. *Sports Med* 33: 783-793, 2003
31. **Pfeffer G, Majamaa K, Turnbull DM, Thorburn D and Chinnery PF.** Treatment for mitochondrial disorders. *Cochrane Database Syst Rev* 4: CD004426, 2012

32. **Wallace DC.** Mitochondrial diseases in man and mouse. *Science* 283: 1482-1488, 1999



# Chapter 8

## *In vivo and in silico studies of the regulation of glycolytic versus mitochondrial flux in normoxic skeletal muscle*

Adapted from:

J.P.J. Schmitz, B. Wessels, W. Groenendaal,  
K. Nicolay, P.A.J. Hilbers, J.J. Prompers, R.W. Wiseman, N.A.W. van Riel, J.A.L. Jeneson  
*In vivo and in silico studies of the regulation of glycolytic versus mitochondrial flux in normoxic skeletal muscle*  
(in preparation)

## ABSTRACT

Skeletal muscle cells contain high amounts of glycolytic enzymes and mitochondria to supply the ATP required for muscle contractions. We investigated the biochemical mechanisms that balance the contribution of glycolytic and mitochondrial flux to net ATP synthesis by an integrated *in vivo* and *in silico* systems biology approach. The mathematical model was developed by combining two previously validated mechanistic models of oxidative phosphorylation and glycolysis. *In vivo* dynamics of ATP metabolism in skeletal muscle were obtained by  $^{31}\text{P}$  MRS of rat tibialis anterior muscle during rest, electrically induced muscle contractions and metabolic recovery. Experimental data were recorded for varying contraction intensities. Comparison of model simulations and experimental data revealed that substrate feedback regulation (ADP, Pi) of oxidative phosphorylation together with substrate feedback (AMP, ADP, Pi) + calcium mediated feed forward activation of glycolysis explained *in vivo* dynamics of ATP metabolism in skeletal muscle for a wide variety of experimental conditions (normoxia, ischemia, 1 – 80Hz muscle excitation frequencies). Additional simulations with the validated model indicated that the relative contribution of oxidative phosphorylation and glycolysis to net ATP generation during exercise is predominantly controlled by the mitochondrial capacity. In contrast, glycolytic capacity influenced the balance only minor. These novel results were explained by the differences in ADP and Pi sensitivity of both pathways.

## INTRODUCTION

Skeletal muscle contains high amounts of glycolytic enzymes and mitochondria to metabolize carbohydrates and fat, respectively, in order to produce the vast amounts of ATP required to maintain energy balance during contraction and relaxation of the tissue. Slow-twitch muscle fibers predominantly rely on mitochondrial fat oxidation for ATP, while fast-twitch fibers generate ATP predominantly by metabolizing glycogen, both oxidatively (i.e., glycolysis coupled to mitochondrial pyruvate oxidation) and non-oxidatively ('anaerobic'; endproduct lactate) (1). The basis for this stratification of metabolic energy source and capacity amongst these different fiber types is genetic (2,3) and maintained, amongst others, by excitation-transcription coupling involving sensing and signal transduction pathways such as CaM2 kinase (2,3).

Recruitment of oxidative versus glycolytic ATP production upon neural excitation of a muscle is thought to be under a combination of excitatory and metabolic control (1). Calcium and the ATP hydrolysis products ADP, AMP and Pi, respectively, are known potent activators of mitochondrial and glycolytic ATP production (1). Depending on the dynamic range of ADP, AMP, Pi and calcium accumulation during a given contractile duty cycle and the particular sensitivities of the oxidative and non-oxidative ATP synthesis pathways to these stimulants, each of these pathways contributes to a varying extent to the maintenance of energy balance in the active muscle. For example, in resting muscle non-oxidative ATP synthesis contributes very little, if any, to cellular ATP production, whereas in maximally activated human gastrocnemius muscle it has been found to contribute as much as 75% of total flux (4). Here, we seek to develop a quantitative formalism to describe the balance between oxidative and glycolytic ATP production over the full dynamic range of muscle metabolic activity. This knowledge is of importance from a fundamental biochemical and physiological perspective, but also may have significant use in exercise physiology and sports science or understanding of clinical symptoms in exercise intolerance. At the core of this effort lies the development of a mechanistic computational model of muscle energy metabolism that features both the oxidative and glycolytic ATP synthetic pathways, as well as captures the main regulatory mechanisms that control flux through each of these pathways. At present, no such model is available.

Typically, the regulation of pathway fluxes *in vivo* has been investigated for conditions when only one of the pathways was active. For example, glycolysis has been predominantly studied during ischemia (5-7). In contrast, the regulation of oxidative phosphorylation has been typically studied during low intensity contractions (8) or post exercise recovery conditions (9). For these conditions it is assumed that the contribution of glycolysis to total ATP synthesis flux is negligible (8-10). A similar experimental design was applied in the studies described in chapters 3, 4 and 5; i.e., glycolysis was studied during ischemia (chapter 3) and the regulation of oxidative phosphorylation was studied during post exercise recovery (chapters 4 and 5). By comparison of *in vivo* recorded pathway dynamics and mechanistic model simulations it was concluded that oxidative ATP metabolism is predominantly controlled by metabolic feedback signals [ADP] and [Pi] (chapter 4 and 5). The dynamics of anaerobic glycolysis were explained by the combined effects of metabolic feedback signals ([AMP], [ADP], [Pi]) and feed forward activation by calcium mediated activation of glycogen phosphorylase (GP) and phosphofructokinase (PFK) (chapter 3). These results are summarized in Figure 1. It remains however elusive if these control mechanisms also explain the observed glycolytic and mitochondrial flux for conditions when both pathways are



active (exercising muscle under aerobic conditions). It is, for example, unknown if the processes connecting glycolytic and mitochondrial pathways (pyruvate import and mitochondrial redox shuttles) have a notable regulatory role on the flux through either of these pathways. As a result it remains unknown which modelling approach should be applied to represent these processes; if it is actually necessary to include detailed mechanistic descriptions of these processes in the computational model, or alternatively, if a relative simple phenomenological representation suffices to explain *in vivo* observed pathway dynamics.

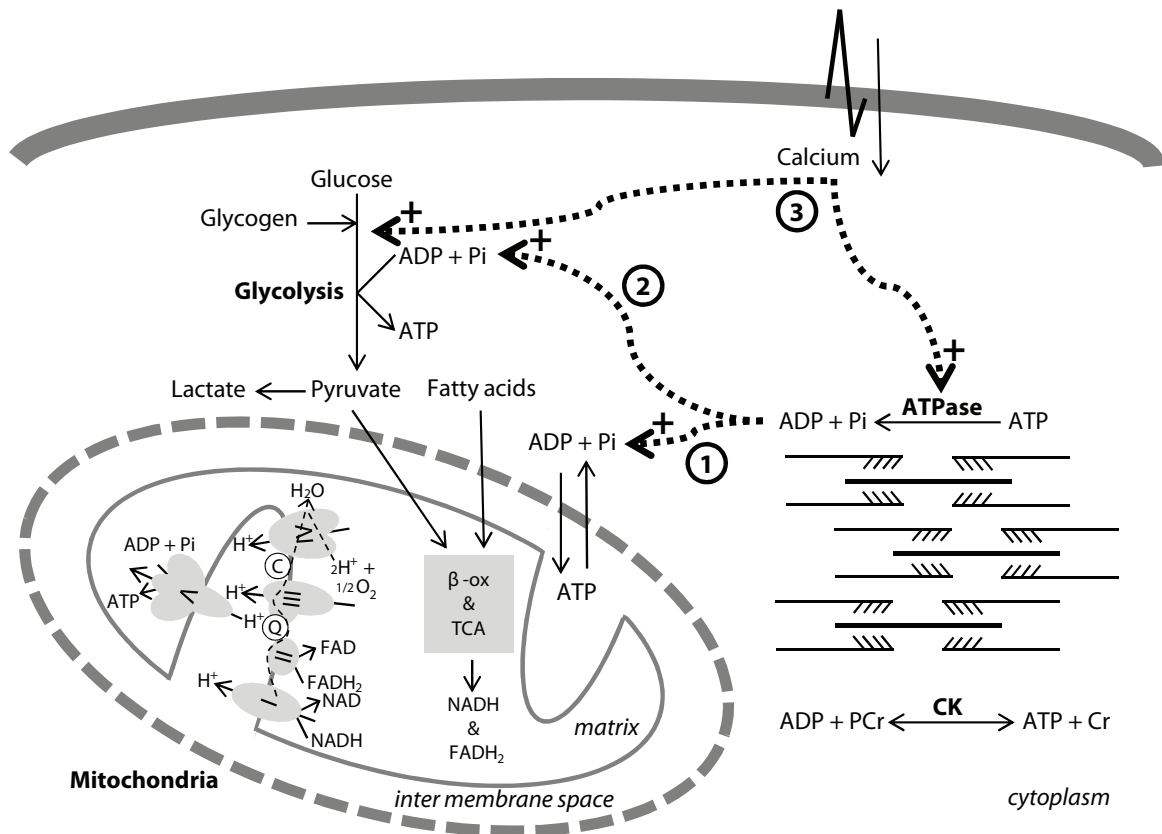


**Figure 1.** Schematic representation of the key regulatory signals controlling ATP generation in skeletal muscle according to the results presented in chapters 3, 4 and 5. Substrate feedback ( $ADP$ ,  $P_i$ ) control has a dominant role in the control of oxidative phosphorylation (1). The dynamics of anaerobic glycolysis were explained by the combined effects of metabolic feedback signals ( $[AMP]$ ,  $[ADP]$ ,  $[P_i]$ ) (2) and feed forward activation by calcium mediated activation of glycogen phosphorylase (GP) and phosphofructokinase (PFK) (3).

In an attempt to further advance our understanding of the control mechanisms that regulate mitochondrial and glycolytic ATP supply during normoxia we combined *in vivo* measurements of muscle ATP metabolism with *in silico* pathway reconstruction and analysis. The *in vivo* read-outs were acquired using  $^{31}P$  MRS of the tibialis anterior (TA) evoking contractions at three different workloads. The computational model of oxidative phosphorylation (chapter 7) was integrated in the model of glycolysis (chapter 3). As a first approximation, mitochondrial pyruvate import flux and redox shuttle flux were modeled phenomenologically. Next, model analyses were applied to test if model predictions were sensitive to possible regulation exerted by these processes. These analyses provided insight in the question if these processes should be modeled in more detail, or if

the phenomenological approach was justified. The first objective of the modeling studies was to test if these regulatory mechanisms (Figure 1) could reproduce the experimentally observed metabolite and pH dynamics. The second objective was to use the integrated model to investigate how different physiological parameters (e.g. mitochondrial content, glycolytic enzyme content) influences the balance between glycolytic and oxidative ATP synthesis.

## METHODS

### Experimental Methods

#### **Animals**

Adult male Wistar rats (376±13 gram, 14 weeks old, n=14, Charles River Laboratories, France) were housed in groups at 20°C and 50% humidity, on a 12-h light dark cycle with ad libitum access to water and chow. Principles of laboratory animal care were followed and all experimental procedures were approved by the Animal Ethics Committee of Maastricht University, the Netherlands. During preparatory surgical procedures and MRS experiments, animals were anesthetized using 0.8-1.2% isoflurane (Forene, Abbot GmbH, Wiesbaden Germany) administered via a face mask with medical air and oxygen (0.2 and 0.1 L/min respectively). Temgesic was used as analgesic (0.3mg/ml Temgesic in saline solution (1:10), 0.10 mg/kg, Schering-Plough). Body temperature was maintained at 37±1°C using heat pads and monitored by a custom build monitoring system. In the MR scanner, respiration was monitored using a pressure sensor registering thorax movement (Rapid Biomedical, Rimpar, Germany).

Contractions were induced by using electrical stimuli applied via acute, subcutaneously implanted platinum electrodes positioned along the distal nerve trajectory of the n. peroneus communis. Excitation of this nerve induced contraction in the tibialis anterior (TA), extensor digitorum longus (EDL), peroneus longus and brevis in the anterior compartment of the rat hind limb (11,12). Stimulation voltage ranged between 6-7 V, pulse length was 1 ms. Contractile duty cycles were varied over a range of frequencies (2, 5 and 80Hz) and pulse train lengths, summarized in Table 1. For each group 4-5 successful measurements were obtained in different animals.

**Table 1.** Muscle excitation parameters for each experimental group.

	<b>Excitation frequency</b>	<b>Pulse train duration (number of excitations)</b>	<b>Number of pulse trains / 5s.</b>	<b>Total number of excitations / 5s.</b>
<b>Group 1</b>	2	8	1	8
<b>Group 2</b>	5	15	1	15
<b>Group 3</b>	80	10	3	30

#### **<sup>31</sup>P NMR acquisition parameters**

All MRS measurements were performed on a 6.3 T horizontal Bruker magnetic resonance spectrometer (MRS) (Bruker, Ettlingen, Germany). Phosphorus (<sup>31</sup>P) MRS was performed by using a two coil configuration. A circular <sup>1</sup>H surface coil (40 mm) was used to adjust the magnetic field homogeneity using the available proton signal from water, while a smaller elliptical surface coil

(10/18 mm) was positioned over the TA to acquire phosphorus data.  $^{31}\text{P}$  spectra were acquired applying an adiabatic excitation pulse with a flip angle of  $90^\circ$ . A fully relaxed spectrum (TR=20 s, 32 averages) was measured at rest. A time series of spectra (TR = 5 s, 2 averages) before, during and after electrical stimulation of the TA. A time series consisted of 2 minutes rest, 3 minutes stimulation and 15 minutes recovery after stimulation.

### **Data processing**

$^{31}\text{P}$  MR spectra were fitted in the time domain by using the nonlinear least squares algorithm in the jMRUI software package (13). The PCr peak was fitted to a Lorentzian line shape. The inorganic phosphate (Pi) and  $\alpha$ - and  $\gamma$ -ATP peaks were fitted to Gaussian line shapes.  $\alpha$ - and  $\gamma$ -ATP peaks were fitted with equal peak areas. Due to the limited bandwidth of the excitation pulse, the  $\beta$ -ATP had lower amplitude and was not fitted. Absolute concentrations were calculated after correction for partial saturation with the assumption that the ATP concentration is 8.2 mM at rest (14,15). Intracellular pH was calculated from the chemical shift difference between the Pi and PCr resonances ( $\delta$ ; measured in part per million), according to Eq. 1 (16).

$$pH = 6.75 + \log\left(\frac{\delta - 3.27}{5.63 - \delta}\right) \quad (\text{Eq. 1})$$

Where,  $\delta$  is the chemical shift difference in part per million (ppm).

The  $^{31}\text{P}$  coil received signal from both contracting muscle (75%) and non-contracting muscle (25%), (see chapter 3 paragraph on *coil sensitivity profile*). The metabolite dynamics in the contracting muscle were derived from the measured dynamics according to the following calculations. The signal received by the  $^{31}\text{P}$  MRS coil is described by equation Eq. 2.

$$X_{\text{observed}}(t) = X_{\text{contraction}}(t) \cdot F_{\text{contraction}} + X_{\text{non-contracting}}(t) \cdot F_{\text{non-contracting}} \quad (\text{Eq. 2})$$

Where,  $X_{\text{observed}}$ ,  $X_{\text{contraction}}$ ,  $X_{\text{non-contracting}}$ ,  $F_{\text{contraction}}$ ,  $F_{\text{non-contracting}}$  denote the measured metabolite concentration, the metabolite concentration in contracting muscle, metabolite concentration in the non-contracting muscle, the fraction of the signal originating from contracting muscle and the fraction of the signal originating from non-contracting muscle, respectively.

$F_{\text{contraction}}$  and  $F_{\text{non-contracting}}$  were set according to the values determined from the 2D-CSI dataset: 0.75 and 0.25, respectively. The values for  $X_{\text{non-contracting}}(t)$  were set to the metabolite concentrations observed in skeletal muscle at rest: i.e., 2, 35 and 8.2 mM for Pi, PCr and ATP, respectively.

## **Computational Methods**

### **Model description**

The glycolytic model described in chapter 3 (model configuration *iii*) was combined with the model of oxidative phosphorylation of chapter 7. A schematic overview of the integrated model is shown in Figure 2.

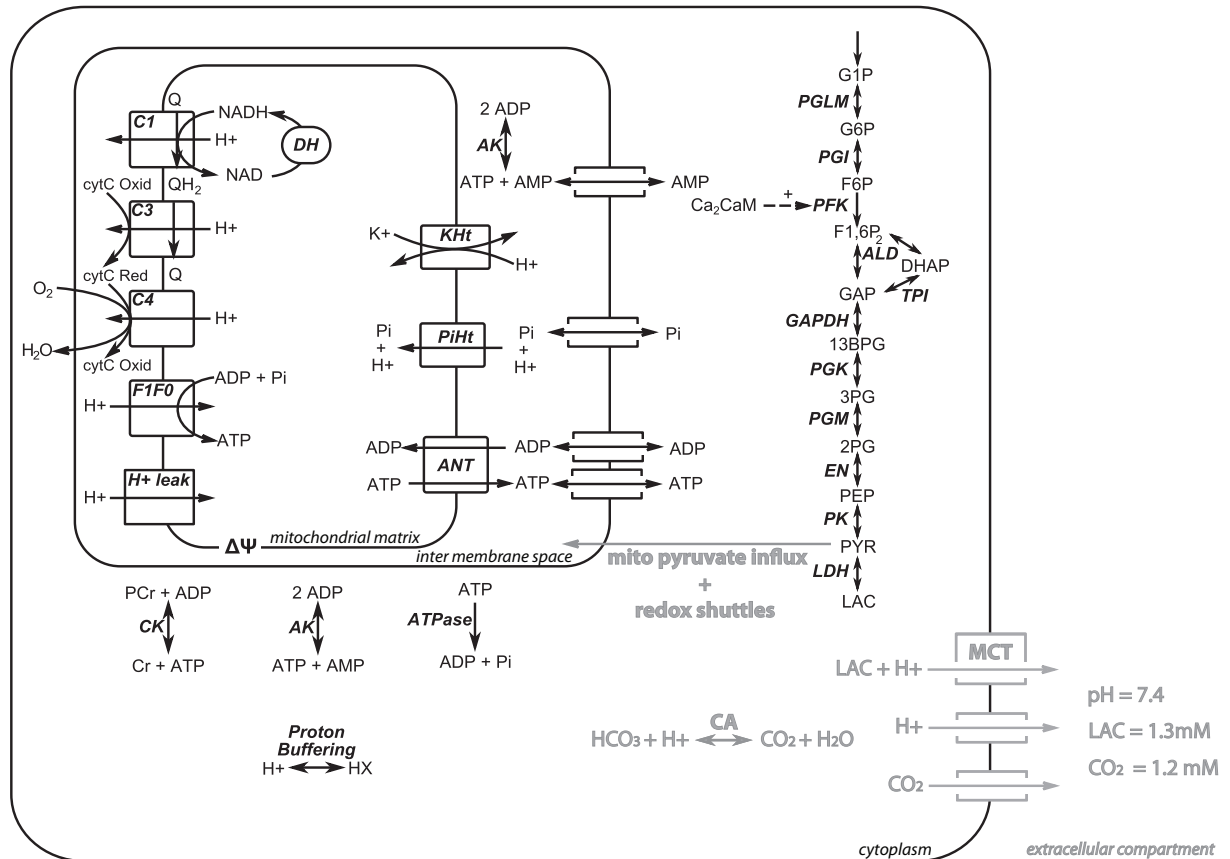


**Figure 2.** Schematic representation of the computational model. The mitochondrial component was described in chapter 7 and the glycolytic pathway was already described in chapter 3. Newly introduced model components are indicated in grey.

Compared to the model described in chapter 3, some small changes were made to the model description of the glycolytic pathway. In addition, the model contained several newly introduced components. These components are indicated in grey in Figure 2. A more detailed description of the changes to the glycolytic model and the newly introduced model components will be provided in the following paragraphs.

### Changes glycolytic model

In chapter 3, experimentally observed PME concentration (Glucose-1P+Glucose-6P+fructose-6P) was used as input to model the carbohydrate pathway supply flux by glycogen phosphorylase. For the current set of spectra, the PME resonance could not be estimated reliably because the concentration stayed below the detection limit of  $\sim 1$  mM in these particular experiments. The sum of glucose-1P, glucose-6P and fructose-6P was therefore assumed to remain at its initial value (0.059mM, 0.6mM and 0.32mM, respectively). This assumption was modelled by setting glucose-1P supply flux equal to PFK flux.

The reaction:  $DHAP + NADH \leftrightarrow G3P + NAD$  catalyzed by glycerol-3-phosphate dehydrogenase (G3PDH) was not included in the model by setting the  $V_{max}$  value of the corresponding flux to zero. The rationale for this choice was that this model component pushed the cytoplasmic NADH/NAD ratio to values close to zero. This resulted in non-physiological predictions of pyruvate concentration ( $\sim 1$  mM) in the cytoplasm at rest, which is about 10 times higher than experimentally

observed (17). Removing the G3PDH flux solved this problem. It was verified that all other state variables were close to the expected values (initial conditions) reported by Lambeth and Kushmerick (18). In addition, the  $V_{\max}$  values of all enzymes downstream of PFK (ALD, TPI, GAPDH, PGK, PMG, EN and PK) were increased 3-fold. This model adaptation was necessary to prevent excessive accumulation ( $>10\text{mM}$ ) of pathway intermediates in this part of the pathway. The 3-fold difference in  $V_{\max}$  values is within the range of variation observed between species (19-21).

#### Monocarboxylate transport + proton efflux

The glycolytic model described in chapter 3 was applied for ischemic conditions. For these conditions it was assumed the muscle cells are a closed system and all lactate and proton molecules remain in the muscle cells. This assumption was certainly not valid for the current study. Therefore a description of lactate and proton efflux was added to the model.

Transport of lactate and protons by the monocarboxylate transporters (MCT) was modelled identical to Vinnakota et al. (22). Extracellular pH and lactate concentration were set at 7.4 and 1.3mM respectively (23).

MCT facilitates efflux of both lactate and protons. There are however many other processes that can contribute to proton efflux (e.g.,  $\text{Na}^+/\text{H}^+$  exchanger). The combined effect of these processes was modelled phenomenological according to Eq. 3.

$$\text{Proton}_{\text{Efflux}} = \lambda \cdot (\text{pH} - \text{pH}_{\text{rest}}) \quad (\text{Eq.3})$$

Where,  $\lambda$  is a phenomenological proton efflux rate constant. The value of  $\lambda$  was estimated from the *in vivo* data (see section: 'parameter estimation').  $\text{pH}_{\text{rest}}$  represents the pH at rest which was set according to the experimental data to 7.15.

#### $\text{CO}_2$ , $\text{HCO}_3^-$ generation and transport

Mitochondrial  $\text{CO}_2$ ,  $\text{HCO}_3^-$  generation and transport was modelled as described in (22). In brief,  $\text{CO}_2$  production was derived from mitochondrial ATP synthesis rate assuming a P/O ratio of 4.2 and a respiratory quotient (RQ) of 1.  $\text{HCO}_3^-$  generation in the myoplasm by carbonic anhydrase (CA,  $\text{CO}_2 + \text{H}_2\text{O} \rightleftharpoons \text{HCO}_3^- + \text{H}^+$ ) and passive  $\text{CO}_2$  transport across the sarcolemma were both included in the model. Extracellular  $\text{CO}_2$  was set to 1.2mM (24).

#### Mitochondrial pyruvate influx + redox shuttles

Mitochondrial pyruvate influx and conversion to acetyl-CoA by pyruvate dehydrogenase (PDH) and redox shuttling between cytoplasm and mitochondrial matrix are highly regulated processes (25). On forehand, it was unknown if it was necessary to model these processes mechanistically. If the control exerted by these processes on glycolytic versus mitochondrial flux was negligible also a much simpler phenomenological rate equation could be applied. As a first approximation, we chose to represent these processes by a phenomenological rate equation. Subsequently, it was tested if model predictions / main study outcomes were sensitive to perturbations ( $\pm 50\%$ ) of these fluxes or if they had a negligible influence on simulation results (see: 'results' + 'discussion' sections). These analyses were used to evaluate if this part of the model required a more mechanistic model description or if, for this particular application, the phenomenological approach sufficed. Mitochondrial pyruvate influx was calculated from mitochondrial ATP synthesis rate assuming one pyruvate molecule yields 15 ATP molecules (Eq. 4). The proposed phenomenological

model agrees well with experimental observations that PDH activity is proportional to oxygen consumption rates (26,27).

$$\text{Mito}_{\text{pyruvate}}^{\text{influx}} = \frac{1}{15} J_p \quad (\text{Eq. 4})$$

Where,  $J_p$  denotes the mitochondrial ATP synthesis flux.

It was assumed that the dynamics of the redox shuttle flux followed the mitochondrial pyruvate influx. For each pyruvate molecule imported in the mitochondria one NADH molecule was converted to NAD in the cytoplasm.

### Parameter estimation

The model contained a subset of parameters for which an accurate value was not available or previously optimized in a computational study. These parameters were therefore (re-)estimated from the *in vivo* recorded pH and PCr dynamics. They are listed in Table 2 and include, the ATPase rate constant ( $k_{\text{ATP\_Hydr}}$ ), mitochondrial volume percentage (*MitoVol%*), proton efflux rate constant ( $\lambda$ ), cytoplasmic buffer capacity (*BuffCapFixed*) and PFK parameters ( $v_{\text{maxPFK}}$ ,  $k_{\text{AMP}}$ ,  $k_{\text{ADP}}$ ,  $k_{\text{AMPact}}$ ,  $k_{\text{ADPact}}$ ,  $k_{\text{on}}$ ,  $k_{\text{off}}$ ). Model parameters were estimated from the three newly recorded datasets in normoxic skeletal muscle (2, 5, and 80Hz) and three datasets previously recorded under ischemic conditions (chapter 3: rest, 10Hz, 80Hz). Parameters were estimated using a non linear least squares optimization algorithm (*lsqnonlin*, Matlab 7.5.0 (the Mathworks Inc., Natick, MA, USA) using manually tuned values as initial conditions. The difference between experimentally obtained and simulated PCr and pH dynamics was used as the error term (Eq. 5).

$$\text{SSE} = \sum_{j=1}^M \sum_{i=1}^N \left( \frac{\text{mean}(\text{PCr}_{\text{observed}}(i)) - \text{PCr}_{\text{predicted}}(i)}{\text{SD}(\text{PCr}_{\text{observed}}(i))} \right)^2 + \sum_{i=1}^N \left( \frac{\text{mean}(\text{pH}_{\text{observed}}(i)) - \text{pH}_{\text{predicted}}(i)}{\text{SD}(\text{pH}_{\text{observed}}(i))} \right)^2 \quad (\text{Eq. 5})$$

Where,  $\text{PCr}_{\text{observed}}(i)$  represents the mean [PCr] (across-animal) at time point  $i$ ;  $\text{PCr}_{\text{predicted}}(i)$  represents the predicted [PCr] at time point  $i$ ;  $\text{pH}_{\text{observed}}(i)$  represents the mean pH (across-animal) at time point  $i$ ;  $\text{pH}_{\text{predicted}}(i)$  represents the predicted pH at time point  $i$ ;  $\text{SD}(\text{PCr}_{\text{observed}}(i))$  represents the across-animal SD of the [PCr] at time point  $i$ ;  $\text{SD}(\text{pH}_{\text{observed}}(i))$  represents the across-animal SD of the pH at time point  $i$ ;  $j$  denotes a specific experimental groups.

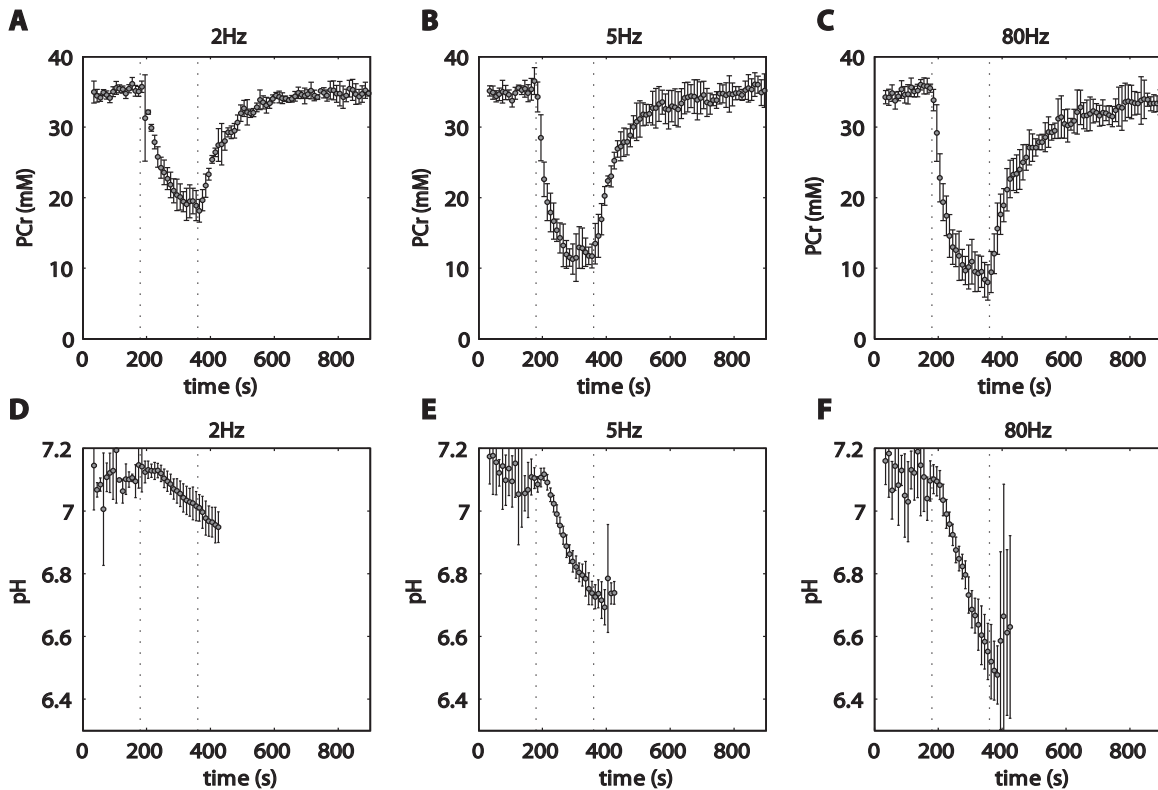


**Figure 3.** PCr and pH dynamics recorded by  $^{31}\text{P}$  MRS during rest – exercise – recovery. Results are shown for 2Hz (A,D), 5Hz (B,E) and 80Hz (C,F) experimental groups. Start and stop of the exercise period is indicated by dotted lines. Error bars denote SEM.

## RESULTS

### $^{31}\text{P}$ magnetic resonance spectroscopy

The dynamics of cellular metabolites: adenosine-triphosphate (ATP), phosphocreatine (PCr), inorganic phosphate (Pi) and intracellular pH were monitored by  $^{31}\text{P}$  magnetic resonance spectroscopy in rat TA muscle, under varying muscle stimulation frequencies (see Table 1). Figure 3A-F show PCr and pH dynamics in the contracting muscle that were used for model testing. In response to muscle contraction and corresponding elevated ATP demand flux, the cellular ATP buffer, PCr, is consumed to balance energy demand and supply. PCr depletion coincides with the production of Pi (data not shown), a product of ATP hydrolysis. In addition, a decrease in muscle pH was observed during the period muscle contractions were induced. The observed proton accumulation was larger for more intense muscle contractions. These observations are consistent with the notion that the contribution of glycolytic ATP supply increases with exercise intensity. After the muscle contractions were stopped (marked by a dotted line), PCr was resynthesized and Pi levels were restored. Consequently, the Pi resonance in the spectra became smaller and even disappeared in the noise after about 60 seconds. As a result, for the remaining part of the recovery period, the estimates of cell pH became unreliable. pH recovery dynamics are therefore only shown for the first 60 seconds of recovery period.

**Table 2.** Optimized parameter values.

Parameter	Unit	Description	Previously used values (chapter 3)	Optimized parameter value
<b><math>k_{ATP\_Hydr}</math> (2Hz)</b>	$s^{-1}$	ATPase rate constant 2Hz	-	0.035
<b><math>k_{ATP\_Hydr}</math> (5Hz)</b>	$s^{-1}$	ATPase rate constant 4Hz	-	0.059
<b><math>k_{ATP\_Hydr}</math> (80Hz)</b>	$s^{-1}$	ATPase rate constant 80Hz	-	0.078
<b><math>k_{ATP\_Hydr}</math> (0Hz) ischemia</b>	$s^{-1}$	ATPase rate constant 0Hz ischemia	0.0017	0.0014
<b><math>k_{ATP\_Hydr}</math> (10Hz) ischemia</b>	$s^{-1}$	ATPase rate constant 10Hz ischemia	0.056	0.046
<b><math>k_{ATP\_Hydr}</math> (80Hz) ischemia</b>	$s^{-1}$	ATPase rate constant 80Hz ischemia	0.050	0.033
<b>BuffCapFixed</b>	M	Fixed buffer cellular proton buffer capacity	0.050	0.014
<b><math>v_{max}PFK</math></b>	$mM s^{-1}$	$V_{max}$ PFK	10.25	23.1
<b><math>k_{AMP}</math></b>	mM	PFK deinhibition constant AMP	0.046	0.0080
<b><math>k_{ADP}</math></b>	mM	PFK deinhibition constant ADP	0.24	0.87
<b><math>k_{AMPact}</math></b>	mM	PFK deinhibition constant AMP activated PFK	$8.97 \cdot 10^{-5}$	$3.33 \cdot 10^{-5}$
<b><math>k_{ADPact}</math></b>	mM	PFK deinhibition constant ADP activated PFK	0.020	0.13
<b><math>k_{on}</math></b>	$\mu M^{-2} s^{-1}$	PFK, calcium – calmodulin binding constant	$5.00 \cdot 10^5$	$6.11 \cdot 10^5$
<b><math>k_{off}</math></b>	$s^{-1}$	PFK, calcium – calmodulin binding constant	106	49.3
<b>MitoVol%</b>	percent	Mitochondrial volume percentage	-	2.0
<b><math>\lambda</math></b>	mM Unit $pH^{-1} s^{-1}$	Proton efflux parameter	-	$5.0 \cdot 10^{-3}$

**Model (hypotheses) testing**

Comparison of model simulations and experimental data was used to test if the control mechanisms captured by the model explained the PCr and pH dynamics for the different contraction intensities, Figure 4 A-F. In order to obtain these results a subset of the model parameters (see, Table 2) was re-estimated. These parameters were previously estimated based on the data recorded during ischemia (chapter 3). In order to ensure that although some parameter values were a little adjusted the model could still reproduce the ischemia data, a part of these datasets (0Hz, 10Hz, 80Hz) was included in the parameter estimation process. Simulation results for these ischemia experiments are shown in Figure 4 G-L.



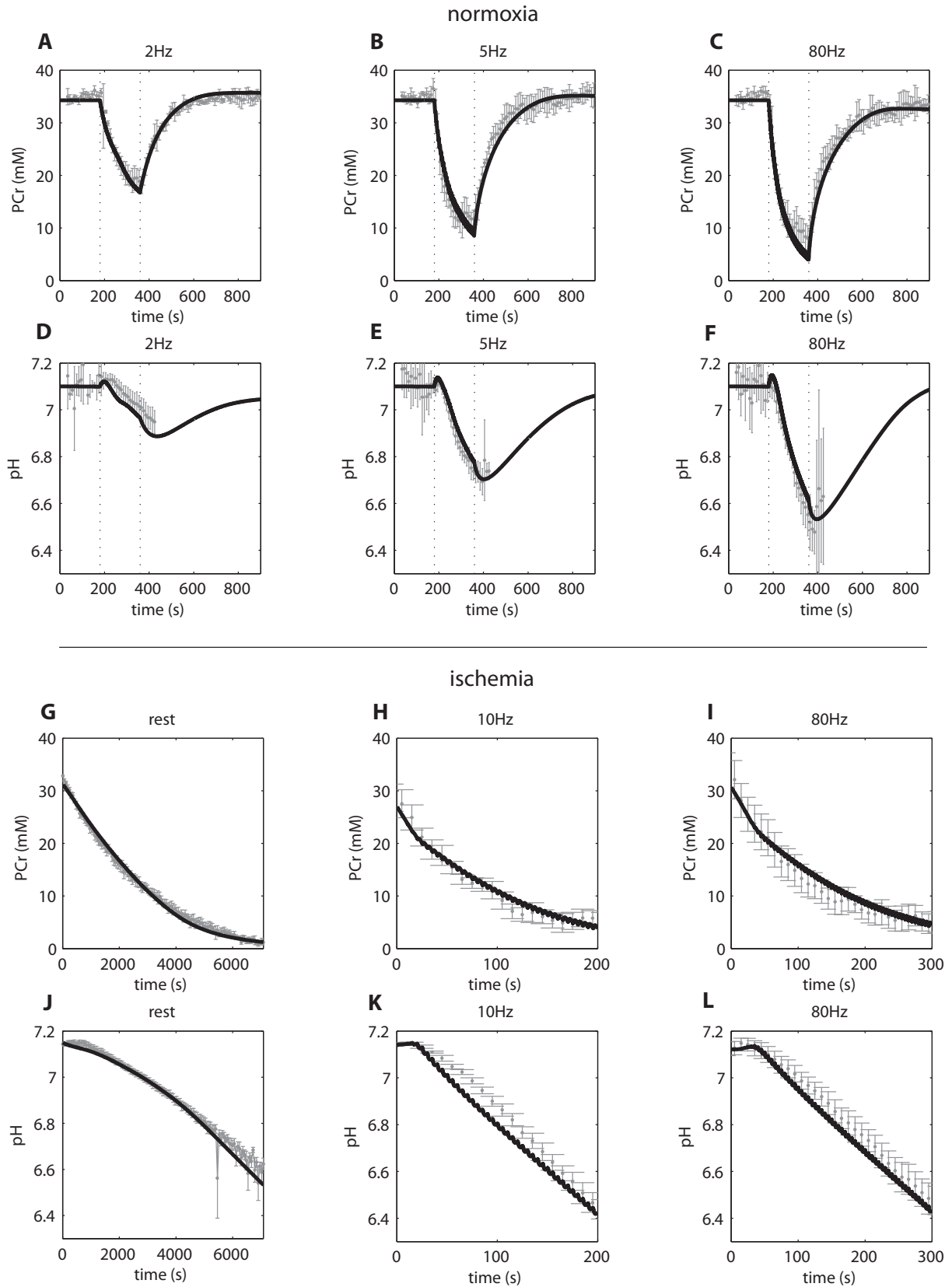


**Figure 4.** Model simulations (black lines) compared to experimental data (PCr and pH dynamics) for normoxic conditions (A-F) and ischemia (G-L). Data recorded during ischemia were already presented in chapter 3. Error bars denote SEM

### Model predictions: mitochondrial versus glycolytic flux

Figure 5A-C shows the predicted glycolytic and mitochondrial ATP synthesis flux during the rest – exercise – recovery protocols. These simulation results were used to quantify the relative contribution of both processes to total ATP production flux, see Figure 6. The predicted contribution of glycolysis was 8.3, 16.2, 37.0 and 48.4% for rest and exercise conditions (1Hz, 5Hz and 80Hz) respectively. These results are in good accordance with several basic notions on muscle physiology: i.e., (i) at rest, ATP is largely supplied via oxidative phosphorylation; (ii) glycolysis is activated during exercise and (iii) its contribution increases at higher workloads; (iv) during recovery phase, the glycolytic flux decreases rapidly and ATP is almost purely synthesized in the mitochondria again.

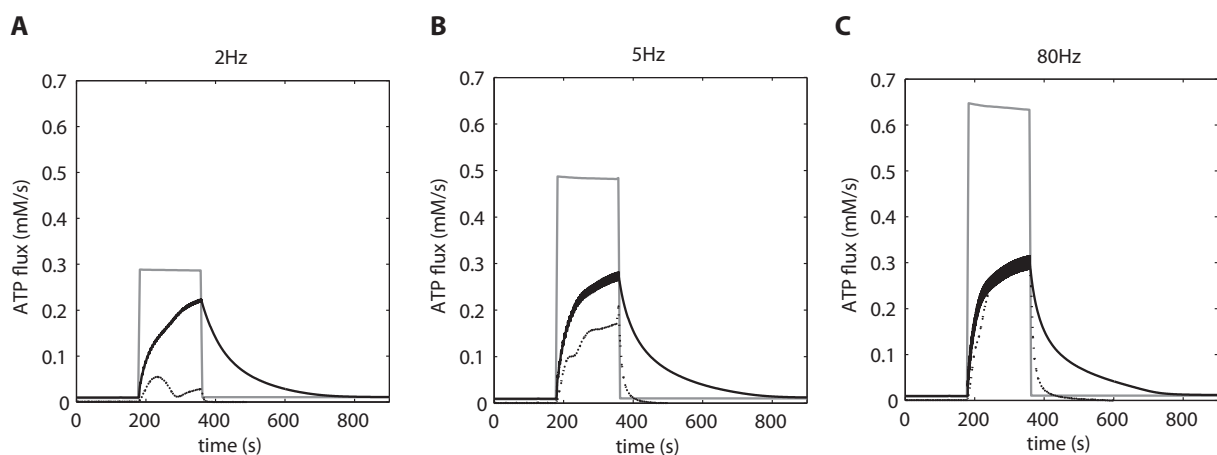


**Figure 5.** Model predictions of ATP consumption flux (grey lines), mitochondrial ATP synthesis (black lines) and glycolytic ATP synthesis flux (dotted lines) during rest – exercise – recovery for 2Hz (A), 5Hz (B) and 80Hz (C) experimental groups.

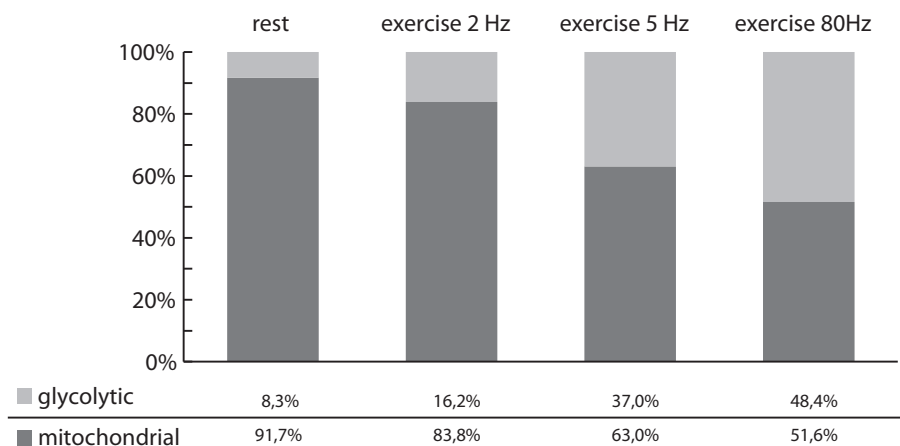
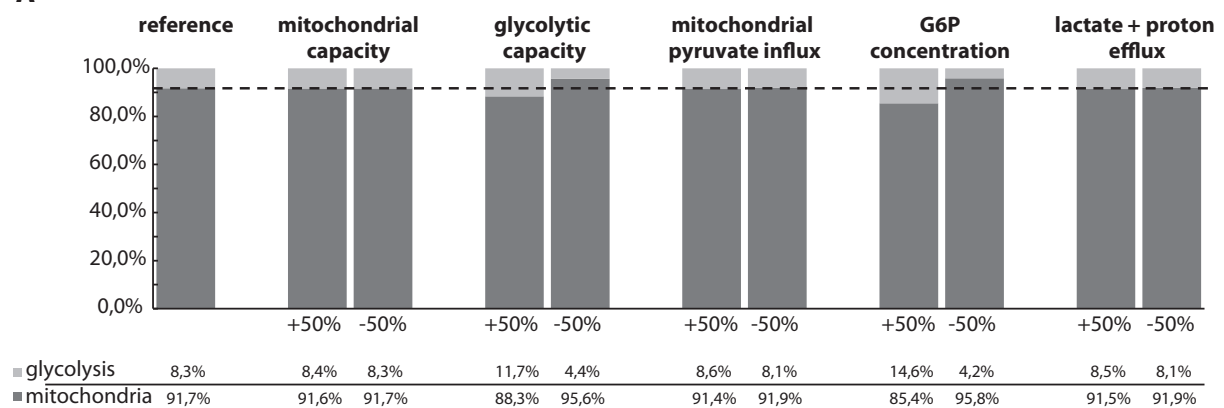


**Figure 6.** Relative contribution of aerobic and anaerobic ATP synthesis fluxes to net ATP generation.

Next, the influence of different cellular processes on the balance between mitochondrial and glycolytic flux was investigated. The processes that were included in this analysis are: (i) mitochondrial capacity, (ii) glycolytic capacity, (iii) lactate + proton efflux, (iv) mitochondrial pyruvate influx, (v) G6P concentration. The set of model parameters that represented each of these processes is listed in Table 3. The influence of +/-50% parameter perturbations on the relative

contribution of glycolytic and mitochondrial flux was quantified for rest and exercise conditions (80Hz), Figure 7. The parameter perturbations had a relatively small effect on the balance between mitochondrial and glycolytic flux at rest (Figure 7A). The effect of adjusting mitochondrial content, mitochondrial pyruvate influx and lactate + proton efflux had a negligible influence on the fluxes. An increased glycolytic capacity and G6P concentration resulted in an increased glycolytic flux at rest. However, also for these parameter perturbations, the large majority of ATP was produced oxidatively. For exercise conditions (Figure 7B) the predictions were somewhat different. The influence of the mitochondrial pyruvate influx and lactate + proton efflux rate was again negligible small. The changes in flux as a result of adjusting glycolytic capacity and G6P concentration, however, were also rather small. In contrast, changes in mitochondrial capacity had a very significant influence in the predicted balance between mitochondrial and glycolytic flux.

A



B

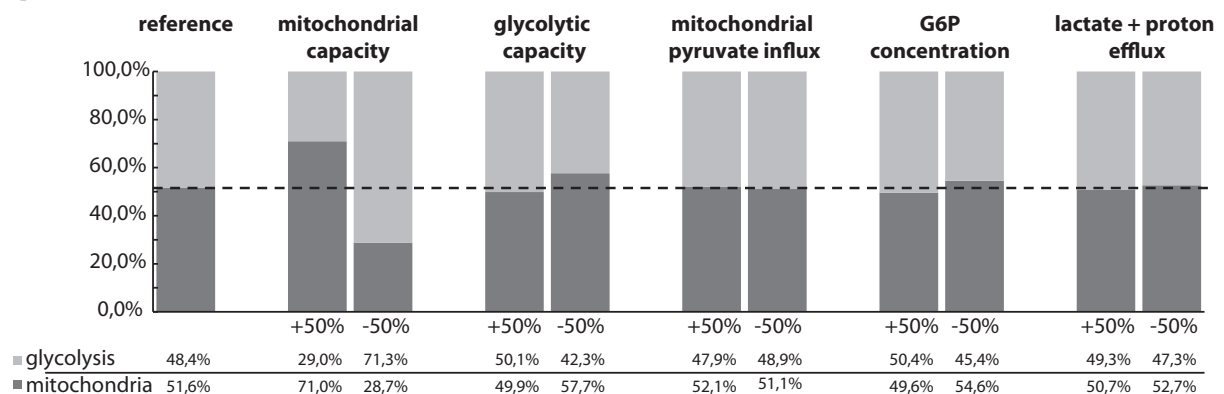


**Figure 7.** The influence of +/-50% parameter perturbations on the relative contribution of glycolytic and mitochondrial flux quantified for rest (A) and exercise conditions (80Hz, B). The set of model parameters that represented each of these processes is listed in Table 3.

**Table 3.** Model parameters that represented a process included in the sensitivity analysis. If a process is represented by more than one parameter (e.g., glycolytic capacity, lactate + proton efflux) all parameters were adjusted at once.

Process	Parameters
Mitochondrial capacity	Mitochondrial volume percentage ( <i>MitoVol%</i> )
Glycolytic capacity	$V_{max}$ parameters of all glycolytic enzymes (PGLM, PGI, PFK, ALD, TPI, GAPDH, PGK, PGM, EN, PK, LDH)
Lactate + proton efflux	$V_{max}$ <i>MCT</i> , proton efflux rate constant ( $\lambda$ ), passive $CO_2$ permeation flux rate constant ( <i>PSVCO<sub>2</sub></i> )
Mitochondrial pyruvate influx	Mito <sup>influx</sup> <sub>pyruvate</sub> (see: Eq. 4)
G6P concentration	Initial [G6P]

The influence of mitochondrial and glycolytic capacity on the observed balance between the contributions of both processes to net ATP synthesis was further investigated. In particular, the relation between changes in mitochondrial and glycolytic capacity and predictions of cellular [ADP] were analyzed. Figure 8 shows predictions of cytoplasmic [ADP] versus mitochondrial and glycolytic ATP synthesis fluxes during exercise in time (colour coding). These results show that adjusting glycolytic or mitochondrial capacities influences [ADP] during exercise. Decreasing glycolytic or mitochondrial capacity (panels B and D) increased the rate of ADP accumulation during exercise and the end-exercise [ADP]. Increasing glycolytic or mitochondrial capacity (panels C and E) had the opposite effect; it decreased [ADP]. The effect of changing the capacity of each of these processes on cellular [ADP] was thus very similar. In addition, the simulations indicated that the observed variation in [ADP] (0.1 – 0.3 mM) as a result of  $\pm 50\%$  perturbations of glycolytic capacity affected mitochondrial flux only minor (compare for example, end-exercise fluxes in panels A, B and C). At these [ADP], mitochondria operated already close to their  $V_{max}$  levels and were consequently rather insensitive to changes in [ADP]. In contrast, the variation in [ADP] as a result of  $\pm 50\%$  perturbations of mitochondrial capacity affected glycolytic flux considerably (compare for example, end-exercise fluxes in panels A, D and E). These differences in pathway sensitivity to ADP explain why adjusting the mitochondrial capacity did influence the glycolytic flux while the opposite was not observed (Figure 7).

## DISCUSSION

The first main result of this investigation was that the developed model successfully described the balance between oxidative and glycolytic ATP production for the full dynamic range of muscle metabolic activity between rest and maximal. These results provided, for the first time, quantitative evidence that the regulation of glycolytic versus mitochondrial ATP synthesis flux is explained by the combined effects of substrate feedback regulation (ADP, Pi) of oxidative phosphorylation and substrate feedback (AMP, ADP, Pi) and feed-forward regulation ( $Ca^{2+}$ ) of glyco(gen)olysis. Second, model predictions revealed that the balance between mitochondrial and glycolytic flux during exercise is very sensitive to mitochondrial capacity. Other factors, like e.g., glycolytic capacity, were predicted to have a much smaller influence. In this section, these main results, their physiological implications and several methodological considerations will be discussed.

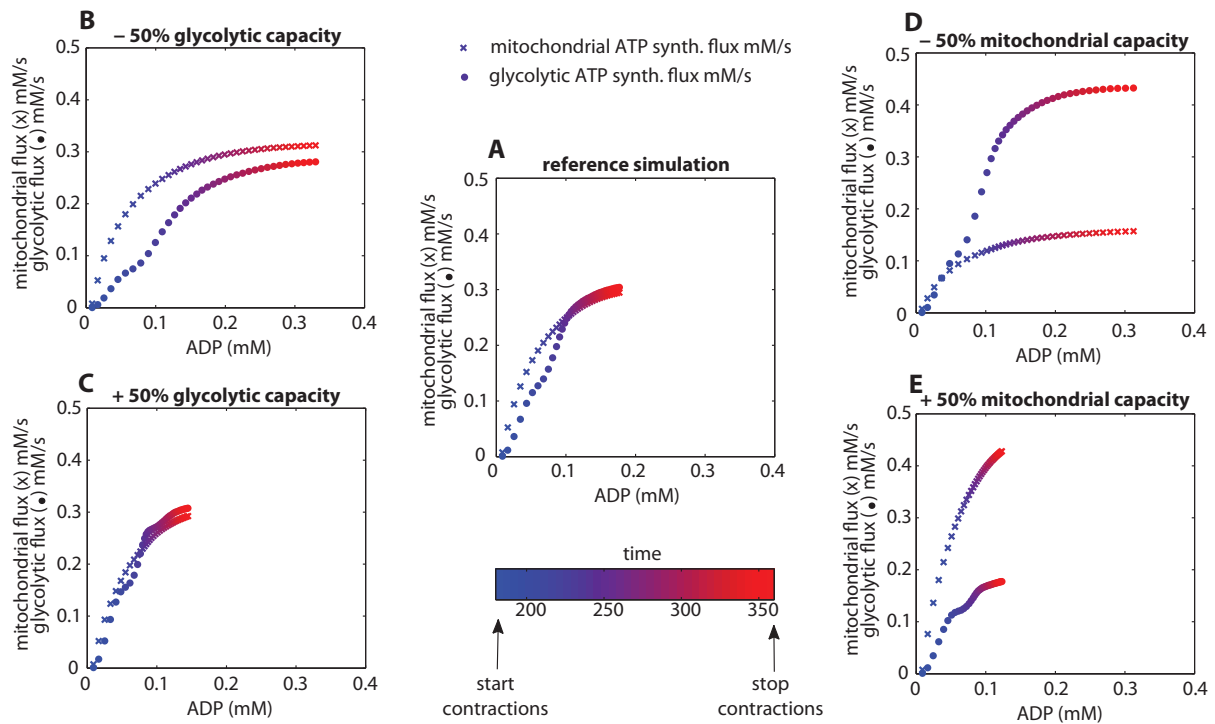


**Figure 8.** Predictions of cytoplasmic ADP concentration versus mitochondrial (crosses) and glycolytic (dots) ATP syntheses fluxes during exercise in time (color coding). Simulation results are shown for the reference simulation (A),  $\pm 50\%$  perturbations of glycolytic capacity (B and C) and  $\pm 50\%$  perturbations of mitochondrial capacity (D and E).

### Methodological considerations

The model that provided the basis for this investigation was constructed by combining a model of oxidative phosphorylation (chapter 4 and 5) with a model of glycolysis (chapter 3). The mitochondrial module did not include a detailed mechanistic descriptions of pyruvate influx, TCA cycle or redox shuttles. The pyruvate influx in the mitochondria and conversion to acetyl-CoA and redox shuttle activity are highly regulated processes (25). On forehand it was unknown if these control mechanisms contribute to the regulation of mitochondrial versus glycolytic flux. It was therefore decided to represent pyruvate influx and redox shuttles by a phenomenological equation and to test if model predictions were sensitive to changes in activity of this flux. These experiments (Figure 7) revealed that these processes had a negligible small influence on the balance between mitochondrial and glycolytic flux, justifying application of a phenomenological model equation. Similar considerations were taken into account for the lactate and proton efflux. As a first approximation, extracellular [lactate],  $[\text{CO}_2]$  and pH were clamped at resting values. It was verified that model predictions were not sensitive to  $\pm 50\%$  perturbations of lactate and proton efflux rates (Figure 7).

For the comparison of model predictions and experimental data a subset of model parameters was optimized (Table 2). These parameters can be divided into three categories: newly introduced parameters (proton efflux rate constant  $\lambda$ ), parameters which modelled specific experimental conditions (ATPase rate constants) and PFK parameters + buffer capacity. The values of this latter category were previously estimated based on PCr and pH time course data during ischemia (chapter 3). It was therefore crucial to verify that the new parameter values were still

consistent with the data during ischemia. The simulations shown in Figure 4G-L confirmed this was indeed the case. These results indicated that these glycolytic pathway dynamics during ischemia and normoxia are explained by a single set of regulatory mechanisms. The new parameter values can therefore be considered an improved and more accurate set, representing the same regulatory mechanisms.

Although the match between experimental data and model simulations was already of high-quality (Figure 4), the predictions of pH dynamics for the 2Hz muscle excitation protocol could be further improved. The predicted pH declined a bit too fast at the onset of exercise, which resulted in a small offset in pH for the remaining part of the time course. The initial peak in glycolytic flux was caused by pathway intermediates that were accumulated during the pre-simulation model equilibration phase. The model fit could be improved by reducing the G6P concentration at rest from 0.6mM to 0.4mM, which resulted in a smaller accumulation of pathway intermediates. To further improve the accuracy of predictions at low exercise intensities it could be necessary to extend the model with key processes controlling G6P concentration: i.e., glycogen phosphorylase, glycogen synthase and cellular glucose import flux and phosphorylation by hexokinase.

#### ***Regulation of mitochondrial and glycolytic fluxes during rest – exercise recovery***

It is widely accepted that during rest – exercise – recovery transitions the relative contribution of glycolysis and mitochondria to total ATP supply shifts (28). It was concluded that this emergent behaviour is largely explained by the combined effects of ADP and Pi substrate feedback regulation of oxidative phosphorylation in combination with AMP, ADP, and Pi substrate regulation + calcium mediated feed-forward activation of glycolysis.

The first piece of evidence supporting this conclusion was the high-quality fit of the mathematical model capturing these control mechanisms and the PCr and pH time course data recorded at different workloads. PCr and pH dynamics have been frequently applied as reporter of glycolytic or mitochondrial ATP synthesis. For example, an increased glycolytic component present at more intense muscle contractions is often reflected by an accelerated muscle acidosis (28). As a result of the high activity of the creatine kinase enzyme *in vivo*, the derivative of PCr dynamics ( $dPCr/dt$ ) represents the difference between ATP demand and supply fluxes (29). PCr time course data are often exploited as measure of mitochondrial ATP synthesis flux during post exercise recovery (9) or to determine glycolytic flux during ischemia (5). The combined PCr and pH dynamics are therefore considered well suited for testing the control mechanisms embedded in the model.

The model predicted that in rest 8.3% of all ATP is provided by glycolysis, which may vary a bit depending on cellular glycolytic capacity or G6P concentrations (see, Figure 7). Assuming that at rest mitochondria rely for 50% on pyruvate as oxidizable substrate (30-32) and that the ATP yield for one glucose molecule is about 15:1 for mitochondria and glycolysis respectively, the expected glycolytic contribution to total ATP supply flux is 3.3%, which is about 2-3 fold lower than predicted. These predictions suggest that skeletal muscle cells at rest release small amounts of lactate, which has been confirmed by experimental data (33-35).

During aerobic exercise the contribution of glycolysis to net ATP synthesis was predicted to increase at higher workloads. These results are in good accordance with traditional notions in muscle physiology (28,36). The predicted shift towards a larger glycolytic contribution was a result

of the increased feed-forward activation signal which acted only on the glycolytic pathway. In addition, differences in ADP and Pi sensitivity between the pathways contributed as well. Oxidative phosphorylation is more sensitive to changes at relatively low [ADP], while the glycolytic pathway is more sensitive to changes at higher ADP levels. Consequently, the relative activation of mitochondria is the largest at low ADP and Pi levels, which occur during low intensity exercise; the contribution of glycolysis increases at higher ADP and Pi levels, which are associated with high intensity exercise.

During the recovery period, ATP supply was predicted to shift rapidly towards a dominant contribution by oxidative phosphorylation. This rapid silencing of glycolytic flux is in good accordance with experimental observations (6,10,37). The model predicted that these deactivation kinetics were not instantaneously, but that glycolytic flux remained elevated for the first few seconds of recovery and were completely silenced after 20 – 30 seconds of recovery period. These results are in good accordance with the deactivation time reported by two other independent studies (6,38). Previously, these deactivation kinetics were already predicted for ischemic conditions. The current analysis shows that they can also be expected during aerobic conditions.

### ***Pasteur versus Crabtree effect***

Model analysis revealed that changes in the mitochondrial capacity have a very strong influence on the contribution of glycolysis and oxidative phosphorylation to net ATP synthesis during exercise: increasing the mitochondrial capacity shifted the balance towards oxidative phosphorylation while decreasing mitochondrial capacity increased glycolytic flux. In classic biochemistry, this regulatory effect (inhibition of glycolysis by respiration) is known as the 'Pasteur effect'. There is some (indirect) experimental evidence that can be explained by the existence of this effect in skeletal muscle tissue. For example: (i) experiments in humans comparing glycogenolytic flux during normoxia and ischemia revealed an increased flux during ischemia (39) (ii) it has been documented that the lactate threshold is correlated with the oxidative capacity of muscle cells (40); (iii) endurance training increases the respiratory capacity of skeletal muscle cells and results in a decreased glycolytic flux during exercise (41,42); (iv) one of the main clinical symptoms of mitochondrial myopathies are high blood lactate concentrations, which are a result of increased glycolytic flux in the muscle cells (43). The current investigation provides a mechanistic explanation for these experimental observations. Glycolysis and oxidative phosphorylation are both activated by ADP and Pi, albeit with a different sensitivity (see section: *regulation of mitochondrial and glycolytic fluxes during rest – exercise recovery*). Changes in the mitochondrial capacity are reflected in the [ADP] and [Pi] during exercise (lower mitochondrial capacity increases [ADP] and [Pi]; higher mitochondrial capacity decreases [ADP] and [Pi]). Via these changes in [ADP] and [Pi], mitochondria influence glycolytic flux. In the computational analyses the mitochondrial capacity was adjusted by adjusting mitochondrial volume percentage (see, Table 3). It is important to note that this is not the only model parameter that influences the mitochondrial capacity (see e.g., chapters 6 and 7). Adjusting for example, mitochondrial enzyme content ( $V_{max}$  values) resulted in a change in mitochondrial capacity, which in turn affected the predicted balance between mitochondrial and glycolytic flux (data not shown). It was concluded that each model parameter that influenced the mitochondrial capacity, via this effect, can also change the relative contribution of mitochondrial versus glycolytic flux.

While changing mitochondrial capacity had a large influence on glycolytic flux, adjusting glycolytic capacity caused only minor changes in mitochondrial flux. This regulatory process (inhibition of respiration by glycolysis) is also known as the 'Crabtree effect'. At first this result may seem counterintuitive, but it is explained by the differences in ADP and Pi sensitivity of both pathways. Mitochondria are very sensitive to changes in ADP at concentrations between 0.01 and 0.1mM, while for ADP > 0.1mM mitochondrial flux approximates  $V_{max}$  (see chapter 4 and Figure 8). Glycolysis is less sensitive for ADP; the pathway is activated at higher ADP concentrations. Adjusting the glycolytic capacity was also reflected in changes in cytoplasmic ADP (Figure 8), but these differences occur in the domain mitochondria are less sensitive (ADP>0.1mM). Consequently, mitochondrial flux remained approximately the same even though glycolytic capacity was adjusted.

Interestingly, at rest the exact opposite was observed. For these conditions (ADP ~ 0.01mM) mitochondria are very sensitive to changes in ADP whereas glycolysis is not. As a result, changes in mitochondrial capacity (and corresponding changes in ADP and Pi) do not affect glycolytic flux while the opposite was observed.

### ***In summary***

In this chapter we demonstrate successful integration of a model of glycolysis (chapter 3) and mitochondria (chapter 7), yielding the first detailed mechanistic model, that is consistent with *in vivo* dynamics of ATP metabolism in skeletal muscle for a wide range of experimental conditions (normoxia, ischemia, 1 – 80Hz muscle excitation frequencies). The primary physiological implication of this result is that the regulation of glycolytic versus mitochondrial flux in skeletal muscle is predominantly controlled by substrate feedback regulation (ADP, Pi) of oxidative phosphorylation combined with substrate feedback (AMP, ADP, Pi) + calcium mediated feed forward activation of glycolysis. To the best of our knowledge, there is, at the moment, no alternative set of mechanisms that was shown to be consistent with *in vivo* data for such a wide range of physiological conditions. In addition, simulations revealed that the relative contribution of oxidative phosphorylation and glycolysis to net ATP generation during exercise is predominantly controlled by the mitochondrial capacity; in contrast, glycolytic capacity influenced the balance only minor. These results also have important physiological implications. They suggest, for example, that the difference in mitochondrial and glycolytic fluxes observed between different muscle fibers (type I (oxidative) versus type IIA and IIX (glycolytic)) are a result of differences in mitochondrial capacities between fibers (36) whereas the observed differences in glycolytic capacity of the muscle fibers (36) are expected to have a much smaller influence.



## REFERENCES

1. **Meyer RA, Foley JM.** The Handbook of Physiology, Volume 12, Exercise: Regulation and Integration of Multiple Systems, Chapter: 18: Cellular processes integrating metabolic responses to exercise 841-869 Bethesda: American Physiological Society, 1996
2. **Chin ER, Olson EN, Richardson JA, Yang Q, Humphries C, Shelton JM, Wu H, Zhu W, Bassel-Duby R and Williams RS.** A calcineurin-dependent transcriptional pathway controls skeletal muscle fiber type. *Genes Dev* 12: 2499-2509, 1998
3. **Chin ER.** Role of Ca<sup>2+</sup>/calmodulin-dependent kinases in skeletal muscle plasticity. *J Appl Physiol* 99: 414-423, 2005
4. **Walter G, Vandenborne K, Elliott M and Leigh JS.** In vivo ATP synthesis rates in single human muscles during high intensity exercise. *J Physiol* 519 Pt 3: 901-910, 1999
5. **Conley KE, Blei ML, Richards TL, Kushmerick MJ and Jubrias SA.** Activation of glycolysis in human muscle in vivo. *Am J Physiol* 273: C306-C315, 1997
6. **Crowther GJ, Kemper WF, Carey MF and Conley KE.** Control of glycolysis in contracting skeletal muscle. II. Turning it off. *Am J Physiol Endocrinol Metab* 282: E74-E79, 2002
7. **Crowther GJ, Carey MF, Kemper WF and Conley KE.** Control of glycolysis in contracting skeletal muscle. I. Turning it on. *Am J Physiol Endocrinol Metab* 282: E67-E73, 2002
8. **Jeneson JA, Westerhoff HV, Brown TR, Van Echteld CJ and Berger R.** Quasi-linear relationship between Gibbs free energy of ATP hydrolysis and power output in human forearm muscle. *Am J Physiol* 268: C1474-C1484, 1995
9. **Kemp GJ, Taylor DJ and Radda GK.** Control of phosphocreatine resynthesis during recovery from exercise in human skeletal muscle. *NMR Biomed* 6: 66-72, 1993
10. **Quistorff B, Johansen L and Sahlin K.** Absence of phosphocreatine resynthesis in human calf muscle during ischaemic recovery. *Biochem J* 291 ( Pt 3): 681-686, 1993
11. **De Feyter HM.** Lipids & Mitochondria in Diabetic Muscle, Dissertation: *Eindhoven University of Technology*, 2007
12. **De Feyter HM, Lenaers E, Houten SM, Schrauwen P, Hesselink MK, Wanders RJ, Nicolay K and Prompers JJ.** Increased intramyocellular lipid content but normal skeletal muscle mitochondrial oxidative capacity throughout the pathogenesis of type 2 diabetes. *FASEB J* 22: 3947-3955, 2008
13. **Vanhamme L, van den BA and Van HS.** Improved method for accurate and efficient quantification of MRS data with use of prior knowledge. *J Magn Reson* 129: 35-43, 1997
14. **Taylor DJ, Styles P, Matthews PM, Arnold DA, Gadian DG, Bore P and Radda GK.** Energetics of human muscle: exercise-induced ATP depletion. *Magn Reson Med* 3: 44-54, 1986
15. **Veech RL, Lawson JW, Cornell NW and Krebs HA.** Cytosolic phosphorylation potential. *J Biol Chem* 254: 6538-6547, 1979
16. **Tobin RB, Mackerer CR and Mehlman MA.** pH effects on oxidative phosphorylation of rat liver mitochondria. *Am J Physiol* 223: 83-88, 1972
17. **Sahlin K, Katz A and Henriksson J.** Redox state and lactate accumulation in human skeletal muscle during dynamic exercise. *Biochem J* 245: 551-556, 1987
18. **Lambeth MJ, Kushmerick MJ.** A computational model for glycogenolysis in skeletal muscle. *Ann Biomed Eng* 30: 808-827, 2002
19. **Scopes RK.** Studies with a reconstituted muscle glycolytic system. The rate and extent of creatine phosphorylation by anaerobic glycolysis. *Biochem J* 134: 197-208, 1973
20. **Shonk CE, Boxer GE.** Enzyme patterns in human tissues I. Methods for the determination of glycolytic enzymes. *Cancer Res* 24: 709-721, 1964
21. **Shonk CE, Koven BJ, Majima H and Boxer GE.** Enzyme patterns in human tissues II. Glycolytic enzyme patterns in nonmalignant human tissues. *Cancer Res* 24: 722-731, 1964
22. **Vinnakota KC, Rusk J, Palmer L, Shankland E and Kushmerick MJ.** Common phenotype of resting mouse extensor digitorum longus and soleus muscles: equal ATPase and glycolytic flux during transient anoxia. *J Physiol* 588: 1961-1983, 2010
23. **Musch TI, Terrell JA.** Skeletal muscle blood flow abnormalities in rats with a chronic myocardial infarction: rest and exercise. *Am J Physiol* 262: H411-H419, 1992
24. **Geers C, Gros G.** Carbon dioxide transport and carbonic anhydrase in blood and muscle. *Physiol Rev* 80: 681-715, 2000
25. **Harris RA, Bowker-Kinley MM, Huang B and Wu P.** Regulation of the activity of the pyruvate dehydrogenase complex. *Adv Enzyme Regul* 42: 249-259, 2002
26. **Putman CT, Jones NL, Lands LC, Bragg TM, Hollidge-Horvat MG and Heigenhauser GJ.** Skeletal muscle pyruvate dehydrogenase activity during maximal exercise in humans. *Am J Physiol* 269: E458-E468, 1995
27. **Spriet LL, Heigenhauser GJ.** Regulation of pyruvate dehydrogenase (PDH) activity in human skeletal muscle during exercise. *Exerc Sport Sci Rev* 30: 91-95, 2002
28. **Guyton AC, Hall JE.** *Textbook of Medical Physiology 10th ed.* Philadelphia: Saunders company, 2000
29. **Kushmerick MJ.** Energy balance in muscle activity: simulations of ATPase coupled to oxidative phosphorylation and to creatine kinase. *Comp Biochem Physiol B Biochem Mol Biol* 120: 109-123, 1998
30. **Bergman BC, Butterfield GE, Wolfel EE, Casazza GA, Lopaschuk GD and Brooks GA.** Evaluation of exercise and training on muscle lipid metabolism. *Am J Physiol* 276: E106-E117, 1999
31. **Bradley SJ, Kingwell BA and McConell GK.** Nitric oxide synthase inhibition reduces leg glucose uptake but not blood flow during dynamic exercise in humans. *Diabetes* 48: 1815-1821, 1999
32. **Jensen MD, Nguyen TT, Hernandez MA, Johnson CM and Murray MJ.** Effects of gender on resting leg blood flow: implications for measurement of regional substrate oxidation. *J Appl Physiol* 84: 141-145, 1998
33. **Bender PR, Groves BM, McCullough RE, McCullough RG, Trad L, Young AJ, Cymerman A and Reeves JT.** Decreased exercise muscle lactate release after high altitude acclimatization. *J Appl Physiol* 67: 1456-1462, 1989
34. **Brooks GA.** Cell-cell and intracellular lactate shuttles. *J Physiol* 587: 5591-5600, 2009

35. **Stanley WC, Gertz EW, Wisneski JA, Neese RA, Morris DL and Brooks GA.** Lactate extraction during net lactate release in legs of humans during exercise. *J Appl Physiol* 60: 1116-1120, 1986
36. **Bottinelli R, Reggiani C.** Human skeletal muscle fibres: molecular and functional diversity. *Prog Biophys Mol Biol* 73: 195-262, 2000
37. **Dawson MJ, Gadian DG and Wilkie DR.** Studies of the biochemistry of contracting and relaxing muscle by the use of <sup>31</sup>P n.m.r. in conjunction with other techniques. *Philos Trans R Soc Lond B Biol Sci* 289: 445-455, 1980
38. **Forbes SC, Paganini AT, Slade JM, Towse TF and Meyer RA.** Phosphocreatine recovery kinetics following low- and high-intensity exercise in human triceps surae and rat posterior hindlimb muscles. *Am J Physiol Regul Integr Comp Physiol* 296: R161-R170, 2009
39. **Greenhaff PL, Soderlund K, Ren JM and Hultman E.** Energy metabolism in single human muscle fibres during intermittent contraction with occluded circulation. *J Physiol* 460: 443-453, 1993
40. **Ivy JL, Withers RT, Van Handel PJ, Elger DH and Costill DL.** Muscle respiratory capacity and fiber type as determinants of the lactate threshold. *J Appl Physiol* 48: 523-527, 1980
41. **Holloszy JO, Coyle EF.** Adaptations of skeletal muscle to endurance exercise and their metabolic consequences. *J Appl Physiol* 56: 831-838, 1984
42. **LeBlanc PJ, Howarth KR, Gibala MJ and Heigenhauser GJ.** Effects of 7 wk of endurance training on human skeletal muscle metabolism during submaximal exercise. *J Appl Physiol* 97: 2148-2153, 2004
43. **Pavlakis SG, Phillips PC, DiMauro S, De Vivo DC and Rowland LP.** Mitochondrial myopathy, encephalopathy, lactic acidosis, and strokelike episodes: a distinctive clinical syndrome. *Ann Neurol* 16: 481-488, 1984



# Chapter 9

*Summarizing discussion and future perspective*

## SUMMARIZING DISCUSSION

The primary function of skeletal muscle tissue is to produce force or cause motion. To perform this task, chemical energy stored in nutrients (glucose and fatty acids) has to be converted into an energy currency that can drive muscle contraction. This process is known as 'energy metabolism' or 'bioenergetics' of skeletal muscle cells. It consists of a large number of chemical reactions, which are organized in metabolic pathways. Unraveling the makeup of this complex network is interesting from a fundamental biological perspective, but also essential to understand how a disturbance of muscle bioenergetics can cause metabolic disorders.

<sup>31</sup>P magnetic resonance spectroscopy (MRS) has emerged as one of the premier methods to study bioenergetics of skeletal muscle *in vivo*. It enables to measure dynamics of key metabolites in energy metabolism of skeletal muscle during rest – exercise – recovery protocols. Extracting relevant information about muscle physiology from these metabolite dynamics is however not a trivial procedure. It remains particularly challenging to relate *in vivo* observed metabolite dynamics to an understanding of the underlying processes at the level of the metabolic pathways. A possible solution for bridging this gap between macroscopic measurements and mechanistic understanding at pathway level is application of detailed computational modeling. This dissertation describes a series of studies in which a mechanistic model of muscle ATP metabolism was developed and applied for analysis of skeletal muscle ATP metabolism.

### ***Application of the iterative cycle of model development***

Developing a model that captures the full complexity of all pathways associated with ATP metabolism in skeletal muscle represents a daunting task. It certainly cannot be achieved in a single effort. In **Chapter 1** we outlined an iterative model building strategy designed to overcome the difficulties associated with developing a mechanistic model of a complex biological system. We proposed that by iteratively (re-)testing the model against (newly recorded) data it is possible to progressively strengthen the models' performance and to improve its predictive power. The subsequent Chapters of this thesis demonstrate the application of this strategy. At the start of this process, the models by Lambeth and Kushmerick (1) and Beard and co-workers (2,3) were the most advanced models of glycolysis and oxidative phosphorylation in skeletal muscle available. However, they failed in reproducing many of the *in vivo* observed metabolite dynamics. After several iterations, the eventual model (Chapter 8) was improved to the point it was consistent with *in vivo* data recorded for a wide range of physiological conditions (normoxia, ischemia, 1 – 80Hz muscle excitation frequencies). On top, the model was successfully applied for integration of *in vivo* and *in vitro* measures of mitochondrial (dys) function in an animal study (Chapter 7). These results have significantly broadened the scope for application of the model in future studies of skeletal muscle bioenergetics (see section '*future perspective*').

In systems biology typically two methods for model building are distinguished (4). Bottom-up approaches try to reconstruct pathways by starting with detailed characterization (e.g. rate equation) of individual pathway components (enzymatic processes). These formulations are subsequently integrated to predict systems level behaviour. In 'top-down' systems biology, the main objective is to discover new molecular mechanisms using an iterative cycle that starts with experimental data, followed by data analysis and data integration to determine correlations between concentrations of molecules, and ends with the formulation of hypotheses concerning

co- and inter-regulation of groups of those molecules (4). The model building strategy applied in the studies described in this thesis does not fit to one of these two approaches, but resembles a hybrid method, which combines characteristics of both approaches. The initial models were developed according to a bottom-up approach. Subsequently, we tried to identify missing regulatory mechanisms from a top-down perspective, i.e., by using experimental data obtained at physiological 'systems' level and mathematical analyses tools (e.g. parameter sensitivity analysis) we defined hypotheses of missing regulations, as illustrated in Chapters 2, 4 and 5. By adopting this strategy we could circumvent some of the limitations of the bottom-up or top-down approaches.

A particular problem for bottom-up approaches is that *in vitro* determined kinetic parameters not necessarily reflect *in vivo* conditions as a result of interactions (e.g. protein – protein interactions, substrate channeling) not present in the *in vitro* assay environment. By (re)optimizing key model parameters based on *in vivo* data it is possible to capture these *in vivo* processes in the model. Another challenge encountered in a pure bottom-up approach is that for some pathways or processes the available mechanistic information is rather limited, which can seriously delay progress of the model building cycle. For example, in Chapter 8 such a problem was encountered. Including a detailed, validated description of the mitochondrial pyruvate import, redox shuttles and TCA cycle would require an enormous effort. On forehand, it was unknown if the model predictions of interest were actually sensitive for these processes and thus, if undertaking this effort was necessary for answering the research questions. We therefore decided to represent these processes, as a first approximation, by simple phenomenological rate equations. Subsequent model analyses revealed that these model components had a negligible small influence on the model predictions of interest. These results justified the choice of a phenomenological rate equation and prevented the model building process from getting stuck at mechanistic descriptions of these processes. A limitation of the 'top – down' approach is that, as a result of their phenomenological nature, they often yield non-predictive models (4). Because the modeling framework used as a basis for our studies was designed according to a bottom – up approach we did not encounter this problem. Instead, the (top-down) adaptations introduced in the model actually strengthened the predictive power of the model, as illustrated in Chapters 3, 6, 7 and 8. In these studies the model was shown to reproduce independent datasets with no or only minor changes to the model.

An important aim of the applied approach was to create a synergy between model development and gaining novel insight in muscle physiology. To facilitate this process, application of a method referred to as: '*quantitative hypothesis testing*' was found particularly helpful. According to this approach, the model is considered a hypothesis formulated in a mathematical language. Testing of model predictions against experimentally observed pathway dynamics provided a means to test this hypothesis. The insights obtained by the results of these tests are summarized in the sections below. In addition, failure of predictions provided an important contribution in the process of model development: it was exploited as opportunity for improving the model. Application of mathematical model analyses (e.g., parameter sensitivity analysis) provided a key tool in this procedure. Identification of sensitive model parameters provided a means to guide model adaptations. Successful application of this strategy was demonstrated, for example in Chapters 2, 4, and 5.

**Regulation of glycolysis in skeletal muscle in vivo**

The Lambeth and Kushmerick model of glycogenolysis was developed by integrating known enzyme kinetics scavenged from different literature sources (1). The main control mechanisms present in this initial model was substrate feedback (AMP, ADP, Pi) regulation of flux. This first version of the model could reproduce PCr, Pi, and pH dynamics in ischemic skeletal muscle at rest (5,6). However, it was also reported that predictions of some pathway intermediates (e.g. hexose – monophosphates (HMP, G1P + G6P + F6P)) were less accurate (7). In addition, the model could not explain the rapid silencing of glycolytic flux in non-contracting muscle. These results indicated that the model might be missing some essential control mechanisms.

In a study described in **Chapter 2**, this possibility was further investigated. First, <sup>31</sup>P MRS was applied for high time resolution *in vivo* measurements of the turnover of phosphorylated glycolytic metabolites (hexose – monophosphates) in human leg muscle after exhaustive exercise. Next, it was tested if the control mechanisms captured by the model were sufficient to explain the observed HMP dynamics. This test revealed that the model could not reproduce the slow consumption dynamics of HMP during post exercise recovery. Model analyses (parameter sensitivity analysis) were applied to identify the most likely hypotheses of missing regulatory mechanisms. Based on these results it was concluded that the mathematical model was missing additional control mechanisms at the level of phosphofructokinase (PFK) and pyruvate kinase (PK). In addition, it was proposed that these missing mechanisms were also involved in the rapid silencing of glycolytic flux in non-contracting muscle.

In a follow-up study part of this hypothesis was further tested, as described in **Chapter 3**. It was investigated if a mechanism explaining the additional control at the level of PFK (i.e., calcium-calmodulin mediated activation of the enzyme) was indeed necessary for explaining pathway dynamics observed in ischemic, contracting muscle. Again, an integrative *in vivo* and *in silico* research approach was applied. Pathway dynamics reflected by PCr and pH dynamics were recorded in ischemic rat TA muscle at rest and for a wide variety of electrically induced muscle contraction frequencies (1 – 80 Hz). Comparison of model simulations and experimental data showed that the addition of this control mechanism was necessary and sufficient to accurately reproduce the recorded pathway dynamics. In addition, model simulations confirmed that deactivation of PFK in the absence of elevated calcium levels provided a mechanistic explanation for the rapid silencing of glycolytic ATP synthesis in non-contracting muscle.

Chapter 3 provided quantitative evidence that the regulation of glycolysis in skeletal muscle *in vivo* is predominantly controlled by the combined effects of substrate feedback (AMP, ADP, Pi) regulation and calcium mediated feed-forward activation of flux. These control mechanisms were however only tested for ischemic conditions. In an attempt to further challenge this hypothesis (and model) we investigated if the model could also reproduce pathway dynamics recorded during aerobic conditions. This study is described in **Chapter 8**. Metabolite dynamics were again recorded in rat TA muscle using <sup>31</sup>P MRS. The glycolytic model was combined with a validated model of oxidative phosphorylation (Chapters 4 - 7). Testing of model predictions against PCr and pH dynamics revealed that the mechanisms captured by the model could also explain the regulation of glycolysis during aerobic conditions.

### ***Regulation of oxidative phosphorylation in skeletal muscle in vivo***

Chapters 4 – 7 describe investigations of mitochondrial bioenergetics. The starting point for these studies was provided by the model developed by Beard and co-workers (2,3). The main regulatory mechanism embedded in this model was substrate feedback (ADP, Pi) regulation of flux. The initial version of this model however failed in reproducing the relation between ADP – mitochondrial ATP synthesis ( $J_p$ ) and phosphate potential ( $\Delta G_p$ ) –  $J_p$  (Chapter 1, Figure 5). These transduction functions capture macroscopic characteristics of the regulation of oxidative ATP synthesis in skeletal muscle and are therefore considered important quality criteria for evaluating the models' performance. It was first investigated if the failing model predictions indicated a problem in the model parameterization or if they were a result of missing regulatory mechanisms.

First, the sensitivity of mitochondria to ADP (captured by the ADP –  $J_p$  relation) was investigated (**Chapter 4**). A new dataset was recorded which sampled the ADP -  $J_p$  and  $\Delta G_p$  –  $J_p$  relations with increased accuracy and sample density. The first main result of this study was that the newly recorded dataset confirmed previous observations that the signal transduction function of oxidative phosphorylation is approximately second order in ADP. The significantly improved accuracy and increased sample density of the experimental data also provided improved opportunities for model testing. This particular property of the dataset was also exploited in Chapter 4. As expected (Chapter 1, Figure 5), the initial model failed in reproducing the data. Multi-parameter sensitivity analysis was applied to identify model components that controlled the ADP sensitivity of mitochondria *in silico*. These results were used to significantly improve the predictive power of the model (ADP –  $J_p$  relation). In addition, they indicated that the apparent ADP sensitivity of oxidative phosphorylation is an emergent property of the mitochondrial control network controlled primarily by the kinetics of the adenine nucleotide transport (ANT).

A similar study design was applied to investigate the control mechanisms underlying the  $\Delta G_p$  –  $J_p$  relation, as described in **Chapter 5**. Initial testing of the modified model presented in Chapter 4 showed that especially at low metabolic rates the cellular [ADP] and [Pi] and corresponding  $\Delta G_p$  were underestimated by the model. Moreover, analysis revealed that this problem could not just be amended by reparameterization. This result suggested that the model was missing essential control mechanisms. Numerical analysis identified OXPHOS complex III as the most likely site for the additional control. In the second part of the study two different control schemes for the missing regulation were tested: (i) substrate feedback regulation by inorganic phosphate or (ii) regulation of flux by parallel activation of ATP consumption and production by a similar signaling event (e.g. calcium). Both hypotheses were implemented and compared to time course data of phosphocreatine (PCr), Pi and ATP dynamics during post-exercise recovery and validation data obtained by  $^{31}\text{P}$  MRS of sedentary subjects and track athletes. The results rejected the hypothesis of regulation by feed forward activation. Instead, it was concluded that feedback control of respiratory chain complexes by inorganic phosphate is essential to explain the regulation of mitochondrial ATP synthesis flux in skeletal muscle throughout its full dynamic range.

**Chapter 8** describes an investigation on the role of ADP and Pi substrate feedback regulation of oxidative phosphorylation on the regulation of relative contribution of mitochondrial versus glycolytic ATP synthesis flux. The mitochondrial model component was combined with the validated model of the glycolytic pathway (Chapters 2 and 3). The integrated model was verified against data recorded in rat TA muscle during rest – exercise – recovery using  $^{31}\text{P}$  MRS. Simulations of the validated model indicated that the ADP, Pi feedback signal is a key mechanism in the



regulation of glycolytic versus mitochondrial flux. In addition, they revealed that the observed balance during exercise is predominantly controlled by physiological parameters that influence the mitochondrial capacity (e.g. mitochondrial enzyme content, mitochondrial volume percentage, oxygen availability). In contrast, glycolytic capacity influenced the balance only minor.

### **Systems biology of mitochondrial function**

*In vivo* mitochondrial capacity quantified by the rate of post exercise PCr recovery is a physiological parameters frequently derived from  $^{31}\text{P}$  MRS datasets. Sometimes, additional analyses of muscle biopsy samples are used to identify changes in the metabolic pathways responsible for observations of a decreased mitochondrial capacity *in vivo*. State-of-the-art approaches for analyses of the combined data remain typically limited to statistical and intuitive strategies (see: e.g. (8,9)). A promise of the current era of biology is to understand the integrated function of complex biological systems in order to predict and rationally manipulate their behavior with the ultimate aim of improving human health (10). In order to obtain such understanding, the analyses of available data have to be advanced beyond the level of statistical and intuitive methods. In Chapters 6 and 7 we described two studies that explored if such more insightful analyses can be performed by integration of *in vivo*, *in vitro* and *in silico* methods.

In the first part of **Chapter 6** an extension of the modeling framework from a single uniform – type cell model to a three – cell type model (type I, IIA, IIX) was presented. In addition, several essential additional verification tests were conducted: (i) It was shown that the model could reproduce the effect of progressive inhibition of individual OXPHOS components on mitochondrial respiration rate, (ii) the three cell model remained consistent with the ADP –  $J_p$  and  $\Delta G_p$  –  $J_p$  transduction functions presented in Chapters 4 and 5, (iii) the mechanistic model was shown to reproduce the PCr recovery time course data just as accurate as the current gold-standard, i.e., the mono-exponential function. Subsequently, the model was applied to investigate to which extend different adaptations in muscle physiology contributed to a decreased rate of post-exercise PCr recovery documented for type 2 diabetes patients with a sedentary lifestyle compared to healthy lean control subjects. The prolongation of the PCr recovery period in these patients was predicted by integrating available data of *in vitro* markers of mitochondrial function in the mechanistic model. These results were used to outline a possible strategy for applying the mechanistic models in future studies of mitochondrial (dys)function.

In a follow-up study the proposed method was tested in an animal model of decreased mitochondrial function: 8 versus 25 week old Wistar rats. This study was described in **Chapter 7**.  $^{31}\text{P}$  MRS revealed a decreased mitochondrial capacity *in vivo* (quantified by PCr recovery rate constant) in the animals at age 25 weeks. Additional *in vitro* analyses of muscle tissue samples identified several changes in muscle physiology which possible contributed to the decreased mitochondrial function *in vivo*. The first principal result of this study was that the mathematical model accurately predicted the decreased mitochondrial function *in vivo* based upon the *in vitro* measurements. In addition, model predictions provided more insight in the contribution of the different factors responsible for the decreased mitochondrial function: a major part of the decreased oxidative capacity was due to the decreased mitochondrial content (~54%); the remaining part was a result of the decreased capacity of ETC and TCA cycle (~32%) and difference in end exercise pH (~12%). These results demonstrate the feasibility of applying the developed model for integration of *in vivo* and *in vitro* markers of mitochondrial dysfunction.

## FUTURE PERSPECTIVES

The developed mathematical model provides an excellent basis for future investigation of skeletal muscle bioenergetics. In this section, we will discuss three possible directions in which this work can be extended: (i) continuing the iterative cycle of model development; (ii) connecting ATP metabolism to other pathways; (iii) application in (pre-) clinical studies.

### ***Continuing the iterative cycle of model development***

The investigations described in this thesis predominantly used *in vivo* data for model testing and development. In addition, it was verified that predictions of (non-observable) internal state variables (e.g., mitochondrial redox potential, membrane potential or glycolytic intermediate metabolites) were in the right order of magnitude (glycolytic intermediates) or matched expected values (mitochondrial redox state (NADH/NAD): ~0.3 - 100, membrane potential: 160 – 180mV). Conducting new experiments that provide an experimental read-out of some of these variables is expected to provide a new impulse to the process of model development.

Some of the processes in the current model were parameterized based on *in vivo* data (e.g., parameters of phosphofrutokinase, adenine nucleotide transport and Pi regulation of respiratory chain activity). An advantage of this method, compared to traditional *in vitro* kinetic assays, is that it circumvents the problem of identifying optimal assay conditions representing the 'true' *in vivo* environment (11). Nevertheless, it would further strengthen the basis of this modeling work if the proposed model adaptations could be supported by *in vitro* determined enzymes kinetics. As explained, the grand challenge for such studies will be to design an *in vitro* assay environment that represents the *in vivo* conditions well.

### ***Connecting ATP metabolism to other pathways***

ATP metabolism is at the center of the metabolic pathways in skeletal muscle cells. It is thus connected to many other relevant pathways. Including some of these processes in the modeling framework provides interesting opportunities for future studies. For example, it is well known that the supply of oxidizable substrates (carbohydrates and fatty acids) to mitochondria switches depending on e.g. metabolic rates (12). A disturbance of this metabolic flexibility is associated with e.g., type 2 diabetes (12). There is evidence that exercise training can (partly) restore this metabolic flexibility which is paralleled by an improved insulin sensitivity of skeletal muscle tissue (13). The molecular mechanisms responsible for this beneficial effect remain however poorly understood (13). Identification of these mechanisms is interesting since they could provide leads for pharmaceutical intervention targets. To investigate these processes by means of a mechanistic modeling approach requires extending the current framework with a detailed description of pyruvate and fatty acid import in the mitochondria, TCA cycle and  $\beta$  – oxidation pathways. Although such a step is certainly non-trivial, a starting point could be provided by e.g., the work of Wu and colleagues, who already started to build a mechanistic description of the TCA cycle (14). The  $\beta$  – oxidation and TCA cycle pathways are certainly not the only pathways relevant for future investigations. Other pathways that are closely linked to ATP turnover rates and also provide interesting opportunities for future directions are, for example, the insulin signaling pathway (15), ROS generation by electron transport chain (16,17) or mitochondrial biogenesis pathways (18,19).

***Application in clinical studies of mitochondrial function***

A decreased mitochondrial function can be caused by many different factors. As explained in Chapters 6 and 7, the origin of a decreased oxidative capacity cannot be deduced from *in vivo* measurements. Analysis of muscle biopsy samples provides additional information of changes in muscle physiology possibly responsible for the decreased mitochondrial function. It remains however very difficult to determine the contribution of these *in vitro* observed adaptations to the functioning of the mitochondria *in vivo*. This information is however crucial for the design of (pharmaceutical) therapies. As described in Chapter 7, we successfully tested application of the computational model to relate *in vivo* and *in vitro* measures of mitochondrial function in an animal study. This study provided a proof-of-principle required for extension of the approach to clinical studies of mitochondrial function in for example, mitochondrial diseases (20), type 2 diabetes (21), chronic heart failure (22), or aging (23). These future studies are essential to further confirm the generic value of the method and may contribute to a more widespread application of systems biology in (clinical) biomedical research.

## REFERENCES

1. **Lambeth MJ, Kushmerick MJ.** A computational model for glycogenolysis in skeletal muscle. *Ann Biomed Eng* 30: 808-827, 2002
2. **Beard DA.** A biophysical model of the mitochondrial respiratory system and oxidative phosphorylation. *PLoS Comput Biol* 1: e36, 2005
3. **Wu F, Jeneson JA and Beard DA.** Oxidative ATP synthesis in skeletal muscle is controlled by substrate feedback. *Am J Physiol Cell Physiol* 292: C115-C124, 2007
4. **Bruggeman FJ, Westerhoff HV.** The nature of systems biology. *Trends Microbiol* 15: 45-50, 2007
5. **Lambeth MJ, Kushmerick MJ, Marcinek DJ and Conley KE.** Basal glycogenolysis in mouse skeletal muscle: in vitro model predicts in vivo fluxes. *Mol Biol Rep* 29: 135-139, 2002
6. **Vinnakota KC, Rusk J, Palmer L, Shankland E and Kushmerick MJ.** Common phenotype of resting mouse extensor digitorum longus and soleus muscles: equal ATPase and glycolytic flux during transient anoxia. *J Physiol* 588: 1961-1983, 2010
7. **Vinnakota K, Kemp ML and Kushmerick MJ.** Dynamics of muscle glycogenolysis modeled with pH time course computation and pH-dependent reaction equilibria and enzyme kinetics. *Biophys J* 91: 1264-1287, 2006
8. **Phielix E, Schrauwen-Hinderling VB, Mensink M, Lenaers E, Meex R, Hoeks J, Kooi ME, Moonen-Kornips E, Sels JP, Hesselink MK et al..** Lower intrinsic ADP-stimulated mitochondrial respiration underlies in vivo mitochondrial dysfunction in muscle of male type 2 diabetic patients. *Diabetes* 57: 2943-2949, 2008
9. **Praet SF, De Feyter HM, Jonkers RA, Nicolay K, van PC, Kuipers H, van Loon LJ and Prompers JJ.** 31P MR spectroscopy and in vitro markers of oxidative capacity in type 2 diabetes patients. *MAGMA* 19: 321-331, 2006
10. **Beard DA, Vendelin M.** Systems biology of the mitochondrion. *Am J Physiol Cell Physiol* 291: C1101-C1103, 2006
11. **van Eunen K, Bouwman J, Daran-Lapujade P, Postmus J, Canelas AB, Mensonides FI, Orij R, Tuzun I, van den Brink J, Smits GJ et al..** Measuring enzyme activities under standardized in vivo-like conditions for systems biology. *FEBS J* 277: 749-760, 2010
12. **Kelley DE, Mandarino LJ.** Fuel selection in human skeletal muscle in insulin resistance: a reexamination. *Diabetes* 49: 677-683, 2000
13. **Meex RC, Schrauwen-Hinderling VB, Moonen-Kornips E, Schaart G, Mensink M, Phielix E, van de Weijer T, Sels JP, Schrauwen P and Hesselink MK.** Restoration of muscle mitochondrial function and metabolic flexibility in type 2 diabetes by exercise training is paralleled by increased myocellular fat storage and improved insulin sensitivity. *Diabetes* 59: 572-579, 2010
14. **Wu F, Yang F, Vinnakota KC and Beard DA.** Computer modeling of mitochondrial tricarboxylic acid cycle, oxidative phosphorylation, metabolite transport, and electrophysiology. *J Biol Chem* 282: 24525-24537, 2007
15. **Thorell A, Hirshman MF, Nygren J, Jorfeldt L, Wojtaszewski JF, Dufresne SD, Horton ES, Ljungqvist O and Goodyear LJ.** Exercise and insulin cause GLUT-4 translocation in human skeletal muscle. *Am J Physiol* 277: E733-E741, 1999
16. **Davies KJ, Quintanilha AT, Brooks GA and Packer L.** Free radicals and tissue damage produced by exercise. *Biochem Biophys Res Commun* 107: 1198-1205, 1982
17. **Jackson MJ.** Reactive oxygen species and redox-regulation of skeletal muscle adaptations to exercise. *Philos Trans R Soc Lond B Biol Sci* 360: 2285-2291, 2005
18. **Irrcher I, Adhietty PJ, Joseph AM, Ljubicic V and Hood DA.** Regulation of mitochondrial biogenesis in muscle by endurance exercise. *Sports Med* 33: 783-793, 2003
19. **Wu H, Kanatous SB, Thurmond FA, Gallardo T, Isotani E, Bassel-Duby R and Williams RS.** Regulation of mitochondrial biogenesis in skeletal muscle by CaMK. *Science* 296: 349-352, 2002
20. **Wallace DC.** Mitochondrial diseases in man and mouse. *Science* 283: 1482-1488, 1999
21. **Lowell BB, Shulman GI.** Mitochondrial dysfunction and type 2 diabetes. *Science* 307: 384-387, 2005
22. **Drexler H, Riede U, Munzel T, Konig H, Funke E and Just H.** Alterations of skeletal muscle in chronic heart failure. *Circulation* 85: 1751-1759, 1992
23. **Trounce I, Byrne E and Marzuki S.** Decline in skeletal muscle mitochondrial respiratory chain function: possible factor in ageing. *Lancet* 1: 637-639, 1989



*Summary*

*Nederlandse samenvatting*

*Dankwoord*

*List of publications*

*Curriculum Vitae*

## SUMMARY

### “Systems Biology of Energy Metabolism in Skeletal Muscle”

The primary function of skeletal muscle tissue is to produce force or cause motion. To perform this task chemical energy stored in nutrients (glucose and fatty acids) has to be converted into an energy currency that can drive muscle contraction (adenosine-tri-phosphate, ATP). This process is known as the energy metabolism of skeletal muscle and consists of a large number of chemical reactions that are organized in metabolic pathways. Unraveling this complex network is important from a fundamental biological perspective, but also essential to understand how a disturbance of muscle bioenergetics can cause metabolic disorders.

<sup>31</sup>P magnetic resonance spectroscopy (MRS) has emerged as one of the premier methods to study skeletal muscle energy metabolism *in vivo*. It, however, remains challenging to relate the observed metabolite dynamics to an understanding of the underlying processes at the level of the metabolic pathways. A possible solution for bridging this gap between macroscopic measurements and mechanistic understanding at pathway level is the application of mechanistic computational modeling. This dissertation describes a series of studies in which a mechanistic model of ATP metabolism was developed and applied in the analysis of skeletal muscle bioenergetics.

Skeletal muscle cells contain two primary processes that are responsible for the conversion of glucose and fatty acids into ATP. These processes are known as glycolysis and oxidative phosphorylation in mitochondria. The initial mathematical models of these processes were obtained by integration of known enzyme kinetics and thermodynamics. Testing of these models, however, showed that they failed to reproduce many of the *in vivo* observed metabolite dynamics, as has been described in chapter 1 and 2. These results indicated that the models might be missing essential regulatory mechanisms or that the model parameterization required changes. First, the physiological implications of necessary model adaptations were investigated in a series of studies described in chapters 2 – 5.

Numerical analysis of the initial glycolysis model revealed that the experimentally observed slow turnover rate of phosphorylated sugars post exercise could only be explained by rapid deactivation of phosphofructokinase (PFK) and pyruvate kinase (PK) in non-contracting muscle. In particular the deactivation of PFK was crucial for adequate control of pathway flux. Therefore, in a follow-up study, it was tested if the missing regulation at the level of PFK could be explained by calcium – calmodulin mediated activation of this enzyme. To this end, pathway behavior, represented by phosphocreatine (PCr) and pH dynamics, was measured in ischemic skeletal muscle for a wide variety of muscle excitation frequencies (0 – 80 Hz). Next, it was shown that addition of the calcium – calmodulin mediated activation of PFK was necessary to accurately reproduce these data. These results provided important new quantitative support for the hypothesis that this particular mechanism has a key role in the regulation of glycolytic flux in skeletal muscle.

The initial model of oxidative phosphorylation was first tested against empirically determined mitochondrial input – output relations, i.e., [ADP] – mitochondrial ATP synthesis flux ( $J_p$ ) and phosphate potential ( $\Delta G_p$ ) –  $J_p$ . These empirically determined relations were derived from  $^{31}\text{P}$  MRS measurements of metabolite dynamics post-exercise. They capture key features of the regulation of oxidative phosphorylation *in vivo* and are therefore considered relevant for testing the quality of the mathematical model. Numerical model analysis (i.e., parameter sensitivity analysis) was applied to investigate which components significantly influenced predictions of these input – output relations. Based on these results it was concluded that the adenine nucleotide transporter (which facilitates the exchange of ATP and ADP across the inner mitochondrial membrane) has a dominant role in controlling the ADP sensitivity of mitochondria. Furthermore, we identified that Pi feedback control of respiratory chain activity was essential to explain measurements of  $\Delta G_p$  at low metabolic rates. These insights were used to improve the predictive power of the model, as described in chapters 4 and 5.

In the studies described in chapters 2 - 5 the glycolytic and mitochondrial model components were tested for conditions in which only one of the two processes was active (ischemia and post exercise recovery, respectively). It remained therefore unknown if the control mechanisms included in these models could also explain the contribution of mitochondrial versus glycolytic ATP synthesis for conditions in which both processes are active (aerobic exercise). In an attempt to answer this question, dynamics of ATP metabolism were recorded during a full rest – exercise – recovery protocol under aerobic conditions and subsequently used for testing of the integrated mitochondrial + glycolytic model. The results presented in chapter 8 showed that the integrated model could accurately reproduce the observed metabolite and pH dynamics for varying exercise intensities. The main physiological implications of these results were that, substrate feedback control (ADP + Pi) of oxidative phosphorylation combined with substrate feedback control (ADP + AMP + Pi) and control by parallel activation (calcium – calmodulin mediated activation of PFK) of glycolysis, provides a set of key control mechanisms that can explain the regulation of ATP metabolism in skeletal muscle *in vivo* for a wide range of physiological conditions.

By application of several cycles of model development it was possible to improve the models performance to the point it was consistent with  $^{31}\text{P}$  MRS measurements of muscle bioenergetics in both healthy humans and animals. As described in chapters 6 and 7, it was investigated if the model could be applied to analyze the adaptations of muscle physiology that underlie changes in mitochondrial capacity that occur in for instance type 2 diabetes patients or with aging. A decrease of mitochondrial capacity in these subjects can be diagnosed accurately by determining the rate of PCr recovery post exercise. However, the changes in muscle physiology responsible for any observed difference in oxidative capacity cannot be deduced from these measurements. Therefore additional muscle biopsy samples are collected and analyzed for *in vitro* markers of oxidative capacity. State-of-the-art analyses of these data are typically limited to statistical or intuitive approaches. We investigated if the insight obtained from the combined *in vivo* + *in vitro* data sets could be increased by application of our mathematical model. To this end, first, the model was extended from a single uniform cell type model to a three types cell model (type I, IIA, and IIX), capturing the microscopic heterogeneity of muscle tissue. In addition, several key validation tests were conducted, as described in chapter 6. Subsequently, we demonstrated that the model could



explain the prolongation of PCr recovery period observed in type 2 diabetes patients by integrating available literature data of *in vitro* markers of mitochondrial function. Although this result was already very promising, it was also concluded that the approach could be tested more rigorously by obtaining all data (*in vivo* + *in vitro*) in a single study. Therefore, the method was further tested in an animal model of decreased mitochondrial function: 8 versus 25 week old Wistar rats. The first main result of this study was that the mathematical model could accurately reproduce the delayed PCr recovery kinetics in 25 week old animals based on *in vitro* determined changes in muscle physiology. In addition, model predictions provided quantitative insight in the individual contribution of the different factors responsible for the decreased oxidative capacity. This type of information is considered very relevant for the design of (pharmaceutical) therapies aimed at improving mitochondrial function. For example, model predictions of the physiological changes that contribute the most to the decrease in oxidative capacity provide potentially promising targets for therapy design. Based on these considerations it was concluded that application of the mathematical model provides new promising opportunities for future studies of mitochondrial (dys)function in skeletal muscle.

In conclusion, through application of a series of iterative cycles of model development combined with multiple new experimental studies it was possible to develop a detailed mechanistic model of ATP metabolism that was consistent with *in vivo* observations of skeletal muscle bioenergetics for a wide range of physiological conditions. This process provided new insight in the key control mechanisms embedded in the metabolic pathways that have a dominant role in regulating ATP metabolism in skeletal muscle *in vivo*. In addition, we successfully demonstrated the feasibility and added value of application of the model for integration of *in vivo* and *in vitro* measurements of oxidative capacity in future studies of mitochondrial (dys)function in, for example, type 2 diabetes, aging or mitochondrial myopathy.

## NEDERLANDSE SAMENVATTING

### “Systeembioologie van de Energiehuishouding in Skeletspiercellen”

Het leveren van kracht of beweging is een van de belangrijkste taken van skeletspieren. Hiervoor moet chemische energie, aanwezig in voedingsstoffen zoals glucose en vetzuren, omgezet worden in een vorm die cellen kunnen gebruiken voor onder andere contracties (adenosinetrifosfaat, ATP). Dit proces wordt ook wel de energiehuishouding van skeletspiercellen genoemd. Het bestaat uit een groot aantal chemische reacties, welke georganiseerd zijn in zogenaamde ‘metabolic pathways’. Het ontrafelen van de structuur en de regulatie van dit complexe reactienetwerk is interessant vanuit fundamenteel biologisch oogpunt, maar ook essentieel om te kunnen achterhalen hoe een verstoring van de energiehuishouding in spiercellen metabole ziekten tot gevolg kan hebben.

<sup>31</sup>P magnetische resonantie spectroscopie (MRS) is een van de beste technieken om het energiemetabolisme van skeletspieren *in vivo* te bestuderen. Het is echter moeilijk om de *in vivo* gemeten dynamica te relateren aan inzichten in het functioneren van de onderliggende moleculaire processen. Een mogelijke oplossing voor het verbinden van macroscopische *in vivo* metingen en mechanistisch inzicht op het niveau van de metabolic pathways is het ontwikkelen en toepassen van mechanistische wiskundige modellen. Dit proefschrift beschrijft een aantal studies waarin mechanistische wiskundige modellen van ATP metabolisme zijn ontwikkeld en toegepast op het energiemetabolisme van skeletspiercellen.

Skeletspiercellen hebben twee processen die verantwoordelijk zijn voor de omzetting van de chemische energie opgeslagen in glucose en vetzuren in ATP. Deze processen zijn glycolyse and oxidatieve fosforylering in mitochondria. De initiële wiskundige modellen van deze processen zijn ontworpen door integratie van bekende enzymkinetiek en thermodynamica. Zoals beschreven in hoofdstuk 1 en 2, kunnen deze modellen echter veel van de dynamische data verkregen doormiddel van *in vivo* metingen niet reproduceren. Deze bevindingen impliceren dat in de modellen essentiële regulerende mechanismen ontbreken of dat de parameterisering verbeterd moet worden. In een reeks van studies beschreven in hoofdstukken 2 – 5 zijn de fysiologische implicaties van noodzakelijk modelaanpassingen onderzocht.

Numerieke analyse van het initiële glycolyse model heeft aangetoond dat experimentele observaties van trage consumptie van gefosforyleerde suikers in de herstelperiode na inspanning alleen kunnen worden verklaard door snelle deactivering van fosfofructokinase (PFK) en pyruvaat kinase. In het bijzonder de deactivering van PFK was belangrijk voor adequate regulatie van pathway activiteit. Daarom hebben we in een vervolgstudie getest of de ontbrekende regulatie van PFK verklaard kan worden door activering van dit enzym als gevolg van binding van een calcium – calmoduline complex. Eerst is dynamische data van glycolyseactiviteit verkregen in ischemische spier voor verschillende frequenties waarop spiercontracties geïnduceerd werden (0 – 80 Hz). Op basis van het vergelijken van modelsimulaties en deze data is geconcludeerd dat activering van PFK door binding van een calcium – calmoduline complex noodzakelijk is om de experimentele data nauwkeurig te reproduceren. Deze resultaten verschaffen nieuw kwantitatief

bewijs dat dit mechanisme een belangrijke rol speelt in de regulatie van de glycolyseactiviteit in skeletspiercellen.

Het initiële model van de oxidatieve fosforylering hebben we getest tegen empirisch bepaalde mitochondriële input – output relaties ( $[ADP]$  – mitochondriële ATP synthese ( $J_p$ ) en fosfaatpotentiaal ( $\Delta G_p$ ) –  $J_p$ ). Deze empirisch bepaalde relaties zijn afgeleid van  $^{31}P$  MRS metingen tijdens de herstelperiode na inspanning en reflecteren de regulatie van mitochondriële ATP synthese *in vivo*. Deze datasets zijn daarom zeer geschikt voor het testen van de kwaliteit van de wiskundige modellen. Numerieke analysetechnieken (bijvoorbeeld parameter gevoeligheidsanalyse) zijn toegepast om te identificeren welke model componenten de voorspellingen voor deze input – output relaties sterk beïnvloedt. Op basis van deze resultaten is geconcludeerd dat de adenine nucleotide transporter, welke verantwoordelijk is voor transport van ADP en ATP over het binnenmembraan van de mitochondria, een dominante rol heeft bij het reguleren van de ADP gevoeligheid van dit organel. Daarnaast hebben we door middel van simulaties aangetoond dat Pi feedback regulatie van de activiteit van de ademhalingsketen essentieel is voor het verklaren van de gemeten  $\Delta G_p$  bij condities van laag ATP verbruik. Deze inzichten zijn gebruikt om de voorspellende waarde van het model te verbeteren, zoals beschreven in hoofdstuk 4 en 5.

In de studies beschreven in hoofdstukken 2 tot en met 5 zijn de modellen voor glycolyse en mitochondria afzonderlijk getest voor condities waarbij maar één van deze processen actief was (ischemische condities en herstel na inspanning, respectievelijk). Op basis van deze resultaten blijft onduidelijk of de regulerende mechanismen aanwezig in de modellen ook verantwoordelijk zijn voor de relatieve bijdrage van mitochondriële en glycolytische ATP synthese onder omstandigheden dat beide processen tegelijkertijd actief zijn (inspanning onder aerobe condities). In een poging deze vraag te beantwoorden hebben we, doormiddel van  $^{31}P$  MRS, dynamische data verkregen tijdens een rust, inspanning en herstel experiment uitgevoerd onder aerobe condities. Deze experimentele gegevens zijn vervolgens gebruikt om het geïntegreerde model van glycolytische en mitochondriële ATP synthese te testen. De resultaten van dit onderzoek zijn gepresenteerd in hoofdstuk 8 en tonen aan dat het gecombineerde model de dynamische data goed kan reproduceren. De belangrijkste fysiologische implicaties van deze resultaten zijn dat substraatfeedback regulatie ( $ADP + Pi$ ) van oxidatieve fosforylering in combinatie met substraatfeedback regulatie ( $ADP + AMP + Pi$ ) van glycolyse en regulatie door parallele activering van glycolyse (activering van PFK door calcium – calmoduline binding) de regulatie van ATP metabolisme in skeletspier *in vivo* kan verklaren voor een grote variatie van fysiologische condities.

Doormiddel van het doorlopen van verschillende cycli van model ontwikkeling was het mogelijk de modellen te verbeteren, zodanig dat ze consistent zijn met  $^{31}P$  MRS metingen van energie metabolisme in gezonde proefpersonen en proefdieren. Zoals beschreven in hoofdstuk 6 en 7 hebben we vervolgens onderzocht of dit model ook toegepast kan worden voor de analyse van veranderingen in de spierfysiologie verantwoordelijk voor een afname van de mitochondriële capaciteit in bijvoorbeeld type 2 diabetes patiënten of bij veroudering. Een afname in de mitochondriële capaciteit kan nauwkeurig worden gediagnosticeerd door het bepalen van de snelheid waarmee de PCr concentratie in cellen herstelt na inspanning. Echter, de veranderingen in

de spierfysiologie die verantwoordelijk zijn voor de afname in oxidatieve capaciteit kunnen niet uit deze metingen afgeleid worden. Daarom worden in sommige studies spierbiopsies uitgevoerd om doormiddel van *in vitro* bepalingen veranderingen in spierfysiologie te identificeren. State-of-the-art technieken om deze data te analyseren blijven meestal gelimiteerd tot statistische en intuïtieve methoden. Wij hebben onderzocht of het inzicht dat verkregen kan worden op basis van deze gecombineerde *in vivo* en *in vitro* datasets vergroot kan worden door applicatie van het model. Hiervoor is het model eerst uitgebreid van een uniform cel model naar een drie celtypes model (type I, IIA en IIX). Dit model kan op basis van informatie over de veranderingen in spierfysiologie, gerapporteerd in vorige studies, het vertraagde herstel van de PCr concentratie in spiercellen van type 2 diabetes patiënten verklaren. Hoewel dit resultaat al veelbelovend is, is op basis van deze studie ook geconcludeerd de toegepaste methode rigoureuzer getest kan worden door alle data (*in vivo* en *in vitro*) te verzamelen in één en dezelfde studie. Dit studieontwerp is toegepast op een diermodel met een verminderde mitochondriële functie, namelijk, 8 versus 25 week oude Wistar ratten. Het eerste belangrijke resultaat van deze studie was dat het model de vertraging in het herstel van PCr in de 25 weken oude dieren zeer nauwkeurig kon reproduceren op basis van de *in vitro* geïdentificeerde veranderingen in spierfysiologie. Daarnaast demonstreert dit onderzoek een belangrijke toegevoegde waarde van het toepassen van het model. Namelijk dat het mogelijk wordt kwantitatief inzicht te verkrijgen in de bijdrage van individuele veranderingen in spierfysiologie aan de totale verandering in mitochondriële capaciteit gemeten *in vivo*. Deze informatie kan van belang zijn voor het ontwerpen van nieuwe (farmaceutische) therapieën voor het herstel van mitochondriële functie. Veranderen in spierfysiologie die de belangrijkste bijdrage leveren aan het totale verlies in oxidatieve capaciteit bieden bijvoorbeeld potentieel de meest belovende aanknopingspunten voor het ontwikkelen van nieuwe therapieën. Op basis van deze studies hebben we geconcludeerd dat het wiskundig model nieuwe, veel belovende mogelijkheden biedt voor toekomstige studies naar mitochondriële (dis)functie in skeletspiercellen.

Concluderend, door het combineren van verschillende cycli van modelontwikkeling en experimentele studies was het mogelijk een mechanistisch model van ATP metabolisme te ontwerpen dat consistent is met *in vivo* observaties van de energiehuishouding in skeletspiercellen voor een grote verscheidenheid aan fysiologische condities. Dit proces heeft nieuwe inzichten opgeleverd over de moleculaire mechanismen die een dominante rol spelen bij de regulatie van ATP metabolisme in skeletspiercellen. Daarnaast, heeft dit onderzoek succesvol de haalbaarheid en toegevoegde waarde aangetoond van het toepassen van het ontwikkelde model voor de integratie van *in vivo* en *in vitro* metingen van oxidatieve capaciteit in toekomstige studies naar mitochondriële (dis)functie in bijvoorbeeld, type 2 diabetes, veroudering of mitochondriële spieraandoeningen.

## DANKWOORD

Zo, het zit er bijna op. Deze laatste drie pagina's moeten nog geschreven worden en dan is mijn proefschrift echt voltooid. In de afgelopen 4 jaar heb ik ondervonden dat een belangrijk aspect van het succesvol uitvoeren van een promotieonderzoek ligt in het hebben van plezierige samenwerking en het vinden van voldoende momenten om juist even niet bezig te zijn met wetenschap. Ik wil deze laatste zinnen dan ook gebruiken om iedereen die op deze manier een bijdrage heeft geleverd aan dit proefschrift daarvoor te bedanken.

Peter, ik heb altijd met veel plezier in jouw onderzoeksgroep gewerkt. Nadat in het voorjaar van 2008 mijn subsidieaanvraag bij NWO niet gehonoreerd werd, zag jij toch mogelijkheden om mijn ideeën te realiseren binnen het 'predicct' project. Je hebt altijd veel vertrouwen in mijn beslissingen getoond, mij de vrijheid gegund zelf een eigen koers uit te stippelen en de mogelijkheden gecreëerd om dit plan ook daadwerkelijk tot uitvoer te brengen. Hiervoor ben ik je erg dankbaar.

Klaas, hoewel ik eigenlijk 'te gast' was in jouw onderzoeksgroep heeft het voor mij nooit zo aangevoeld. Ik kijk met veel plezier terug op de interacties die wij gehad hebben. Jouw enthousiasme voor wetenschappelijk onderzoek en *in vivo* NMR hebben altijd erg aanstekelijk op mij gewerkt.

Natal, een academische omgeving is niet altijd even goed of duidelijk georganiseerd, ook dat heb ik de afgelopen vier jaar geleerd. En, een promotie kent hoogtepunten, maar zeker ook tegenslagen. Gelukkig was jij, als stabiele factor, altijd aanwezig om tegenslagen of organisatorische problemen te bespreken en samen te zoeken naar oplossingen. Het is leuk om successen te vieren, maar zeker zo fijn als er mensen om je heen zijn die helpen als zaken niet zo lopen als gepland.

Jeroen, de dynamiek die ontstaat als wij samen aan een wetenschappelijk probleem werken is een grote drijfveer geweest voor mijn onderzoek. Ik zou geen recht doen aan je bijdrage aan dit werk als ik niet zou vermelden dat jouw ideeën, in bijna alle gevallen, de basis vormden voor de projecten waar ik aan gewerkt heb. Ik kijk met een grote glimlach terug op onze werk- en congresbezoeken in het buitenland; ook aan het 'in leven houden' van onze antieke MRI scanner heb ik goede herinneringen overgehouden. Je betrokkenheid, enthousiasme en kijk op het leven maken je een goede mentor en een fijn mens.

Jeanine, onze samenwerking is de afgelopen 4 jaar steeds intensiever geworden en, al terugblikkend, onmisbaar voor het slagen van mijn promotieonderzoek. De pH - studie van Nicole vormt de experimentele basis voor hoofdstukken 4 en 5, en de studies beschreven in hoofdstukken 3, 7 en 8 waren onmogelijk zonder de experimentele opstelling die onder jouw leiding ontwikkeld is. Jij stond altijd klaar om met mij mee te denken hoe we nieuwe experimenten uit konden voeren en, in veel gevallen, je eigen AIO's in te schakelen om mij te helpen. Bedankt!

De verschillende technieken die nodig waren om dit onderzoek uit te voeren zijn erg divers. Gelukkig kon ik altijd rekenen op de hulp van fijne collega's om te zorgen dat moeilijke experimenten toch een succes werden, daar ben ik jullie erg dankbaar voor. Willemijn, ons gezamenlijk werk dat geleid heeft tot hoofdstuk 3 en 8 heb ik altijd erg inspirerend gevonden. Jolita, I am very grateful for your help with all the *in vitro* measurements. Bart en Nicole, de MRS experimenten die met proefdieren uitgevoerd moesten worden, waren geen succes geweest zonder jullie hulp. Richard, zoals je ziet heeft jouw bijdrage aan mijn onderzoek een zeer prominente plek gekregen.

Larry, Leonie, David en Jo, het beantwoorden van wetenschappelijke vragen is alleen mogelijk als proefopstellingen slim ontworpen zijn en dierexperimenten met de grootste zorg worden voorbereid en uitgevoerd. Het is fijn dat ik hiervoor op jullie expertise heb kunnen bouwen.

Bob, Dan, Ron, Kalyan and Fan, I always really enjoyed the visits to Wisconsin and Michigan. Your advice and suggestions, sharing of model codes, or expertise on how to conduct complex experiments helped me a lot in performing my research.

Joep, Chu, Jan-Jurre, Robert, Fianne, Gijs, Sandra, Boris, Bram, João, Linsen en Niek, jullie hebben allemaal bijgedragen aan mijn onderzoek tijdens een stage of afstudeerproject. Ik vond het erg leuk en leerzaam om jullie op deze manier ook te kunnen helpen bij jullie eigen studie.

Bob, Hans, Klaas, Bas, Jeanine, thank you for participating as member of the reading committee or defense committee. I am very much aware of your busy agendas and I am grateful that you made time available for reading my thesis, preparing questions and being present at my defense ceremony.

Hans en Dick, hoewel het combineren van high density surface EMG en <sup>31</sup>P MRS uiteindelijk een zijproject binnen mijn promotieonderzoek is geworden, heb ik hier wel altijd met veel genoegen aan gewerkt. Onze gezamenlijke meetings bij Dick op de kamer vond ik altijd erg inspirerend. Ik ben blij dat we uiteindelijk een mooi artikel hebben kunnen publiceren over dit onderzoek.

Hanny, Harm, Luc, Stephan, René, Jeanine, Victor, Jolita, Chu en Carlijn, het project dat wij samen hebben opgestart en de tijdsplanning die we voor ogen hadden is erg ambitieus gebleken. Gelukkig kan Miranda nu het stokje van mij overnemen zodat het project gewoon voltooid kan worden. Ik heb onze samenwerking altijd als heel plezierig ervaren, waarvoor dank. Al terugblikkend, heb ik veel geleerd van het opstarten van dit onderzoek; ervaringen waar ik in de toekomst nog veel aan denk te gaan hebben.

Koen, bedankt voor het helpen met de 'final touch' van het coverdesign.

I also want to thank all members of the Computational Biology and Biomedical NMR group for the feedback and suggestions during group meetings, for the nice discussions during lunch and joyful drinks and dinners in the evenings or weekends.

Promoveren is als een berglandschap, het heeft pieken en dalen. Om hier goed mee om te kunnen gaan is relativeren en het hebben van voldoende momenten van afleiding erg belangrijk. Ik ben dan ook erg blij dat ik een fijne groep vrienden en familie heb die hier, waarschijnlijk onbewust, veel bij geholpen hebben.

Pap en mam, jullie volgen mijn stappen letterlijk al vanaf het eerste moment. Gaande mijn ontwikkeling is ook jullie rol blijven veranderen, maar altijd wel heel belangrijk voor me gebleven. Het geeft me een fijn gevoel te weten dat ik altijd terug kan vallen op jullie adviezen, steun en oprechte interesse. Ik vind dan ook dat het gereedkomen van dit proefschrift bovenal gezien moet worden als een symbolische kroon op de stappen die we samen gezet hebben.

Lieve Hanneke, woorden schieten eigenlijk tekort om jouw bijdrage aan dit werk op papier uit te drukken. Ik zal het toch proberen ...

Promoveren wordt vaak omschreven als een zwaar traject, met veel tegenslagen, frustraties en onzekerheden. Ondanks dat ik deze ervaringen deel, ben ik de afgelopen vier jaar altijd heel gelukkig geweest. Het samen opzoeken en genieten van leuke dingen, de steun en begrip waar ik altijd op kan rekenen, maar bovenal je liefde vormen het belangrijkste fundament voor dit geluk. Door de energie die jij me geeft, was het voor mij heel eenvoudig negatieve ervaringen om te buigen in iets positiefs en in oplossingen te blijven denken.

Ik hoop dan ook dat we nog lang samen onze dromen kunnen najagen, zodat we elkaar als individuen kunnen blijven versterken.

*Joep*

---

## LIST OF PUBLICATIONS

### International refereed journal publications

**Schmitz J.P.J.**, Wessels B., Groenendaal W., Nicolay K., Hilbers P.A.J., Prompers J.J., Wiseman R.W., van Riel N.A.W., Jeneson J.A.L., *In vivo and in silico studies of the regulation of glycolytic versus mitochondrial flux in normoxic skeletal muscle* (manuscript in preparation)

**Schmitz J.P.J.**, Ciapaite J., van den Broek N.M.A., Jonkers R.A.M., Nicolay K., Hilbers P.A.J., Prompers J.J., Jeneson J.A.L., van Riel N.A.W., *Integration of in vivo, in vitro and in silico methods for systems biology of mitochondrial function* (manuscript in preparation)

**Schmitz J.P.J.**, Jeneson J.A.L., Prompers J.J., Nicolay K., Hilbers P.A.J., van Riel N.A.W., *Mitochondrial function in skeletal muscle: Numerical dissection of a multi-factorial process* (manuscript submitted)

**Schmitz J.P.J.**, Groenendaal W., Wessels B., Wiseman R.W., Hilbers P.A.J., Nicolay K., Prompers J.J., Jeneson J.A.L., van Riel N.A.W., *Combined in vivo and in silico investigations of activation of glycolysis in contracting skeletal muscle* (manuscript submitted)

**Schmitz J.P.J.**, Jeneson J.A.L., van Oorschot J.W.M., Prompers J.J., Nicolay K., Hilbers P.A.J., van Riel N.A.W., *Prediction of muscle energy states at low metabolic rates requires feedback control of mitochondrial respiratory chain activity by inorganic phosphate*, (2012) PLoS ONE; 7(3):E34118

**Schmitz J.P.J.**, van Dijk J.P., Hilbers P.A.J., Nicolay K., Jeneson J.A.L., Stegeman D.F., *Unchanged muscle fiber conduction velocity relates to mild acidosis during exhaustive bicycling*, (2012) European Journal of Applied Physiology; 112(5):1593-1602

**Schmitz J.P.J.**, Vanlier J., van Riel N.A.W., Jeneson J.A.L., *Computational modeling of mitochondrial energy transduction*, (2011) Critical Reviews in Biomedical Engineering; 39(5):363-377

Jeneson J.A.L., ter Veld F., **Schmitz J.P.J.**, Meyer R.A., Hilbers P.A.J., Nicolay K., *Similar mitochondrial activation kinetics in wild-type and creatine kinase-deficient fast-twitch muscle indicate significant Pi control of respiration*, (2011) American Journal of Physiology Regulatory Integrative and Comparative Physiology; 300(6):R1316-R1325

Jeneson J.A.L., **Schmitz J.P.J.**, Hilbers P.A.J., Nicolay K., *An MR-compatible bicycle ergometer for in-magnet whole body human exercise testing*, (2010) Magnetic Resonance in Medicine; 63(1): 257-261

**Schmitz, J.P.J.**, van Riel N.A.W., Nicolay K., Hilbers P.A.J., *Silencing of glycolysis in muscle: experimental observation and numerical analysis*, (2010) Experimental Physiology; 95(2):380-397



Jeneson J.A.L., **Schmitz J.P.J.**, van den Broek N.M.A., van Riel N.A.W., Hilbers P.A.J., Nicolay K., Prompers J.J., *Magnitude and control of mitochondrial ADP sensitivity*, (2009) American Journal of Physiology Endocrinology and Metabolism; 297(3):E774- E784

Balguid A., Driessen N.J., Mol A., **Schmitz J.P.J.**, Verheyen F., Bouten C.V., Baaijens F.P., *Stress related collagen ultrastructure in human aortic valves – implications for tissue engineering*, (2008) Journal of Biomechanics; 41(12):2612-2617

**Abstracts selected for oral presentation at international conferences  
(first author only)**

**Schmitz J.P.J.**, Wessels B., Groenendaal W., Wiseman R.W., Nicolay K., Hilbers P.A.J., Prompers J.J., Jeneson J.A.L., van Riel N.A.W., *In vivo and in silico investigations of the regulation of glycolytic versus mitochondrial ATP synthesis in skeletal muscle*. Proceedings of the 15th Workshop of the International Study Group for Systems Biology (ISGSB 2012), 23 - 26 September 2012, Ameland, Netherlands

**Schmitz J.P.J.**, van den Broek N.M.A., Ciapaite J., Jonkers R.A.M., van Riel N.A.W., Prompers J.J., Nicolay K., Hilbers P.A.J., Jeneson J.A.L., *Understanding the origin of mitochondrial (dys)function: a new systems biology based research strategy*. Proceedings of the 14th Workshop of the International Study Group for Systems Biology (ISGSB 2010), 6 - 10 September 2010, Vladimir, Russia

**Schmitz J.P.J.**, van Riel N.A.W., Jeneson J.A.L., Nicolay K., Hilbers P.A.J., *A multi scale computational model of human skeletal muscle to quantify metabolite dynamics in individual fiber types from 31P MRS measurements*. Book of abstracts of the 2nd Dutch Conference on Bio-Medical Engineering (BME 2009), 22 - 23 January 2009, Egmond aan Zee, Netherlands

**Schmitz J.P.J.**, van Dijk J.P., Jeneson J.A.L., Hilbers P.A.J., Nicolay K., Stegeman D.F., *Alternating motor unit recruitment during bicycle exercise: indications from HDsEMG and 31P NMR spectroscopy*. Proceedings of the XVIIth International Society of Electrophysiology and Kinesiology Conference (ISEK 2008), 18 - 21 June 2008, Niagara Falls, Canada

**Schmitz J.P.J.**, Jeneson J.A.L., Nicolay K., Hilbers P.A.J., van Riel N.A.W., *Modeling the glycolytic pathway in human skeletal muscle tissue; understanding the regulation of its hundredfold dynamic range*. 9th International Conference on Systems Biology (ICSB 2008), 22 - 28 August 2008, Gothenburg, Sweden

**Schmitz J.P.J.**, Jeneson J.A.L., Nicolay K., Hilbers P.A.J., van Riel N.A.W., *A multi-scale model of human skeletal muscle*. Proceedings of the BMES 2008 Annual Fall Meeting (BMES 2008), 2 - 4 October 2008, St. Louis, Missouri, United States



## CURRICULUM VITAE



Joep Schmitz was born December 7, 1984, in Roermond, The Netherlands. He grew up in Helden and graduated from secondary school (gymnasium, *cum laude*) at the Bouwens van der Boijecollege in Panningen in 2003. In the same year he started his study Biomedical Engineering at Eindhoven University of Technology. During his study he conducted extra-curricular activities as a research assistant in the Tissue Engineering lab of the department of Biomedical Engineering. Joep carried out an internship at the Clinical Neurophysiology group of Radboud University Nijmegen Medical Centre under the supervision of prof.dr.ir. Dick Stegeman. During this internship he combined high density surface electromyography and  $^{31}\text{P}$  magnetic resonance spectroscopy to study motor unit recruitment patterns during bicycle exercise. His master project was carried out in the Computational Biology group (prof.dr. Peter Hilbers) and Biomedical NMR group (prof.dr. Klaas Nicolay) of Eindhoven University of Technology. His masters' thesis described how computational modeling and  $^{31}\text{P}$  magnetic resonance spectroscopy were successfully combined to study energy metabolism in skeletal muscle. For this thesis he received the best master project award from the department of Biomedical Engineering in 2008. In the same year he also obtained his masters degree (*cum laude*). Joep continued his research on energy metabolism of skeletal muscle during a PhD study. This project was again carried out in Computational Biology group and Biomedical NMR group of Eindhoven University of Technology under the supervision of prof.dr. Peter Hilbers, dr. Natal van Riel and dr. Jeroen Jeneson. During the project he also collaborated with the research groups of prof.dr. Daniel Beard at the Medical College of Wisconsin and dr. Robert Wiseman at Michigan State University and visited these groups on several occasions. The results of this PhD project are described in this dissertation, entitled 'Systems Biology of Energy Metabolism in Skeletal Muscle'. At the moment, Joep is continuing his academic career as postdoctoral research fellow at the molecular cell physiology group of the VU University Amsterdam, where he studies the regulation of glycolysis in yeast.